



Geneeskundige Stichting Koningin Elisabeth
Fondation Médicale Reine Elisabeth
Königin-Elisabeth-Stiftung für Medizin
Queen Elisabeth Medical Foundation

Verlag – Rapport – Bericht – Report

2024

G.S.K.E. – F.M.R.E. – K.E.S.M. – Q.E.M.F.

www.fmre-gske.be
www.fmre-gske.eu
www.fmre-gske.com

Progress reports of the research projects of young researchers, supported by the Queen Elisabeth Medical Fondation in collaboration with the following professors and doctors (2024)

1. Interuniversity research projects

Prof. dr. Geert Van Loo (UGent)	9
Prof. Kiavash Movahedi (VUB)	9
Prof. dr. Renzo Manusco (UAntwerpen)	21
Prof. dr. Joris De Wit (KU Leuven)	21
Prof. dr. Karelle Leroy (ULB)	27
Prof. dr. Laurence Ris (UMONS)	27
Prof. dr. Kristel Slegers (UAntwerpen)	27
Prof. dr. Sarah Weckhuysen (UAntwerpen)	43
Prof. dr. Bjorn Menten (UGent)	43
Prof. dr. Ann Massie (VUB)	49
Prof. dr. Lutgarde Arckens (KU Leuven)	49

2. University research projects

Prof. dr. Bart De Strooper (KU Leuven-VIB)	63
Prof. dr. Pierre Vanderhaeghen (KU Leuven-VIB)	69
Prof. dr. Veerle Baekelandt (KU Leuven)	75
Prof. dr. Thomas Voets (KU Leuven)	85
Prof. dr. Pierre Maquet (ULiège)	95

3. Research projects of young researchers

Sielke Caestecker (PhD student) & promotor prof. Robrecht Raedt (UGent)	103
Dr. Delfien Syx (UGent)	111
Dr. Marijne Vandenbergh (UAntwerpen)	123
Dr. Barbara M.P. Willekens (UAntwerpen)	131
Dr. Wouter Peelaerts (KU Leuven)	137
Dr. Sarah van Veen (KU Leuven)	149
Prof. Giulia Liberati (UCLouvain)	179
Prof. dr. Jeroen Bogie (UHasselt)	189
Prof. dr. Bieke Broux (UHasselt)	213
Dr. Sophie Laguesse (ULiège)	221



Geneeskundige Stichting Koningin Elisabeth
Fondation Médicale Reine Elisabeth
Königin-Elisabeth-Stiftung für Medizin
Queen Elisabeth Medical Foundation

Interuniversitaire onderzoeksprojecten
2023-2025 gefinancierd door de G.S.K.E.

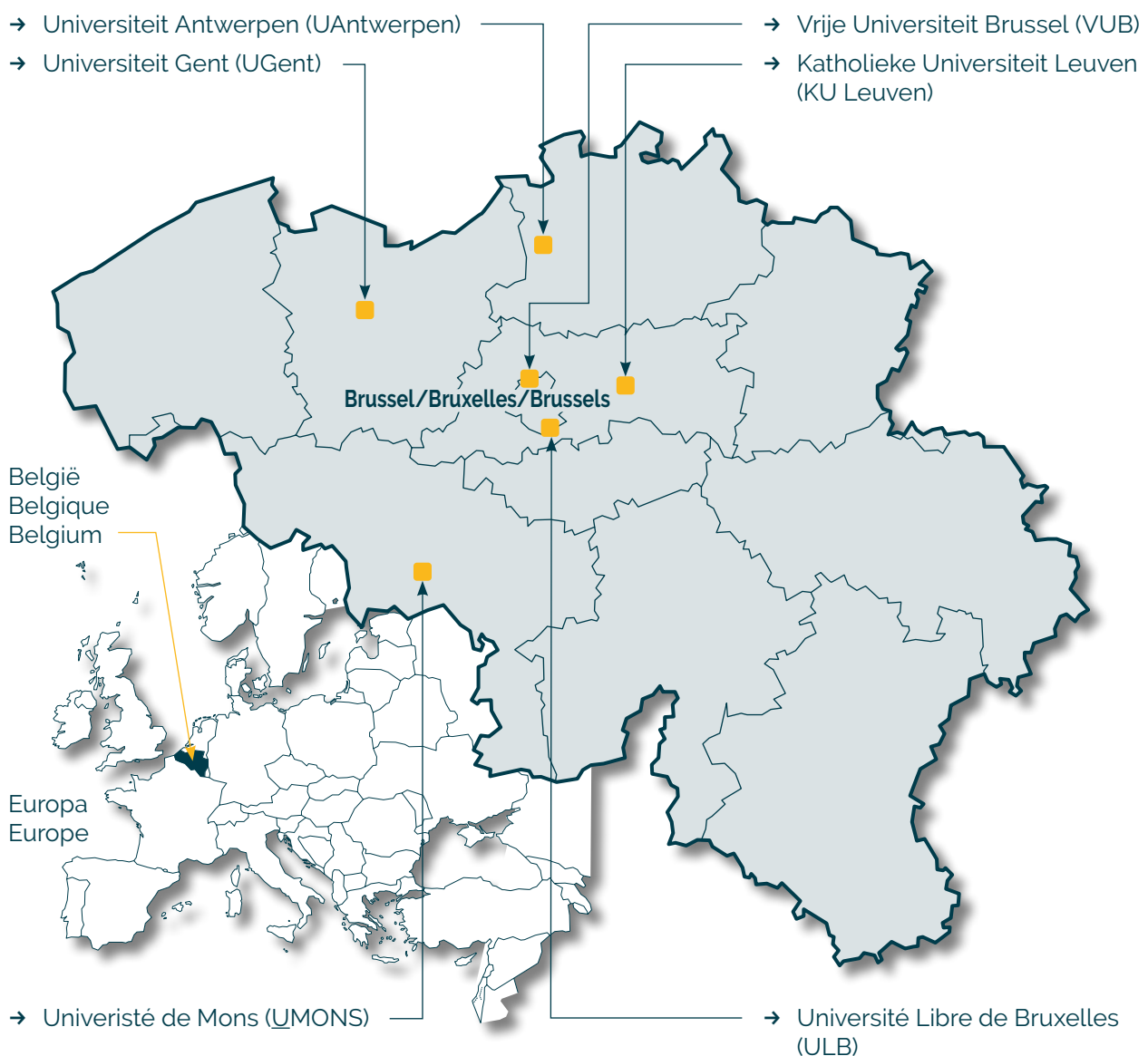
Projets de recherche interuniversitaire
2023-2025 subventionnés par la F.M.R.E.

Interuniversity research projects
2023-2025 funded by the Q.E.M.F.

Universiteiten met onderzoeksprogramma's die gesteund worden door de G.S.K.E.

Universités ayant des programmes de recherche subventionnés par la F.M.R.E.

Universities having research programs supported by the Q.E.M.F.



Interuniversitaire onderzoeksprojecten 2023-2025 gefinancierd door de G.S.K.E.

Projets de recherche interuniversitaire 2023-2025 subventionnés par la F.M.R.E.

Interuniversity research projects 2023-2025 funded by the Q.E.M.F.

Prof. dr. Geert Van Loo (UGent)

Prof. Kiavash Movahedi (VUB)

OTULIN in neuroinflammation and Alzheimer pathology

Prof. dr. Sarah Weckhuysen (UAntwerpen)

Prof. dr. Bjorn Menten (UGent)

Detection of somatic mutations and disease-defining methylation patterns in brain tissue and cerebrospinal fluid of patients with non-acquired focal epilepsy

Prof. dr. Renzo Manusco (UAntwerpen)

Prof. dr. Joris De Wit (KU Leuven)

Dissecting the molecular basis of microglia-synapse communication in AD

Prof. dr. Ann Massie (VUB)

Prof. dr. Lutgarde Arckens (KU Leuven)

The xCT^{-/-} killifish to validate the potential of system xc⁻ as therapeutic target in Parkinson's disease

Prof. dr. Karelle Leroy (ULB)

Prof. dr. Laurence Ris (UMONS)

Prof. dr. Kristel Slegers (UAntwerpen)

Involvement of diabetes and antidiabetic treatment on tau pathology propagation



Geneeskundige Stichting Koningin Elisabeth
Fondation Médicale Reine Elisabeth
Königin-Elisabeth-Stiftung für Medizin
Queen Elisabeth Medical Foundation

Progress report of the interuniversity research project of

Prof. dr. Geert Van Loo (UGent)
Prof. Kiavash Movahedi (VUB)

Prof. dr. Geert van Loo (UGent)

VIB-UGent Inflammation

Technologiepark 71

9052 Gent-Zwijnaarde

Belgium

T +32-(0)9 3313761

Geert.vanloo@irc.vib-ugent.be

Prof. dr. Kiavash Movahedi (VUB)

Research Center Vrije Universiteit Brussel

Laarbeeklaan 103 building E, room E234

1090 Jette-Brussels

Belgium

T +32-(0)2 4774569

kiavash.movahedi@vub.be

OTULIN in neuroinflammation and Alzheimer pathology

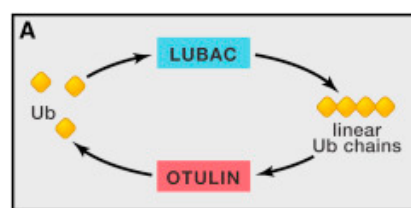
1. Summary of the research project:

Inflammatory signaling pathways are subjected to tight regulation to avoid chronic inflammation and the development of inflammatory pathology. One of the proteins involved in such regulation is the deubiquitinating enzyme OTULIN. In this project, we investigate the role of OTULIN in neuroinflammation and Alzheimer pathology.

OTULIN in neuroinflammation and Alzheimer pathology

Introduction

Inflammation is a protective response that induces repair in conditions of cellular damage and stress. However, strict control of inflammatory signaling pathways is essential to prevent chronic inflammation and the development of inflammatory pathologies. This control is exercised at various levels, including the reversible modification of signaling proteins. Ubiquitination is a posttranslational protein modification in which ubiquitin chains are covalently attached to target proteins. This process earmarks these proteins for proteasomal degradation or allows them to function as scaffolds to recruit other proteins and mediate downstream signaling [1,2]. Linear ubiquitination involves the linkage of ubiquitin via its amino-terminal methionine residue (Met1 or M1) to another ubiquitin molecule, a process mediated by the linear ubiquitin chain assembly complex (LUBAC) (Figure 1). **LUBAC is the sole E3 ubiquitin ligase complex known to generate linear chains**, and is essential for i) NF- κ B-mediated inflammatory gene expression in response to various stimuli, including TNF, IL-1 β , and ligands activating TLRs, NOD2 and NLRP3; and ii) for preventing TNF-induced cell death [3–12]. Genetic loss of LUBAC proteins causes immunodeficiency and auto-inflammation in humans [13,14], and embryonic lethality or inflammatory phenotypes in mice [4,10,11,15–17], establishing the importance of LUBAC-mediated M1 signaling for normal mammalian physiology.



Ubiquitination is reversed by **deubiquitinating enzymes (DUBs)** that cleave ubiquitin chains from their substrates [2]. About a hundred different DUBs have been identified so far, but mainly A20, Cyldromatosis (CYLD) and **OTULIN have been characterized as key DUBs involved in the negative regulation of NF- κ B activation and cell death** [18] (Figure 1). OTULIN (OTU Deubiquitinase with Linear Linkage Specificity), also known as Fam105b or Gumby, was only recently discovered in mice and human [19,20]. Homozygous hypomorphic mutations in the human *OTULIN* gene have been identified as causing an early-onset, potentially fatal, autoinflammatory disease [21–24]. Mice harboring a point mutation in *OTULIN*, abolishing its activity to cleave M1 chains, are not viable and die during development [20,25], while mice with inducible (postnatal) deletion of *OTULIN* develop acute systemic inflammation due to dysregulated NF- κ B activation and cytokine

production [22]. **Together, these data identify OTULIN as a crucial regulatory mechanism in inflammatory signaling.**

Very little is known about the role of OTULIN in the central nervous system (CNS) and in CNS inflammation. A recent study showed that OTULIN controls microglia activation and suppresses neuroinflammation in a rat model of stroke [26]. Microglia, the resident tissue macrophages of the CNS, are important for maintaining CNS homeostasis, but also critically contribute to CNS pathology [27]. Interestingly, **a large meta-genome-wide association study (GWAS) by the European Alzheimer and Dementia Biobank reaffirmed the implication of microglia in AD and provided genetic evidence linking LUBAC and OTULIN to AD** [28].

The aim of the project is to characterize the role of OTULIN in neuroinflammation and Alzheimer disease (AD), the most common progressive form of dementia, affecting over 25 million people worldwide [29,30]. Neuroinflammation is increasingly regarded as a key component that actively contributes to AD pathology. NF- κ B signaling, activated by amyloid- β (A β) and/or by the microtubule-associated protein Tau, has been shown to drive microglia-mediated A β and Tau toxicity leading to AD-associated learning and memory deficits [31-33]. However, **the specific immune mechanisms through which microglia contribute to AD-associated neuroinflammation, as well as the eventual role of OTULIN in this process, remain largely elusive and require further exploration.** In our project, using a CNS myeloid-specific OTULIN knockout model in combination with AD disease models, **we aim to investigate the specific role of OTULIN in the regulation of microglia activation, neuroinflammation and AD pathology.**

2. Results so far

2.1. Characterization of unchallenged OTULIN^{Cx3Cr1-KO} mice

To specifically address the role of OTULIN in microglia in CNS homeostasis and pathology, the van Loo lab generated mice with a 'floxed' *OTULIN* allele [34] and crossed these mice with *Cx3Cr1-CreErt2* transgenic mice, allowing Cre-mediated gene deletion in myeloid cells following tamoxifen treatment [35] (Figure 2A). CNS-resident macrophage populations including microglia can be specifically targeted using this approach which relies on microglial longevity and its self-renewing capacity [36].

Successful OTULIN deletion in microglia was confirmed by Western blot analysis of fluorescence-activated cell sorted (FACS) microglia *ex vivo* and of primary cultured microglia *in vitro* (Figure 2B). Tamoxifen-induced ablation of OTULIN in mice did not induce any gross abnormalities, as could be observed by histological analysis of the brain using H&E staining (Figure 2C). However, immunohistochemical analysis using the microglial marker Iba-1 revealed a spatially restricted increase in microglia number in the hippocampi, but not the cortex, of OTULIN^{Cx3Cr1-KO} mice compared to control littermates (Figure 2D). The enhanced presence of microglia in OTULIN^{Cx3Cr1-KO} CNS was confirmed by manual counting of Iba-1⁺ microglia (Figure 2E). This regional difference in the number of Iba-1⁺ cells suggest that the lack of OTULIN induces proliferation of adult microglia. We next analyzed how OTULIN deficiency in CNS resident myeloid cells has an impact on T-cell recruitment to the spinal cord in steady state conditions. Interestingly, the number of both CD4⁺ T-cells, CD8⁺ T-cells and Foxp3⁺ Tregs were significantly increased in the spinal cord of OTULIN^{Cx3Cr1-KO} mice (Figure 2F). This suggests that deficiency of OTULIN in microglia induces strong recruitment of different types of leukocytes to the spinal cord.

To reveal how microglial OTULIN deficiency is associated with CNS-wide inflammatory dys-homeostasis, we expression profiled by single-cell RNA sequencing CD45^{int}CD11b⁺ microglia sorted from brains of 10-12 week old OTULIN^{Cx3Cr1-KO} and control littermate mice. We performed clustering analysis, which resulted in the identification of 7 major subpopulations of microglia (Figure 3A). Three of these clusters express high levels of so-called homeostatic microglia (HoM, H1M and H2M) markers (*Ptprc*, *Itgam*, *P2ry12*, *Slc2a5*, *Tmem119*, *Tgfbr1*, *Siglech*, *Sall1*, *Fcrls*, *Mertk*, *Gpr34*, *Rhob*, *Olfml3*). This clustering analysis also identifies a distinct non-microglial CNS macrophage population, the 'Border-associated macrophages' ('BAM' cluster) (Figure 3A). Of particular interest are the clusters that show downregulated expression of homeostatic microglial genes in OTULIN^{Cx3Cr1-KO} and instead upregulate specific expression profiles associated with distinct functionalities of the activated microglia. These clusters, designated as 'interferon response microglia' (IRM), 'activated response microglia' (ARM), and 'cycling and proliferating microglia' (CPM), show upregulated expression of genes associated with interferon signalling (*Ifit2*, *Ifit3*, *Oasl2*, *Ifitm3*, *Irf7*), with a 'disease-associated microglia' (DAM) phenotype involved in inflammatory processes (*Cst7*, *Itgax*, *Cd74*, *Lgals3*, *Clec7a*, *Lpl*, *Csf1*, *Lilbr4a*), and with cell cycle regulation and proliferation (*Mki67*, *Cdk1*, *Top2a*, *Mcm2*), respectively, and are represented more strongly in conditions of OTULIN deficiency (Figure 3B-C) [37-39]. The ARM cluster also displays genes linked to inflammatory signaling (*Nfkb1*, *Nfkb2*, *Relb*, *Il1b*, *Tnf*, *Ccl4*) as being upregulated in OTULIN^{Cx3Cr1-KO} microglia (Figure 3B).

Together, these data demonstrate the importance of OTULIN in microglia activation and suggest that defects in OTULIN function may contribute to CNS pathology and neurodegeneration.

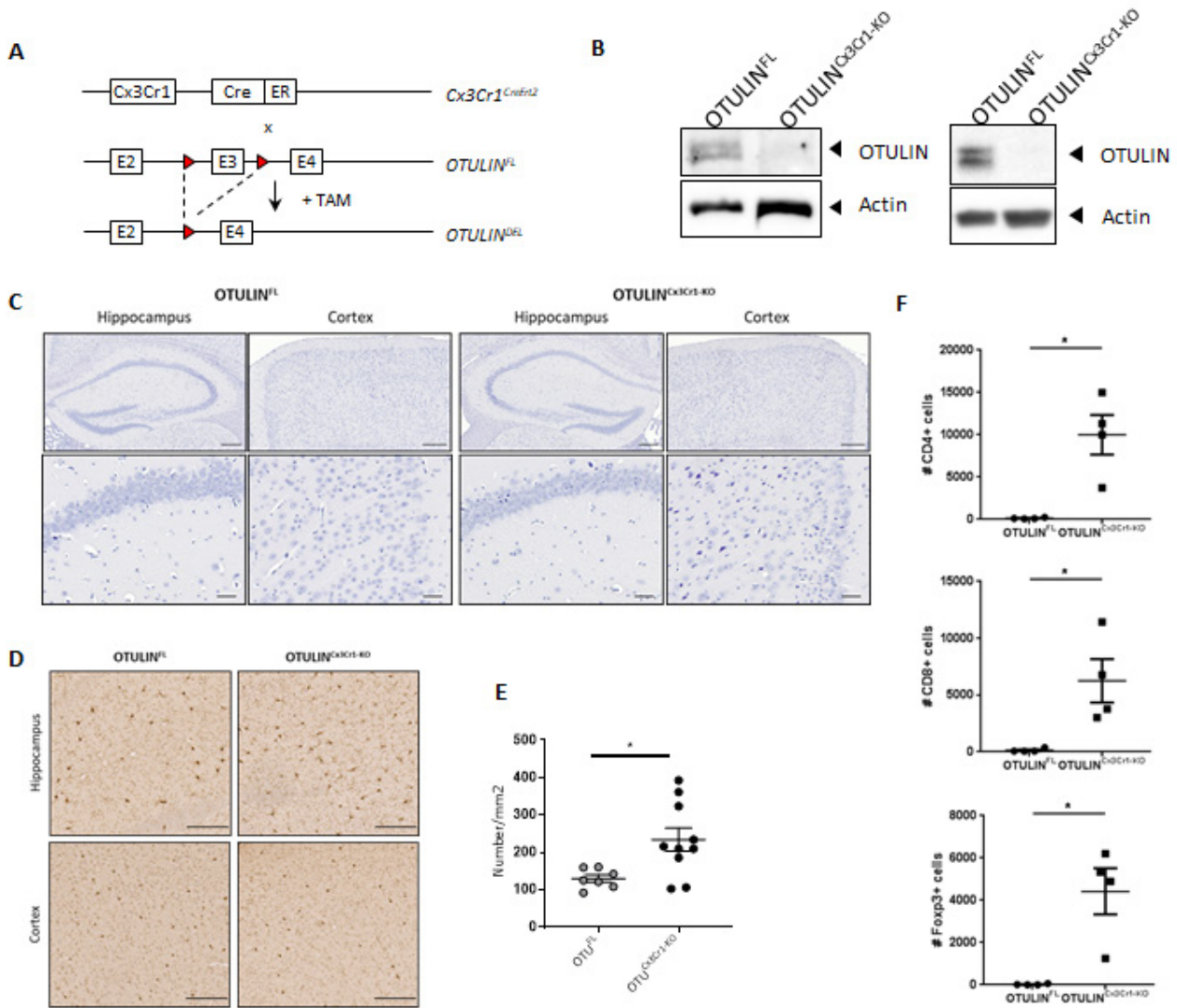


Figure 2. OTULIN deletion in CNS-resident myeloid cells induces a spontaneous neuroinflammatory phenotype. (A) Scheme for the Tam-inducible induction of Cre recombination and OTULIN deletion in CNS-resident myeloid cells. (B) Immunoblot for OTULIN expression in *ex vivo* FACS-sorted microglia from control (OTULIN^{FL}) and OTULIN^{Cx3Cr1-KO} mice 5 weeks after TAM injection (left), and in lysates from primary microglia from control (OTULIN^{FL}) and OTULIN^{Cx3Cr1-KO} mice after stimulation with 4-OH-TAM (right). Actin is shown as loading control. (C) H&E staining on section of cortex and hippocampus of 10–12 week old OTULIN^{FL} and OTULIN^{Cx3Cr1-KO} mice (5 weeks after TAM injection). Scale bars represent 200 μ m (overview, upper) and 50 μ m (zoom, lower). (D) Immunohistochemistry for Iba-1⁺ microglia in the hippocampus and cerebral cortex of control (OTULIN^{FL}) and OTULIN^{Cx3Cr1-KO} mice. Representative images are displayed and scale bars represent 100 μ m. (E) Number of Iba-1⁺ ramified parenchymal microglia. Each symbol represents one mouse, with 7 and 10 mice per group. Data presented as mean \pm SEM. Significant differences determined by a Mann–Whitney U-statistical test (* $p < 0.05$). (F) Flow cytometric quantification of the number of CD3⁺CD4⁺ T cells, CD3⁺CD8⁺ T cells and CD3⁺CD4⁺Foxp3⁺ Tregs in the spinal cord of control (OTULIN^{FL}) and OTULIN^{Cx3Cr1-KO} mice 4 weeks post TAM injection. Each symbol represents one mouse and data are presented as mean \pm SEM. Significant differences were determined by Mann–Whitney U-statistical test (* $p < 0.05$).

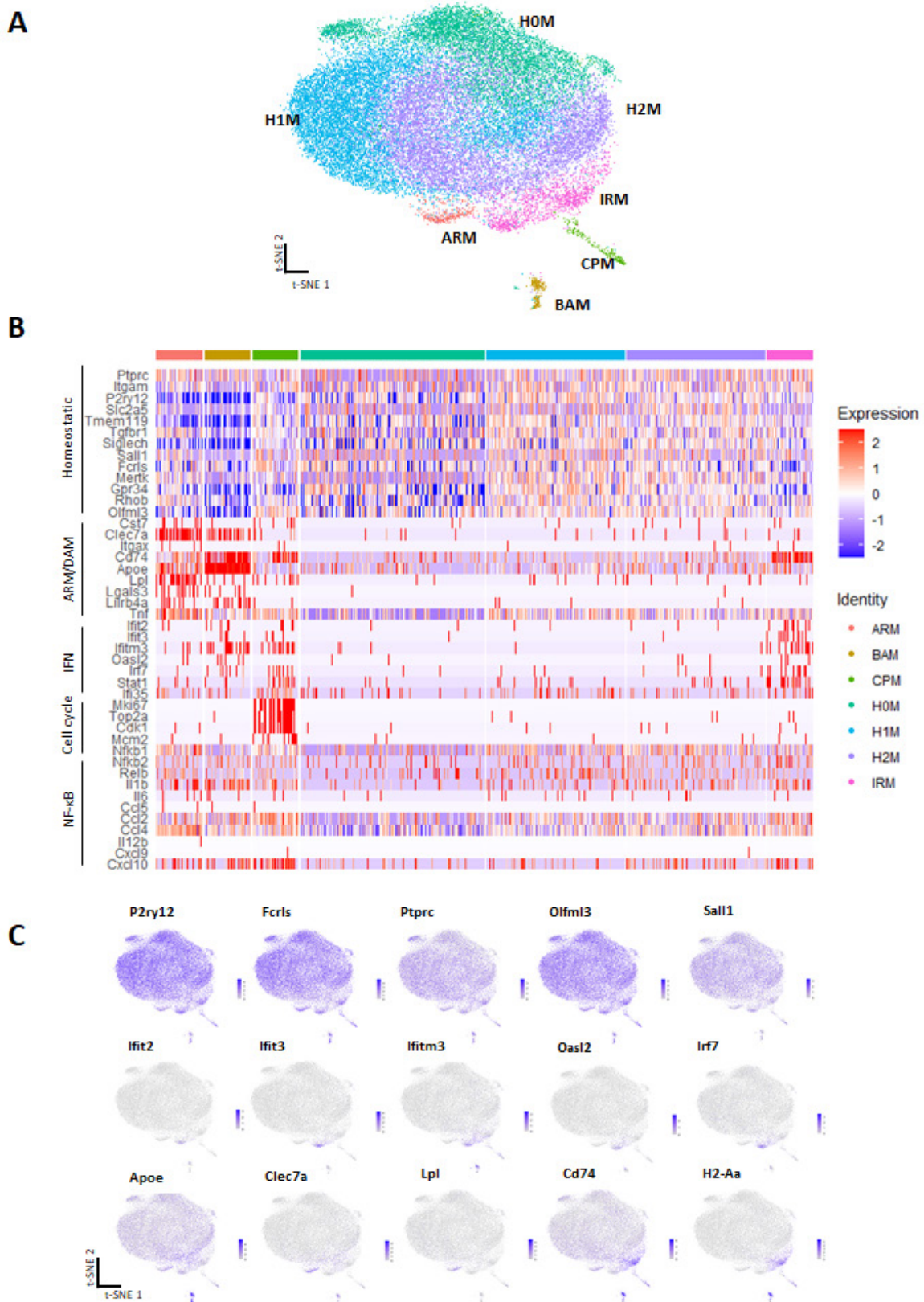


Figure 3. Single cell RNA sequencing reveals distinct subpopulations of activated microglia in conditions of OTULIN deficiency (A) t-distributed stochastic neighbour embedding (t-SNE) plot visualizing 13500 single microglial cells. Cells are coloured according to clusters identified with Seurat's k-nearest neighbours approach (H0M, H1M and H2M, homeostatic microglia; ARM, activated response microglia; IRM, interferon response microglia; CPM, cycling and proliferating microglia). (B) Heatmap showing clustering analysis of single cells, featuring 40 variable genes subdivided by cluster. (C) t-SNE plot as in (A), coloured by the level of normalized expression of selected genes listed in text. The ARM cluster shows increased expression of Apoe and inflammation markers (*Cst7*, *Itgax*, *Clec7a*), while the IRM cluster is enriched for interferon genes (*Ifit2*, *Ifit3*, *Ifitm3*, *Oasl2*, and *Irf7*). Both ARM and IRM clusters display a reduction in expression of homeostatic genes.

2.2. Study of OTULIN in AD pathology

A recent genome-wide association study (GWAS) identified *OTULIN* as a new risk locus for Alzheimer disease AD [28]. To experimentally validate the importance of OTULIN for microglia activation and AD pathology, OTULIN^{Cx3Cr1-KO} mice and control littermates have been crossed with three genetic models of AD : the *AppNL-G-F* knock-in mouse model of β -amyloid-induced neuropathology, the *APP/PS1* knock-in mouse model of β -amyloid-induced neuropathology, and the P301S Tau transgenic mouse model. *APP/PS1* mice ectopically overexpress the KM670/671NL 'Swedish' mutation in the amyloid precursor protein (APP) concomitant with mutant human presenilin-1 (PS1) in CNS neurons, and develop an early and robust AD pathology [40]. In contrast, *AppNL-G-F* mice express the human A sequence which harbors the Swedish (KM670/671NL), Beyreuther/Iberian (I716F) and Arctic (E693G) mutations in the *App* gene [41]. These mice develop typical A pathology, neuroinflammation, synaptic defects and memory impairment in an age-dependent manner, most similar to the defects which develop in human AD patients [41]. P301S Tau transgenic mice develop filamentous Tau lesions in association with neuroinflammation, prominent microgliosis and neuron loss [42]. Disease development in control (OTULIN-expressing) and microglia OTULIN-deficient (OTULIN^{Cx3Cr1-KO}) AD mice (*AppNL-G-F*, *APP/PS1* or P301S Tau) is being evaluated at different ages of the mice (20 weeks, 40 weeks and 60 weeks of age). At endpoint, brain sections are being evaluated for degree of A deposition, Tau hyperphosphorylation, astro- and microgliosis, presence of inflammatory markers and neuronal cell death. These studies are still ongoing, but our preliminary results on the first group of *APP/PS1* mice demonstrate that OTULIN^{Cx3Cr1-KO} hippocampus shows more microglia and a higher number of A plaques, suggest that OTULIN deletion in CNS-resident myeloid cells exacerbates AD pathology in *APP/PS1* mice. (Figure 4).

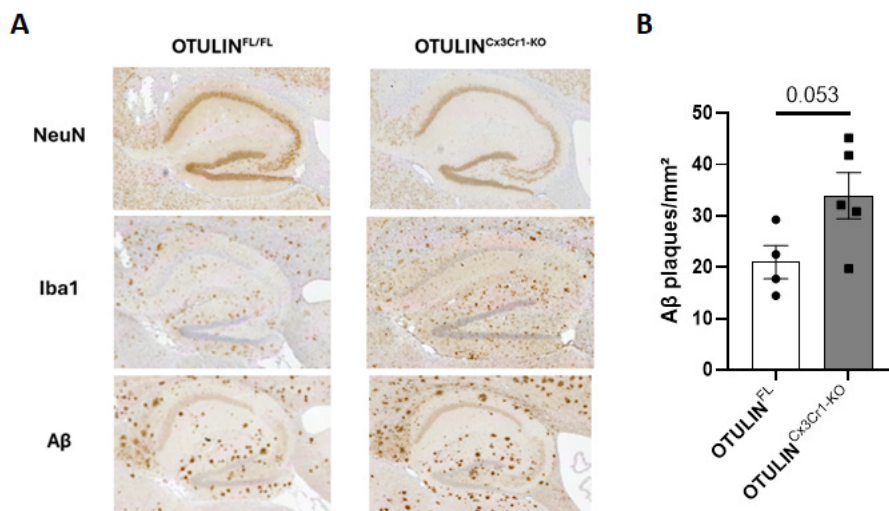


Figure 4. OTULIN deletion in CNS-resident myeloid cells exacerbates AD pathology in *APP/PS1* mice. (A) Immunohistochemistry for NeuN⁺ neurons, Iba1⁺microglia and 6E10⁺ amyloid plaque load in the hippocampus of 50 week-old OTULIN^{FL} and OTULIN^{Cx3Cr1-KO} *APP/PS1* mice. Representative images are displayed. (B) Quantification of the area covered by 6E10⁺ amyloid plaque deposits in hippocampus of 50 week-old OTULIN^{FL} and OTULIN^{Cx3Cr1-KO} *APP/PS1* mice. Each symbol represents one mouse. Data are represented as mean \pm SEM.

In parallel with the studies described above, we are performing CITE-seq of immune cells obtained from control and OTULIN^{Cx3Cr1-KO} *APP/PS1* and P301S Tau transgenic brains at young (20 weeks) and older (60 weeks) age. CITE-seq offers the possibility to combine transcriptome-wide gene expression analysis with simultaneous profiling of hundreds of surface protein markers, as previously shown by the Movahedi lab [43]. In-depth analysis of these single-cell RNA profiles will allow us to identify the tissue signals that drive neuroinflammation and AD pathology and help to understand the molecular interplay between the different cell types (glial cells, neurons,

immune cells) during AD development. CITE-Seq data will be complemented with single-cell spatial profiling using the newly introduced Akoya PhenoCycler-Fusion platform.

The Movahedi lab has been optimizing the Akoya PhenoCycler-Fusion technology for fixed frozen brain tissue. In short, the PhenoCycler-Fusion system is an automated fluidics control unit coupled to a microscope that allows automatic successive rounds of staining on the same tissue slide. To do so, Akoya uses barcoded antibodies and complementary oligonucleotides labeled with fluorophores. In each cycle, up to three oligonucleotides specifically interact with their corresponding tissue-bound barcoded antibodies, thus allowing imaging of the corresponding antibodies. Afterwards, the imaged reporters are washed away and new reporters are added in a new cycle, altogether resulting in the visualization of up to 100 markers in the same tissue slide. The Movahedi lab successfully custom-conjugated several markers relevant for studying neurodegenerative disease and DAMs: GFAP (astrocytes), Iba1 (microglia), Clec7a (DAMs), Lyve-1 (border associated macrophages), ERTR7 (dural fibroblasts), and Nestin (neuronal stem cells). Together with commercially available antibodies, they compiled a 30-marker panel that allows in-depth characterization of different immune populations in the mouse brain, which are being used for disease profiling in *APP/PS1* and P301S mice. Analysis is still ongoing.

2.3. Study of OTULIN in MS/EAE pathology

Finally, to address the role of microglial OTULIN in the context of CNS pathology, OTULIN^{Cx3Cr1-KO} and control littermate mice will be immunized with a myelin antigen (MOG35-55) and the development and progression of multiple sclerosis (MS)-like disease, so-called experimental autoimmune encephalomyelitis (EAE), will be monitored by assessing clinical disease symptoms and body weight. Pathology will be evaluated by histology on spinal cord sections at day 14 post immunization, and demyelination, immune cell infiltration (of both T-cells and macrophages), and neurodegeneration in the spinal cord of these mice will be assessed. In addition, the mechanisms by which OTULIN regulates microglia activation will be addressed by *in vitro* and *ex vivo* studies. These studies have been initiated and are ongoing.

3. References

1. Iwai, K. et al. (2014) Linear ubiquitin chains: NF- κ B signalling, cell death and beyond. *Nat. Rev. Mol. Cell Biol.* 15, 503–508
2. Clague, M.J. et al. (2019) Breaking the chains: deubiquitylating enzyme specificity begets function. *Nat. Rev. Mol. Cell Biol.* 20, 338–352
3. Haas, T.L. et al. (2009) Recruitment of the Linear Ubiquitin Chain Assembly Complex Stabilizes the TNF-R1 Signaling Complex and Is Required for TNF-Mediated Gene Induction. *Mol. Cell* 36, 831–844
4. Gerlach, B. et al. (2011) Linear ubiquitination prevents inflammation and regulates immune signalling. *Nature* 471, 591
5. Zak, D.E. et al. (2011) Systems analysis identifies an essential role for SHANK-associated RH domain-interacting protein (SHARPIN) in macrophage Toll-like receptor 2 (TLR2) responses. *Proc. Natl. Acad. Sci.* 108, 11536–11541
6. Damgaard, R.B. et al. (2012) The Ubiquitin Ligase XIAP Recruits LUBAC for NOD2 Signaling in Inflammation and Innate Immunity. *Mol. Cell* 46, 746–758
7. Rodgers, M.A. et al. (2014) The linear ubiquitin assembly complex (LUBAC) is essential for NLRP3 inflammasome activation. *J. Exp. Med.* DOI: 10.1084/jem.20132486
8. Kumari, S. et al. (2014) Sharpin prevents skin inflammation by inhibiting TNFR1-induced keratinocyte apoptosis. *eLife* 3, e03422
9. Rickard, J.A. et al. (2014) TNFR1-dependent cell death drives inflammation in Sharpin-deficient mice. *eLife* 3, e03464
10. Peltzer, N. et al. (2014) HOIP Deficiency Causes Embryonic Lethality by Aberrant TNFR1-Mediated Endothelial Cell Death. *Cell Rep.* 9, 153–165
11. Peltzer, N. et al. (2018) LUBAC is essential for embryogenesis by preventing cell death and enabling haematopoiesis. *Nature* 557, 112–117
12. Taraborrelli, L. et al. (2018) LUBAC prevents lethal dermatitis by inhibiting cell death induced by TNF, TRAIL and CD95L. *Nat. Commun.* 9, 3910
13. Boisson, B. et al. (2012) Immunodeficiency, autoinflammation and amylopectinosis in humans with inherited HOIL-1 and LUBAC deficiency. *Nat. Immunol.* 13, 1178–1186
14. Boisson, B. et al. (2015) Human HOIP and LUBAC deficiency underlies autoinflammation, immunodeficiency, amylopectinosis, and lymphangiectasia. *J. Exp. Med.* 212, 939–951
15. Tokunaga, F. et al. (2011) SHARPIN is a component of the NF- κ B-activating linear ubiquitin chain assembly complex. *Nature* 471, 633–636
16. Ikeda, F. et al. (2011) SHARPIN forms a linear ubiquitin ligase complex regulating NF- κ B activity and apoptosis. *Nature* 471, 637
17. Zinngrebe, J. et al. (2016) LUBAC deficiency perturbs TLR3 signaling to cause immunodeficiency and autoinflammation. *J. Exp. Med.* 213, 2671–2689
18. Lork, M. et al. (2017) CYLD, A20 and OTULIN deubiquitinases in NF- κ B signaling and cell death: so similar, yet so different. *Cell Death Differ.* 24, 1172–1183
19. Keusekotten, K. et al. (2013) OTULIN Antagonizes LUBAC Signaling by Specifically Hydrolyzing Met1-Linked Polyubiquitin. *Cell* 153, 1312–1326
20. Rivkin, E. et al. (2013) The linear ubiquitin-specific deubiquitinase gumby regulates angiogenesis. *Nature* 498, nature12296
21. Zhou, Q. et al. (2016) Biallelic hypomorphic mutations in a linear deubiquitinase define otulipenia, an early-onset autoinflammatory disease. *Proc. Natl. Acad. Sci. U. S. A.* 113, 10127–10132
22. Damgaard, R.B. et al. (2016) The Deubiquitinase OTULIN Is an Essential Negative Regulator of Inflammation and Autoimmunity. *Cell* 166, 1215–1230.e20
23. Damgaard, R.B. et al. (2019) OTULIN deficiency in ORAS causes cell type-specific LUBAC degradation, dysregulated TNF signalling and cell death. *EMBO Mol. Med.* 11, e9324
24. Nabavi, M. et al. (2019) Auto-inflammation in a Patient with a Novel Homozygous OTULIN Mutation. *J. Clin. Immunol.* 39, 138–141
25. Heger, K. et al. (2018) OTULIN limits cell death and inflammation by deubiquitinating LUBAC. *Nature* 559, 120–124
26. Xu H, Qin W, Hu X, et al. (2018) Lentivirus-mediated overexpression of OTULIN ameliorates microglia activation and neuroinflammation by depressing the activation of the NF- κ B signaling pathway in cerebral ischemia/reperfusion rats. *J Neuroinflammation*.15(1).
27. Voet S, Prinz M, van Loo G. (2019) Microglia in Central Nervous System Inflammation and Multiple Sclerosis Pathology. *Trends Mol Med.* 25(2):112-123.
28. Bellenquez, C. et al. (2022) New insights into the genetic etiology of Alzheimer's disease and related dementias. *Nat. Genet.* 54(4):412-436.

29. Heppner, F. L., Ransohoff, R. M. & Becher, B. (2015) Immune attack: the role of inflammation in Alzheimer disease. *Nat. Rev. Neurosci.* 16, 358-372.
30. Scheltens, P. et al. (2016) Alzheimer's disease. *Lancet* 388, 505-517.
31. Kaltschmidt, B., Uherek, M., Volk, B., et al. (1997). Transcription factor NF-kappaB is activated in primary neurons by amyloid beta peptides and in neurons surrounding early plaques from patients with Alzheimer disease. *Proc. Natl Acad. Sci. USA* 94, 2642-2647.
32. Chen, J. et al. (2005) SIRT1 protects against microglia-dependent amyloid-beta toxicity through inhibiting NF-kappaB signaling. *J. Biol. Chem.* 280, 40364-40374.
33. Wang, C. et al (2022) Microglial NF-B drives tau spreading and toxicity in a mouse model of tauopathy. *Nat. Commun.* 13(1), 1969.
34. Verboom, L. et al. (2020) OTULIN Prevents Liver Inflammation and Hepatocellular Carcinoma by Inhibiting FADD- and RIPK1 Kinase-Mediated Hepatocyte Apoptosis. *Cell Rep.* 30, 2237-2247.e621
35. Goldmann T, Wieghofer P, Müller PF, et al. (2013) A new type of microglia gene targeting shows TAK1 to be pivotal in CNS autoimmune inflammation. *Nat Neurosci.* 16(11):1618-1626.
36. Goldmann T, Wieghofer P, Joana M, et al. (2016) Origin, fate and dynamics of macrophages at central nervous system interfaces. *Nat Immunol.*17(7):797-805.
37. Van Hove, H., Martens, L., Scheytljens, I et al. (2019) A single-cell atlas of mouse brain macrophages reveals unique transcriptional identities shaped by ontogeny and tissue environment. *Nat. Neurosci.*, 22, 1021-1035.
38. Sala Frigerio C, Wolfs L, Fattorelli N, et al. (2019) The Major Risk Factors for Alzheimer's Disease: Age, Sex, and Genes Modulate the Microglia Response to A Plaques. *Cell Rep.* 27(4):1293-1306.e6.
39. Keren-Shaul H, Spinrad A, Weiner A, et al. (2017) A Unique Microglia Type Associated with Restricting Development of Alzheimer's Disease. *Cell.*169(7):1276-1290.e17.
40. Radde, R., Bolmont, T., Kaeser, S.A., et al. (2006). Abeta42-driven cerebral amyloidosis in transgenic mice reveals early and robust pathology. *EMBO Rep* 7, 940-946.
41. Saito, T. et al. (2014) Single App knock-in mouse models of Alzheimer's disease. *Nat. Neurosci.* 17, 661-663.
42. Yoshiyama, Y. et al. (2007) Synapse loss and microglial activation precede tangles in a P301S tauopathy mouse model. *Neuron* 53, 337-351.
43. Pombo Antunes, A.R., Scheytljens, I., Lodi, F., et al. (2021) Single-cell profiling of myeloid cells in glioblastoma across species and disease stage reveals macrophage competition and specialization. *Nat. Neurosci.*, 24, 595-610.

4. Publications van Loo-Movahedi groups 2024 (acknowledging GSKE support)

- Srinivasan, S*, Kancheva, D*, De Ren, S*, Saito, T*, Jans, M., Boone, F., Vandendriessche, C., Paesmans, I., Maurin, H., Vandenbroucke, R.E., Hoste, E., Voet, S., Scheytljens, I., Pavie, B., Lippens, S., Schwabenland, M., Prinz, M., Saido, T., Bottelbergs, A+, Movahedi, K+, Lamkanfi, M+ and van Loo, G+. Inflammasome signaling is dispensable for β -amyloid-induced neuropathology in preclinical models of Alzheimer's disease. *Frontiers Immunol.*, 15:1323409.
*shared first author
+shared last author
- Paesmans, I., Van Kolen, K., Vandermeeren, M., Shih, P-Y., Wuyts, D., Boone, F., Garcia Sanchez, S., Grauwen, K., Van Hauwermeiren, F., Van Opdenbosch, N., Lamkanfi, M., van Loo, G+ and Bottelbergs, B.+ (2024) NLRP3 Inflammasome Activation and Pyroptosis Are Dispensable for Tau Pathology. *Front Aging Neurosci.*,16:1459134
+shared last author



Geneeskundige Stichting Koningin Elisabeth
Fondation Médicale Reine Elisabeth
Königin-Elisabeth-Stiftung für Medizin
Queen Elisabeth Medical Foundation

Progress report of the
interuniversity research project of

Prof. dr. Renzo Manusco (UAntwerpen)
Prof. dr. Joris De Wit (KU Leuven)

Dr. Renzo Mancuso (he/him/his) (UAntwerpen)

Group Leader

Laboratory of Microglia and Inflammation in Neurological Disorders (MIND)

VIB-Center for Molecular Neurology (CMN), VIB.

Universiteit Antwerpen-CDE, Parking P4, Gebouw V 0.10

Universiteitsplein 1, B-2610 Antwerpen

T +32 (0) 3 265 25 28

Prof. Joris De Wit (KU Leuven)

Group Leader at VIB-KU Leuven

Center for Brain & Disease Research

Department of Neurosciences

ON5 Herestraat 49 – bus 602

3000 Leuven

Microglia-synapse molecular interactions in neurodegenerative disease (MicroSyn-MIND)

The goal of this project is to identify proteins that play a role in microglia-synapse interactions, and specifically those proteins whose expression is affected in Alzheimer's Disease (AD). We are currently well underway with aim 1, and provide an update on our findings and progress below.

First, a short description of our projects' original aim and strategy. It is unclear what drives AD progression. Genetic risk¹, Amyloid- (A) plaques, neurofibrillary tau tangles, and vascular alterations lead to a loss of neurons and synapses²⁻⁴, followed by the patient's memory, cognition, and grasp on reality. However, A builds up years before cognitive symptoms set-in⁵, and is not always followed by neurodegeneration³. Microglia prune synapses during development and could be key players in mediating synaptic loss in AD⁶. However, how microglia interact with neurons and synapses, and how AD affects these interactions, is poorly understood. Here, we combine the expertise of two labs to transplant human microglia in a mouse model of AD, perform a deep characterization of human microglia-synapse interactions at the molecular level using split-TurboID proximity labeling, and determine how these interactions are impacted by AD pathology. To address this overall goal, we formulated two main aims:

1. Identify AD-related changes to the microglial-synaptic cell surface interactome.

Following our update of January 2024, we are proceeding with aim 1. The key insights we obtained last year helped us to put an adjusted strategy in place, which has helped us make significant progress. We have generated "stable" iPSC lines for all the previously reported TurboID constructs, and are generating Mass Spectrometry samples of *in vitro* differentiated iPSC-derived human microglia. After extensive optimization experiments for our extremely small-yield protein samples, and for our various sample types (biotinylated protein from a) *in vitro* differentiated iPSC-derived human microglia as well as b) *in vivo* xenotransplanted iPSC-derived microglia), we've arrived at an optimized sample processing pipeline for our these samples. We are currently processing a large number of biotinylated protein samples, which will provide the detailed map of the subcellular compartmental proteomes of human *in vitro* microglia. As we stated before, this will serve as a valuable resource to the field in general. In addition to the proteomes map, we are stimulating *in vitro* iPSC-derived human microglia with soluble Amyloid-beta fibrils, to determine whether this induces specific compartmental protein changes in the human microglia. In parallel, we continue to transplant these "stable" iPSC-derived microglia that express these various constructs, *in vivo* in immunosuppressed WT mice as well as AD model mice. Once enough of these transplanted mice mature to an age where sufficient cortical A build-up has occurred (6 months of age), we will activate the TurboID through biotin injections, and attempt to extract protein for mass spectrometry analysis, like we originally intended in our proposal. The gathering and analysis of these specific *in vivo* data should be ready within the next 6 months. Once these data are in, we can proceed with the analysis as intended, to identify cell-type specific cell surface proteins, and infer potential ligand-receptor pairs of interest. From the differential expression of these proteins, comparing microglia from healthy WT mice compared to our AD model mice, we should be able to infer potential targets to study in aim 2.

2. Identify microglial cell surface proteins that mediate excessive synaptic loss in AD.

The original strategy for aim 2 still stands. As we discussed in our previous update, we have switched to our back-up strategy due to time-constraints and the prolonged initial phase of optimization, and are in the process of selecting potential key targets from the bioinformatics analysis in aim 1. Subsequently, we aim to validate a sub-section of these first through an ELISA-based interaction assay, whereby we test whether these microglial proteins can interact with a broad spectrum of synaptic proteins, in collaboration with prof. Davide Comoletti (University of New Zealand). Once we have reduced the number of potential targets, we will directly knock these out using CRISPR/Cas9, in iPSCs. With these lines, we will generate iPSC-derived microglia, which we will use in an *in vitro* synaptosome phagocytosis assay, to test the effects of the knockouts on the microglial capacity to phagocytose synapses. Following this, we will transplant one or several of these lines *in vivo*, to validate whether they affect synapse phagocytosis. We remain confident that we will provide an answer to our original question, of which key receptors-ligands affect the communication between microglia and synapses.

We hope this update provides sufficient information, and would love to answer any additional questions you might have regarding the progress of our project.

1. Bellenguez, C. *et al.* Large meta-analysis of genome-wide association studies expands knowledge of the genetic etiology of Alzheimer's disease and highlights potential translational opportunities. *medRxiv* 17, 10 (2020).
2. Mucke, L. & Selkoe, D. J. Neurotoxicity of amyloid β -protein: Synaptic and network dysfunction. *Cold Spring Harb Perspect Med* 2, (2012).
3. Serrano-Pozo, A., Frosch, M. P., Masliah, E. & Hyman, B. T. Neuropathological alterations in Alzheimer disease. *Cold Spring Harb Perspect Med* 1, 1–24 (2011).
4. Mecca, A. P. *et al.* In vivo measurement of widespread synaptic loss in Alzheimer's disease with SV2A PET. *Alzheimer's and Dementia* 16, 974–982 (2020).
5. Mintun, M. A. *et al.* PIB in a nondemented population. *Neurology* 67, 446 LP – 452 (2006).
6. Werneburg, S. *et al.* Targeted Complement Inhibition at Synapses Prevents Microglial Synaptic Engulfment and Synapse Loss in Demyelinating Disease. *Immunity* 52, 167–182.e7 (2020).
7. Cho, K. F. *et al.* Proximity labeling in mammalian cells with TurboID and split-TurboID. *Nat Protoc* 15, 3971–3999 (2020).
8. Tzioras, M. *et al.* Altered synaptic ingestion by human microglia in Alzheimer's disease. *bioRxiv* (2019) doi:10.1101/795930.
9. Pluvinage, J. V. *et al.* CD22 blockade restores homeostatic microglial phagocytosis in ageing brains. *Nature* 568, 187–192 (2019).



Geneeskundige Stichting Koningin Elisabeth
Fondation Médicale Reine Elisabeth
Königin-Elisabeth-Stiftung für Medizin
Queen Elisabeth Medical Foundation

Progress report of the
interuniversity research project of

Prof. dr. Karelle Leroy (ULB)
Prof. dr. Laurence Ris (UMONS)
Prof. dr. Kristel Slegers (UAntwerpen)

Prof. dr. Karelle Leroy (ULB)

Assistant professor, ULB

Head of the Alzheimer

research group in the

laboratory of Histology

<https://alzheimer-research.medecine.ulb.be>

Prof. dr. Laurence Ris (UMONS)

Department of

Neurosciences

Prof. dr. Kristel Slegers (UAntwerpen)

Dr Slegers Kristel

Professor, UA

Head of the Complex Genetics of

Alzheimer's disease group at

VIB – UA Center for Molecular

Neurology

<https://uantwerpen.vib.be/group/kristelSlegers>

Involvement of diabetes and antidiabetic treatment on tau pathology propagation

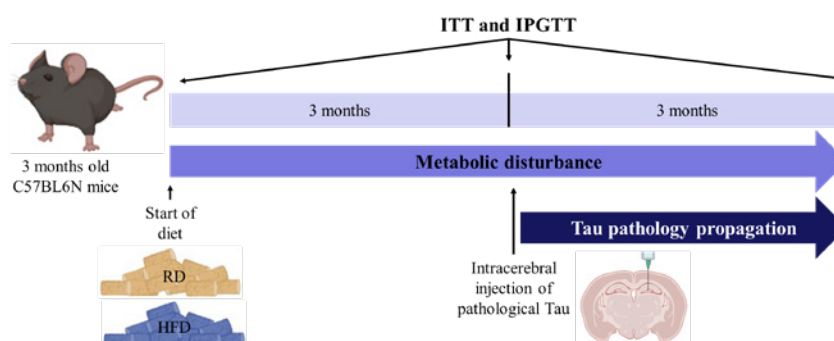
1. State of the art:

The etiopathogenesis of Alzheimer's disease (AD) is relatively unknown as only 5 % of AD cases can be explained by familial mutations. However, several risk factors have been described in AD. Among them, epidemiological studies showed a clear link between AD and type 2 diabetes mellitus (T2D), a medical condition frequent in industrial but also in developing countries. Indeed, T2D increases the risk of AD by at least twice. Moreover, a study has shown that T2D in elderly population with mild cognitive impairment influences the progression to dementia. The features of T2D are high levels of blood glucose (hyperglycemia) and insulin resistance. Most insulin is produced by beta-pancreatic cells and is transported to the brain by crossing the blood brain barrier. Insulin binds to the insulin receptors that are present in neurons triggering the brain insulin signaling pathway by activating AKT resulting in the inhibition of GSK3beta. Interestingly, a recent study has shown that beta-pancreatic cells and neurons shared common mechanisms such as the ability to express tau proteins or shared causal genes or pathways. Under conditions of insulin resistance, GSK3beta is converted to its active form by the decrease of the inhibitory serine 9 phosphorylation therefore conducting to the degradation of IRS1 (Insulin receptor 1) leading to insulin pathway disturbances. As the activity of GSK3beta is increased in AD and is involved in tau phosphorylation in this disease, this kinase could be the possible link between these two pathologies. Indeed, an abnormal tau phosphorylation appears in beta-pancreatic cells of T2D patients and in the brain of T2D mouse models (High fat diet model) in which the brain insulin signaling pathway is impaired. The possibility that targeting AD and T2D through antidiabetic agents may constitute an approach to treat defective brain insulin signaling, cognitive impairment and neurodegeneration.

2. Aim of the study:

This study will be devoted to the analysis of the role played by **metabolic disturbances observed in type 2 diabetes mellitus (T2D)** but also the **effect of an anti-diabetic treatment** on tau seeding and on the **propagation of tau pathology in Alzheimer's models** mice fed with high fat diet (HFD) to mimic T2D. These experiments will be conducted in mice models in which tau seeding will be induced by intracerebral injection of PHF-tau proteins from AD brain.

The texts concerning the results obtained in 2023 are colored in grey.



3. Results

3.1. Analysis of metabolic disturbances after the intracerebral injection of pathological Tau.

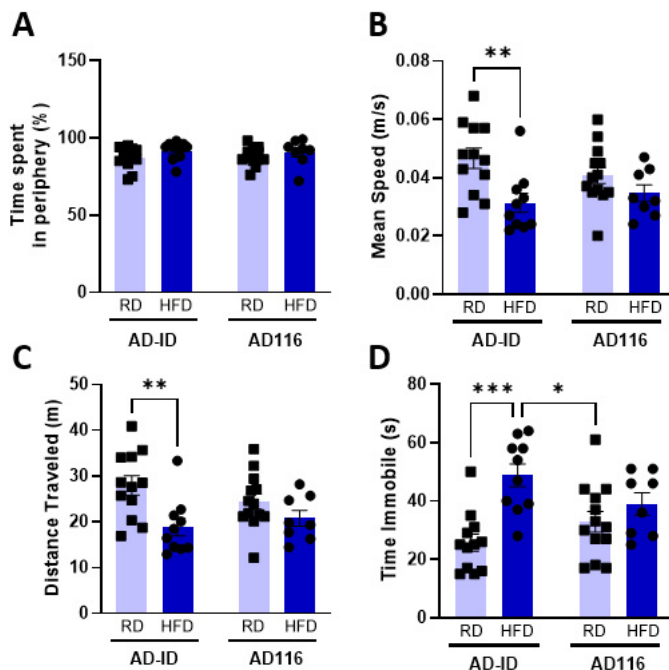
3 months after the intracerebral injection of AD sarkosyl fraction containing pathological tau or ADID sarkosyl fraction, we analyzed the metabolic parameters in RD and HFD fed mice. HFD fed mice showed insulin resistance and hyperinsulinemia but, surprisingly, mice fed with RD and injected with AD sarkosyl fraction developed insulin resistance.

3.2. Characterization of sarkosyl fractions.

The seeding ability of AD116 sarkosyl fractions have been evaluated in a bioassay based on the formation of a FRET signal when tau is seeded. We observed a FRET signal when cells were treated with AD sarkosyl fraction but not with ADID sarkosyl fraction (AD sarkosyl fraction immunodepleted for tau). These results confirmed that AD sarkosyl fraction can be used in vivo to induce tau pathology propagation and ADID sarkosyl fraction can be used as a control.

3.3. Analysis of anxiety and exploratory behavior after the intracerebral injection of pathological Tau.

To assess the anxiety-like behavior, the exploration, and the locomotion of the mice, an Open Field test was used after 5 months of diet and 2 months after the stereotaxic injection. The mice were placed into the middle part of a box, and the recording started immediately after placement and lasted for 10 min. Time spent in the periphery, mean speed, distance and immobility time were measured. Regarding graph A, we can tell that the treatments do not change the anxiety behavior of our mice. Indeed, all the mice spent more time in the periphery of the Open Field. But interestingly, we can see that HFD mice injected with AD-ID have exploration and locomotor problems (B-D). The same tendency appears in HFD mice injected with AD116 but is not significant, maybe due to the insufficient number of mice. More mice would be analyzed to reach a number of 15-20 mice per group.

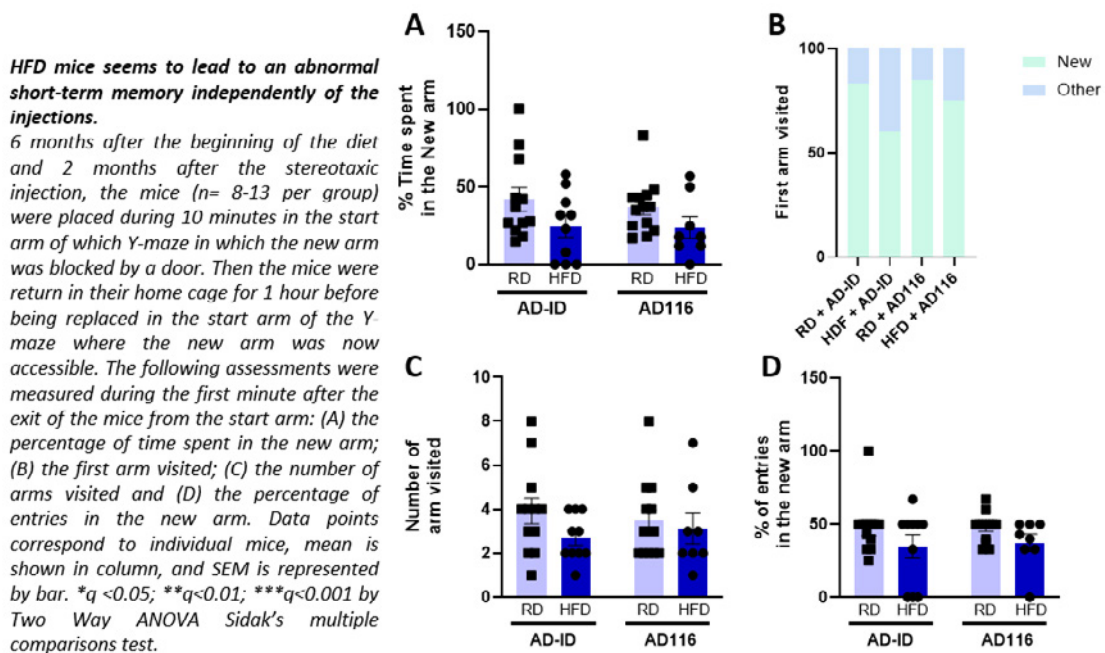


High-fat diet (HFD) mice have an abnormal exploratory behavior.

3-month-old C57BL6N mice were fed a normal diet (RD) or a high-fat diet (HFD) for 3 months and then randomized to receive stereotaxic injection of AD116 or AD-ID for 3 months of incubation (n= 8-13 per group). The exploratory behavior was assessed in these mice 1 month before the dissection. The mice were placed during 10 minutes in an Open Field and the following assessments were measured: (A) the percentage of time spent in the periphery; (B) the mean speed; (C) the total distance travelled by the mice and (D) the time that the mice spent immobile. Data points correspond to individual mice, mean is shown in column, and SEM is represented by bar. * $q < 0.05$; ** $q < 0.01$; *** $q < 0.001$ by Two Way ANOVA Sidak's multiple comparisons test.

3.4. Analysis of short-term spatial memory after the intracerebral injection of pathological Tau.

Short-term spatial memory was tested by a Y-maze behavioral test. 5 months after the start of diet and 2 months after the stereotaxic injection, the mice were placed in the start arm of the Y-maze and were free to explore for 10 minutes the start arm and the other arm (the new arm being blocked by a door). After this phase of habituation, the mice returned to their home cage for one hour. Then the mice were put back in the start arm and the following parameters were measured during the first minute after the mice exited the start arm: time spent in the new arm, first arm visited, number of arms visited and percentage of entries in the new arm. HFD mice tend to spend less time in the new arm and to enter less in this arm (A and C). Those results are not significant but as said before, more mice will be analyzed.



3.5. Analysis of the learning after the intracerebral injection of pathological Tau.

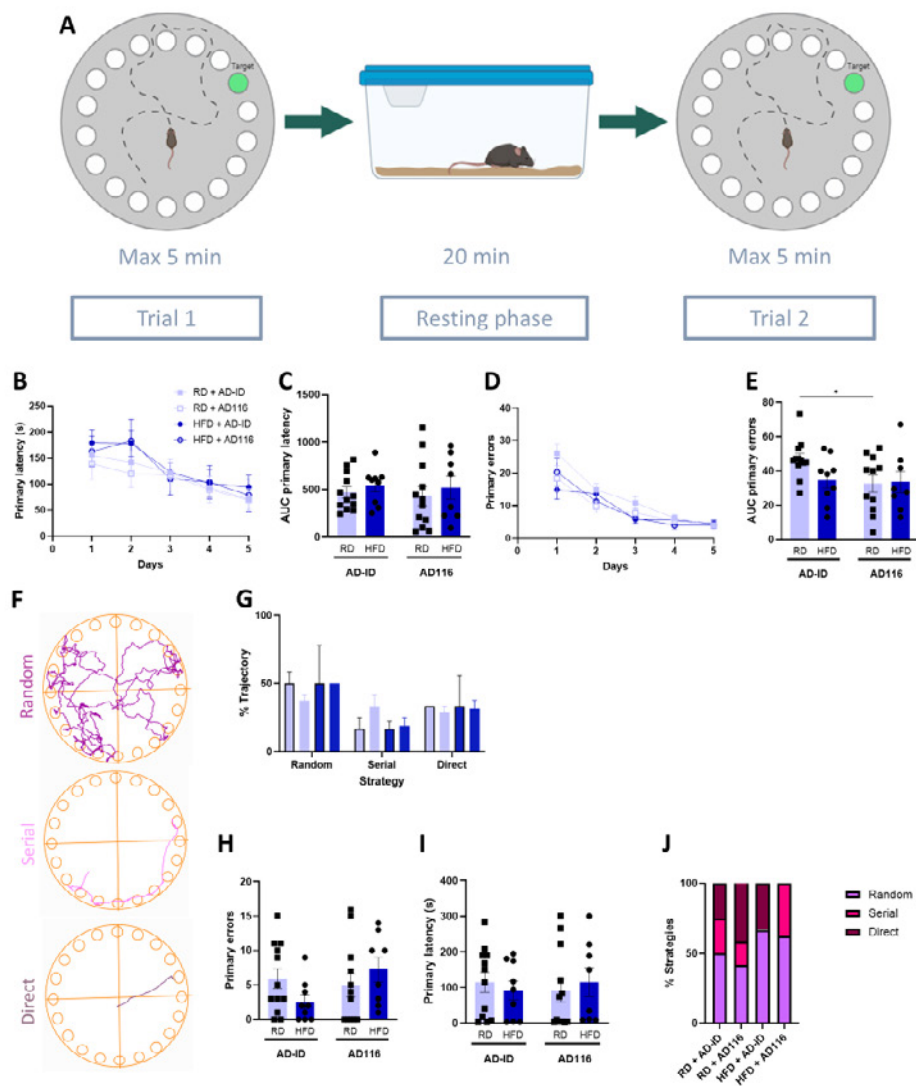
Barnes maze test is used to study hippocampus-dependent spatial learning. Briefly, the Barnes maze is a circular platform (1 m diameter) with 20 holes equally spaced and located close to the edge of the platform. A black escape box is placed under one of the holes (target) and spatial cues are located at the 4-cardinal points above the platform. The mice were placed in the middle of the maze and allowed to explore. The session ended when the mice found the box or after 5 min had elapsed. The mice performed 2 trials per day with a 20 min inter-trial interval for 5 consecutive days. The mice were tested 2 months after injection of AD-ID or AD116 fraction (n=10). To evaluate the spatial learning of the mice, several parameters were analyzed for each trial. These include the time spent trying to find the correct hole (latency), the number of incorrect holes checked prior to finding the target (number of errors) and the search strategy used by the mice to find the escape box. The search strategies are defined as direct, serial or random (F). When the mice move directly to the target hole or they make 2 errors that are adjacent to the target, the strategy is direct. Trials in which the mice investigate 3 or more adjacent holes in a sequential order that start at a minimum of 3 holes from the target and follow a clockwise or anticlockwise direction are serial searches. All other trials are counted as random strategies, including those in which the mice failed to find the target.

Our results showed that HFD or AD116 do not have any effect on the latency of the mice to find the target, on the number of errors or on the strategies used during the 5 days of learning. Moreover,

learning performance was measured by calculating the area under the learning curve (AUC) for latency and errors. RD-AD116 had a reduced AUC compared to RD-ADID but this result is probably due to the bigger number of errors made by RD-ADID mice the first day of the learning phase. We have observed no significant differences between HFD and RD conditions or between RD-AD116 and HFD-AD116. Other mice will be tested between April and August to confirm these results.

3.6. Analysis of long-term spatial memory after the intracerebral injection of pathological Tau.

3 days after the last training trial on the Barnes maze, the mice were put again on the Barnes to assess the long-term memory. The same parameters were analyzed during the learning phase. As for learning, we do not see any differences between the different conditions meaning that HFD or tau pathology do not lead to long-term memory deficits.



No difference between the treatments in the learning or in the long-term spatial memory.

Learning and long-term memory parameters were measured at the end of the study. For this the mice were placed twice a day on a Barnes Maze during 5 consecutive days (A), this represent the learning phase. During the tests, different parameters were measured: (B) primary latency; (C) AUC of the primary latency; (D) primary errors; (E) AUC of the primary error and (F-G) strategies. On day 8, the mice were replaced on the Barnes to assess the long-term memory by measuring (H) the primary latency; (I) primary error and (J) the kind of strategy used. Data points correspond to individual mice, mean is shown in column, and SEM is represented by bar. * $q < 0.05$; ** $q < 0.01$; *** $q < 0.001$ by Two Way ANOVA Sidak's or Tukey's multiple comparisons test.

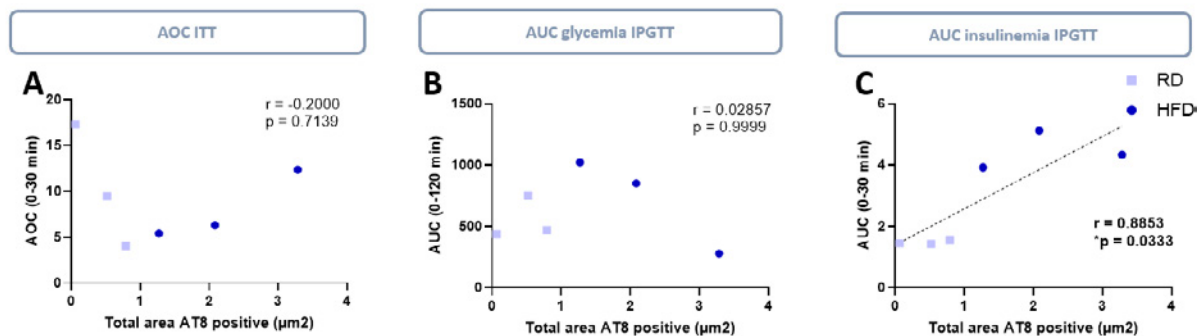
3.7. Analysis of Tau pathology propagation.

As expected, we didn't observe tau pathology in mice intracerebrally injected with ADID sarkosyl fractions and fed with RD or HFD. In AD injected mice, there is a tendency to an increased tau pathology in HFD fed mice compared to RD fed mice but it is not significant probably due to the low number of mice analyzed. Another group of mice have been dissected, and the brains have been cut. Immunolabelings will be done beginning 2025.

The results are similar with PHF1 antibody which recognizes tau proteins phosphorylated on Ser 396/404 to those observed with AT8 antibody: tendency to an increase of tau pathology propagation.

We also performed immunolabellings with T22 antibody which oligomers of tau proteins, with MC1 antibody which recognizes tau proteins in an abnormal conformation. A Gallyas staining was also performed to detect tau aggregates. In our injected model, we do not detect MC1 positives structures but with T22 and Gallyas, we observe a tendency to an increase of tau pathology maturation.

Interestingly, Tau pathology labeled with AT8 antibody correlates significantly with the insulin secretion after glucose injection (C).



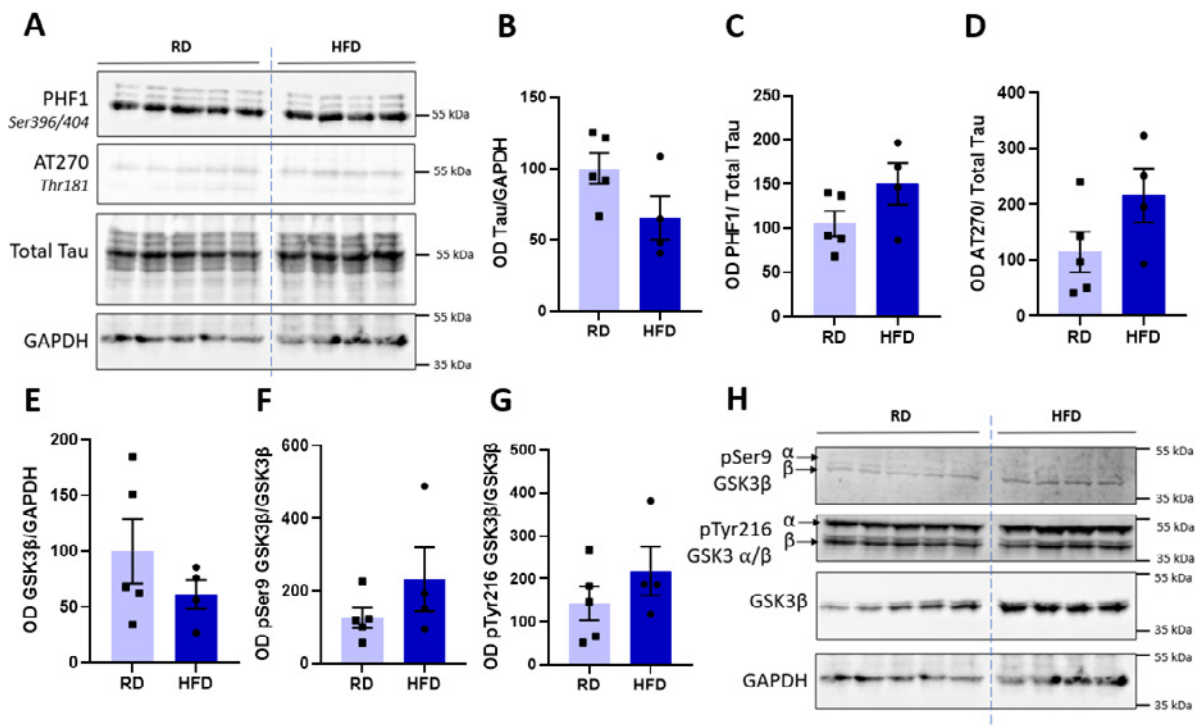
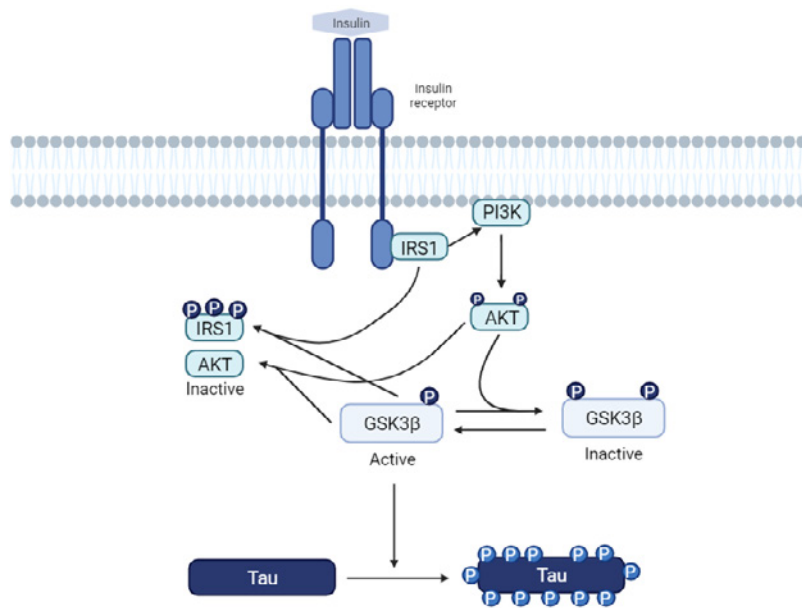
3.8. Analysis of the neuroinflammation

Because inflammation is a common risk factor for AD and T2D, we wanted to analyze the neuroinflammation and the neuronal loss after 3 months of diet and before the stereotaxic injection. We did not observe significant astrocyte activation or neuronal loss after 3 months of diet.

3.9. Analysis of the insulin pathway in the brain.

As explained in the introduction, GSK3beta could be the possible link between diabetes and Alzheimer disease. In physiological conditions, insulin binds to the insulin receptors that are present in neurons triggering the brain insulin signaling pathway by activating AKT resulting in the inhibition of GSK3beta (see figure below). Under conditions of insulin resistance, GSK3beta is converted to its active form by the decrease of the inhibitory serine 9 phosphorylation therefore conducting to the phosphorylation of Tau.

Therefore, we analyzed by western blot the effect of insulin resistance on tau phosphorylation and on GSK3beta activity after 3 months of diet (RD n= 5; HFD n=4). As shown with the PHF1 and AT270 antibodies (recognizing respectively tau phosphorylated on Ser 396/404 and Thr181) in C and D, HFD doesn't lead to a change of tau phosphorylation or GSK3beta activity. Indeed, HFD doesn't change GSK3beta phosphorylation on Sery9, an inactivator site of GSK3 and on Tyr216, an activator site of GSK3 (F and G).

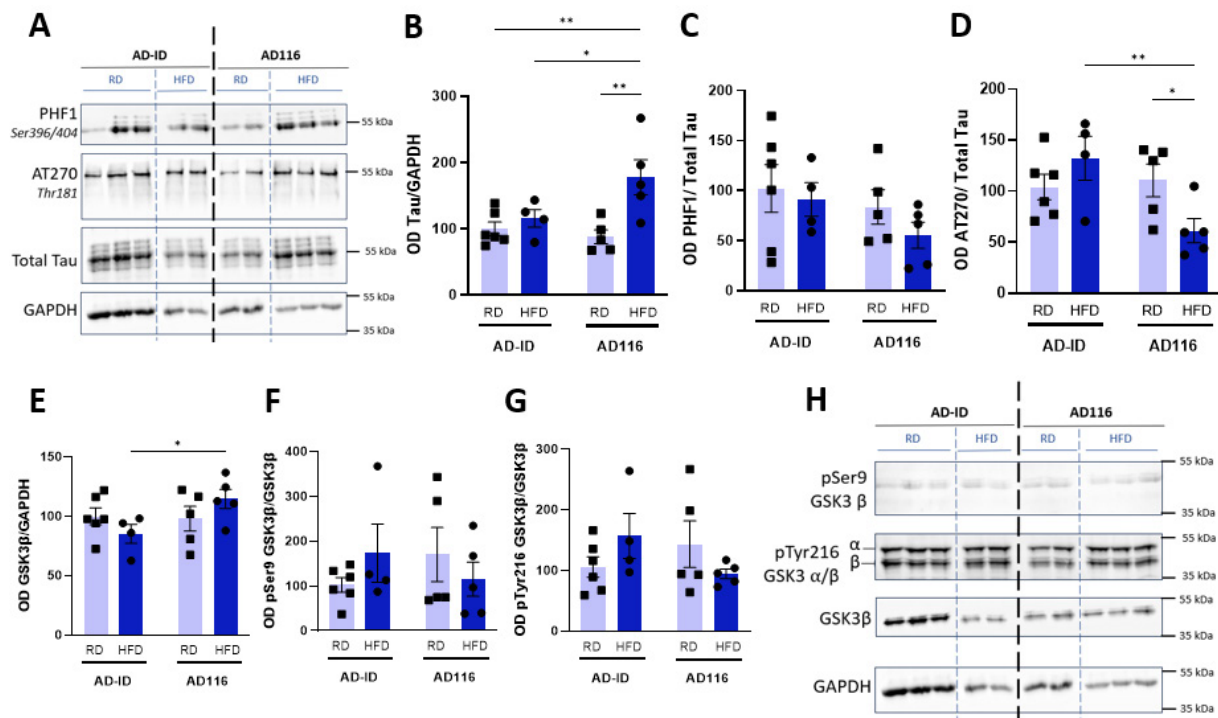


High-fat diet (HFD) do not change Tau phosphorylation or GSK3β activity after 3 months of diet.

3-month-old C57BL6N mice were fed a normal diet (RD) or a high-fat diet (HFD) for 3 months (n= 4-5 per group). (A-D) Western blotting analysis with anti-phosphoTau antibodies (PHF1, Ser396/404 and AT270, Thr181) of mouse brain homogenate. (E-H) Western blotting analysis with anti-phosphoGSK3β antibodies (pSer9, Inactive GSK3 and pTyr216, active GSK3) of mouse brain homogenate. Data points correspond to individual mice, mean is shown in column, and SEM is represented by bar. *q < 0.05; **q < 0.01; ***q < 0.001 by Mann Whitney T test.

3 months after the intracerebral injection of AD sarkosyl fraction containing pathological tau or ADID sarkosyl fraction, we analyzed tau expression/phosphorylation and GSK3beta expression/activity through phosphorylation in RD and HFD fed mice. Here we see an effect of HFD only in the mice injected with AD116. In those mice we observe an increase in tau content (B) and an increase in GSK3beta content (E). These increased expressions of these two proteins could be explained by two mechanisms: an increase in the transcription or a decrease in the degradation of these proteins. The first hypothesis is going to be tested by checking the level of mRNA by

sequencing. Moreover, we observe a decreased Tau phosphorylation on Thr181 (AT270 antibody) in HFD mice injected with AD116 compared to HFD-ADID and RD-AD116. This decrease is probably due to the higher expression of tau (B) in this condition as the result for AT270 is expressed as a ratio between AT270 and total tau OD signals.



High-fat diet (HFD) do not change Tau phosphorylation or GSK3β activity after 3 months of diet.

3-month-old C57BL6N mice were fed a normal diet (RD) or a high-fat diet (HFD) for 3 months and then randomized to receive stereotaxic injection of AD116 or AD-ID for 3 months of incubation (n= 4-6 per group). (A-D) Western blotting analysis with anti-phosphoTau antibodies (PHF1, Ser396/404 and AT270, Thr181) of mouse hippocampus homogenate. (E-H) Western blotting analysis with anti-phosphoGSK3β antibodies (pSer9, Inactive GSK3 and pTyr216, active GSK3) of mouse brain homogenate. Data points correspond to individual mice, mean is shown in column, and SEM is represented by bar. *q < 0.05; **q < 0.01; ***q < 0.001 by Two Way ANOVA Uncorrected Fisher's test.

3.10. Analysis of synaptic function after the intracerebral injection of pathological Tau.

Synaptic function was assessed in mice by recording long-term potentiation and paired-pulses facilitation in ex-vivo hippocampal slices.

Long-term potentiation (LTP) is recognized as the cellular model of plasticity processes occurring during learning and memory. The duration of LTP reflects the short and long-term memory process. A Theta Burst Stimulation is used to mimick axonal input and post-synaptic response is measured at the level of dendrites.

Paired-pulses facilitation is used assessed pre-synaptic plasticity. It was measured before and after LTP. By stimulating two times at short intervals the axons, we evaluate the pre-synaptic release of glutamate.

The mouse is first sedated with isoflurane before being sacrificed by decapitation and dissected. The brain is maintained in an artificial cerebrospinal fluid (aCSF) bath at room temperature. The bath is oxygenated with carbogen (95% O₂/5% CO₂). The hippocampus of the left hemisphere is dissected and cut into 400 μm-thick slices using a chopper. The slices are then placed in both installations (3 slices per installation) containing an oxygenated aCSF bath at 28°C. After 90 minutes' rest, the stimulation electrodes are placed on a slice in the CA1 region, stimulating Schaffer's collaterals. The recording electrode will be placed in the stratum radiatum to measure field excitatory post-synaptic potentials (Fig.1). Stimulation intensity is determined

by the stimulation that will give 40% of the maximum amplitude on this slice. Paired pulses are recorded before and after LTP. They consist of two stimulations sent at 25, 50, 100 and 200 ms intervals. Two stimulations are averaged per interval and per electrode. After a stable baseline for 30 minutes, LTP is induced by 2 TBSs separated by 20 seconds on one of the stimulation electrodes, with the other electrode acting as a control channel. These TBS comprise 10 packs of 4 stimulations sent at 200 ms intervals. Recording is maintained for 4 hours after LTP induction. Each point corresponds to 4 averaged stimulations separated by 60 seconds. Slope is measured and expressed as a percentage of baseline.

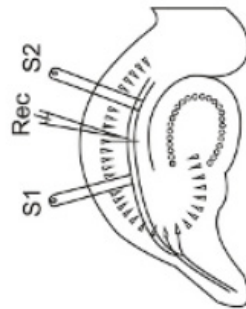


Figure 1. Recording and s-mula-ng electrodes posi-ning

LTP was maintained at 170% after 4 hours in all groups. There were therefore no differences between groups (repeated measures ANOVA; $F(3,12) = 0.253$, $P = 0.858$) (Fig. 2).

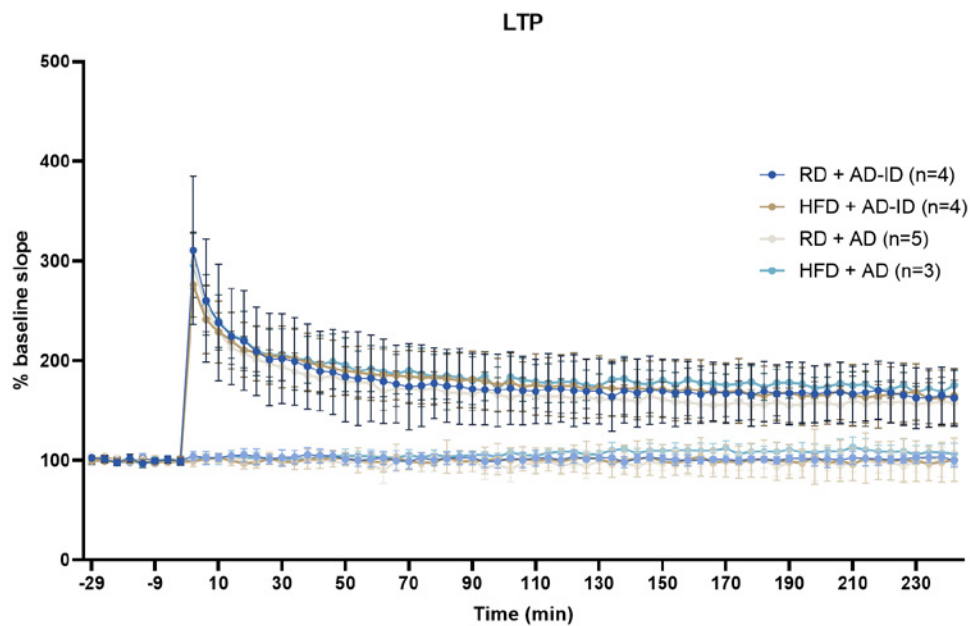


Figure 2. LTP

No differences were found for the paired-pulses either (Fig. 3).

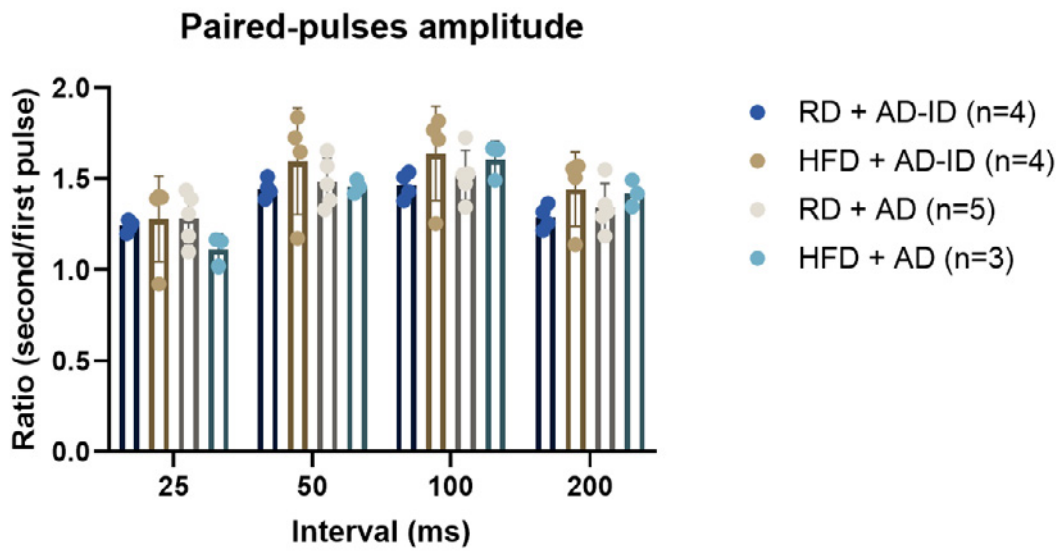


Figure 3a. Paired-pulses with amplitude measure

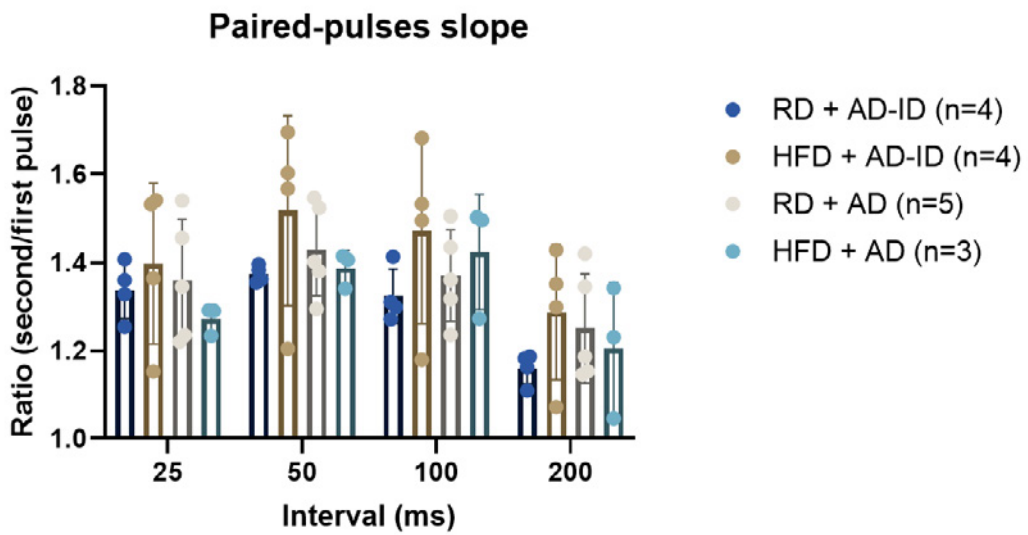


Figure 3b. Paired-pulses with slope measure

Paired-pulses post- VS pre-LTP

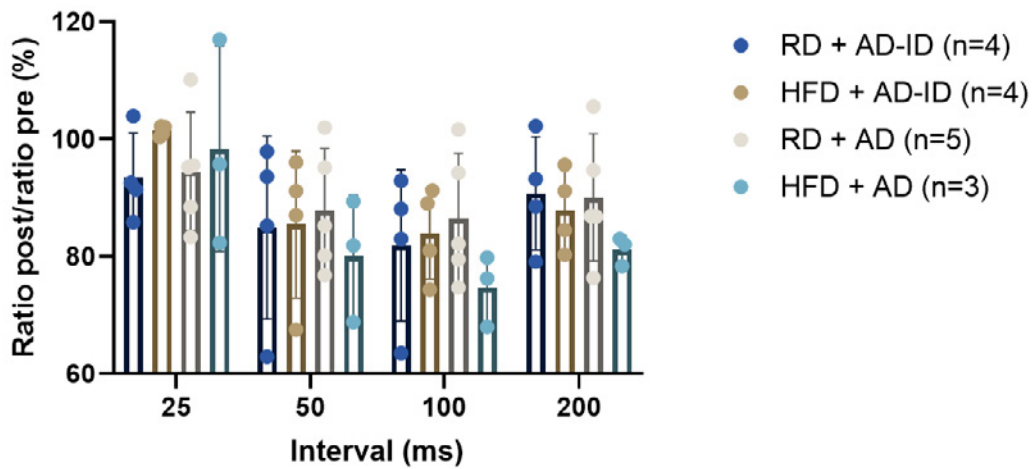


Figure 3c. Post- VS pre-LTP ratio with amplitude measure

Paired-pulses post- VS pre-LTP

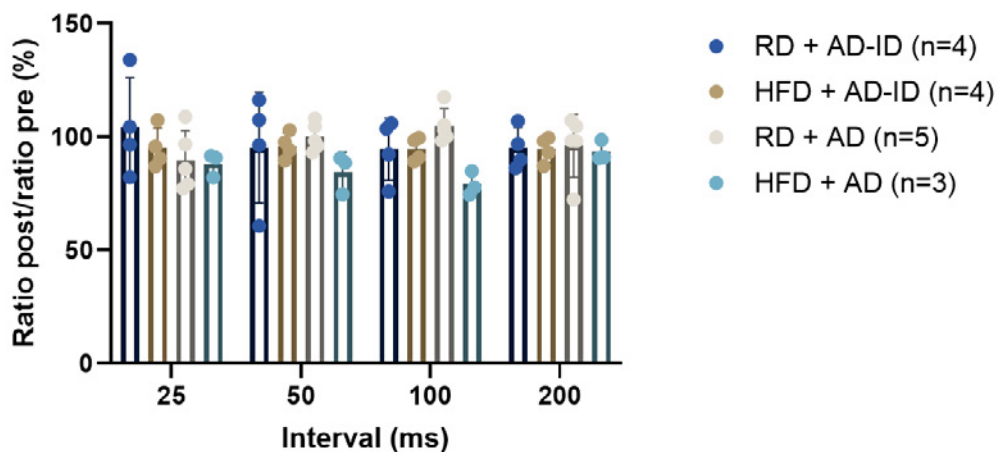
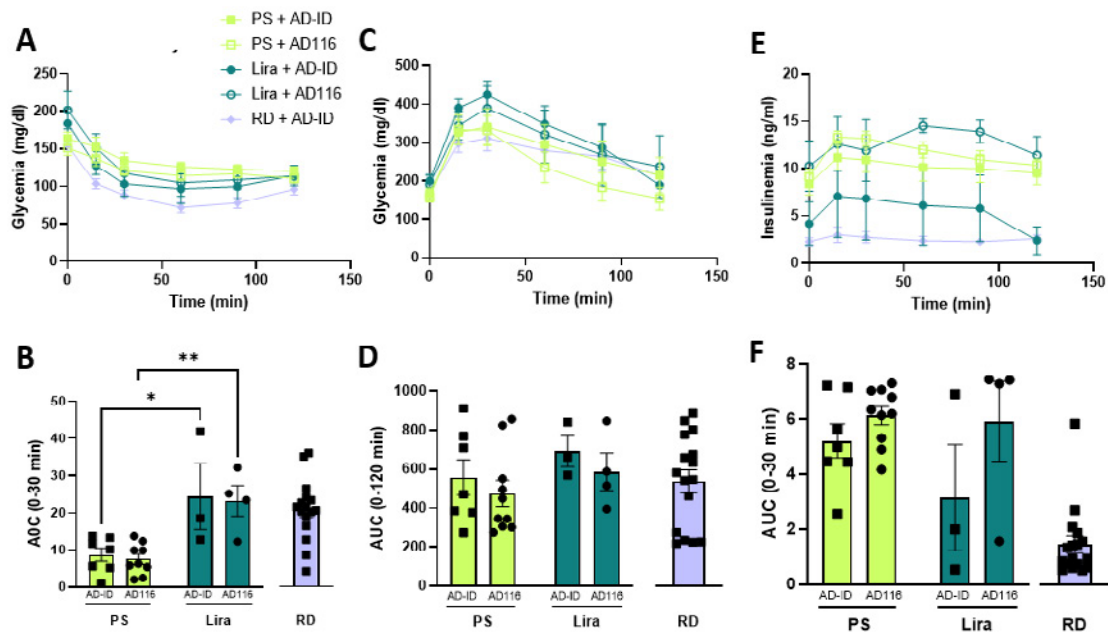


Figure 3d. Post- VS pre-LTP ratio with slope measure

3.11. Analysis of Liraglutide on metabolism.

The effect of an antidiabetic treatment (liraglutide) on the metabolic disturbances shown in our HFD mice was analyzed by ITT and IPGTT as explained before. After 3 months of HFD, mice were treated with physiological serum (PS) or with liraglutide (Lira; 300µg/kg/day) via an osmotic pump placed subcutaneously in the back of the mice. Liraglutide can rescue the insulin resistance in HFD mice to reach the same level as the RD mice but is not able to rescue the glucose sensitivity in those mice. Interestingly, Liraglutide tends to decrease the insulin level in AD-ID injected mice but not in AD116 injected mice.



Liraglutide (Lira) rescue insulin sensitivity in high-fat (HFD) mice.

3-month-old C57BL6N mice were fed a normal diet (RD) or a high-fat diet (HFD) for 3 months and then randomized to receive stereotaxic injection of AD116 or AD-ID and an osmotic pump placement containing physiological serum (PS) or Liraglutide (Lira; 300µg/kg/day). 3 months after the surgery metabolic parameters were measured in these mice. The following assessments were made at the end of the study: (A) blood glucose during the insulin tolerance test (ITT). Insulin sensitivity was quantified by the area on the curve (AOC) during (B) the insulin tolerance test. (C) Blood glucose, (D) AUC for glucose, and (E-F) insulin levels during intraperitoneal glucose tolerance test (IPGTT). Data points correspond to individual mice, mean is shown in column, and SEM is represented by bar. * $q < 0.05$; ** $q < 0.01$; *** $q < 0.001$ by Two Way ANOVA Tukey's multiple comparisons test.

4. Conclusions and perspectives:

Metabolic tests showed that WT mice are a good model to study the effect of metabolic disturbances induced by high-fat diet on tau pathology propagation. AD sarkosyl fractions induced a tau pathology that tends to increase when the mice are fed with HFD compared to RD but it is not significant. New samples are available to finish the analysis of tau pathology propagation and are going to be finished at the beginning of 2025. AD sarkosyl fractions induced an increase in Tau and GSK3 proteins expression level in HFD mice. Those results would be furthermore investigated by sequencing. Regarding the behavior test, we conclude that AD sarkosyl fraction does not have any effects, but HFD tends to lead to a change of exploratory behavior and to short-term memory deficit. Liraglutide can rescue some metabolism parameters in HFD mice and the effects of this treatment on tau pathology and on the insulin pathway in the hippocampus are going to be further investigated.

More mice would be treated to complete the groups for histology and western blot as planned in the table below.

	Electrophysiology	Sequencing
RD + AD-ID	4	5
RD + AD116	5	3
HFD + AD-ID	4	2
HFD + AD116	3	0
	N = 5	N = 10
Next availabilities	04/25	04/25 and 06/26

	Western blot	Histology
PS + AD-ID	4	3
PS + AD116	6	4
Lira + AD-ID	0	3
Lira + AD116	0	4
	N = 6	N = 5
Next availabilities	08/25	08/25



Geneeskundige Stichting Koningin Elisabeth
Fondation Médicale Reine Elisabeth
Königin-Elisabeth-Stiftung für Medizin
Queen Elisabeth Medical Foundation

Progress report of the interuniversity research project of

Prof. dr. Sarah Weckhuysen (UAntwerpen)
Prof. dr. Bjorn Menten (UGent)

Prof. dr. Sarah Weckhuysen, MD, PhD (UAntwerpen)
Applied&Translational Neurogenomics Group VIB-UAntwerp
Center for Molecular Neurology UAntwerp CDE
Parking P4, Building V Universiteitsplein 1, 2610 Antwerpen
Belgium
uantwerpen.vib.be

Neurology Department
Antwerp University Hospital
Drie Eikenstraat 655
2650 Edegem
www.UZA.be/neurologie

Prof. dr. ir. Björn Menten (UGent)
Lab for Genome Research, Center for Medical Genetics, Department of biomolecular Medicine (UGent)
Associate professor (Faculty of Medicine and Health Sciences, UGent)
Lab supervisor Cytogenomics Laboratory Center for Medical Genetics, UZGent
Lab address: UZ Gent, Medical Research Building 1 (entrance 34),
Corneel Heymanslaan 10
9000 Gent

Detection of somatic mutations and disease-defining methylation patterns in brain tissue and cerebrospinal fluid of patients with non-acquired focal epilepsy

1. Background

The majority of non-acquired focal epilepsies (NAFE) have a presumed genetic etiology. However, the current yield of diagnostic genetic testing in affected patients is very low. This diagnostic gap is an important barrier to the broader use of gene-targeted therapies. Increasing evidence from resected brain tissue of individuals with NAFE points towards an important role of pathogenic somatic variants and methylation abnormalities. Most NAFE patients, however, do not undergo brain surgery, and the lack of brain tissue precludes a genetic diagnosis. In this project, we aim to prove that cell-free DNA (cfDNA) circulating in cerebrospinal fluid (CSF) and serum of patients with NAFE can be used to bridge this diagnostic gap. 1) We will apply a deep-sequencing protocol to detect novel somatic variants and 2) pathognomonic methylation patterns in cfDNA from CSF. 3) Simultaneously, we will use nanopore sequencing on native cfDNA to identify somatic copy number changes. We prioritize patients who undergo epilepsy surgery for our study cohort to validate the detected somatic and epigenetic changes in paired brain tissue. By identifying the genetic etiology and disease methylation profiles from cfDNA, we can improve the diagnostic yield and clinical decision-making in this severely affected population.

The previous report outlines significant in-roads in sample collection, sample preparation, and library preparation. In our new report, we would like to highlight important developments in library preparation, data analysis, and ongoing sample acquisition.

2. Summary of achievements

2.1. Sample Acquisition

In the past year, we have added 12 additional paired brain-CSF-blood samples from focal epilepsy patients. This expands our cohort from 30 to 42 individuals. This is three fewer samples than we had targeted for 2024, due to unexpectedly fewer surgeries at UZ Leuven. However, we initiated a collaboration with the Stefanie Baulac laboratory in Paris to analyze their paired brain-CSF samples, which included 90 individuals with FCD-I, FCD-II, Rasmussen Syndrome, HME, PMG, and TSC. This access provides us with twice the number of samples we targeted for the whole project.

Additionally, we have received ethical approval for our multicenter study, so this year, we will collect additional samples from UZ Gent, HUB-Erasme, and UCL-Saint Luc. This should add 20-30 additional samples per year, greatly improving our detection power.

2.2. Library Preparation

a) Targeted Methylation Sequencing

We construct methylation sequencing libraries for 16 of our cfDNA samples. Of the 16 samples, 4 were from patients with FCD (3 FCD2B and 1 FCD2A) based on post-operative histopathology, and two samples were from patients with non-FCD Temporal Lobe Epilepsy (TLE). The remaining samples were controls with diagnoses ranging from dementia to normal pressure hydrocephalus.

Our pretrained neural network machine model was able to **discern and classify methylation differences between these FCD, TLE, and control samples** (Figure). The classification scoring is derived by calculating the relative proximity of the model output encodings to known target encodings or combinations of target encodings. The model consistently gave higher focal epilepsy scores (EPI) for the FCD and TLE samples compared to controls ($p < 1e-3$) and higher FCD scores for FCD samples compared to controls ($p < 1e-3$).

Furthermore, this model gave higher FCD scores for FCD samples compared to TLE, and higher TLE scores for TLE samples compared to controls, though these comparisons are not yet significant due to the lower TLE sample size ($n = 2$). We will continue to improve our machine model by mining the cfDNA methylation data to simulate true background noise better. This is expected to widen the score differences between different focal epilepsy subtypes. Nonetheless, this first round of analysis demonstrates that our methylation sequencing protocol and analysis pipeline can distinguish major subtypes based on cfDNA.

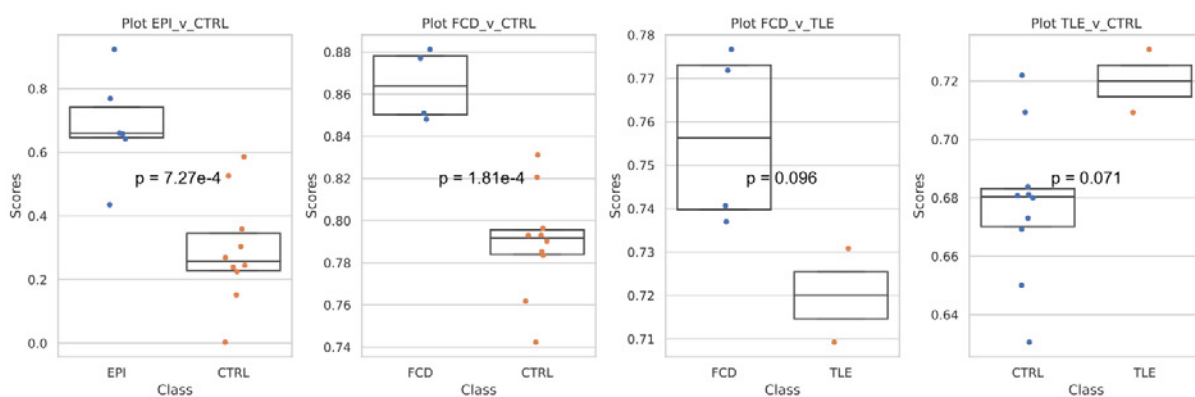


Figure. Classification scoring of cfDNA methylation using a pretrained neural network machine model.

Plot EPI_v_CTRL: Epilepsy scoring for EPI (FCD + TLE) vs. CTRL (controls). **Plot FCD_v_CTRL:** FCD scoring for FCD (focal cortical dysplasia) vs. CTRL samples. **Plot FCD_v_TLE:** FCD scoring for FCD vs. TLE (temporal lobe epilepsy) samples. **Plot TLE_v_CTRL:** TLE scoring for TLE vs. CTRL samples.

b) Targeted Deep Mosaicism Sequencing

We also initiated the library preparation and sequencing protocol to analyze for somatic mosaicism. As a preliminary trial, we performed library preparation and sequencing on 8 brain samples and paired CSF cfDNA (3 TLE, 4 FCD2B, 1 FCD2A). Target capture efficiency was consistently >80% for all samples. We have not yet observed deleterious somatic mutations with this initial sample set. Given the ~30% diagnostic yield in FCD2 (TLE as a negative control), there is an 18% likelihood to expect this negative result by chance alone. The mutation yield shall increase as we continue to sequence more samples.

c) Shallow whole genome nanopore sequencing

At the same time, we've been optimizing protocols for shallow whole genome sequencing with Oxford Nanopore Technologies (ONT) on cfDNA. This protocol is especially challenging as the techniques are optimized for very long DNA fragments, in contrast to the very short cfDNA fragments. However, by performing ONT sequencing, we can simultaneously interrogate the methylome and copy number aberrations.

3. Further Planning

In the next months, we plan to analyze the data generated from the first batch of samples from UZ Leuven. Once the ethical committee agreement for the multicenter study involving the other academic hospitals is received, we expect to start receiving samples from these centers and exponentially increase our sample size. With this additional cohort, we will be able to validate our results and improve our power for signal detection.



Geneeskundige Stichting Koningin Elisabeth
Fondation Médicale Reine Elisabeth
Königin-Elisabeth-Stiftung für Medizin
Queen Elisabeth Medical Foundation

Progress report of the
interuniversity research project of

Prof. dr. Ann Massie (VUB)
Prof. dr. Lutgarde Arckens (KU Leuven)

Prof. dr. Ann Massie (VUB)

Vrije Universiteit Brussel
Center for Neurosciences
Laarbeeklaan 103
1090 Brussels
ann.massie@vub.be
T 02 477 45 02

Prof. dr. Lutgarde Arckens (KU Leuven)

Katholieke Universiteit Leuven
Department of Biology
Naamsestraat 59
3000 Leuven
lut.arckens@kuleuven.be
T 016 32 39 51

The xCT^{-/-} killifish to validate the potential of system x_c⁻ as therapeutic target in Parkinson's disease

1. Summary

Targeting the cystine/glutamate antiporter system x_c⁻ has great potential in the treatment of age-related neurological diseases. We recently showed lifespan extension with reduced age-related *inflammaging*, and preservation of hippocampal function and memory in aged mice lacking the specific xCT subunit of this antiporter. xCT deletion in mice also results in protection of the nigrostriatal dopaminergic pathway against toxin-induced degeneration (as a model for Parkinson's disease; PD). This protection, however, seems to be age- and toxin-dependent. Access to a spontaneous -and therefore toxin free- PD animal model is of paramount importance to create indisputable evidence about the power of system x_c⁻ inhibitors for the treatment of PD patients.

The African turquoise killifish *Nothobranchius furzeri* is the shortest-living vertebrate laboratory species showing all cellular and molecular hallmarks of human aging, including spontaneous α -synuclein accumulation with degeneration of dopaminergic neurons. These features make the killifish an excellent model to study PD, as there is no need for toxins to induce dopaminergic neurodegeneration. In this project, we will therefore generate a transgenic killifish with a deletion of xCT. We will characterize the aging process of this fish and study its susceptibility to spontaneous age-related neurodegeneration. The severity of neurodegeneration will be correlated to changes in the activity of the most important transporters that regulate extracellular glutamate levels (as a first indication of excitotoxicity), to neuroinflammation, to metabolic changes in the killifish brain, and to function of the ubiquitin-proteasome system.

This study will not only allow us to confirm or refute the therapeutic potential of targeting system x_c⁻ in PD and to generate a valuable tool to further investigate the function of system x_c⁻ in aging and age-related (neurological) diseases, but it will also provide a detailed characterization of the aging brain of the shorter-lived GRZ-AD *N. furzeri* strain (until now most studies were done on the longer-lived MZM strain) that will be of interest for studying other potential neuroprotective targets in PD.

2. Project outline

2.1. State-of-the-art

The **cystine/glutamate antiporter system x_c⁻**, with xCT (Slc7a11) as specific subunit, imports cystine in exchange for glutamate and is the major source of extracellular glutamate in several mouse brain regions, including hippocampus and striatum^{1,2}. In the central nervous system (CNS), system x_c⁻ is mainly expressed on astrocytes^{3,4}. Glutamate released by system x_c⁻ is believed to be confined to the extrasynaptic space. This glutamate can act on metabotropic glutamate receptors to modulate glutamatergic transmission, and on ionotropic NMDA receptors thereby decreasing the threshold for glutamate toxicity (excitotoxicity). System x_c⁻ also regulates (neuro)inflammation: genetic xCT deletion (xCT^{-/-}) in mice⁵ results in a faster normalization of peripheral cytokine levels after i.p. injection of a sublethal dose of bacterial lipopolysaccharide (LPS) -thereby reducing LPS-induced sickness and neuroinflammation⁶- and favors the anti- over the pro-inflammatory microglial phenotype in pathological conditions^{7,8}. Accordingly, absence of system x_c⁻ is protective in neurological disorders that are characterized by excitotoxicity and (neuro)inflammation^{1,2,9-11}. The therapeutic potential of targeting system x_c⁻ in age-related neurological disorders has

however been questioned, as the oxidative shift in the plasma cystine/cysteine ratio of xCT^{-/-} mice was suggested to accelerate the aging process⁵. We therefore studied the effect of genetic deletion of xCT on aging and indeed unveiled system x_c⁻ as a regulator of life- and healthspan¹². Contrary to the expectations, however, mice with a genetic deletion of xCT showed a significant lifespan extension, while preserving their hippocampal function and spatial memory¹². Possible underlying mechanisms include attenuated *inflammaging* as well as metabolic changes at the level of the aged xCT^{-/-} brain, including reduced levels of N6-carboxymethyllysine¹², an advanced glycation end product (AGE) that has been linked to cognitive decline and neurodegenerative disorders¹³.

Glutamate toxicity and neuroinflammation are central to Parkinson's disease (PD) pathogenesis, and an accumulation of AGE levels has been linked to oxidative stress and α -synuclein (α -syn) aggregation in PD^{14,15}. Given the effect of system x_c⁻ deficiency on these pathogenic mechanisms, we validated the therapeutic potential of targeting system x_c⁻ in PD, by comparing the impact of three different toxin-based PD models between young-adult and aged xCT^{-/-} and xCT^{+/+} mice^{2,11}. Although we obtained very promising results, we remain somehow inconclusive. Whereas both young-adult and aged xCT^{-/-} mice were protected against neurodegeneration induced by intrastriatal 6-hydroxydopamine injection², the dopaminergic neurons of only aged (and not adult) xCT^{-/-} mice were protected against lactacystin (inhibitor of the ubiquitin proteasome system (UPS); intranigral injection)-induced degeneration, and neither young-adult nor aged xCT^{-/-} mice showed reduced susceptibility in the chronic, progressive 1-methyl-4-phenyl-1,2,3,6-tetrahydropyridine (MPTP) model¹¹.

2.2. Objectives

With this project we aim at developing a novel short-lived vertebrate model with spontaneous age-related degeneration of dopaminergic neurons that will allow us to unambiguously -and independent of PD-inducing toxins- reinforce or refute the potential of system x_c⁻ as therapeutic target in PD and to study the mechanisms underlying the anticipated neuroprotection.

To reach our **overarching goal**, i.e. reinforcing the validity of system x_c⁻ inhibition as a therapeutic target in PD, we defined four objectives:

The **first objective** is to create and validate an xCT^{-/-} African turquoise killifish.

The **second objective** is to investigate whether the beneficial effects on lifespan and general health, that we observed in aged xCT^{-/-} mice, can be replicated in aged xCT^{-/-} killifish.

The **third objective** is to study the effect of xCT deletion on the spontaneous age-related α -syn accumulation and dopaminergic neurodegeneration in the killifish brain.

The **fourth objective** is to investigate how xCT deletion affects the age-related pathogenic mechanisms that underlie neurodegenerative disorders, in the fast-aging killifish.

*One additional objective has been added to our study. As most of the available data on the aging killifish brain have been collected from the longer-lived MZM strain and we here use the shorter-lived GRZ-AD strain to fully exploit the advantages of a short-lived model, our **fifth objective** is to map age-related neurodegeneration, protein accumulation and proteasome function in the GRZ-AD strain.*

3. Workplan (*results obtained in 2024 are in italic*):

3.1. Workpackage 1 (WP1): Generation and validation of an xCT^{-/-} killifish

xCT is expressed in the killifish¹⁶, showing a 73-75% DNA sequence homology with mouse and human xCT, and we have preliminary findings supporting the presence of system x_c⁻ activity in synaptosomes that were prepared from adult and aged killifish brains. In this WP we are generating a xCT^{-/-} killifish that allows time-efficient and in-depth investigation of the molecular mechanisms of aging and spontaneous age-related neurodegeneration that are affected by system x_c⁻ and could underlie our promising observations -both in the context of aging and in PD- in mice^{2,11,12}.

To induce **xCT deletion** by a CRISPR-Cas9 strategy, proven to be efficient in *N. furzeri*^{17,18}, the Cas9-sgRNA complex targeting *slc7a11* is injected into the one-cell stage of killifish embryos, that are grown to adulthood. The knockout (KO) is confirmed on genomic DNA extracted from the caudal fin, followed by sequencing of the targeted region. After extensive training of our new PhD student for the injection of fish embryos, she obtained a heterozygous male fish. However, we lost this fish due to breeding issues (not related to the genotype) before he could fertilize eggs.

*Given the low success rate when using the approach described above, we adopted a new approach to create the xCT KO killifish by replacing the Cas9 mRNA by the Cas9 protein, to facilitate CRISPR-Cas9 expression within the cell. The Cas9 protein was co-injected with a sgRNA targeting the *slc7a11* gene and a plasmid encoding the GFP protein. This construct enables knock out of the xCT gene by inserting the GFP gene into the *slc7a11* locus, thereby disrupting the *slc7a11* gene and allowing GFP expression instead. Using this strategy we simultaneously generate a reporter killifish as GFP will be expressed in those cells that would express xCT in case of a wildtype (WT) fish.*

*Using this construct, we confirmed the successful insertion of the GFP gene into the killifish genome, however, until now, we have been unable to confirm GFP gene insertion in the *slc7a11* gene. We are now breeding with the fish expressing the GFP gene to collect fertilized embryos for further analysis to confirm successful *slc7a11* gene targeting. In the next steps, when the GFP-positive fish are too old to breed, fish will be sacrificed and their brains will be used for assays to evaluate system x_c⁻ activity. If no downregulation of xCT is observed, an alternative strategy to induce xCT deletion will be implemented. We previously successfully generated heterozygous xCT killifish by injecting two different gRNAs targeting xCT (see above) in the embryo. We will repeat this strategy by using three different gRNAs targeting the xCT gene, co-injected at the single cell stage with the Cas9 protein. This approach simplifies the process by enabling genotype confirmation through sequencing.*

In addition, we further investigated xCT expression in the killifish brain. We successfully optimized a Western blotting protocol to detect xCT in killifish brain lysates, confirming its presence. Furthermore, single-nuclei RNA sequencing data from the telencephalon of young and old killifish brains, both before and after brain injury²⁰, revealed almost no xCT expression in young killifish telencephalon, with upregulation following brain injury and during aging. Interestingly, according to findings in mice, xCT was predominantly localized in an astrocyte-like subcluster. Moreover, these results align with findings from the system x_c⁻ activity assay in synaptosomes of the killifish brain, which also demonstrated enhanced system x_c⁻ activity in aged compared to young killifish brain.

3.2. WP2: Characterization of the general health status and aging process of the xCT^{-/-} killifish

We previously observed that xCT deletion results in lifespan extension without deterioration of general health status and with preservation of spatial memory in aged mice¹². In this WP, we will evaluate whether these findings can be generalized to *N. furzeri* by comparing life- and healthspan of xCT^{+/+} and xCT^{-/-} killifish. The use of this short-lived small vertebrate will allow a longitudinal study including several life stages within six months.

While generating a xCT^{-/-} killifish, we have been optimizing the behavioral test battery and a strategy for detailed analysis of longitudinal age-dependent changes in locomotor function in WT killifish. We used the open field and the novel tank diving test to study killifish locomotion, exploration-related behavior, and behavioral changes over their adult lifespan. The characterization of this behavioral baseline is important for future experiments in our xCT^{-/-} fish. Fish were tested from the age of 6 weeks to the age of 24 weeks, and measurements were performed every 3 weeks. In the open field test, we found an increase in the time spent in the center zone from 18 weeks onward, which indicates altered exploration behavior. Upon aging, the fish also showed an increased immobility frequency and duration. In addition, after the age of 15 weeks, their locomotion decreased. In the novel tank diving test, we did not observe this aging effect on locomotion or exploration. Killifish spent around 80% of their time in the bottom half of the tank. We could not observe habituation effects, indicating slow habituation to novel environments. Moreover, we observed that killifish showed homebase behavior in both tests. These homebases are mostly located near the edges of the open field test and at the bottom of the novel tank diving test. Altogether, in the open field test, the largest impact of aging on locomotion and exploration was observed beyond the age of 15 weeks. In the novel tank diving test, no effect of age was found. Therefore, to test the effects of xCT-related interventions on the aging process, the open field test is ideally suited. The novel tank test is better suited to test possible effect on anxiety as there is no confounding effect of aging in this readout. Whether the preference to spend time at the bottom of the tank truly reflects anxiety still needs to be confirmed with proven anxiolytic drugs though. These data have been published (Mariën et al, 2024, *Frontiers in Behavioral Neuroscience*).

We validated spinal curvature as a longitudinal measure of aging in several batches of killifish, with and without drug treatment to alter aging. This has created optimized baseline data to compare the xCT^{-/-} killifish to, once available.

3.3. WP3: Validation of the protective effect of xCT deletion on the spontaneous age-related α -synuclein accumulation and dopaminergic neurodegeneration in the killifish brain

The neuroprotective effects of xCT deletion in mouse models for PD were shown to be age- and toxin/model-dependent^{2,11}. We will therefore use the xCT^{-/-} killifish to investigate how the absence of system x_c⁻ affects the occurrence and extent of spontaneous degeneration of dopaminergic neurons and the accumulation of α -syn, as was observed previously in WT killifish brain¹⁹.

In collaboration with the lab of Prof. Lies De Groef (KU Leuven), we optimized a set of protocols to detect the presence of A plaques and tauopathy in the aged WT killifish brain, mainly using histological and immunofluorescent stainings as well as a staining protocol to identify protein aggregates, with the aim to validate the potential of new PD models in killifish.

3.4. WP4: Identification of the mechanisms underlying the anticipated neuroprotective effect of xCT deletion in the aged killifish brain

Multiple mechanisms that can underlie the neuroprotective potential of genetic xCT deletion have been identified in the mouse brain. Using the xCT^{-/-} killifish we will investigate how xCT deletion affects the (age-related) pathogenic mechanisms described below and correlate them to the degree of neurodegeneration throughout the lifespan.

(WP4a) Glutamate transporters: *We identified the presence of different excitatory amino acid transporters (EAAT) in our single-nuclei RNA sequencing data from the telencephalon of young and old killifish brains²⁰. Specifically, we detected EAAT1 (GLAST) and EAAT2 (GLT), which are known to be present on murine astrocytes. Our single nuclei data revealed that GLAST is expressed across different cell types in the killifish telencephalon, whereas GLT expression is restricted to astro-like glia (mainly RG1). Now that the presence of these glutamate transporters in the killifish telencephalon has been confirmed, we will develop different assays to quantify, detect and measure the activity of these transporters in the killifish brain.*

(WP4b) (Neuro)Inflammation: For this WP all methods are already optimized on WT fish (immunocytochemistry for L-Plastin; Hybridization Chain Reaction for APOEB; RT-qPCR for inflammatory marker genes il6, il8, il10 sirt, il1 β , tnf, csfr1a).

(WP4c) Metabolic changes: *we are optimizing a protocol to cultivate killifish brain cells to enable metabolic assays on cultivated cells. The goal is to use these cultivated cells for Seahorse metabolic flux analysis.*

(WP4d) The ubiquitin-proteasome system: While generating the xCT^{-/-} killifish, we developed different assays to study the UPS in the killifish. Dysfunction of the UPS has been implicated in several neurodegenerative diseases including PD. However, the UPS remains unexplored in the killifish.

By analyzing our single nuclei sequencing data from the telencephalon of young and aged killifish²⁰, we identified four of the six proteasome subunits described in humans and mice. These proteasome subunits are responsible for the enzymatic activity of the UPS. Notably, we observed that some subunits of the constitutive proteasome were broadly expressed across various cell subtypes, while the inducible subunits were restricted to microglia. Some of the inducible subunits -and not the constitutive subunits- are upregulated upon aging (the same subunit is also upregulated in post-mortem brain tissue of PD patients), and after traumatic brain injury. We confirmed these findings using qPCR on brains of killifish of different ages. These findings are very novel as until now nothing is known about the inducible subunits of the immunoproteasome -a proteasome type which is only present in inflammatory conditions- in the killifish brain.

We also optimized several tools to investigate the function of the UPS in the killifish brain: a proteasome activity assay using different fluorogenic substrates to measure the activity of the different proteasome subunits in the killifish brain as well as qPCR protocols to quantify the expression of the different proteasome subunits. Additionally, we are working on other RNA-level techniques such as hybridization chain reaction, to visualize the localization of the different proteasome subunits.

All these assays will help us better understand the working mechanism of the UPS and its involvement in neurodegenerative diseases such as PD. Over the past months, we collected brain tissue of killifish at different ages (young and aged), which will be used to perform the assays and characterize the evolution of the proteasome during aging.

To conclude, although we do not have a confirmed and validated xCT^{-/-} killifish yet, we further optimized different novel assays that allow us to investigate different aspects of neurodegeneration that are related to PD and we are ready to efficiently start the analyses proposed in our application, as soon as the transgenic fish has been validated.

Finally, in the event we would not be able to overcome the transgenesis issues in the context of this project, we will still have created relevant and needed baseline knowledge about the role of glutamate signaling, proteasome function and neuroinflammatory microglia in brain aging, and we will have gathered more data to strengthen the overall belief that the killifish shows many cellular and molecular signs of spontaneous development of PD with age.

4. **References** (*own references are in bold*)

1. **De Bundel, D. et al. Loss of system x_c⁻ does not induce oxidative stress but decreases extracellular glutamate in hippocampus and influences spatial working memory and limbic seizure susceptibility. *Journal of Neuroscience* 31, 5792–5803 (2011).**
2. **Massie, A. et al. Dopaminergic neurons of system x_c⁻ deficient mice are highly protected against 6 hydroxydopamine induced toxicity. *The FASEB Journal* 25, 1359–1369 (2011).**
3. **Ottestad-Hansen, S. et al. The cystine-glutamate exchanger (xCT, Slc7a11) is expressed in significant concentrations in a subpopulation of astrocytes in the mouse brain. *Glia* 66, 951–970 (2018).**
4. Batiuk, M.Y. et al. Identification of region-specific astrocyte subtypes at single cell resolution. *Nature Communications* 11, 1220 (2020).
5. Sato, H. et al. Redox imbalance in cystine/glutamate transporter-deficient mice. *Journal of Biological Chemistry* 280, 37423–37429 (2005).
6. **Albertini, G. et al. Genetic deletion of xCT attenuates peripheral and central inflammation and mitigates LPS-induced sickness and depressive-like behavior in mice. *Glia* 66, 1845–1861 (2018).**
7. Mesci, P. et al. System x_c⁻ is a mediator of microglial function and its deletion slows symptoms in amyotrophic lateral sclerosis mice. *Brain* 138, 53–68 (2015).
8. **Sprimont, L. et al. Cystine–glutamate antiporter deletion accelerates motor recovery and improves histological outcomes following spinal cord injury in mice. *Scientific Reports* 11, 12227 (2021).**
9. **Massie, A., Boillée, S., Hewett, S., Knackstedt, L. & Lewerenz, J. Main path and byways: Non-vesicular glutamate release by system x_c⁻ as an important modifier of glutamatergic neurotransmission. *Journal of Neurochemistry* 135, 1062–1079 (2015).**
10. **Leclercq, K. et al. Anticonvulsant and antiepileptogenic effects of system x_c⁻ inactivation in chronic epilepsy models. *Epilepsia* 60, 1412–1423 (2019).**
11. **Bentea, E. et al. Aged xCT-Deficient Mice Are Less Susceptible for Lactacystin-, but Not 1-Methyl-4-Phenyl-1,2,3,6-Tetrahydropyridine-, Induced Degeneration of the Nigrostriatal Pathway. *Frontiers in Cellular Neuroscience* 15, 796635 (2021).**
12. **Verbruggen, L. et al. Lifespan extension with preservation of hippocampal function in aged system x_c⁻ deficient male mice. *Molecular Psychiatry* 27, 2355–2368 (2022).**
13. Akhter, F. et al. High Dietary Advanced Glycation End Products Impair Mitochondrial and Cognitive Function. *Journal of Alzheimer's Disease* 76, 165–178 (2020).
14. Padmaraju, V., Bhaskar, J. J., Prasada Rao, U. J. S., Salimath, P. v. & Rao, K. S. Role of advanced glycation on aggregation and DNA binding properties of α -synuclein. *Journal of Alzheimer's Disease* 24, 211–221 (2011).
15. Li, J., Liu, D., Sun, L., Lu, Y. & Zhang, Z. Advanced glycation end products and neurodegenerative diseases: Mechanisms and perspective. *Journal of the Neurological Sciences* 317, 1–5 (2012).
16. Baumgart, M. et al. RNA-seq of the aging brain in the short-lived fish *N. furzeri* - conserved pathways and novel genes associated with neurogenesis. *Aging Cell* 13, 965–974 (2014).
17. Harel, I. et al. A platform for rapid exploration of aging and diseases in a naturally short-lived vertebrate. *Cell* 160, 1013–1026 (2015).
18. Harel, I., Valenzano, D. R. & Brunet, A. Efficient genome engineering approaches for the short-lived African turquoise killifish. *Nature Protocols* 11, 2010–2028 (2016).
19. Matsui, H., Kenmochi, N. & Namikawa, K. Age- and α -Synuclein-Dependent Degeneration of Dopamine and Noradrenaline Neurons in the Annual Killifish *Nothobranchius furzeri*. *Cell Rep* 26, 1727–1733.e6 (2019).
20. **Ayana, R., Zandekci, C. et al. Single-cell sequencing unveils the impact of aging on the progenitor cell diversity in the telencephalon of the female killifish *N. furzeri*. *Aging Cell* 23, e14251 (2024).**



Geneeskundige Stichting Koningin Elisabeth
Fondation Médicale Reine Elisabeth
Königin-Elisabeth-Stiftung für Medizin
Queen Elisabeth Medical Foundation

Universitaire onderzoeksprojecten
2023-2025 gefinancierd door de G.S.K.E.

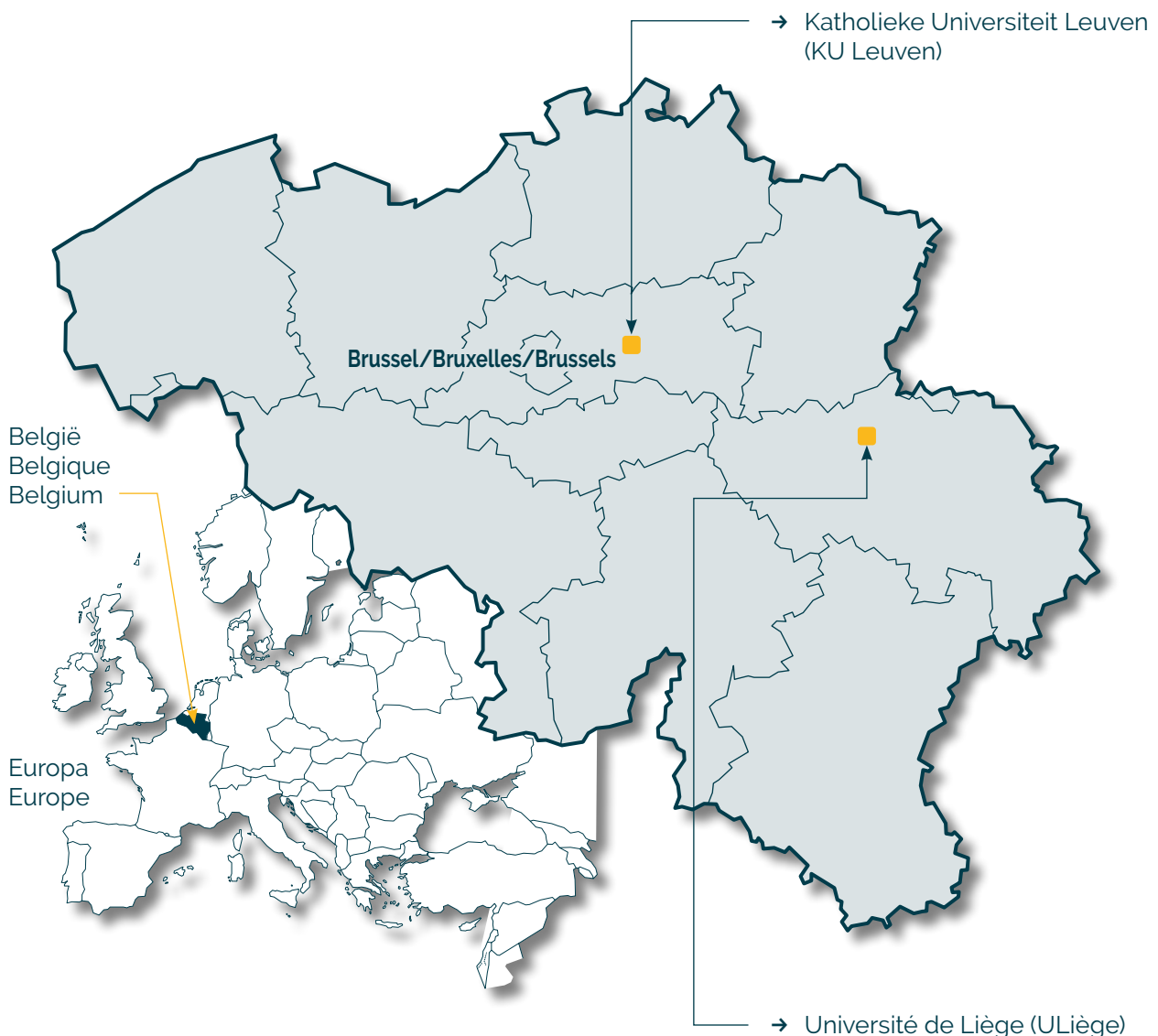
Projets de recherche universitaire
2023-2025 subventionnés par la F.M.R.E.

University research projects
2023-2025 funded by the Q.E.M.F.

Universiteiten met onderzoeksprogramma's die gesteund worden door de G.S.K.E.

Universités ayant des programmes de recherche subventionnés par la F.M.R.E.

Universities having research programs supported by the Q.E.M.F.

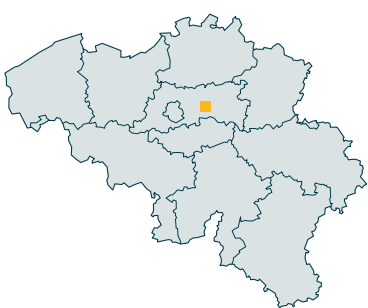


Universitaire onderzoeksprojecten 2023-2025 gefinancierd door de G.S.K.E.

Projets de recherche universitaire 2023-2025 subventionnés par la F.M.R.E.

University research projects 2023-2025 funded by the Q.E.M.F.

KU Leuven



Prof. dr. Bart De Strooper (VIB)

A vicious A β oligomers-dependent neuron-microglia cycle fuels Alzheimer's Disease

Prof. dr. Pierre Vanderhaeghen (VIB)

Deciphering the mechanisms underlying neurogenesis defects in mitochondrial diseases

Prof. dr. Veerle Baekelandt

The role of LRRK2 in the peripheral immune system and gut-to-brain spreading of alpha-synuclein pathology in Parkinson's disease

Prof. dr. Thomas Voets

Unraveling the etiology of TRPM3-dependent neurodevelopmental disorders

ULiège



Prof. dr. Pierre Maquet

Quantitative MRI at 7 Tesla addresses ten questions about brain small vessel diseases



Geneeskundige Stichting Koningin Elisabeth
Fondation Médicale Reine Elisabeth
Königin-Elisabeth-Stiftung für Medizin
Queen Elisabeth Medical Foundation

Progress report of the
university research project of

Prof. dr. Bart De Strooper
Katholieke Universiteit Leuven
(KU Leuven-VIB)

Prof. dr. Bart De Strooper (KU Leuven-VIB)
VIB Center for Brain and Disease Research
Herestraat 49
3000 Leuven
Belgium
T +32 495 77 10 44
Bart.Destrooper@vib.be

A vicious A β oligomers-dependent neuron-microglia cycle fuels Alzheimer's Disease

Over the past year, my research has focused on understanding the role of microglia and astrocytes in Alzheimer's disease (AD) pathology, particularly their involvement in amyloid aggregation, plaque formation, and neurodegeneration. The studies conducted have contributed to clarifying the functional states of microglia and their interaction with amyloid pathology, as well as exploring novel mechanisms of neuronal death, such as necroptosis, that could serve as therapeutic targets.

1. Single-cell transcriptomic profiling of human microglia in an AD model

To address challenges in analyzing human microglial states in AD, we generated 138,577 single-cell expression profiles of human stem cell-derived microglia xenotransplanted into the brains of AppNL-G-F amyloid pathology models and wild-type controls. Our findings demonstrated that human microglia adopt a disease-associated state akin to that observed in mouse models but exhibit a more pronounced human leukocyte antigen (HLA) signature, likely related to antigen presentation in response to amyloid plaques. Furthermore, a pro-inflammatory cytokine/chemokine response to oligomeric A (CRM response) was identified. Genetic modifications in APOE and TREM2 significantly altered these microglial responses, highlighting their impact on disease progression and therapeutic strategies.

2. Microglia as key modulators of plaque formation and clearance

Using genetic and pharmacological approaches, we examined the role of microglia in A plaque dynamics. Our results demonstrated that microglial depletion before plaque formation reduced plaque deposition and neuritic dystrophy, reinforcing the role of microglia in plaque initiation. Transplantation of human microglia restored A plaque formation, confirming their active contribution to amyloid pathology. However, while microglial depletion decreased insoluble A levels, soluble A remained unaffected, challenging the assumption that microglia are primary A-clearance mediators. In later disease stages, microglial depletion resulted in reduced plaque compaction and increased neuritic dystrophy, suggesting a dual role in both plaque formation and protection. Moreover, human microglia expressing the TREM2R47H mutation exacerbated plaque pathology, underscoring the influence of microglial activation states on disease progression.

3. APOE isoform expression in astrocytes drives amyloid pathology

To investigate the impact of astrocyte-derived APOE isoforms on A pathology, we expressed human APOE isoforms in astrocytes within an Apoe-deficient AD mouse model. This was sufficient to restore amyloid plaque formation and induce transcriptional changes in adjacent Apoe-deficient microglia. Notably, both APOE4 (a major genetic risk factor for AD) and the protective APOE2 variant increased fibrillar plaque deposition but differentially influenced soluble A aggregates. The findings emphasize astrocytes as central regulators of APOE-driven amyloid pathology and microglial activation.

4. Necroptosis and neuronal death in Alzheimer's Disease

Beyond amyloid and Tau pathology, we explored the role of regulated cell death pathways in AD-associated neurodegeneration. Our findings indicate that necroptosis plays a significant role in AD progression, with necroptosis markers accumulating in granulovacuolar neurodegeneration vesicles (GVD) and closely linked to Tau pathology. We identified neuron-specific activation of a GVD-mediated necroptosis pathway, suggesting a potential link between necrosome activation and endo-lysosomal dysfunction. Importantly, inhibiting necroptosis in AD models reduced neuronal loss, positioning necroptosis as a promising therapeutic target to preserve cognitive function when combined with amyloid-lowering strategies.

Using mouse models and primary neuronal cultures, we demonstrated that necroptosis-related proteins were upregulated in APP-Tau transgenic mice and neurons treated with phosphorylated Tau seeds. However, APP transgenic mice with only A deposits did not show the same activation pattern. Additionally, necroptosis inhibitors effectively reduced GVD-associated neuronal loss, suggesting that "GVD-necroptosis" represents a delayed but targetable form of neurodegeneration in AD.

5. Conclusion and future directions

This year's research has significantly advanced our understanding of microglial and astrocytic contributions to AD pathology, particularly their roles in amyloid aggregation, inflammatory responses, and neuronal loss. Key findings include:

- Identification of disease-associated human microglial states and their genetic modulation by APOE and TREM2.
- Clarification of microglial roles in amyloid plaque formation and compaction.
- Demonstration of astrocyte-driven APOE-mediated amyloid pathology and its influence on microglia.
- Discovery of necroptosis as a novel, potentially targetable mechanism of neuronal death in AD.

Future work will focus on:

- Further dissecting the molecular mechanisms underlying microglial and astrocytic interactions in AD.
- Investigating therapeutic interventions targeting necroptosis in preclinical models.
- Exploring the impact of mixed oligomeric A species on microglial states to refine therapeutic strategies.

These findings pave the way for novel treatment approaches aimed at modulating glial responses and preserving neuronal function in Alzheimer's disease.

6. Publications:

1. Baligács N, Albertini G, Borrie SC, Serneels L, Pridans C, Balusu S, De Strooper B. Homeostatic microglia initially seed and activated microglia later reshape amyloid plaques in Alzheimer's Disease. *Nat Commun.* 2024 Dec 5;15(1):10634. doi: 10.1038/s41467-024-54779-w. PMID: 39639016; PMCID: PMC11621353. **IF: 16.6; Q1**
2. De Strooper B, Haass C, Hardy J, Zetterberg H. Divisions over the regulation of lecanemab. *Lancet.* 2024 Nov 30;404(10468):2160-2161. doi: 10.1016/S0140-6736(24)02513-3. Epub 2024 Nov 14. PMID: 39551058. **IF: 98.4; Q1 (but is only a letter)**
3. Preman P, Moechars D, Fertan E, Wolfs L, Serneels L, Shah D, Lamote J, Poovathingal S, Snellinx A, Mancuso R, Balusu S, Klenerman D, Arranz AM, Fiers M, De Strooper B. APOE from astrocytes restores Alzheimer's A-pathology and DAM-like responses in APOE deficient microglia. *EMBO Mol Med.* 2024 Dec;16(12):3113-3141. doi: 10.1038/s44321-024-00162-7. Epub 2024 Nov 11. PMID: 39528861; PMCID: PMC11628604. **IF 9.0 Q1**
4. Koper MJ, Moonen S, Ronisz A, Ospitalieri S, Callaerts-Vegh Z, T'Syen D, Rabe S, Staufenbiel M, De Strooper B, Balusu S, Thal DR. Inhibition of an Alzheimer's disease-associated form of necroptosis rescues neuronal death in mouse models. *Sci Transl Med.* 2024 Oct 30;16(771):eadf5128. doi: 10.1126/scitranslmed.adf5128. Epub 2024 Oct 30. PMID: 39475569. **IF 15.8, Q1**
5. Balusu S, De Strooper B. The necroptosis cell death pathway drives neurodegeneration in Alzheimer's disease. *Acta Neuropathol.* 2024 Jun 9;147(1):96. doi: 10.1007/s00401-024-02747-5. PMID: 38852117; PMCID: PMC11162975. **IF 13.1, Q1**
6. Mancuso R, Fattorelli N, Martinez-Muriana A, Davis E, Wolfs L, Van Den Daele J, Geric I, Premereur J, Polanco P, Bijnens B, Preman P, Serneels L, Poovathingal S, Balusu S, Verfaillie C, Fiers M, De Strooper B. Xenografted human microglia display diverse transcriptomic states in response to Alzheimer's disease-related amyloid- pathology. *Nat Neurosci.* 2024 May;27(5):886-900. doi: 10.1038/s41593-024-01600-y. Epub 2024 Mar 27. PMID: 38539015; PMCID: PMC11089003. **IF: 21.2, Q1**



Geneeskundige Stichting Koningin Elisabeth
Fondation Médicale Reine Elisabeth
Königin-Elisabeth-Stiftung für Medizin
Queen Elisabeth Medical Foundation

Progress report of the
university research project of

Prof. dr. Pierre Vanderhaeghen
Katholieke Universiteit Leuven
(KU Leuven-VIB)

Prof. dr. Pierre Vanderhaeghen (KU Leuven-VIB)
VIB Center for Brain & Disease Research
Department of Neurosciences, KU Leuven
Stem Cell and Developmental Neurobiology Lab
O&N5 Herestraat 49 box 602 | 3000 Leuven | Belgium
Email: pierre.vanderhaeghen@kuleuven.be
T +32 16 3 77038
F +32 16 3 30827
<https://pvdhlab.org>

Deciphering the mechanisms underlying neurogenesis defects in mitochondrial diseases.

1. State of the art and objectives

Mitochondrial dysfunction can result in various forms of neurodevelopmental diseases (NDD), from microcephaly to intellectual disability. This suggests important roles for mitochondria in neural development, but these have remained poorly known, as their links with diseases. We had previously shown that mitochondria dynamics play a key role in neurogenesis of mouse and human NSPCs of the cerebral cortex^{1,2}. We also identified intriguing differences in this process between mouse and human cortical cells, which could be linked to increased cortical size and complexity in our species.

In this project we aim to study the molecular mechanisms by which mitochondria dynamics and metabolic activity impact neuronal fate acquisition, and relate these to human corticogenesis in normal and pathological conditions.

This project will yield to deep mechanistic insights on mitochondria function during neural development, and will enable to build a robust and diverse pipeline of analysis of mitochondria/metabolic defects in human neural development, which could be applied further to dissect pathogenic mechanisms and to establish screening platforms for diagnostic or therapeutic purposes.

2. Results

In the frame of this project we have first shown that mitochondria metabolism exerts a direct effect on neuronal differentiation in a species-specific fashion, not only *in vitro* but also *in vivo* in xenotransplanted human cortical neurons³. We are now focusing on the downstream mechanisms by implementing epigenetic and proteomic analyses to our systems in control conditions and following metabolic reprogramming^{4,5}. We have thus obtained the important result that protein turnover is two-fold lower human neurons than in mouse counterparts, and that manipulation of mitochondria does not seem to alter these differences. We now implement the epigenetic profiling experiments testing the impact of mitochondria on post-translational modifications in developing mouse and human cortical neurons *in vitro*. We have also started to test whether and how acceleration of neuronal developmental timing of human neurons actually impacts their functional properties. In this context we have recently obtained the important proof of principle that acceleration of synaptogenesis, obtained by loss of function of the SYNGAP1 synaptic protein, can lead to precocious responsiveness to visual stimulation and altered plasticity of human neurons^{6,7}, as we previously hypothesized. We are now pursuing these findings by testing the direct impact of metabolism on neuronal functional development and plasticity, and plan to explore the relationships between mitochondria metabolism and important synaptogenesis proteins such as SYNGAP1.

On the other hand, we have now obtained interesting evidence that ETC activity is higher on mouse than human cortical progenitors, while it also increases with developmental time in the mouse. As these differences could lead to distinct NAD⁺/NADH metabolism, we have now implemented successfully ad hoc sensory imaging on cortical cultures (using sonar imaging⁸), to test this during neuronal fate acquisition, in relation to timing differences, species differences, or both. In parallel we have found that metabolic changes induced by blockade of glycolysis or stimulation of fatty acid oxidation, leads to dramatic changes in the fate of generated neurons,

which could be compatible with an impact of mitochondria oxidative metabolism on cortical temporal patterning, in line with previous findings in the fly nervous system⁹. We are now consolidating these data using human cortical cultures and organoids, using systems developed in the lab to this purpose¹⁰.

3. References

1. Iwata, R. & Vanderhaeghen, P. Regulatory Roles of Mitochondria and Metabolism in Neurogenesis. *Curr Opin Neurobiol* **69**, 231–240 (2021).
2. Iwata, R., Casimir, P. & Vanderhaeghen, P. Mitochondrial dynamics in postmitotic cells regulate neurogenesis. *Science (1979)* **862**, 858–862 (2020).
3. Iwata, R. *et al.* Mitochondria Metabolism Sets the Species-Specific Tempo of Neuronal Development. *Science* **379**, eabn4705 (2023).
4. Casimir, P., Iwata, R. & Vanderhaeghen, P. Linking mitochondria metabolism, developmental timing, and human brain evolution. *Current Opinion in Genetics and Development* vol. 86 Preprint at <https://doi.org/10.1016/j.gde.2024.102182> (2024).
5. Iwata, R. & Vanderhaeghen, P. Metabolic mechanisms of species-specific developmental tempo. *Dev Cell* (2024) doi:10.1016/j.devcel.2024.05.027.
6. Libé-Philippot, B. *et al.* Synaptic neoteny of human cortical neurons requires species-specific balancing of SRGAP2-SYNGAP1 cross-inhibition. *Neuron* **112**, 3602–3617.e9 (2024).
7. Vermaercke, B. *et al.* SYNGAP1 deficiency disrupts neoteny in xenotransplanted human cortical neurons in vivo. *Neuron* **112**, 1–11 (2024).
8. Zhao, Y. *et al.* SoNar, a Highly Responsive NAD⁺/NADH Sensor, Allows High-Throughput Metabolic Screening of Anti-tumor Agents. *Cell Metab* (2015) doi:10.1016/j.cmet.2015.04.009.
9. Van Den Ameele, J. & Brand, A. H. Neural stem cell temporal patterning and brain tumour growth rely on oxidative phosphorylation. doi:10.7554/eLife.47887.001.
10. Van Heurck, R. *et al.* CROCCP2 acts as a human-specific modifier of cilia dynamics and mTOR signaling to promote expansion of cortical progenitors. *Neuron* **111**, 65–80 (2023).

4. Publications 2025 in the frame of GSKE

- Metabolic mechanisms of species-specific developmental tempo.
Iwata R, Vanderhaeghen P.
Dev. Cell (2024) 59, 1628–1639. *IF: 14*
- Human synaptic neoteny requires species-specific balancing of SRGAP2-SYNGAP1 cross-inhibition.
Libé-Philippot B, Iwata R, Recupero AJ, Wierda K, Ditkowska M, Gaspariunaite V, Vermaercke B, Peze-Heidsieck E, Remans D, Charrier C, Polleux F, Vanderhaeghen P.
Neuron (2024) 112, 3602–3617. *IF: 18*
- CTNND2 moderates the pace of synaptic maturation and links human evolution to synaptic neoteny.
Assendorp N, Fossati M, Libé-Philippot B, Christopoulou E, Depp M, Rapone R, Dingli F, Loew D, Vanderhaeghen P, Charrier C.
Cell Reports (2024) 43, 114797. *IF: 8*
- Linking Mitochondria Metabolism, Developmental Timing, and Human Brain Evolution.
Casimir P, Iwata R, Vanderhaeghen P.
Curr. Opin. Gen. & Dev. (2024) 86:102182. *IF: 5*
- SYNGAP1 deficiency disrupts neoteny in xenotransplanted human cortical neurons in vivo.
Vermaercke B, Iwata R, Weirda K, Boubakar L, Rodriguez P, Ditkowska M, Bonin V, Vanderhaeghen P.
Neuron (2024) 112, 3058–3068. *IF: 18*



Geneeskundige Stichting Koningin Elisabeth
Fondation Médicale Reine Elisabeth
Königin-Elisabeth-Stiftung für Medizin
Queen Elisabeth Medical Foundation

Progress report of the
university research project of

Prof. dr. Veerle Baekelandt
Katholieke Universiteit Leuven (KU Leuven)

Prof. dr. Veerle Baekelandt (KU Leuven)
Laboratory for Neurobiology and Gene Therapy
Division of Molecular Medicine K.U.Leuven –
Faculty of Medicine Kapucijnenvoer 33 VCTB+5
B-3000 Leuven
Belgium
Tel.: +32 16 37 40 61
Fax: +32 16 33 63 36
E-mail: Veerle.Baekelandt@kuleuven.be

The role of LRRK2 in the peripheral immune system and gut-to-brain spreading of alpha-synuclein pathology in Parkinson's disease

The role of LRRK2 in the peripheral immune system and gut-to-brain spreading of alpha-synuclein pathology in Parkinson's disease

1. Introduction

Parkinson's disease (PD) is the second most common neurodegenerative disorder. The neuropathological hallmarks consist of dopaminergic (DA) neuron loss in the *substantia nigra pars compacta* (SNpc) and cytoplasmic alpha-synuclein (Syn) aggregates, termed Lewy bodies. **Cell-to-cell transmission** of misfolded Syn has been proposed to account for the pathology stages described by Braak^{1,2}, suggesting that synucleinopathy might start in the periphery within the gastrointestinal tract (GI) and progress towards the brain via the vagus nerve. Mutations and variations in **LRRK2** (leucine-rich repeat kinase 2) are the most common cause of both familial and sporadic forms of PD³. Most pathogenic mutations are associated with enhanced kinase activity, thus making LRRK2 a very attractive therapeutic target⁴.

However, many questions remain, especially on how LRRK2 gain-of-function affects disease pathophysiology and how it correlates with PD.

1.1. Summary progress report year 1

The link between the gut and the brain in PD pathogenesis is currently a subject of intense research. Indeed, gastrointestinal dysfunction is known as an early symptom in PD and inflammatory bowel disease (IBD) has recently been recognised as a risk factor for PD. The leucine-rich repeat kinase 2 (LRRK2) is a PD- and IBD-related protein with highest expression in immune cells. We have completed a study to provide evidence for a central role of LRRK2 in gut inflammation and PD. The presence of the gain-of-function G2019S mutation significantly increased the disease phenotype and inflammatory response in a mouse model of experimental colitis based on chronic dextran sulphate sodium (DSS) administration. Bone marrow transplantation of wild-type cells into G2019S knock-in mice fully rescued this exacerbated response, proving the key role of mutant LRRK2 in immune cells in this experimental colitis model. Furthermore, partial pharmacological inhibition of LRRK2 kinase activity also reduced the colitis phenotype and inflammation. Moreover, chronic experimental colitis also induced neuroinflammation and infiltration of peripheral immune cells into the brain of G2019S knock-in mice. Finally, combination of experimental colitis with overexpression of -synuclein in the substantia nigra aggravated motor deficits and dopaminergic neurodegeneration in G2019S knock-in mice. Taken together, our results link LRRK2 with the immune response in colitis and provide evidence that gut inflammation can impact brain homeostasis and contribute to neurodegeneration in PD.

1.2. Progress report year 2

In the second year we have focused on the role of LRRK2 on neuroinflammation and neurodegeneration induced by Syn in the brain. While no direct interaction between LRRK2 and Syn has been consistently reported, numerous indirect interplays have been described, highlighting the intricate relationship between these two key proteins⁵. Preclinical studies have shown increased Syn pathology and neurodegeneration in LRRK2-G2019S mouse and cell

models^{6,7}, but the molecular mechanisms linking LRRK2 and Syn remain to be unraveled. In addition, we have extended our study to tau-induced neurodegeneration. Indeed, in 60-80% of LRRK2-PD patients no typical Lewy body pathology is found, while tau pathology is reported in a larger portion of these patients^{8,9}.

For this study we induced overexpression of the human WT Syn in the SN by injecting unilaterally our in house recombinant adeno-associated vector (rAAV 2/7). This model displays progressive dopaminergic neurodegeneration, behavioural deficits and neuroinflammation as previously described in¹⁹. Behavioural analysis was conducted at 2, 4, 8 and 14 weeks post-injection but no differences were observed between LRRK2 KI and WT mice (Fig 1). Animals were sacrificed at 4 and 14 weeks post injection and we assessed the dopaminergic cell loss in the SN with stereological quantification of the TH+ cells. At the latest time point, the neurodegeneration induced by Syn overexpression was significantly higher in the LRRK2 KI mice (Fig. 1).

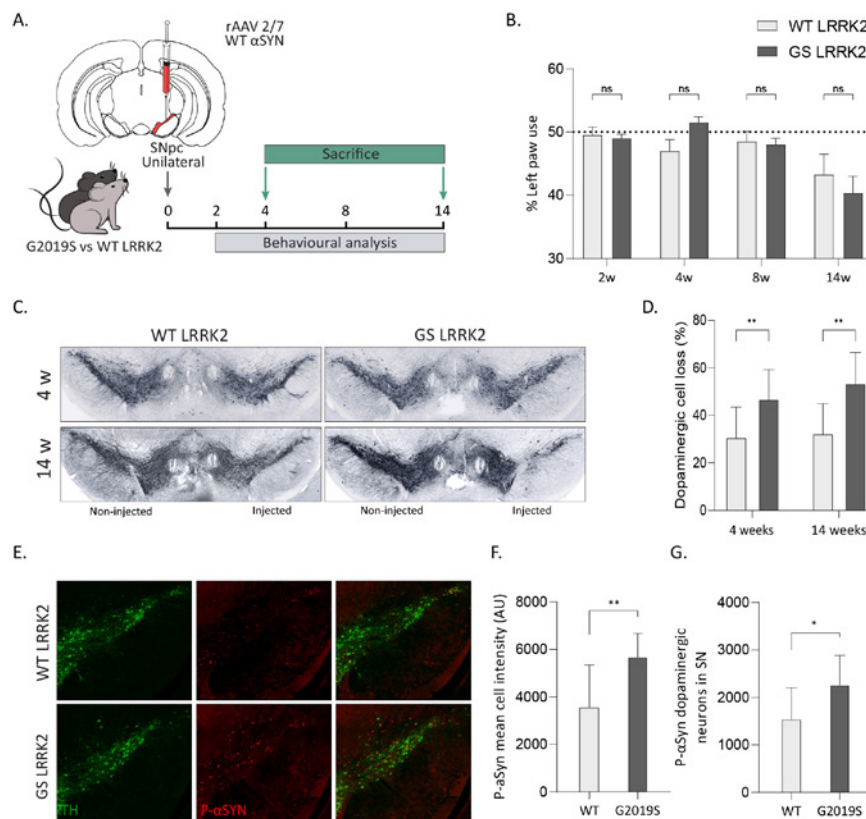


Figure 1. The G2019S LRRK2 mutation aggravates Syn-induced neurodegeneration A) Experimental design. Mice were unilaterally injected with AAV2/7-Syn in the substantia nigra. B) Cylinder test. Graph displays the % left forepaw use 3 and 5 weeks after AAV2/7-Syn injection in WT and GS mice. C) TH immunostaining on coronal sections of the SN 4 and 8 weeks after with AAV2/7-Syn injection in WT and GS mice. D) Stereological quantification of TH+ cells in the right SN relative to the non-injected side 4 and 8 weeks p.i. Graphs represent mean \pm SD. E) Double TH and pS129 Syn immunostaining on coronal sections of the SN 4 weeks post injection. F) Mean fluorescent intensity of pS129 Syn immunoreactivity in the transduced neurons. G) Mean fluorescent intensity of pS129 Syn immunoreactivity in the TH+ neurons of the SN. Graphs represent mean \pm SD

To study the mechanisms involved in the effect of the G2019S mutation on Syn we focused our subsequent analysis on the 4 week timepoint, so prior to the extensive neurodegeneration in SN. Next to the neuronal cell loss we assessed the levels of pathological Syn in the remaining neurons in SN. Neurons double positive for TH and phosphorylated S129 (p-S129) Syn as well as the levels of total and p-S129 Syn were measured (Figure 1G-I). Significantly more double positive cells and higher levels of pathological -synuclein were found in the G2019S injected animals compared to the WT controls, with similar levels of dopaminergic neurodegeneration.

Given the growing body of evidence reporting the role of LRRK2 in regulating inflammatory responses we characterised the inflammation in the SN of the injected mice. First, we performed a flow cytometry immunophenotyping (Figure 2A). 4 weeks post injection Syn overexpression induced more inflammatory response in the injected area compared to a control luciferase vector both for WT and G2019S LRRK2 mice. Interestingly, LRRK2 G2019S mice showed significant infiltration of peripheral immune cells such as total myeloid cells (CD45⁺ CD11b⁺), Ly6C⁺ monocytes, and natural killer (NK) cells (CD161⁺), while a clear reduction in the levels of CD25 marker, a marker indicating regulatory T cell phenotype, was observed (Figure 2B). Similar but non-significant trends were observed for Ly6C⁻ and MHCII⁺ monocytes. In addition, proinflammatory cytokine quantification in SN revealed elevated levels of CCL2, CCL3, V α VL10, IFN γ , IL10, IL-1, IL-2, and TNF α in GS-LRRK2 compared to the WT mice (Figure 2C). Histological characterisation in the SN showed increased accumulation of astrocytes (GFAP⁺ cells) and CD68⁺ cells but no differences in the microglia numbers and activation status (Figure 2D, E).

Further biochemical characterisation of our model revealed an accumulation of proteins related to the endolysosomal pathway in the SN of G2019S mice. Particularly, LAMP2, cathepsin D, B, H, and L were significantly increased in the SN of G2019S mice compared to WT LRRK2 mice (Figure 3). Nevertheless, no differences were found in the levels of other lysosome related proteins such as LAMP1, p62, and GBA (data not shown).

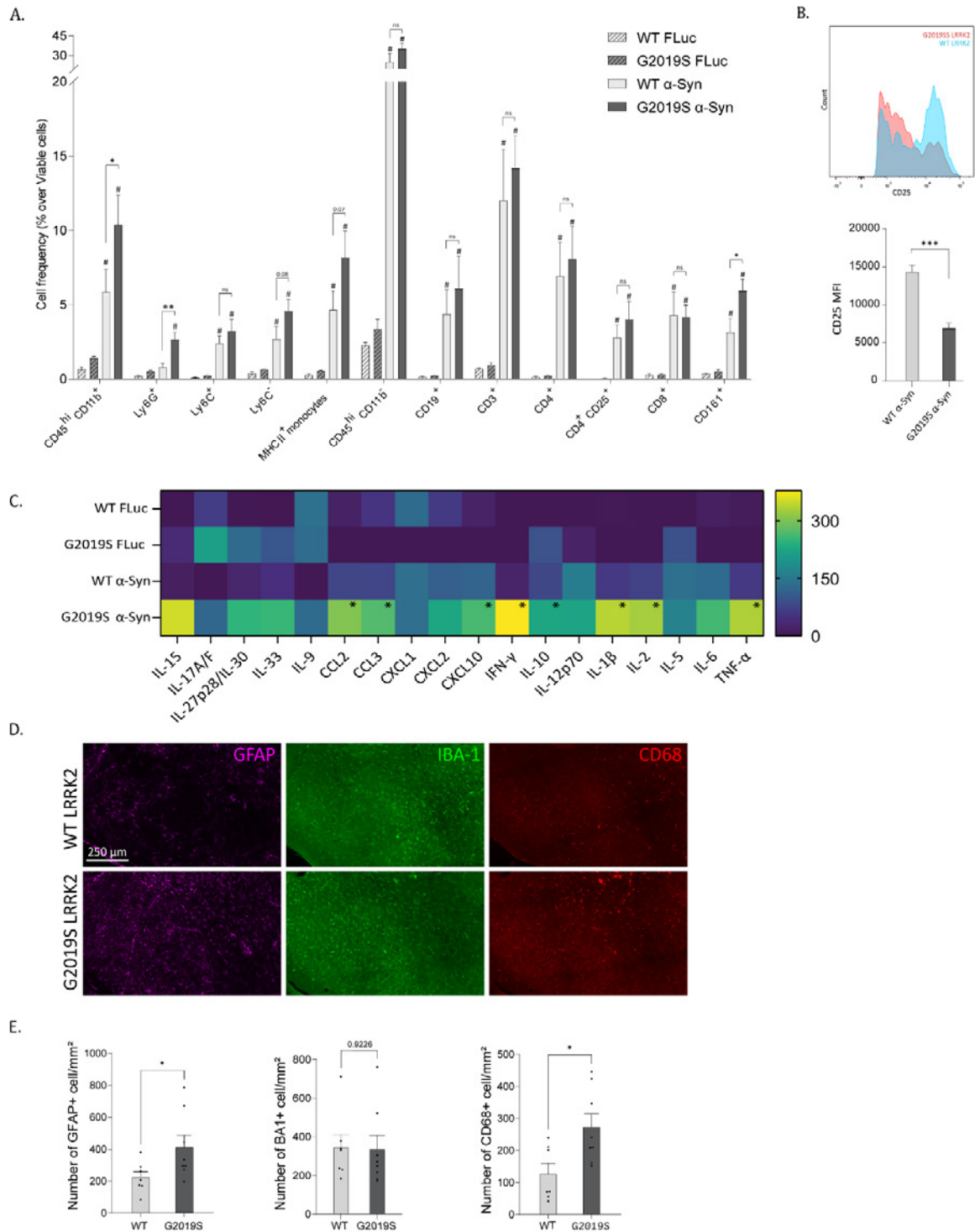
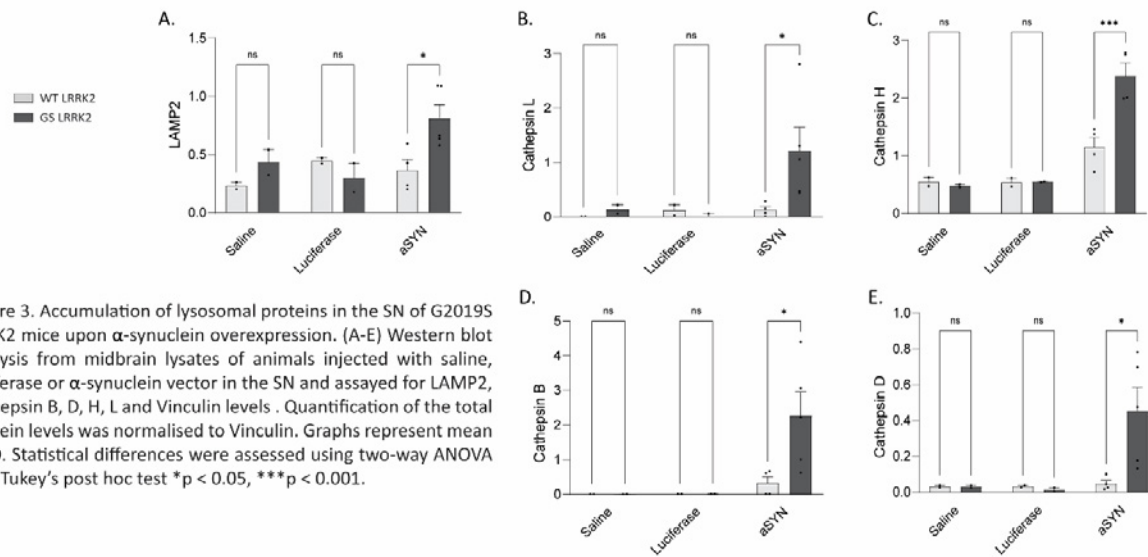


Figure 2. Increased inflammatory response in the SN of G2019S LRRK2 mice after α -Synuclein overexpression. (A) Flow cytometry immunophenotyping in SN of WT and GS LRRK2 mice one month post injection. Number of total leukocytes (CD45⁺), myeloid cells (CD45⁺ CD11b⁺), Ly6C⁺ and Ly6C⁻ monocytes, MHCII⁺ monocytes, dendritic cells (CD11c⁺), neutrophils (Ly6G⁺), lymphocytes (CD45⁺ CD11b⁻), T cells (CD8⁺ and CD4⁺), and NK cells (CD161⁺) are shown. Graphs represent mean \pm SD. Statistical differences were assessed using Student's t-test, * p < 0.05 (B) MFI of the CD25 CD4⁺ T cells. Graph represent mean \pm SD and statistical differences were assessed using Student's t-test, *** p < 0.001 (C) Cytokines were measured in midbrain protein extracts from WT and GS LRRK2 mice one month post injection as well as control mice injected with Luciferase control vector (FLuc). Increased levels of CCL2, CCL3, CXCL10, IFN- γ , IL-10, IL-1 β , IL-2, and TNF- α were found upon α -Synuclein overexpression in G2019S mice. Graphs represent mean \pm SD. Statistical differences were assessed using Student's t-test * p < 0.05. (D) Representative pictures of immunostaining for astrocytes (GFAP), microglia (IBA-1) and CD68 in the SN of WT and G2019S LRRK2 mice. (E) Respective quantification of the marker, graphs represent mean \pm SD. Statistical differences were assessed using Student's t-test, * p < 0.05.



In order to compare the effect of Syn with tau expression, we have already initiated experiments using AAV2/7-2N4R tau injections. Remarkably, pilot injections with a serial dilution to determine the optimal vector dose revealed that AAV2/7-2N4R tau induced more pronounced neurodegeneration than a similar titer of AAV2/7-Syn. We decided to proceed with a dose of 0.6×10^8 GC AAV2/7-2N4R tau in order to reach an intermediate degree of DA cell loss. The mice were followed for behavior at 2 and 4 weeks and sacrificed at 4 weeks post injection. Preliminary quantifications revealed an increased loss of DA neurons, as well as significantly higher levels of hyperphosphorylated tau in the LRRK2 G2019S KI mice compared to WT mice (Fig 4).

Another cohort of mice injected with AAV2/7-2N4R tau is planned to be analysed at 8 weeks post injection in order to reach a similar DA neuron loss in the LRRK2 G2019S KI mice as with Syn overexpression. In view of the proposed role of LRRK2 in lysosomal function, we will characterize potential lysosomal changes by immunohistochemical analysis and western blot. We will conduct immunofluorescent staining of different late endosomal/lysosomal markers such as LAMP1, LAMP2a, Cathepsin B, and GCase together with TH in the SNpc. In addition, nigral extracts will be analysed by western blotting to assess levels of lysosomal markers such as LAMP2a, cathepsin B, D, L and H. Given the suggested role of LRRK2 in the regulation of the cytoskeletal dynamics, as well as the important role of tau stabilizing neuronal microtubules, we will characterize axonal and neuritic morphology and growth, using Imaris software on coronal and/or sagittal brain sections. We will also quantify different cytoskeletal-associated proteins via western blot, focusing on known LRRK2 interactors (PAK6, LIMK1, and F-, G-actin)¹⁰.

Interestingly, pilot data suggest a considerable microglial response to AAV2/7-Syn in G2019S LRRK2 KI mice, which appeared in contrast very mild after AAV2/7-2N4R tau injection (data not shown). This suggests that LRRK2 might regulate Syn and tau neuropathology through distinct pathways, but this needs further analysis.

In addition, quantitative analysis of immune cell populations will be performed by flow cytometry of nigral brain extracts¹¹. This will give a detailed characterization of the presence of myeloid cells (CD45hi, CD11b+), classical (Ly6C+) and non-classical (Ly6C-) monocytes, dendritic cells (CD11c+), granulocytes (Ly6G+, Ly6C+, CD11b+) and the lymphoid population (CD45hi, CD11b-), more specifically the CD8+ and CD4+ T cells.

Finally, pro- and anti-inflammatory proteins will be analysed in protein fractions of midbrain extracts using a multiplex Meso-Scale panel. This will allow us to describe in more depth the possible inflammatory environment in the SN.

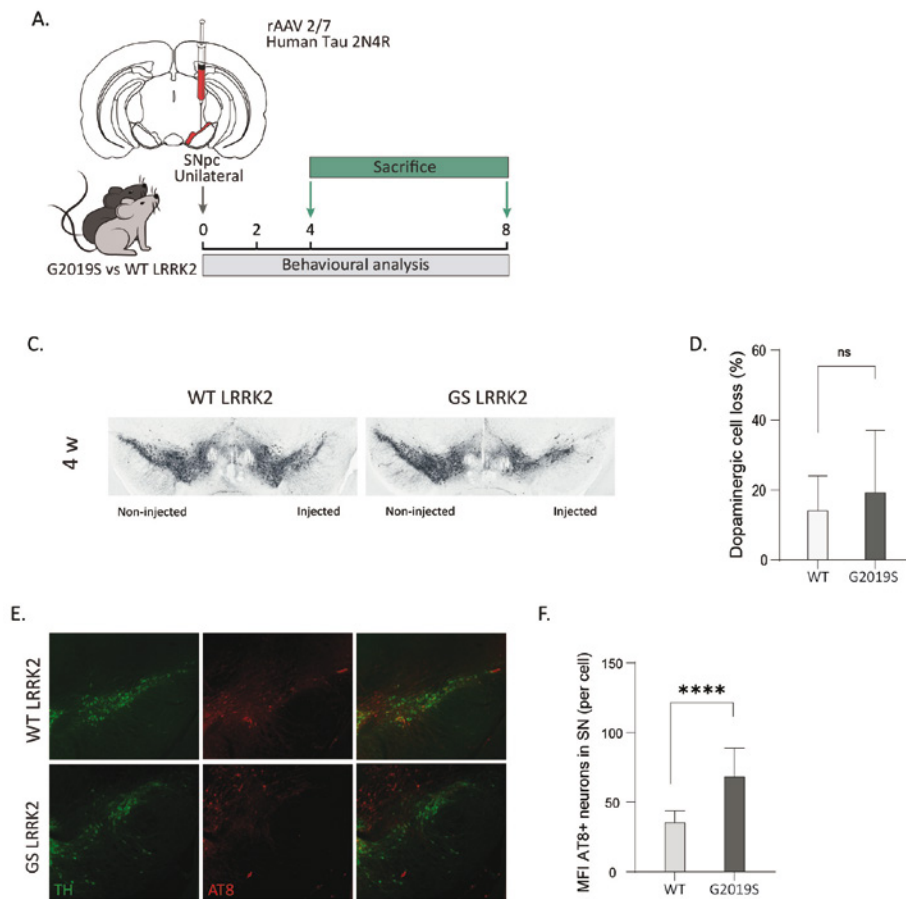


Figure 4. The G2019S LRRK2 mutation enhances tau phosphorylation and neurodegeneration. A) Experimental design. Mice were unilaterally injected with Tau 2N4R rAAV 2/7 in the substantia nigra. B) TH immunostaining on coronal sections of the SN 4 weeks after tau 2N4R rAAV injection in WT and GS mice. C) Stereological quantification of TH⁺ cells in the right SN relative to the non-injected side 4 weeks p.i. D) Double immunostaining for TH and Tau AT8 on coronal sections of the SN 4 weeks post injection. E) Mean fluorescent intensity of AT8 p-Tau in the transduced neurons. Graphs represent mean ± SD

2. Publications with Q.E.M.F. acknowledgement

- Cabezudo D, Tsafaras G, Van Acker E, Van den Haute C, [Baekelandt V.](#) (2023) Mutant LRRK2 exacerbates immune response and neurodegeneration in a chronic model of experimental colitis. *Acta Neuropathologica*, 146(2):245-261. (IF 15.9, cit 11)

3. References

1. Braak, H., Tredici, K. D., Rub, U., de Vos, R. A., Jansen Steur, E. N. & Braak, E. Staging of brain pathology related to sporadic Parkinson's disease. *Neurobiol Aging* **24**, 197-211 (2003).
2. Peelaerts, W. & Baekelandt, V. α -Synuclein strains and the variable pathologies of synucleinopathies. *J Neurochem* **139 Suppl 1**, 256-274, doi:10.1111/jnc.13595 (2016).
3. Monfrini, E. & Di Fonzo, A. Leucine-Rich Repeat Kinase (LRRK2) Genetics and Parkinson's Disease. *Adv Neurobiol* **14**, 3-30, doi:10.1007/978-3-319-49969-7_1 (2017).
4. Tolosa, E., Vila, M., Klein, C. & Rascol, O. LRRK2 in Parkinson disease: challenges of clinical trials. *Nat Rev Neurol* **16**, 97-107, doi:10.1038/s41582-019-0301-2 (2020).
5. O'Hara, D. M., Pawar, G., Kalia, S. K. & Kalia, L. V. LRRK2 and alpha-Synuclein: Distinct or Synergistic Players in Parkinson's Disease? *Front Neurosci* **14**, 577, doi:10.3389/fnins.2020.00577 (2020).
6. Bieri, G., Brahic, M., Bousset, L., Couthouis, J., Kramer, N. J., Ma, R., Nakayama, L., Monbureau, M., Defensor, E., Schule, B., Shamloo, M., Melki, R. & Gitler, A. D. LRRK2 modifies alpha-syn pathology and spread in mouse models and human neurons. *Acta Neuropathol* **137**, 961-980, doi:10.1007/s00401-019-01995-0 (2019).
7. Henderson, M. X., Cornblath, E. J., Darwich, A., Zhang, B., Brown, H., Gathagan, R. J., Sandler, R. M., Bassett, D. S., Trojanowski, J. Q. & Lee, V. M. Y. Spread of alpha-synuclein pathology through the brain connectome is modulated by selective vulnerability and predicted by network analysis. *Nat Neurosci* **22**, 1248-1257, doi:10.1038/s41593-019-0457-5 (2019).
8. Sosero, Y. L. & Gan-Or, Z. LRRK2 and Parkinson's disease: from genetics to targeted therapy. *Ann Clin Transl Neurol* **10**, 850-864, doi:10.1002/acn3.51776 (2023).
9. Henderson, M. X., Sengupta, M., Trojanowski, J. Q. & Lee, V. M. Y. Alzheimer's disease tau is a prominent pathology in LRRK2 Parkinson's disease. *Acta Neuropathol Commun* **7**, 183, doi:10.1186/s40478-019-0836-x (2019).
10. Iannotta, L., Emanuele, M., Favetta, G., Tombesi, G., Vandewynckel, L., Lara Ordonez, A. J., Saliou, J. M., Drouyer, M., Sibrán, W., Civiero, L., Nichols, R. J., Athanasopoulos, P. S., Kortholt, A., Chartier-Harlin, M. C., Greggio, E. & Taymans, J. M. PAK6-mediated phosphorylation of PPP2R2C regulates LRRK2-PP2A complex formation. *Front Mol Neurosci* **16**, 1269387, doi:10.3389/fnmol.2023.1269387 (2023).
11. Cabezudo, D., Tsafaras, G., Van Acker, E., Van den Haute, C. & Baekelandt, V. Mutant LRRK2 exacerbates immune response and neurodegeneration in a chronic model of experimental colitis. *Acta Neuropathol* **146**, 245-261, doi:10.1007/s00401-023-02595-9 (2023).



Geneeskundige Stichting Koningin Elisabeth
Fondation Médicale Reine Elisabeth
Königin-Elisabeth-Stiftung für Medizin
Queen Elisabeth Medical Foundation

Progress report of the
university research project of

Prof. dr. Thomas Voets
Katholieke Universiteit Leuven (KU Leuven)

Prof. dr. Thomas Voets

Laboratory of Ion Channel Research
VIB-KU Leuven Center for Brain & Disease Research
KU Leuven, Department of Cellular and Molecular Medicine
Herestraat 49 bus 801
3000 Leuven
Tel: +32 16 33 02 17
Thomas.voets@kuleuven.vib.be

Table of contents

1. Background and aim
2. Results
 - TRPM3-dependent brain disease – a growing number of patients and variants
 - Towards the development of pharmacotherapy for TRPM3-dependent brain diseases
3. Next steps and outlook
4. Publications in 2024 with support from GSKE
5. References

Unraveling the etiology of TRPM3-dependent neurodevelopmental disorders

1. Background and aim

TRPM3, a member of the transient receptor potential (TRP) superfamily of tetrameric ion channels, is a Ca^{2+} -permeable cation channel activated by increasing temperature and by ligands, including the endogenous neurosteroid pregnenolone sulphate (PS)¹⁻³. Several studies, including pioneering work from our research group, have established the channel's role in peripheral somatosensory neurons, where it is involved in heat sensation and in the development of pathological pain^{1,4-8}. In addition, TRPM3 is expressed in kidney, eye, pancreas, and several regions of the central nervous system, such as the hippocampal formation, the choroid plexus and the cerebellum, but little is known about the channel's physiological role in these tissues⁹⁻¹³.

Recently, rare heterozygous *de novo* variants in TRPM3 were identified in patients with neurodevelopmental disorders, consistently presenting with global developmental delay and mild to severe intellectual disability, in variable combination with other symptoms such as childhood-onset epilepsy, hypotonia, altered heat and/or pain sensitivity and cerebral palsy¹⁴⁻¹⁹. At the start of this project, our team had performed for the first time a detailed analysis of the electrophysiological and pharmacological properties of two disease-associated TRPM3 variants, following heterologous expression in the HEK293 cell line^{20,21}. We found that these variants show a dominant gain of function (GoF) when co-expressed with wild type TRPM3 (mimicking the situation in patients), seen as increased basal activity and enhanced responses to heat and PS. In particular, the recurrent TRPM3^{V1002M} variant, which to date has been described in 24 patients worldwide, provokes a more than 10-fold increase in inward currents. Moreover, our team initiated an international consortium around TRPM3-related disease, via which we (1) facilitate rapid exchange of knowledge between geneticists, neurologists and basic scientists working on TRPM3¹⁸, (2) perform functional characterization of new variants, thereby allowing the diagnosis in new patients, and (3) organize information and Q&A sessions with parents of affected children.

The aim of this project is to better understand how disease-associated TRPM3 variants lead to human neurodevelopmental disease, and use this knowledge as a basis for the development of TRPM3-based therapies to treat brain disease. In the past year, important progress was made regarding (1) further characterization of novel patient variants and the corresponding phenotypes, (2) development of pharmacotherapy for TRPM3-dependent brain diseases, and (3) characterization of a first mouse model of TRPM3-related brain disease.

2. Results

2.1. TRPM3-dependent brain disease – a growing number of patients and variants

As initiating team in the international consortium around TRPM3-related neurodevelopmental disease, we have been directly involved in the biophysical characterization of disease-associated TRPM3 variants, and in the systematic description of the phenotype of the patients. At this point, we have described the gain of function characteristics of 9 disease-associated variants in three publications^{20,22,23}, and summarized the current knowledge on the disease and disease-associated variants in a comprehensive review²⁴. However, the number of new patients carrying additional variants of unknown significance is steadily growing. In the last year, we optimized our

plate reader-based analytical pipeline, which now allows us to provide a rapid assessment of the functionality of new variants, thus providing information to the patients and their caretakers whether the variants are the likely cause of neurodevelopmental disease. In this assay, we co-express equal amounts of cDNA of wild type and variant TRPM3, cloned into an IRES-GFP vector, together with the red calcium indicator jRCAMP1b. Then, in an automated fluorescence plate (96-well) reader system, we quantify changes in jRCAMP1b fluorescence to high doses of the antagonist primidone, and to a concentration-range of the neurosteroid PS. For the WT channel, primidone has little effect on the fluorescence, since the channel has low basal channel activity. However, in the case of gain-of-function variants, primidone leads to a quantifiable decrease in jRCAMP1b fluorescence, which can be used as a direct measure of the degree of basal channel activity (Figure 1A). Moreover, from the responses to PS, EC_{50} values are determined to assess possible changes in neurosteroid sensitivity. Overall, this approach has now allowed us to demonstrate gain-of-function in TRPM3 channel function as the underlying cause of disease for 20 different patient variants (Figure 1B). Notably, whereas in the primary structure these mutants appear to be randomly distributed over the different domains of the protein, in the cryo-EM structures of TRPM3 the majority of the disease-associated mutations cluster in a domain of the channel at the cytosolic side of transmembrane domains S1-S4, and the S4-S5 linker. A publication of the analytical approach, including characterization of novel patient variants is currently being drafted.

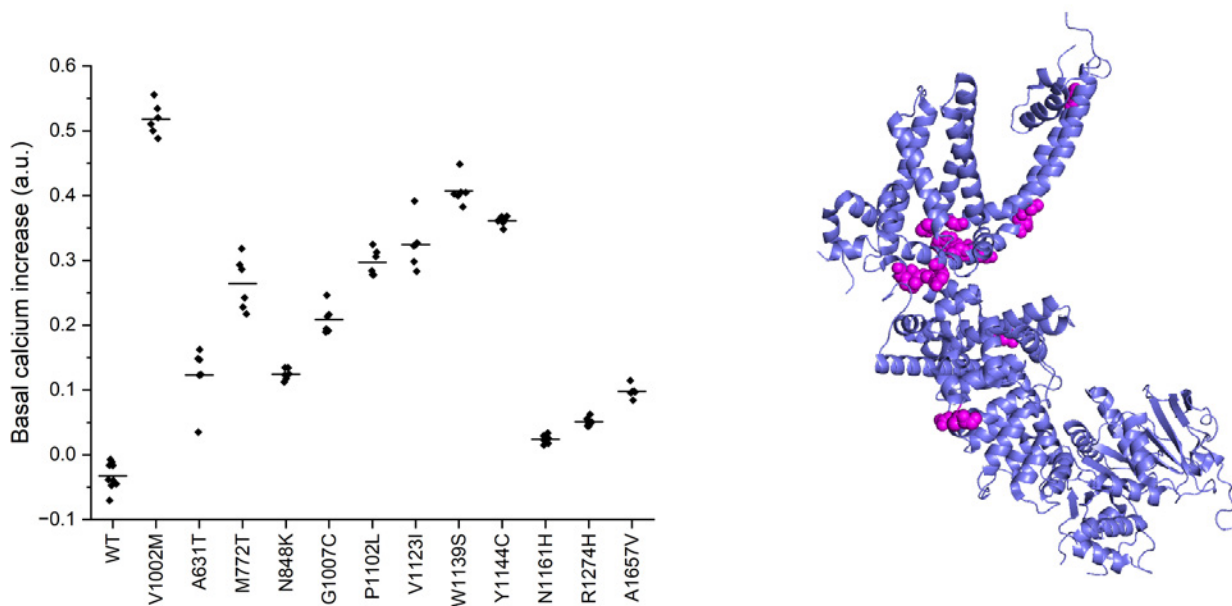


Figure 1: Properties of brain-permeant TRPM3 antagonists (left) Summary of basal activity of WT TRPM3 channels and channels consisting of equal amounts of WT and the indicated mutant subunits, as analysed by the established analytical pipeline. (right) Indication of all known disease-associated mutants on the structure of TRPM3²⁵. Plasma membrane is indicated in grey.

2.2. Towards the development of pharmacotherapy for TRPM3-dependent brain diseases

Based on our assessment of the sensitivity of disease-associated TRPM3 variants to primidone, a well-known medication to treat epilepsy and tremor, several children suffering from TRPM3-dependent neurodevelopmental disease have been treated with primidone. In a first case report, we were involved in the description of two children suffering from pharmacoresistant developmental and epileptic encephalopathy with spike-and-wave activation in sleep (DEE-SWAS) due to TRPM3 mutations. Following treatment with primidone, developmental regression was stopped, psychomotor development improved, and epileptic activity was fully suppressed²². Currently, more than 50% of the known patients are being treated with primidone, often (but not always) with beneficial effects on developmental progress and the occurrence of

seizures. One issue is that primidone is not very selective, and is metabolized to the barbiturate phenobarbital, leading to important central side effects occlude potential beneficial effects of the suppression of overactive TRPM3²⁶. Therefore, the development of more selective TRPM3 antagonists would likely allow a better treatment of these patients.

In this regard, our team is collaborating with the Center for Drug Design and Discovery (CD3; www.cd3.be), in partnership with the company Biohaven (www.biohaven.com), to develop highly potent and specific TRPM3 antagonists (described in the granted patent US 12,209,081 B2 (Thomas Voets is one of the inventors) and in related patent filings). In 2024, an important milestone of this drug development was reached, with the successful finalization of a Phase I study with of BHV-2100, an orally available, potent and selective TRPM3 antagonists developed in this collaboration (described in the granted patent US 12,209,081 B2; Thomas Voets is one of the inventors). Most importantly, this Phase 1 study revealed that BHV-2100 did not cause any relevant adverse effects, indicating that TRPM3 inhibition can be safely achieved in human. Currently, BHV-2100 is being tested in phase 2 studies for migraine and neuropathic pain.

However, BHV-2100 is largely peripherally restricted, and is therefore not optimally suited to treat the major CNS impact of disease-associated TRPM3 gain-of-function variants. Therefore, in the collaboration with CD3 and Biohaven LTD, we have recently achieved to develop **potent, selective, brain-permeant TRPM3 antagonists**. Key properties of one example compound (CIM796) are shown in **Figure 2**: it inhibits wild type and mutant (V1002M) TRPM3 with single-digit nanomolar concentrations and, following oral dosing, shows potent antiseizure activity in established models of epilepsy, such as the maximal electroshock (MES) model in mice.

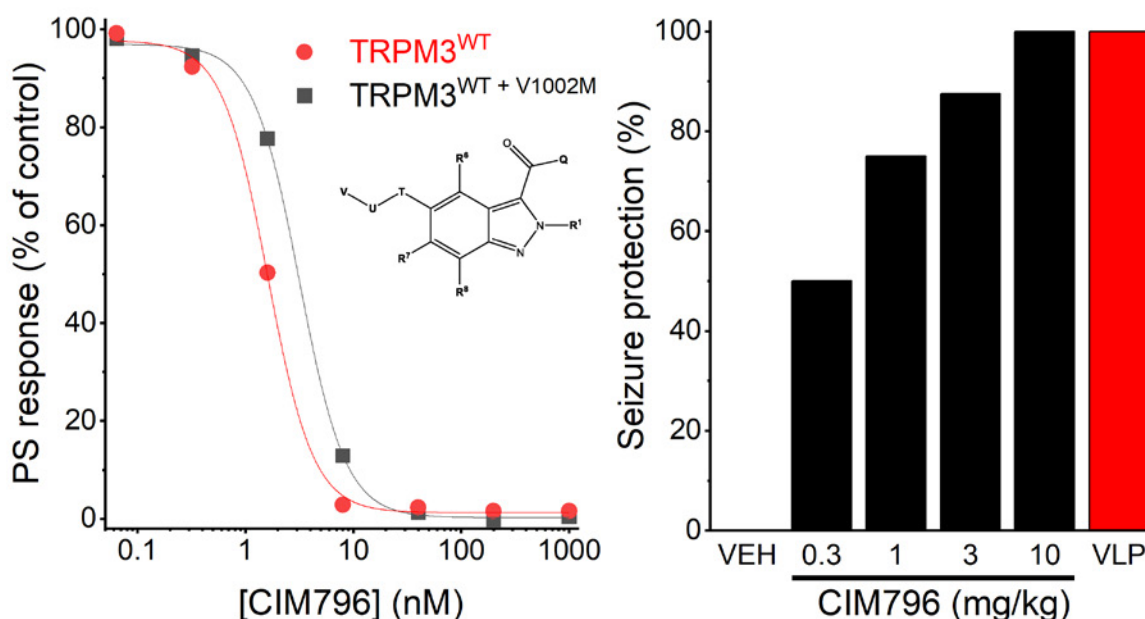


Figure 2: Properties of brain-permeant TRPM3 antagonists (left) Concentration-dependent inhibition of neurosteroid (PS) responses of channels composed of WT and WT + V1002M subunits by CIM796. (inset) General structure of selective TRPM3 antagonists described in US 12,209,081 B2. (right) Seizure protection following p.o. dosing of CIM796 or the positive control valproate (VLP; 250 mg/kg) in the mouse MES model.

These tools put us in a unique position to evaluate the feasibility of targeted pharmacological therapies to treat TRPM3-DEE, and also provide strong evidence that TRPM3 represents a druggable target for the treatment of other forms of epilepsy. Currently, in collaboration with our partners Biohaven and CD3, we are evaluating the efficacy of this and related brain-permeant TRPM3 antagonists in a battery of models of epilepsy and pain, and are evaluating their pre-

clinical safety, with the aim of obtaining a clinical candidate for treatment of patients in the course of 2026.

2.3. Initial characterization of the heterozygous TRPM3^{V1002M} mutation in mice

As described in our previous report, we have produced a mouse heterozygous for the most recurrent disease-associated variant (V1002M) in patients. Importantly, we found that these mice recapitulate several aspects of the human disease, including developmental delay, sleep-wake anomalies and unprovoked tonic-clonic seizures. Unfortunately, due to the extensive alternative splicing of TRPM3 and the particular design of the floxed allele, we did not succeed in making the mutation conditional. The seizure phenotype of global knockin mouse turned out to be so severe, with many mice dying from tonic-clonic seizures induced by gentle handling, that more detailed behavioral studies were not directly feasible. At this point, we are performing detailed structural and molecular analyses of the brains of $Trpm3^{+/V1002M}$ E18.5 embryos, which we anticipate to yield important insights into the brain areas that are most affected.

In addition, we are currently in the process of developing two new mouse strains, including one carrying a mutant with a milder phenotype in humans, and with a different strategy to ensure a higher chance of successful conditional knockin mouse production.

3. Next steps and outlook

Thanks to the support of the GSKE, we have been able to make important progress in understanding TRPM3-dependent neurodevelopmental disease and the role of TRPM3 in the brain. By establishing a quantitative functional pipeline of novel TRPM3 variants, we were able to support the diagnosis of patients with neurodevelopmental disease by establishing gain of channel function as the underlying cause. Moreover, since we are making great progress in the development of brain-permeant TRPM3 antagonists, along with encouraging results using primidone, there is a realistic outlook that this research may lead to the development of an effective treatment for patients with rare mutations in TRPM3. Interestingly, our recent findings indicate that TRPM3 antagonists have strong antiseizure activity in models of non-genetic epilepsy, suggesting that they may be of use to patients with refractory epilepsy, beyond rare TRPM3 mutations.

Overall, the project is yielding important new insights into TRPM3-dependent brain disease, with a high translational value, both for the diagnosis of the cause of disease in patients with newly identified variants in the TRPM3 gene, and for the development of therapy. Thanks to our close interactions with geneticists, neurologists and parents of affected children, new findings and potential treatments can be directly communicated to the relevant stakeholders.

4. Publications in 2024 with support from GSKE

(*: shared last and corresponding authors)

- Toth BI, Bazeli B, Janssens A, Lisztes E, Racsco M, Kelemen B, Herczeg M, Nagy TM, Mitra A, Biro T, Voets T: Direct modulation of TRPM8 ion channels by rapamycin and analog macrolide immunosuppressants. *eLife* (2024), in press.
- Roelens R, Peigneur ANF, Voets T, Vriens J: Neurodevelopmental disorders caused by variants in TRPM3. *Biochim Biophys Acta Mol Cell Res* (2024): 119709.

5. References

1. Vriens, J. *et al.* TRPM3 is a nociceptor channel involved in the detection of noxious heat. *Neuron* **70**, 482-494 (2011). <https://doi.org/10.1016/j.neuron.2011.02.051>
2. Wagner, T. F. *et al.* Transient receptor potential M3 channels are ionotropic steroid receptors in pancreatic beta cells. *Nat Cell Biol* **10**, 1421-1430 (2008). <https://doi.org/10.1038/ncb1801>
3. Held, K. *et al.* Activation of TRPM3 by a potent synthetic ligand reveals a role in peptide release. *Proc Natl Acad Sci U S A* **112**, E1363-1372 (2015). <https://doi.org/10.1073/pnas.1419845112>
4. Mulier, M. *et al.* Upregulation of TRPM3 in nociceptors innervating inflamed tissue. *Elife* **9** (2020). <https://doi.org/10.7554/eLife.61103>
5. Mulier, M., Vandewauw, I., Vriens, J. & Voets, T. Reply to: Heat detection by the TRPM2 ion channel. *Nature* **584**, E13-E15 (2020). <https://doi.org/10.1038/s41586-020-2511-6>
6. Su, S., Yudin, Y., Kim, N., Tao, Y. X. & Rohacs, T. TRPM3 channels play roles in heat hypersensitivity and spontaneous pain after nerve injury. *J Neurosci* **41**, 2457-2474 (2021). <https://doi.org/10.1523/JNEUROSCI.1551-20.2020>
7. Vangeel, L. *et al.* Functional expression and pharmacological modulation of TRPM3 in human sensory neurons. *Br J Pharmacol* **177**, 2683-2695 (2020). <https://doi.org/10.1111/bph.14994>
8. Vandewauw, I. *et al.* A TRP channel trio mediates acute noxious heat sensing. *Nature* **555**, 662-666 (2018).
9. Grimm, C., Kraft, R., Sauerbruch, S., Schultz, G. & Harteneck, C. Molecular and functional characterization of the melastatin-related cation channel TRPM3. *J Biol Chem* **278**, 21493-21501 (2003). <https://doi.org/10.1074/jbc.M300945200>
10. Oberwinkler, J., Lis, A., Giehl, K. M., Flockerzi, V. & Philipp, S. E. Alternative splicing switches the divalent cation selectivity of TRPM3 channels. *J Biol Chem* **280**, 22540-22548 (2005). <https://doi.org/10.1074/jbc.M503092200>
11. Zamudio-Bulcock, P. A., Everett, J., Harteneck, C. & Valenzuela, C. F. Activation of steroid-sensitive TRPM3 channels potentiates glutamatergic transmission at cerebellar Purkinje neurons from developing rats. *J Neurochem* **119**, 474-485 (2011). <https://doi.org/10.1111/j.1471-4159.2011.07441.x>
12. Becker, A. *et al.* Control of Insulin Release by Transient Receptor Potential Melastatin 3 (TRPM3) Ion Channels. *Cell Physiol Biochem* **54**, 1115-1131 (2020). <https://doi.org/10.33594/000000304>
13. Held, K. & Toth, B. I. TRPM3 in Brain (Patho)Physiology. *Front Cell Dev Biol* **9**, 635659 (2021). <https://doi.org/10.3389/fcell.2021.635659>
14. de Sainte Agathe, J. M. *et al.* Confirmation and Expansion of the Phenotype Associated with the Recurrent p.Val837Met Variant in TRPM3. *Eur J Med Genet* **63**, 103942 (2020). <https://doi.org/10.1016/j.ejmg.2020.103942>
15. Dymont, D. A. *et al.* De novo substitutions of TRPM3 cause intellectual disability and epilepsy. *Eur J Hum Genet* **27**, 1611-1618 (2019). <https://doi.org/10.1038/s41431-019-0462-x>
16. Gauthier, L. W. *et al.* Description of a novel patient with the TRPM3 recurrent p.Val837Met variant. *Eur J Med Genet* **64**, 104320 (2021). <https://doi.org/10.1016/j.ejmg.2021.104320>
17. Kang, Q. *et al.* A Chinese patient with developmental and epileptic encephalopathies (DEE) carrying a TRPM3 gene mutation: a paediatric case report. *BMC Pediatr* **21**, 256 (2021). <https://doi.org/10.1186/s12887-021-02719-8>
18. Lines, M. A. *et al.* Phenotypic spectrum of the recurrent TRPM3 p.(Val837Met) substitution in seven individuals with global developmental delay and hypotonia. *Am J Med Genet A* (2022). <https://doi.org/10.1002/ajmg.a.62673>
19. Sundaramurthi, J. C. *et al.* De novo TRPM3 missense variant associated with neurodevelopmental delay and manifestations of cerebral palsy. *Cold Spring Harb Mol Case Stud* **9** (2023). <https://doi.org/10.1101/mcs.a006293>
20. Van Hoeymissen, E. *et al.* Gain of channel function and modified gating properties in TRPM3 mutants causing intellectual disability and epilepsy. *Elife* **9** (2020). <https://doi.org/10.7554/eLife.57190>
21. Zhao, S., Yudin, Y. & Rohacs, T. Disease-associated mutations in the human TRPM3 render the channel overactive via two distinct mechanisms. *Elife* **9** (2020). <https://doi.org/10.7554/eLife.55634>
22. Becker, L. L. *et al.* Primidone improves symptoms in TRPM3-linked developmental and epileptic encephalopathy with spike-and-wave activation in sleep. *Epilepsia* **64**, e61-e68 (2023). <https://doi.org/10.1111/epi.17586>

23. Burglen, L. *et al.* Gain-of-function variants in the ion channel gene TRPM3 underlie a spectrum of neurodevelopmental disorders. *Elife* **12** (2023). <https://doi.org/10.7554/eLife.81032>
24. Roelens, R., Peigneur, A. N. F., Voets, T. & Vriens, J. Neurodevelopmental disorders caused by variants in TRPM3. *Biochim Biophys Acta Mol Cell Res* **1871**, 119709 (2024). <https://doi.org/10.1016/j.bbamcr.2024.119709>
25. Yin, Y. *et al.* Molecular basis of neurosteroid and anticonvulsant regulation of TRPM3. *Nat Struct Mol Biol* (2025). <https://doi.org/10.1038/s41594-024-01463-8>
26. Jolitz, L. *et al.* Phenotype Spectrum of TRPM3-Associated Disorders. *Ann Neurol* **97**, 561-570 (2025). <https://doi.org/10.1002/ana.27141>



Geneeskundige Stichting Koningin Elisabeth
Fondation Médicale Reine Elisabeth
Königin-Elisabeth-Stiftung für Medizin
Queen Elisabeth Medical Foundation

Progress report of the
university research project of

Prof. dr. Pierre Maquet
Université de Liège (ULiège)

Prof. dr. Pierre Maquet (ULiège)
Faculté de Médecine
Département des sciences cliniques
Neurologie
GIGA CRC In vivo Imaging – Sleep and chronobiology

Bât. B35 Neurologie
Quartier Hôpital
avenue de l'Hôpital 13
4000 Liège 1
Belgique
Téléphone de service: +32 4 366 23 67
Téléphone de service: +32 4 366 23 62

Quantitative MRI at 7 Tesla addresses ten questions about brain small vessel diseases

1. GIGA CRC *in vivo* imaging

Our research project uses ultra-high field MRI to characterize the various aspects of brain small vessel diseases, frequent disorders that alter the cerebral small perforating arterioles, capillaries, and venules.

During the past year, we finalized the quantitative sequences to be used in the project. The bottom line was to reduce the acquisition time as far as possible, without compromising a homogeneous quantitation throughout the brain.

From the data acquired during this initial phase of the project, we progressed with an automatic detection of extravascular spaces, which constitute one of our main features of interest in this project. Building on the generalized segmentation available in SPM12, we designed a Bayesian framework including the extravascular spaces as a separate tissue type. The segmentations obtained on control participants are encouraging and should be generalized to small vessel disease (SVD) patients.

Two PhD students, both MD, were trained to run these sequences on the 7T Terra MRI scan and are now actively involved in the study. The first patient officially enrolled and scanned in the project is scheduled by early April 2025.

Meanwhile, we have collected a database of about ~50 SVD patients, who are being contacted back to participate in the study. We intend to scan these volunteers by the end 2025, possibly by September 2025.



Geneeskundige Stichting Koningin Elisabeth
Fondation Médicale Reine Elisabeth
Königin-Elisabeth-Stiftung für Medizin
Queen Elisabeth Medical Foundation

Projecten jonge onderzoekers
2023-2025 gefinancierd door de G.S.K.E.

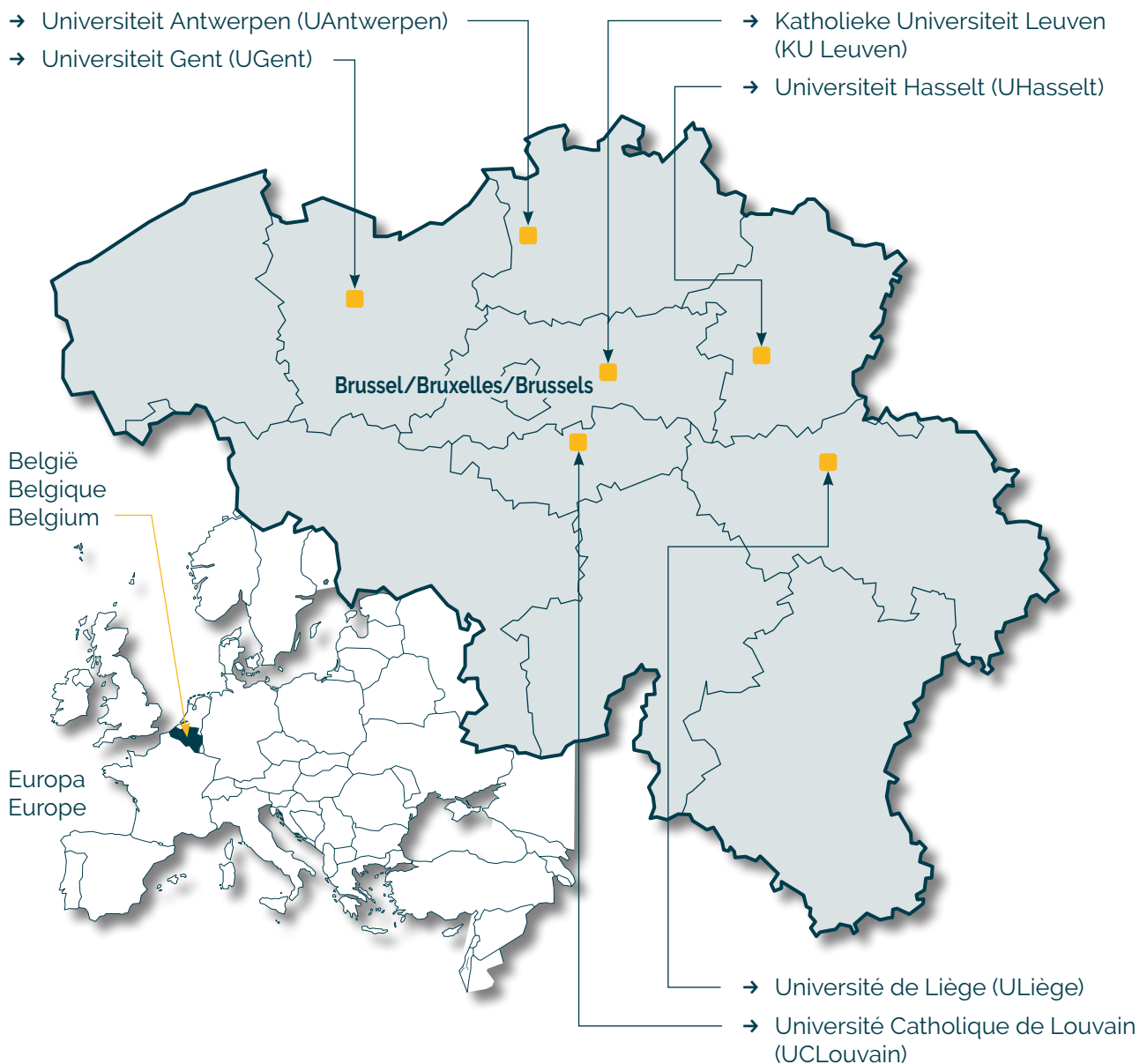
Projets de recherche de jeunes chercheurs
2023-2025 subventionnés par la F.M.R.E.

Research projects of young researchers
2023-2025 funded by the Q.E.M.F.

Universiteiten met onderzoeksprogramma's die gesteund worden door de G.S.K.E.

Universités ayant des programmes de recherche subventionnés par la F.M.R.E.

Universities having research programs supported by the Q.E.M.F.



Projecten jonge onderzoekers 2023-2025 gefinancierd door de G.S.K.E.

Projets de recherche de jeunes chercheurs 2023-2025 subventionnés par la F.M.R.E.

Research projects of young researchers 2023-2025 funded by the Q.E.M.F.

UGent



Sielke Caestecker (PhD student) & promotor prof. Robrecht Raedt

The role of the locus coeruleus noradrenergic system in seizures and epilepsy

Dr. Delfien Syx

Zebrafish as a model to study pain in Ehlers-Danlos syndromes

UAntwerpen



Dr. Marijne Vandebergh

World-wide systematic characterization of TMEM106B and ATXN2 genetic status Towards implementation of genetic testing of modifiers in clinical practice

Dr. Barbara M.P. Willekens

Unravelling the role of antigen-specific T cells in NMOSD and MOGAD

KU Leuven



Dr. Wouter Peelaerts

Peripheral infections as a trigger of multiple system atrophy

Dr. Sarah van Veen

The impact of ATP13A4-mediated polyamine transport in astrocytes on synaptogenesis and neurodevelopmental disorders

UCLouvain



Prof. Giulia Liberati

STIM-WAVES: Identifying pain biomarkers with invasive and non-invasive brain stimulation targeting ongoing neural oscillations

(UHasselt)



Prof. dr. Jeroen Bogie

Getting a grip on slippery protein modifications in multiple sclerosis

Prof. dr. Bieke Broux

High salt diet causes blood-brain barrier disturbances in multiple sclerosis: involvement of the renin-angiotensin-aldosterone system

ULiège



Dr. Sophie Laguesse

Unveiling the alcohol-dependent alterations in mRNA local translation and its consequences on adolescent prefrontal cortex maturation and function



Geneeskundige Stichting Koningin Elisabeth
Fondation Médicale Reine Elisabeth
Königin-Elisabeth-Stiftung für Medizin
Queen Elisabeth Medical Foundation

Progress report of the research project of the young researcher

Sielke Caestecker (PhD student) &
promotor prof. Robrecht Raedt
Universiteit Gent (UGent)

Prof. dr. Robrecht Raedt (UGent)

Principal investigator – 4BRAIN

Associate Professor (Faculty of Medicine and Health Sciences)

Director of the Animal Facility of the Faculty of Medicine and Health Sciences

Member of GATE steering committee

Secretary of the Belgian Society for Neuroscience

Lab address: 4BRAIN,

Campus UZ Gent, o Blok B (entrance 36),

Corneel Heymanslaan 10,

9000 Gent, Belgium

Robrecht.Raedt@UGent.be

Sielke Caestecker (UGent)

PhD student

Lab address: 4BRAIN,

Campus UZ Gent, o Blok B (entrance 36),

Corneel Heymanslaan 10,

9000 Gent, Belgium

sielke.caestecker@ugent.be

The role of the locus coeruleus noradrenergic system in seizures and epilepsy

1. Project overview

This project was based on preliminary data which showed changes in the firing of locus coeruleus (LC) neurons in relation to acute hippocampal seizures in rats and hippocampal release of noradrenaline (NA). Since the initiation of this project, we have completed two studies, one which was published in 2023 in *Neurobiology of Disease* and one that was accepted for publication in *Frontiers in Neuroscience* in February 2025 (submitted in 2024).

We have initiated a follow-up experiment to investigate noradrenaline release in an intrahippocampal kainic acid mouse model of temporal lobe epilepsy. Our goal is to modulate noradrenaline release using optogenetics and assess its impact on seizure duration and frequency.

1.1. **Study 2: Chemogenetic modulation of the rat locus coeruleus alters hippocampal noradrenaline release and modulates perforant-path evoked potentials (accepted for publication in *Frontiers in Neuroscience*).**

The locus coeruleus (LC)—noradrenaline (NA) system plays a crucial role in modulating neuronal excitability and plasticity. In epilepsy, the LC-NA system plays an important role in regulating seizure thresholds and severity, with elevated NA release mediating the seizure-suppressing effects of vagus nerve stimulation (VNS). We investigated whether chemogenetic LC activation is able to increase hippocampal NA release and affect hippocampal electrophysiology in anesthetized rats.

22 male Sprague–Dawley rats were injected with the viral vector AAV9-hSyn-NE2m in the hippocampus to induce expression of the GRAB_{NE2m} biosensor to locally measure changes in extracellular NA. 15/22 rats were injected with the CAV2-PRsX8-hM3Dq hSyn-mCherry viral vector in the LC to express the excitatory DREADD hM3Dq, allowing LC activation with deschloroclozapine (DCZ), and 7/22 with CAV2-PRsX8-GtACR2 as a control. A perforant path stimulation electrode and a dentate gyrus (DG) recording electrode were implanted for local field potential (LFP) and evoked potential (EP) recording as well as a DG optical fiber for GRAB_{NE2m} fluorescence measurement.

In a significant number of rats (7/15) we found an increase in hippocampal NA release (**Figure 1**), field excitatory post synaptic potential (fEPSP) slope (**Figure 2**) and population spike (PS) amplitude (**Figure 3**), indicating an increase in excitatory neurotransmission and neuronal output. 4/15 rats showed a decrease in NA release without changes in fEPSP slope or PS amplitude, and 4/15 showed no change in NA release.

These findings indicate that chemogenetic activation of the LC-NA system can modulate hippocampal evoked responses, supporting further exploration of its role in health and disease, such as in epilepsy.

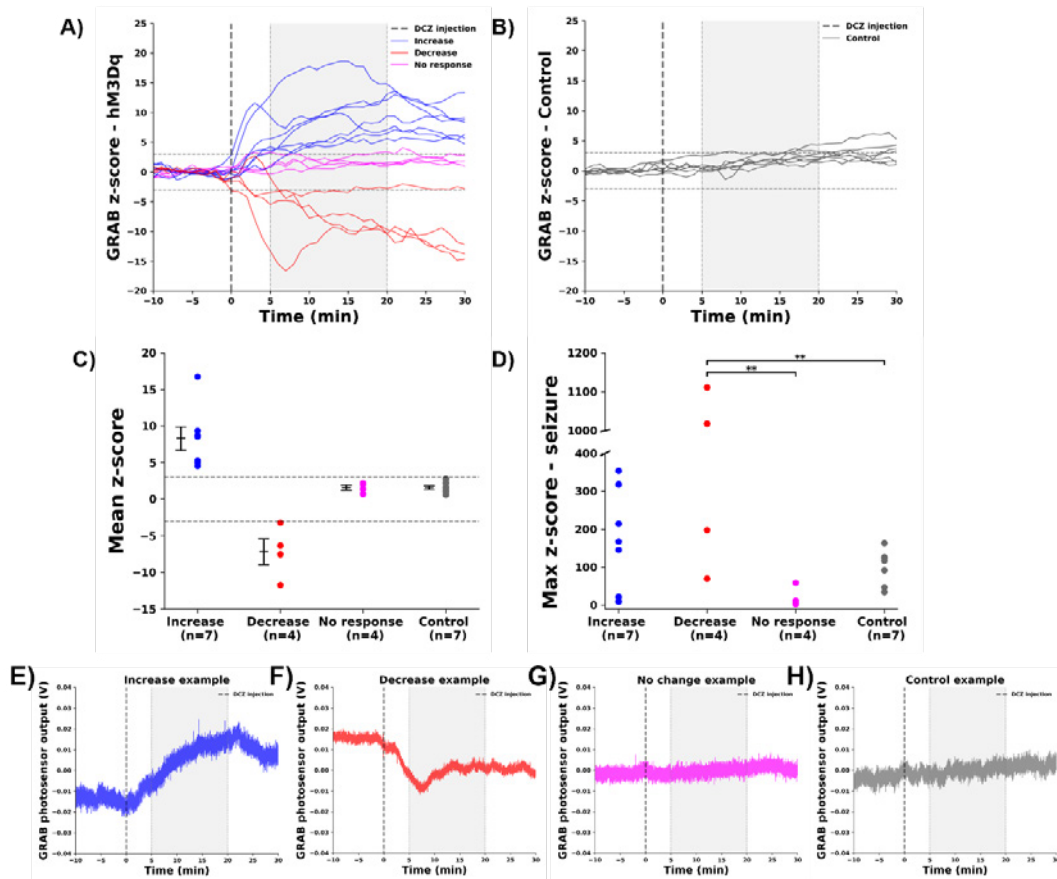


Figure 1. Effect of DCZ injection and seizures on hippocampal GRAB_{NE2m} fluorescence. (A) GRAB_{NE2m} fluorescence signal of hM3Dq-expressing rats before and after DCZ injection (dashed vertical line), every line represents one animal. Grey window indicates the selected 5–20 min period to determine the mean z-score. Dashed horizontal lines indicate the significance levels (z-score > 3 or < -3). (B) GRAB_{NE2m} fluorescence signal of control rats. (C) Mean z-score per group (increase: blue, decrease: red, no change: magenta, control: grey, every dot represents the mean of one animal). (D) Max z-score during a seizure for different groups. ** indicates difference between groups with p<0.01. (E–H) Representative examples of native GRAB photosensor output in V, reflecting GRAB_{NE2m} fluorescence, for every group (E: increase, F: decrease, G: no change, H: control).

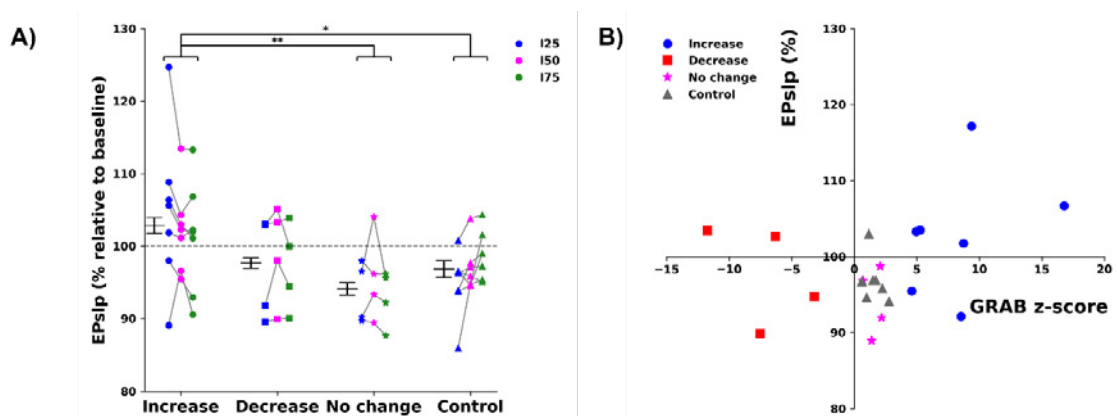


Figure 2. Effect of DCZ injection on the fEPSP slope (EPslp). (A) Mean % change relative to baseline per group (increase: , decrease: , no change: *, control:), per stimulation intensity (125: blue, 150: magenta, 175: green). Every dot depicts one animal, grey lines connect data points from one animal. * indicates difference between groups with p<0.05, ** indicates difference between groups with p<0.01. (B) No correlation between mean % change in EPslp and mean z-score of GRAB_{NE2m} fluorescence was observed.

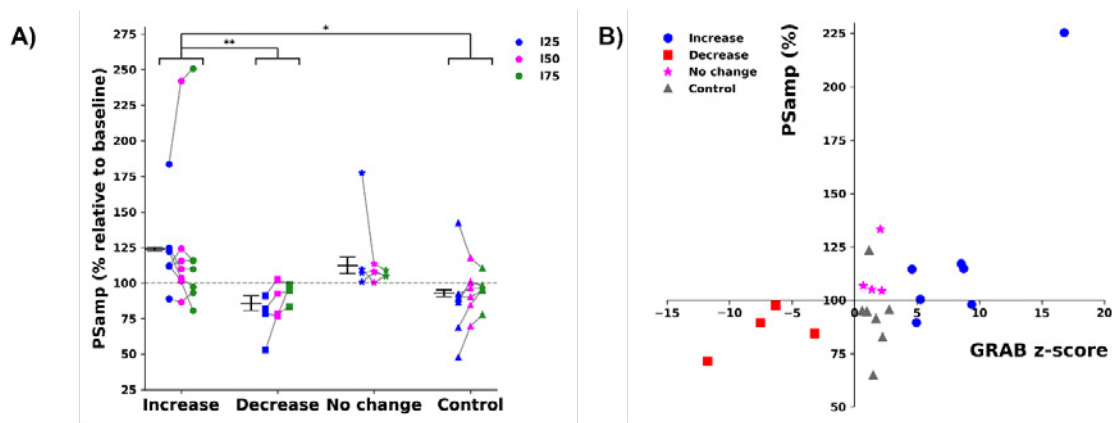


Figure 3. Effect of DCZ injection on the PS amplitude (PSamp). (A) Mean % change relative to baseline per group (increase: ., decrease: ., no change: *, control: .), per stimulation intensity (125: blue, 150: magenta, 175: green). Every dot depicts one animal, grey lines connect data points from one animal. * indicates difference between groups with $p < 0.05$, ** indicates difference between groups with $p < 0.01$. (B) A significant correlation between mean % change in PSamp and mean z-score of GRAB_{NE2m} fluorescence was observed.

1.2. Study 3: Optogenetic modulation of the locus coeruleus in the intrahippocampal kainic acid mouse model for chronic temporal lobe epilepsy

In order to investigate changes in noradrenergic transmission in relation to spontaneous seizures, we opted to study the intrahippocampal kainic acid model in mice. This model is increasingly gaining popularity, due to a high frequency of seizures which makes it possible to capture many seizures within a short period of time. In the 4Brain lab, we have extensive experience with this model. After initial intrahippocampal injection of kainic acid, we waited at least two weeks before further injecting with a viral vector for expression of the GRAB_{NE2m} fluorescent biosensor in the hippocampus and a viral vector for expression of the inhibitory opsin WiChR or the excitatory opsin ChR2 in the LC. The animals were further instrumented with hippocampal EEG electrodes to capture seizures, with an optical fiber over the hippocampus for fiber photometry to capture changes in GRAB_{NE2m} fluorescence and an optical fiber over the LC for activation of the opsins with blue light (470 nm).

The preliminary data shown in the following indicates a clear correlation between hippocampal seizures and a decrease in GRAB_{NE2m} fluorescence. However, rather than an increase in noradrenergic transmission as seen during acute seizures (study 1), spontaneous seizures in chronically epileptic mice are observed to lead to a consistent decrease in noradrenergic transmission (**Figure 4**).

To assess the neuromodulatory impact of LC-noradrenergic transmission on hippocampal seizures, we modulated its activity using optogenetics. An initial analysis revealed that continuous illumination (15 min, 5 Hz, 10 ms pulse width, 10 mW power) of the LC led to a decrease in GRAB_{NE2m} levels when activating the inhibitory WiChR opsin in the LC of 7 animals. In contrast, activation of the excitatory ChR2 opsin in another 7 animals produced no clear effect (**Figure 5**). This reduction in GRAB_{NE2m} fluorescence was accompanied by a slight increase in spiking activity on the hippocampal LFP, consistent with previous literature suggesting that decreased noradrenaline release may have proconvulsant effects. Further analyses are ongoing, and additional results are expected in the coming months.

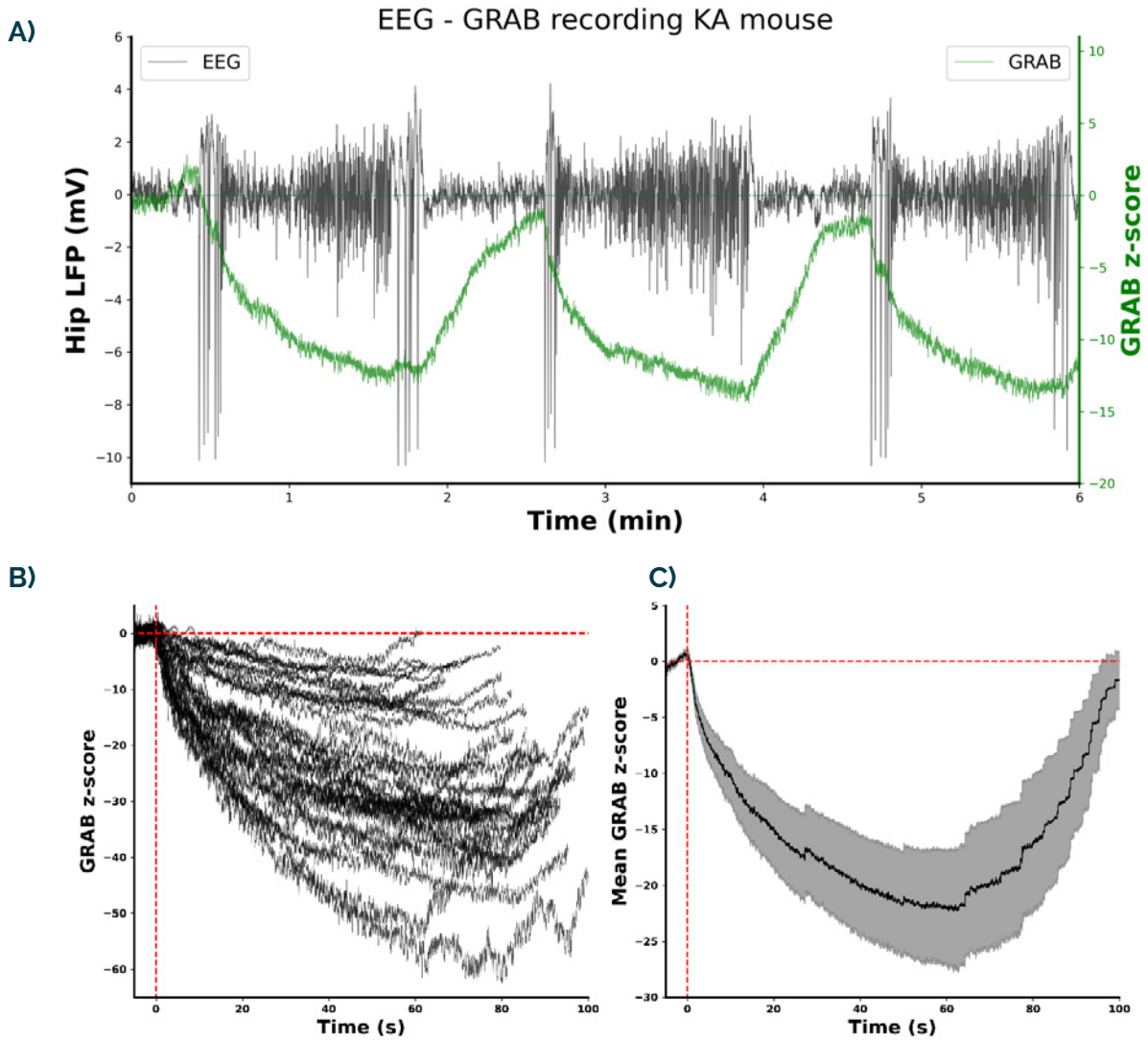


Figure 4. Spontaneous hippocampal seizures lead to a consistent drop in noradrenergic transmission in the hippocampus. **A)** Example of the hippocampal EEG (black) plotted against the GRAB_{NE2m} fluorescence signal (green). **B)** changes in GRAB_{NE2m} fluorescence for a series of individual seizures, **C)** Average of all seizures \pm SEM.

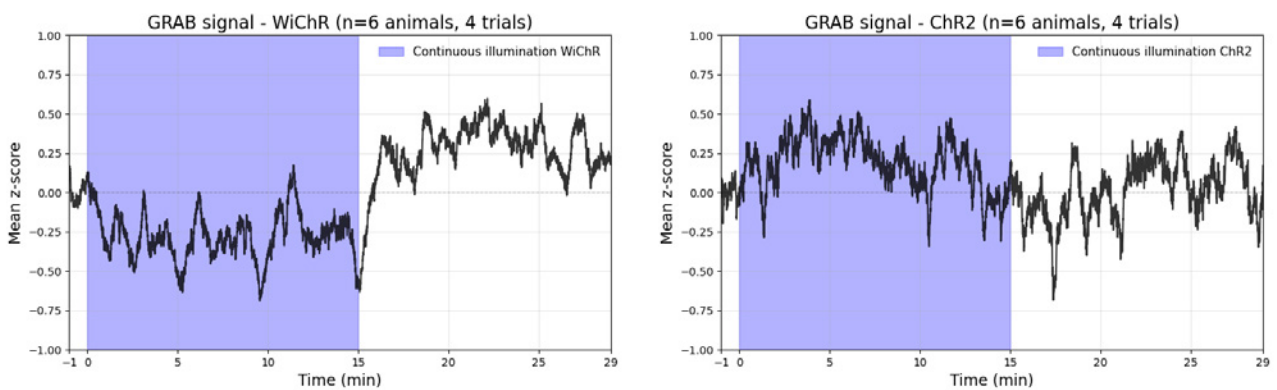


Figure 5. Effect of continuous illumination of the LC (470 nm) on hippocampal GRAB_{NE2m} fluorescence. **A)** Mean z-score of the GRAB_{NE2m} fluorescence signal before, during (blue) and after activation of the inhibitory WiChR opsin in the LC. **B)** Mean z-score of the GRAB_{NE2m} fluorescence signal before, during (blue) and after activation of the excitatory opsin ChR2 in the LC.

2. Status and future directions

One manuscript has already been finalized and one is being prepared for publication with the support of GSKE. The preliminary data presented in this report is further expected to lead to an additional 3rd publication with the continued support of the GSKE.

3. Publications 2024

- Title: Chemogenetic modulation of the rat locus coeruleus alters hippocampal noradrenaline release and modulates perfortant path-evoked responses
Authors: Sielke Caestecker, Emma Lescrauwaet, Kristl Vonck, Mathieu Sprengers, Evelien Carrette, Paul Boon, Lars Emil Larsen, Robrecht Raedt
Journal: Frontiers in Neuroscience – Translational Neuroscience
IF : 3.2 (2023)
Q factor : Q2



Geneeskundige Stichting Koningin Elisabeth
Fondation Médicale Reine Elisabeth
Königin-Elisabeth-Stiftung für Medizin
Queen Elisabeth Medical Foundation

Progress report of the research project of the young researcher

Dr. Delfien Syx
Universiteit Gent (UGent)

Delfien Syx, PhD (UGent)

Department of Biomolecular Medicine

Center for Medical Genetics Ghent (CMGG)

Ghent University Hospital

Medical Research Building I (MRB I) – Ingang 34

C. Heymanslaan 10

B-9000 Ghent

Belgium

T +32 9 33 2 1346

Delfien.Syx@ugent.be

www.cmgg.be

www.ugent.be/ge/biomolecular-medicine

Zebrafish as a model to study pain in Ehlers-Danlos syndromes

1. Background

Chronic pain affects up to 20% of the global population and represents a socio-economical health challenge. [1,2] The etiology of chronic pain is complex, and the underlying mechanisms are poorly understood. Consequently, treatment options are limited and often associated with considerable side effects and serious health risks. [3–5]

Over the years, a role for the extracellular matrix (ECM) in the development and persistence of pain has emerged. The ECM is a complex three-dimensional network that supports and maintains tissue and organ structure. The ECM consists of collagens, glycoproteins, proteoglycans, and secreted factors, which, together with the cells that produce them (e.g., fibroblasts), forms the connective tissue that is found throughout the body (e.g., in skin, bone, tendon and ligaments). [6] An ECM network also surrounds and functionally supports neuronal and non-neuronal cells (including nociceptors) in the peripheral and central nervous systems (PNS/CNS). [7,8] Furthermore, painful peripheral injuries were shown to cause acute and chronic ECM remodeling and/or alter ECM modifying enzymes. [8–10]

The link between the ECM and pain is further reinforced by the presence of chronic widespread pain in several monogenic heritable connective tissue disorders, caused by genetic defects affecting individual ECM components. [11–14] One of these disorders are the Ehlers-Danlos syndromes (EDS), a heterogeneous group of conditions hallmarked by joint hypermobility, soft and hyperextensible skin, abnormal wound healing and generalized tissue fragility. [15] To date, 13 distinct EDS types are recognized, of which 12 are molecularly elucidated and caused by defects in 20 different genes, mainly affecting collagens, proteoglycans and glycoproteins. [15,16] All these EDS-related defects compromise ECM architecture, often visible as ultrastructural changes in the organization and/or structure of collagen fibrils. [17] Chronic widespread pain occurs in 90% of EDS patients and is often one of the main reasons patients seek medical care. [12,18] Despite its high prevalence, little is known about the precise origins and mechanisms contributing to EDS-related pain and the pain is usually inadequately controlled by currently used treatments. An important reason for this is the lack of studies investigating the existing knowledge gaps.

Zebrafish (*Danio rerio*) has emerged as a promising animal model to reliably study pain-related behavior and associated mechanisms since their nervous system shows great similarity to humans. [19–23] Over the years, our group has invested in the generation of several knockout zebrafish models of EDS and validated them as robust models for the respective human EDS types. [24–26] We created *b4galt7*^{-/-} and *b3galt6*^{-/-} zebrafish, models of spondylodysplastic EDS (spEDS) [25,26] and *chst14*^{-/-} zebrafish, a model of musculocontractural EDS (mcEDS) (unpublished). Both spEDS and mcEDS result from genetic defects in enzymes involved in proteoglycan biosynthesis. In addition, a zebrafish model with defective collagen biosynthesis was previously investigated: *col1a2*^{-/-} zebrafish, a model of cardiac-valvular EDS (cvEDS). [24]

My research aims to assess the contribution of the abnormal ECM and untangle the specific mechanisms that induce pain and peripheral nervous system changes using EDS zebrafish as a model.

2. Preliminary results

2.1. Evaluating pain-related behavior in EDS zebrafish

Potentially painful events lead to behavioral and physiological changes in zebrafish. [19] Studies have demonstrated that healthy zebrafish are usually swimming constantly, using mid-water and all areas of their tank. In contrast, zebrafish subjected to potentially painful treatment showed increased use of the bottom of the tank (diving behavior) and reduce swimming and activity. [23,27]an automated method, the Fish Behaviour Index (FBI

To analyze the general swimming behavior of young wild-type zebrafish of 5 days post fertilization (dpf), several experimental setups were tested, including the use of different container sizes (e.g., zebrafish individually placed in 6, 12, 24 or 48 well plates) and several setups with different duration in light and dark conditions. Following this initial exploratory phase in wild-type zebrafish, we opted to use 12-well plates to accommodate 5 dpf zebrafish for subsequent testing since this gave the most consistent results and still allows for a relatively high throughput during testing. The first 10 minutes of the experiment were considered an acclimatization period and were not used for analyses. During the experiment, the temperature was kept constant at 28°C using a Temperature Control Unit (Noldus, The Netherlands). Locomotor activity was analyzed using the DanioVision Observation Chamber (Noldus, The Netherlands) equipped with a Basler GenlCam camera capturing 30 frames/second for image acquisition. Data was recorded and analyzed using the EthoVision XT 15 software (Noldus, The Netherlands). For each zebrafish, center-point detection was used. Movement was expressed as cumulative time spent moving (%), movement frequency and distance moved (mm). Following behavioral analysis, all zebrafish were genotyped. For each EDS zebrafish line, wild-type (+/+), heterozygotes (+/-), and knockout (-/-) animals were examined.

We confirmed decreased movement of 5 dpf wild-type zebrafish following addition of 0.25% acetic acid to the water (Figure 1A-C), which mimics published findings [23]0.1% and 0.25%, and indicates that our experimental setup and conditions can pick up altered swimming behavior in response to a known stimulus.

Analysis of the behavior (movement, movement frequency and distance travelled) of 5 dpf *chst14*^{-/-}, *b3galt6*^{-/-} and *col1a2*^{-/-} zebrafish, models for mcEDS-*CHST14*, spEDS-*B3GALT6* and cvEDS, respectively, did not show differences in movement compared to wild-type siblings (Figure 1D-F, 1G-I and 1M-O). For these models no differences could be observed between the knockout zebrafish or wild-type and heterozygous zebrafish from the same clutch, except for the *chst14* line where wild-type siblings moved less compared to heterozygous siblings (Figure 1D), but with unaltered movement frequency and distance traveled.

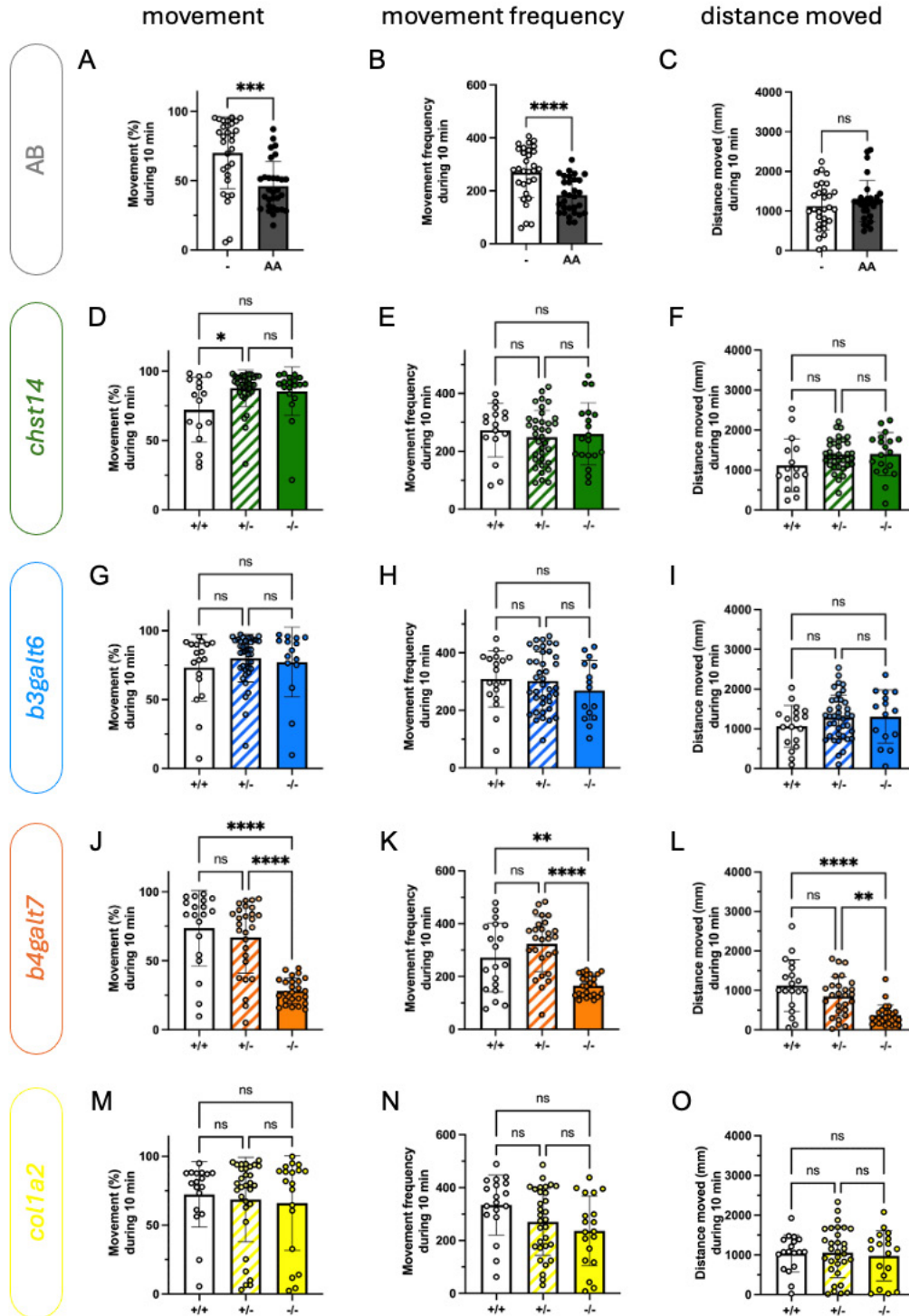


Figure 1. Behavioral analysis of 5 dpf zebrafish. Movement (in %), movement frequency and distance moved (in mm) during 10 minutes tracking in light conditions. (A-C) Positive control without (-) or with (AA) addition of 0.25% acetic acid in the water of wild-type (AB) zebrafish. (D-F) *chst14*^{-/-}, (G-I) *b3galt6*^{-/-}, (J-L) *b4galt7*^{-/-} and (M-O) *col1a2*^{-/-} zebrafish and their wild-type and heterozygous siblings. Data is presented as mean ± standard deviation. Every dot represents an individual zebrafish. +/+ : wild-type, +/- : heterozygous, and -/- : homozygous zebrafish. * p<0.05; ** p<0.001, **** p<0.0001, t-test (A) or one-way ANOVA (B-E).

When studying locomotor activity of 5 dpf *b4galt7*^{-/-} zebrafish, a model for spEDS-*B4GALT7*, we found that *b4galt7*^{-/-} zebrafish moved significantly less compared to wild-type and *b4galt7*^{-/-} zebrafish (Figure 1J-L). The findings for the movement and movement frequency parameters is similar to what is seen when treating 5dpf zebrafish with a painful stimulus (Figure 1A-C). Given

the observed variability in behavior between wild-type 5 dpf zebrafish and the fact that different clutches (= offspring from one breeding) can show differences in severity of the phenotype, the behavior experiments were repeated at least three times starting from independent clutches, which resulted in comparable results.

To confirm that the altered behavior in *b4galt7*^{-/-} zebrafish, corresponds to a pain-related response, we tried to reverse the behavior by addition of analgesics. Several analgesics have been shown to lead to effective pain-relief in zebrafish. [28] Addition of the non-steroidal anti-inflammatory drugs aspirin (0.01 mg/ml) to the water of the *b4galt7* line did not convincingly show amelioration of the phenotype. Other analgesics will be administered to ameliorate the observed behavioral changes.

Since pain-related behavior can also develop at a later age, behavioral analysis will also be performed in adult zebrafish (> 3 months).

2.2. Monitoring neuronal development in EDS zebrafish

To acquire information about the effect of an aberrant ECM on **neuronal development**, EDS zebrafish models will be crossed with the *Tg(neurog1:EGFP)* line (available in our lab), expressing the pro-neural transcription factor neurogenin1 which is a key regulator for dorsal root ganglion (DRG) neuron development. [29]

To introduce a less time-consuming method to evaluate neuronal development, we started optimizing the NeuroTracer Dil tissue-labeling paste (Thermo Fisher Scientific) that serves as an alternative staining to visualize the nervous system. Several experiments did not result in proper visualization of the nervous system.

Breeding of the EDS zebrafish models will require some time to obtain homozygous zebrafish in the *Tg(neurog1:EGFP)* background. We are currently exploring alternative imaging techniques to obtain proper visualization of the nervous system.

2.3. Generation and phenotypic characterization of *col5a1*^{-/-} zebrafish

Our group previously demonstrated the presence of pain in patients with classical EDS (cEDS), caused by genetic defects in the *COL5A1* and *COL5A2* genes. [30] In addition, we showed the presence of pain-related behavior and concomitant alterations in the dermal nociceptive innervation in *Col5a1*^{-/-} mice, a validated model of cEDS. [31] In view of these findings, we aimed to create a zebrafish counterpart that mimics the human cEDS phenotype to assess pain-related behaviors as a proof-of-concept. Since young zebrafish are well-suited for large-scale drug/compound screenings, these EDS zebrafish would open opportunities to start exploring potential therapeutic options.

CRISPR/Cas9-based genome editing was used to generate mutant *col5a1* zebrafish lines (Figure 2). The aim is to obtain zebrafish carrying a premature termination codon, predicted to result in *col5a1* haploinsufficiency, the most common molecular defect observed in cEDS patients and similar to the defect in *Col5a1*^{-/-} mice. Two different models were generated to account for possible off-target effects.

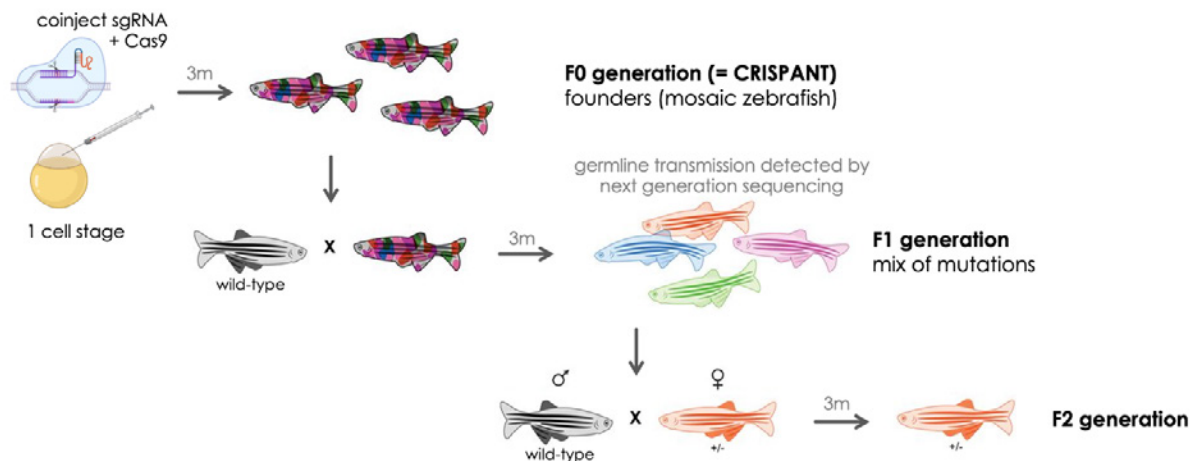


Figure 2. Schematic overview of the generation of the *col5a1* zebrafish lines using CRISPR/Cas9 genome editing. Adapted from Varshney *et al.* Genome Research, 2015. [32]we present a high-throughput targeted mutagenesis pipeline using CRISPR/Cas9 technology in zebrafish that will make possible both saturation mutagenesis of the genome and large-scale phenotyping efforts. We describe a cloning-free single-guide RNA (sgRNA)

Two sgRNAs were designed that target either exon 8 or exon 10 of the zebrafish *col5a1* gene and were individually injected with Cas9 protein into one-cell stage zebrafish eggs. This resulted in an overall indel efficiency of 86,6% for exon 8 and 95,4% for exon 10. Overall, there was a high mortality of injected zebrafish. The surviving zebrafish represent the F0 generation, also called crispants, and are mosaic for different genetic alterations in the *col5a1* gene. These crispants were grown till 3 months of age, bred with wild-type zebrafish and their offspring was tested for germline transmission of the out-of-frame indel variants. Next, a founder crispant zebrafish which carries a high frequency of out-of-frame variants was selected for each of the targeted exons. These founders were subsequently crossed with a wild-type zebrafish and their offspring was allowed to grow till adulthood. This resulted in a mixture of zebrafish, each carrying a particular mutation. We selected zebrafish with a 5bp deletion in exon 8 (cmg109) and 1bp duplication in exon 10 (cmg111) for establishing stable mutant zebrafish lines.

To further validate the *col5a1* zebrafish lines, the consequences of the mutations were examined. However, the study of the effect of the generated defects on type V collagen quantity (and quality) was severely hampered by the lack of an antibody to detect type V collagen. This is a known problem that is frequently encountered when working with zebrafish proteins. Testing of different antibodies for Western blot analysis did unfortunately not result in visualization of the type V collagen protein in zebrafish.

To overcome the issue with detection of the (mutant) type V collagen protein, expression levels of the *col5a1* gene were evaluated using reverse transcription quantitative PCR (RT-qPCR). In line with the expected haploinsufficiency, caused by the introduction of a premature termination codon, a significant decrease of the *col5a1* expression levels were observed in both the heterozygous *col5a1* cmg109 and cmg111 lines (Figure 3). This suggests that the mutant allele is subject to nonsense-mediated mRNA decay, which mimics the most common molecular defect seen in cEDS patients.

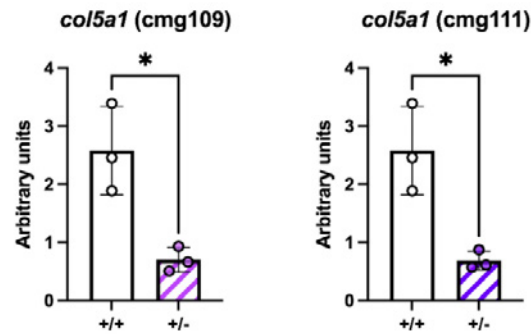


Figure 3. Expression analysis. Decreased expression of *col5a1* in *cmg109* and *cmg111* lines. Every dot represents an individual zebrafish. +/+ : wild-type, and +/- : heterozygous zebrafish. * $p < 0.05$, t-test.

Behavior testing of the *col5a1* *cmg109* and *cmg111* lines was performed. Behavior analysis of 5 dpf heterozygous *col5a1*^{-/-} zebrafish (the expected model of cEDS) did not show differences in movement compared to wild-type siblings (Figure 4). However, we found that homozygous *col5a1*^{-/-} zebrafish moved significantly less compared to wild-type and *col5a1*^{+/-} zebrafish. This finding resembles what is seen when treating 5 dpf zebrafish with a painful stimulus (Figure 1A-C) and the altered behavior in *b4galt7*^{-/-} zebrafish (Figure 1J-L).

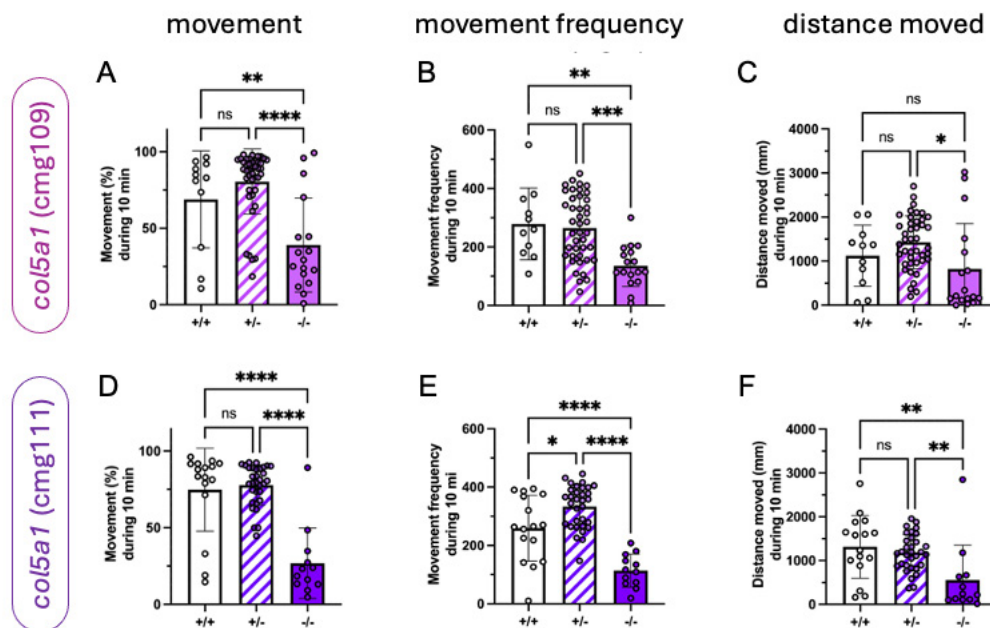


Figure 4. Behavioral analysis in *col5a1* zebrafish. Movement (in %), movement frequency and distance moved (in mm) during 10 minutes tracking in light conditions. (A-C) *col5a1* *cmg109* line and (D-E) *col5a1* *cmg111* line. Data is presented as mean \pm standard deviation. Every dot represents an individual zebrafish. +/+ : wild-type, +/- : heterozygous, and -/- : homozygous zebrafish. * $p < 0.05$; ** $p < 0.01$; *** $p < 0.001$; **** $p < 0.0001$, one-way ANOVA.

Given the reported embryonic lethality of homozygous knockout (*Col5a1*^{-/-}) mice, it was initially surprising to notice that homozygous knockout (*col5a1*^{-/-}) zebrafish were found at the 5 dpf timepoint when performing genotyping following behavior analysis. [33]type I collagen accounts for the majority of the collagen mass, and collagen type V, the functions of which are poorly understood, is a minor component. Type V collagen has been implicated in the regulation of fibril diameter, and we reported recently preliminary evidence that type V collagen is required for collagen fibril nucleation (Wenstrup, R. J., Florer, J. B., Cole, W. G., Willing, M. C., and Birk, D. E. (2004 This prompted us to evaluate the genotype of for the *col5a1* zebrafish lines over time.

This showed that at 1 dpf, the different genotypes approximate the expected Mendelian ratios. This ratio changes during the early stages of development with a clear decrease to absence of homozygous zebrafish at 14 dpf (Figure 5). This indicates that, at least in early developmental stages in zebrafish, the lack of type V collagen is viable, but is associated with behavioral alterations.

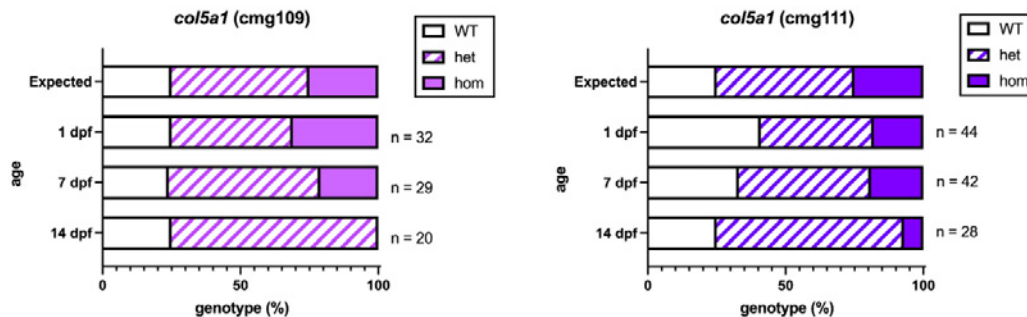


Figure 5. Genotyping experiment. A clutch of zebrafish offspring from the *col5a1* cmg109 line and the *col5a1* cmg111 line were divided in three equal parts (initial number of zebrafish per part: n = 32 for cmg109 and n = 44 for cmg111) and genotypes were determined after 1, 7 and 14 dpf. The number of surviving animals at each age is indicated next to the bars.

The *col5a1* zebrafish lines will be further phenotypically and molecularly characterized by assessing general body morphology (e.g., length, (kypho)scoliosis, pigmentation), mechanical properties of soft connective tissue specimens as well as ultrastructural analysis to assess collagen architecture in the ECM using transmission electron microscopy, since similar alterations are seen in the human (and murine) counterpart of cEDS.

3. Output

Part of this work was presented as a poster at the Annual Symposium of the Belgian Society of Human Genetics in Leuven.

Abstract details:

Zoë Malfait, Filipa Oliveira, Fransiska Malfait, Delfien Syx, **Zebrafish as a model to study pain in Ehlers-Danlos syndromes.** Annual Symposium of the Belgian Society of Human Genetics, Leuven, Belgium, April 12, 2024.

4. References

- Goldberg, D.S. and McGee, S.J. (2011) Pain as a global public health priority. *BMC Public Health* 11
- Breivik, H. *et al.* (2006) Survey of chronic pain in Europe: Prevalence, impact on daily life, and treatment. *Eur. J. Pain* 10, 287
- Wolfe, M.M. *et al.* (1999) Gastrointestinal toxicity of nonsteroidal antiinflammatory drugs. *N. Engl. J. Med.*
- Shipton Elspeth E Shipton Ashleigh J Shipton, E.A. (2018) A Review of the Opioid Epidemic: What Do We Do About It? *Pain Ther.* 7, 23–36
- Skolnick, P. (2018) The Opioid Epidemic: Crisis and Solutions. *Annu. Rev. Pharmacol. Toxicol. Annu. Rev. Pharmacol. Toxicol* 58, 143–59
- Frantz, C. *et al.* (2010) The extracellular matrix at a glance *Journal of Cell Science.* 1234195–4200
- Barros, C.S. *et al.* (2011) Extracellular Matrix: Functions in the nervous system. *Cold Spring Harb. Perspect. Biol.* 3, 1–24
- Tajerian, M. and Clark, J.D. (2015) The role of the extracellular matrix in chronic pain following injury *Pain*, 156 Lippincott Williams and Wilkins, 366–370

9. Tajerian, M. and Clark, J.D. (2019) Spinal matrix metalloproteinase 8 regulates pain after peripheral trauma. *J. Pain Res.* 12, 1133–1138
10. Parisien, M. *et al.* (2019) Genetic pathway analysis reveals a major role for extracellular matrix organization in inflammatory and neuropathic pain. *Pain* 160, 932–944
11. Velvin, G. *et al.* (2016) Systematic review of chronic pain in persons with Marfan syndrome *Clinical Genetics*, 89 Blackwell Publishing Ltd, 647–658
12. Voermans, N.C. *et al.* (2010) Pain in Ehlers-Danlos Syndrome is common, severe, and associated with functional impairment. *J. Pain Symptom Manage.* 40, 370–378
13. Nghiem, T. *et al.* (2017) Pain Experiences of Children and Adolescents with Osteogenesis Imperfecta: An Integrative Review *Clinical Journal of Pain*, 33 Lippincott Williams and Wilkins, 271–280
14. Nghiem, T. *et al.* (2018) Pain experiences of adults with osteogenesis imperfecta: An integrative review. *Can. J. Pain* 2, 9–20
15. Malfait, F. *et al.* (2020) The Ehlers–Danlos syndromes. *Nat. Rev. Dis. Prim.* 6, 64
16. Malfait, F. *et al.* (2017) The 2017 international classification of the Ehlers–Danlos syndromes. *Am. J. Med. Genet. Part C Semin. Med. Genet.* 175, 8–26
17. Malfait, F. *et al.* (2021) Collagens in the Physiopathology of the Ehlers–Danlos Syndromes pp. 55–119
18. Sacheti, A. *et al.* (1997) Chronic Pain Is a Manifestation of the Ehlers-Danlos Syndrome. *J. Pain Symptom Manage.* 14, 88–93
19. Sneddon, L.U. (2019) Evolution of nociception and pain: Evidence from fish models *Philosophical Transactions of the Royal Society B: Biological Sciences*, 374 Royal Society Publishing
20. Braithwaite, V.A. and Boulcott, P. (2007) Pain perception, aversion and fear in fish. *Dis. Aquat. Organ.* 75, 131–138
21. Costa, F. V. *et al.* (2021) The use of zebrafish as a non-traditional model organism in translational pain research: the knowns and the unknowns. *Curr. Neuropharmacol.* 19
22. Sneddon, L.U. (2015) Pain in aquatic animals *Journal of Experimental Biology*, 218 Company of Biologists Ltd, 967–976
23. Lopez-Luna, J. *et al.* (2017) Reduction in activity by noxious chemical stimulation is ameliorated by immersion in analgesic drugs in zebrafish. *J. Exp. Biol.* 220, 1451–1458
24. Gistelinc, C. *et al.* (2018) Zebrafish type I collagen mutants faithfully recapitulate human type I collagenopathies. *Proc. Natl. Acad. Sci. U. S. A.* 115, E8037–E8046
25. Delbaere, S. *et al.* (2020) Hypomorphic zebrafish models mimic the musculoskeletal phenotype of 4GalT7-deficient Ehlers-Danlos syndrome. *Matrix Biol.* 89, 59–75
26. Delbaere, S. *et al.* (2020) b3galt6 Knock-Out Zebrafish Recapitulate 3GalT6-Deficiency Disorders in Human and Reveal a Trisaccharide Proteoglycan Linkage Region. *Front. Cell Dev. Biol.* 8
27. Deakin, A.G. *et al.* (2019) Automated monitoring of behaviour in zebrafish after invasive procedures. *Sci. Rep.* 9
28. Chatigny, F. *et al.* (2018) Updated Review of Fish Analgesia. *J. Am. Assoc. Lab. Anim. Sci.* 57, 5–12
29. McGraw, H.F. *et al.* (2008) Zebrafish dorsal root ganglia neural precursor cells adopt a glial fate in the absence of neurogenin1. *J. Neurosci.* 28, 12558–12569
30. Colman, M. *et al.* (2023) Sensory Profiling in Classical Ehlers-Danlos Syndrome: A Case-Control Study Revealing Pain Characteristics, Somatosensory Changes, and Impaired Pain Modulation. *J. Pain* 24, 2063–2078
31. Syx, D. *et al.* (2020) Pain-related behaviors and abnormal cutaneous innervation in a murine model of classical Ehlers-Danlos syndrome. *Pain* 161, 2274–2283
32. Varshney, G.K. *et al.* (2015) High-throughput gene targeting and phenotyping in zebrafish using CRISPR/Cas9. *Genome Res.* 25, 1030–1042
33. Wenstrup, R.J. *et al.* (2004) Type V collagen controls the initiation of collagen fibril assembly. *J. Biol. Chem.* 279, 53331–53337



Geneeskundige Stichting Koningin Elisabeth
Fondation Médicale Reine Elisabeth
Königin-Elisabeth-Stiftung für Medizin
Queen Elisabeth Medical Foundation

Progress report
of the research group of

Dr. Marijne Vandenberg
Universiteit Antwerpen (UAntwerpen)

Dr. Marijne Vandenberg (UAntwerpen)

Campus Drie Eiken

Center for Molecular Neurology

Universiteitsplein 1

2610 Wilrijk

marijne.vandenberg@uantwerpen.be

Tel. +3232653978

World-wide systematic characterization of TMEM106B and ATXN2 genetic status Towards implementation of genetic testing of modifiers in clinical practice

1. Research Summary

Frontotemporal lobar degeneration (FTLD) is a quickly progressing debilitating neurodegenerative disease and one of the leading causes of young-onset dementia. There are no treatments available that delay the onset or slow down disease progression. The most common form causes changes in behavior and personality, hence FTLD imposes a dramatic impact on social life. In about 30% of patients, a strong family history is present. Autosomal dominant mutations in the chromosome 9 open reading frame 72 (*C9orf72*) gene, the microtubule-associated protein tau (*MAPT*) gene and the progranulin (*GRN*) gene are the most common causes of genetic frontotemporal dementia (FTD). FTD is characterized by variability in age at onset and clinical presentation, even within families. This variability remains poorly understood. Previous studies suggest the transmembrane protein 106 B (*TMEM106B*) and ataxin 2 (*ATXN2*) loci as genetic modifiers of disease risk, especially in patients who already carry dominant disease mutations. The discovery of these loci is exciting; however, studies have been limited in sample size and detailed characterization of the patient cohorts.

In this project, the aims are to:

- 1) Characterize the *TMEM106B* protective haplotype and *ATXN2* intermediate repeat carrier status by systematic genotype screens in well-characterized large FTD cohorts and within families
- 2) Investigate whether the *TMEM106B* protective haplotype and *ATXN2* intermediate repeats correlate with progression of disease by linking genetic data with detailed longitudinally collected clinical, neurophysiological and imaging data

2. Progress Report

2.1. Characterization of the *TMEM106B* protective haplotype and *ATXN2* intermediate repeat carrier status in large FTD cohorts

Over the past year, the distribution of the *TMEM106B* protective haplotype and *ATXN2* intermediate repeat carrier status was determined in the ARTFL/LEFFTDS Longitudinal Frontotemporal Lobar Degeneration study (ALLFTD, NCT04363684). ALLFTD is a consortium with 27 centers across the US and Canada. For this study, participants were enrolled between 2015 and 2023.

In a cohort of 1789 individuals, we genotyped the *TMEM106B* rs1990622 single nucleotide variant (SNV) and determined the repeat length of *ATXN2* (**Table 1**). A repeat length of at least 27 was defined as intermediate repeat.

Table 1. Distribution of *TMEM106B* rs1990622 and *ATXN2* intermediate repeats in ALLFTD

	Non-mutation carriers	<i>C9orf72</i>	<i>GRN</i>	<i>MAPT</i>
Total number	1275	254	118	124
<i>TMEM106B</i> rs1990622				
A/A	405	97	54	47
A/G	626	120	56	60
G/G	244 (19%)	37 (15 %)	8 (7%)	17 (14%)
<i>ATXN2</i>				
Repeat length \geq 27	2.8 %	8.8%	1.5%	2.4%

TMEM106B rs1990622 is a common variant, with a minor allele frequency of ~ 40 % in the European non-Finnish population (gnomAD v4.0). Comparing the genetic groups, there is a lower percentage of *TMEM106B* rs1990622*G/G carriers in the *GRN* group. The distribution of the rs1990622 genotype is significantly lower in *GRN* mutation carriers than in participants not carrying a pathogenic mutation in any of the known FTD genes and *C9orf72* mutation carriers (Fisher exact test $p < 0.05$, adjusted for multiple pairwise comparisons with the false-discovery rate method). The *TMEM106B* locus was identified as a genetic modifier of disease risk in individuals with *GRN* mutations, with carriers of the protective haplotype (rs1990622*G) having a 50% lower odds to develop disease symptoms compared to *TMEM106B* non-protective haplotype carriers with *GRN* mutations¹. Furthermore, our group has shown that *TMEM106B* alters the penetrance of *GRN* mutation. A patient in their 50s presented in the clinic with symptoms of behavioral variant FTD, and genetic testing revealed a pathogenic *GRN* mutation. The patient's asymptomatic parent who was in their 80s was also found to carry the *GRN* mutation, but also carried two copies of the protective *TMEM106B* allele². Hence, we believe that that *GRN* mutation carriers with *TMEM106B* rs1990622*GG are seen less often in the clinic as they remain without symptoms, and are hence not enrolled in research studies. This would explain the lower proportion of *TMEM106B* rs1990622*GG carriers across *GRN* mutation carriers. We are currently collecting data of *GRN* carriers beyond ALLFTD to characterize the *TMEM106B* haplotype in other large populations of *GRN* carriers. The aim is to identify *GRN* mutation carriers with the *TMEM106B* protective haplotype beyond ALLFTD to demonstrate further its protective effects (manuscript in preparation).

In the ALLFTD study, intermediate length repeats in *ATXN2* are more frequent in *C9orf72* mutation carriers than in participants not carrying a pathogenic mutation in any of the known FTD genes (Fisher exact test $p < 0.05$, adjusted for multiple pairwise comparisons with the false-discovery rate method). Interestingly, upon comparison of the clinical phenotypes of *C9orf72* carriers with *ATXN2* intermediate repeats, we observed that there are two *C9orf72* mutation carriers in ALLFTD with the progressive supranuclear palsy (PSP) phenotype, a phenotype only rarely associated with *C9orf72*, and both individuals carry an intermediate *ATXN2* repeat (**Figure 1**). Currently, screenings for *ATXN2* in individuals with a *C9orf72* mutation and a PSP phenotype are currently being conducted, to investigate whether *ATXN2* is acting as a modifier of the PSP phenotype in *C9orf72* mutation carriers (manuscript in preparation).

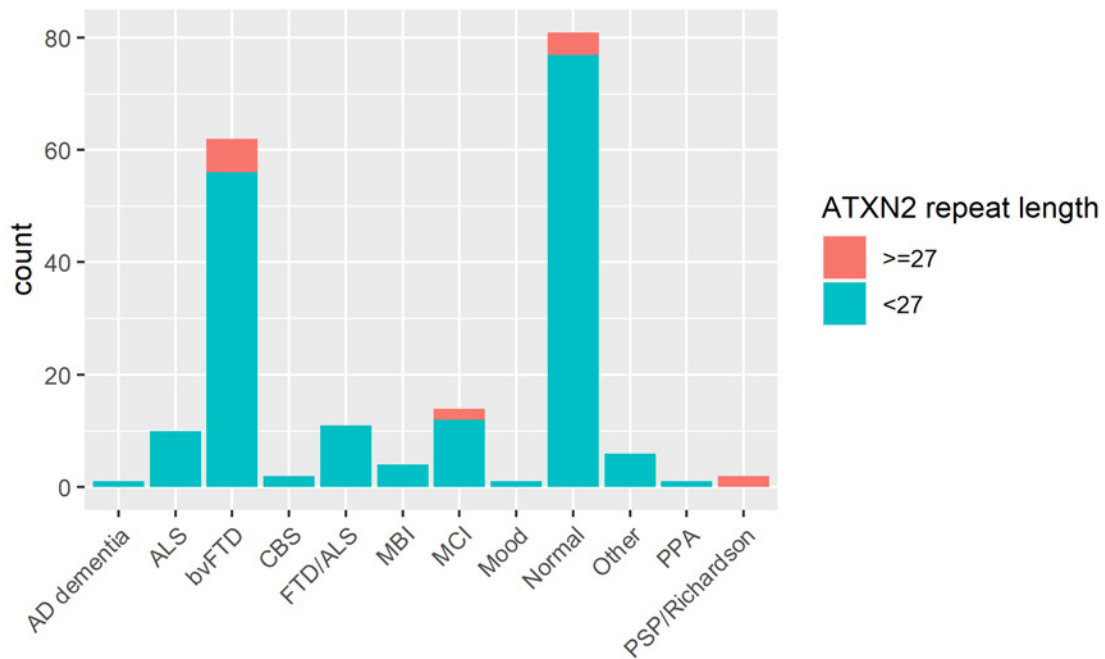


Figure 1. The distribution of ATXN2 intermediate repeats across the clinical phenotypes of C9orf72 mutation carriers in ALLFTD.

2.2. Investigation whether the TMEM106B protective haplotype correlate with progression of disease

In ALLFTD participants, I have investigated the effect of *TMEM106B* on disease development. Looking at changes in volumetric gray matter measures, *GRN* carriers homozygous for the protective allele (rs1990622*GG) had significantly greater total gray matter volumes than *GRN* mutation carriers without or with only one protective allele (linear mixed model with years of education, sex, age at visit and the CDR+NACC-FTLD sum of boxes as covariate and with pedigree as random effect, $\beta = 3.25$ [0.37,6.19], $p = 0.034$). Looking at individual (sub)cortical regions of interest, the left thalamic region was the top individual region of interest ($p = 0.006$).

To further map the modifying effect of *TMEM106B*, we've investigated the association between *TMEM106B* and the National Alzheimer's Coordinating Center Uniform Data Set (v3.0) executive function composite score (UDS3-EF). This is an item response theory-based composite score derived from 7 total UDS3-EF test scores: category fluency (animals and vegetables, total correct), lexical fluency (F and L words, total correct), number span backward (total correct trials), Trail Making Test parts A and B (correct lines per minute). In *C9orf72* carriers, we identified an association between the protective *TMEM106B* allele and higher cognitive scores ($\beta = 0.36$ [0.05,0.66], $p = 0.021$). This was retained considering only presymptomatic *C9orf72* mutation carriers ($\beta = 0.33$ [0.03,0.63], $p = 0.036$). In conclusion, we identified associations of *TMEM106B* with gray matter volume and cognition in the presence of *GRN* and *C9orf72* pathogenic variants. The association of *TMEM106B* with outcomes of interest in presymptomatic *GRN* and *C9orf72* pathogenic variant carriers could additionally reflect *TMEM106B*'s effect on divergent pathophysiologic changes before the appearance of clinical symptoms. This study has now been published (Vandebergh et al., *Neurology*, 2024)³.

3. Presentation at international conferences

AFTD Holloway Summit 2025 – Miami, Florida, USA (January 22nd, 2025)

14th International Conference on Frontotemporal Dementias – Amsterdam, the Netherlands (September 19th, 2024)

CReATe Consortium Annual Meeting – Miami Beach, Florida, USA (August 19th, 2024)

4. Publications in 2024 with Q.E.M.F. acknowledgement

Gene-Specific Effects on Brain Volume and Cognition of TMEM106B in Frontotemporal Lobar Degeneration

Marijne Vandebergh, Eliana Marisa Ramos, Nick Corriveau-Lecavalier, Vijay K. Ramanan, John Kornak, Carly Mester, Tyler Kolander, Danielle E. Brushaber, Adam M. Staffaroni, Daniel H. Geschwind, Amy A. Wolf, Kejal Kantarci, Tania Gendron, Leonard Petrucelli, Marleen Van den Broeck, Sarah Wynants, Matthew Baker, Sergi Borrego-Écija, Brian Appleby, Sami Barmada, Andrea C. Bozoki, David Clark, R. Ryan Darby, Bradford C. Dickerson, Kimiko Domoto-Reilly, Julie A. Fields, Douglas Galasko, Nupur Ghoshal, Neill R. Graff-Radford, Ian M. Grant, Lawrence S. Honig, Ging-Yuek R. Hsiung, Edward D. Huey, David J. Irwin, David S. Knopman, Justin Y. Kwan, Gabriel C. Léger, Irene Litvan, Joseph C. Masdeu, Mario F. Mendez, Chiadi U. Onyike, Belen Pascual, Peter S. Pressman, Aaron Ritter, Erik D. Roberson, Allison Snyder, Anna Campbell Sullivan, Maria Carmela Tartaglia, Dylan Wint, Rosa Rademakers, ALLFTD Consortium.

Accepted for publication: August 19, 2024

Journal: *Neurology*

Impact factor: 8.4

Q factor: Q1

5. References

1. Pottier C, Zhou X, Perkerson RB, 3rd, et al. Potential genetic modifiers of disease risk and age at onset in patients with frontotemporal lobar degeneration and GRN mutations: a genome-wide association study. *Lancet Neurol* 2018; **17**(6): 548-58.
2. Perneel J, Manoochehri M, Huey ED, Rademakers R, Goldman J. Case report: TMEM106B haplotype alters penetrance of GRN mutation in frontotemporal dementia family. *Front Neurol* 2023; **14**: 1160248.
3. Vandebergh M et al. Gene-Specific Effects on Brain Volume and Cognition of TMEM106B in Frontotemporal Lobar Degeneration. *Neurology* 2024; **103**(8): e209832



Geneeskundige Stichting Koningin Elisabeth
Fondation Médicale Reine Elisabeth
Königin-Elisabeth-Stiftung für Medizin
Queen Elisabeth Medical Foundation

Progress report of the research project of the young researcher

Dr. Barbara M.P. Willekens
Universiteit Antwerpen (UAntwerpen)

Prof. dr. Barbara Willekens (UAntwerpen)
Neurologist | MS & CNS Neuroimmune Disorders
T +32 3 821 34 23
Barbara.willekens@uza.be

Department of Neurology
UZA, Drie Eikenstraat 655, 2650 Edegem
T +32 3 821 30 00
www.uza.be/neurologie

University of Antwerp
Translational Neurosciences Research Group
Laboratory of Experimental Hematology, Vaccine & Infectious Disease Institute (VAXINFECTIO)
Faculty of Medicine and Health Sciences
Universiteitsplein 1, 2610 Antwerp, Belgium
Barbara.willekens@uantwerpen.be

Unravelling the role of antigen-specific T cells in NMOSD and MOGAD: first progress report

1. Project overview

Neuromyelitis Optica Spectrum Disorders (NMOSD) and Myelin Oligodendrocyte Glycoprotein Antibody Associated Disease (MOGAD) are rare autoimmune diseases of the central nervous system (CNS) that are distinct from multiple sclerosis (MS), a more prevalent CNS autoimmune disease [1, 2]. The key role of T cells in the pathogenesis of NMOSD and MOGAD remains underinvestigated. Improved understanding of antigen-specific T cell functions is relevant to improve understanding of disease pathogenesis and develop more targeted therapies, such as antigen-specific cell based treatments [3].

The importance of T cells in the pathogenesis of NMOSD and MOGAD is supported by (i) pathological features in human tissue, (ii) T cell help is needed for blood-brain-barrier breakdown and pathogenicity of auto-antibodies, (iii) Th1 and Th17 pro-inflammatory cytokine profile. However, detection of antigen-specific T cells in the peripheral blood of people with AQP4+ NMOSD and even more so in MOGAD, has been challenging so far [4].

Previous research of our group in the field of MS has demonstrated that longitudinal analysis of myelin-specific T cells with IFN- ELISPOT assay in a cohort of MS patients treated with natalizumab showed a high variability over time [5]. The low frequencies of MOG-specific T cells when measured in a cross-sectional setting could be a potential explanation for the previous failure of Hofer et al. to detect MOG-specific T cells in a small cohort of MOGAD patients [4].

Detection and functional characterisation of antigen-specific autoreactive T cells in the peripheral blood is a necessary step to demonstrate and strengthen the evidence for the pivotal role of T cells in the pathogenesis of NMOSD and MOGAD and may pave the way towards future development of antigen-specific T cell modulatory treatments [3, 6].

2. Research hypothesis and objectives

Unravelling the role of antigen-specific T cells in AQP4+ NMOSD and MOGAD will aid in paving the road towards development of antigen-specific tolerance inducing cell-based treatments for NMOSD and MOGAD [3]. The main hypothesis is that T cell responses are detectable in a substantial proportion of patients with MOGAD and AQP4+ NMOSD [4]. The second hypothesis is that antigen-specific T cells are functionally different between NMOSD and MOGAD patients versus healthy controls. Furthermore, antigen-specific T cell responses are likely variable over time and could be associated with disease activity and clinical disease phenotypes.

The objectives are:

1. To identify MOG specific and AQP4 specific T cells in patients with MOGAD and AQP4+ NMOSD.
2. To characterize the functional phenotype of antigen-specific T cells in patients with MOGAD and AQP4+ NMOSD

3. Achievements and ongoing work

Study protocol and informed consent documents have been written, submitted and approved by the ethical committee. Final approval by the ethics committee was obtained on July 24, 2023. A challenge was to organize the administration of the grant at the University of Antwerp in an appropriate manner, but this was settled and organized successfully. The project was registered in the Antwerp Biobank, for which contracts between University Hospital Antwerp and the University of Antwerp have been put in place. All necessary documents and contracts were finalized in December 2023. Identification of potential study participants has been done and a workflow has been set up. Due to familial reasons occurring unexpectedly in the summer months of 2024 additional delay in this project has occurred. We anticipate the cross-sectional analysis of antigen-specific T cell responses in AQP4+ NMOSD (n=10) and MOGAD (n=10) patients, in comparison to healthy controls (n=10) to start in May 2025. In MS patients, we have demonstrated that the number of circulating myelin specific T cells is variable over time between and within individuals [5]. Hence, longitudinal analysis, with multiple sampling points in individual patients, may increase the chance to detect MOG specific T cells in MOGAD patients. While others have used the same myelin peptides as have been implicated in multiple sclerosis, we will use intact MOG protein [4]. Our research group has established a unique protocol for enrichment of autoreactive T cells in MS using a broad antigen panel of myelin peptides [7, 8]. This protocol will be optimized (IFN- and IL-6 ELISPOT assay) to detect autoreactive T cells towards full-length MOG and AQP4+ peptides as described before [4]. Supernatant of cell cultures will be collected and frozen for later cytokine analysis using ELISA to measure IFN-, IL-6, IL-22 and GM-CSF [4, g]. These results can provide information on the proinflammatory character of antigen-specific T cells. As pathogenic CD4+ T cells have been detected in brain lesions of MOGAD and AQP4+ NMOSD patients [10-12], it is important to clarify the mechanisms through which they may enter the CNS. Identifying expression of brain-homing markers on antigen-specific T cells could help our understanding of cell trafficking from the periphery to the CNS in these disorders [13]. The Flow Cytometry and Cell Sorting Core Facility of the University of Antwerp (FACSUA) recently acquired a new state-of-the-art Cytek Aurora which will be used to analyze surface markers of antigen-specific T cells and retain the remaining cells for downstream applications.

4. Research output with QEMF acknowledgement

One publication is in preparation (Review article, Methods for the detection of T cell epitopes involved in autoimmunity; applicant as co-author), for which QEMF support will be acknowledged.

4.1. Other relevant impact

Prof. dr. B. Willekens performed a short scientific stay (FWO travel grant, December 2024) in Verona, Italy, with Prof. Sara Mariotto, aiming to set up a live Cell Based Assay to detect MOG IgG with a more sensitive assay than the commercially available CBA, at the University of Antwerp. In addition, prof. dr. B. Willekens joined the Medical Advisory Council of the MOG Project (<https://mogproject.org/medical-advisory-board>).

5. References

1. Marignier, R., et al., *Myelin-oligodendrocyte glycoprotein antibody-associated disease*. *Lancet Neurol*, 2021. **20**(9): p. 762-772.
2. Wingerchuk, D.M., et al., *International consensus diagnostic criteria for neuromyelitis optica spectrum disorders*. *Neurology*, 2015. **85**(2): p. 177-89.
3. Derdelinckx, J., et al., *Cells to the Rescue: Emerging Cell-Based Treatment Approaches for NMOSD and MOGAD*. *Int J Mol Sci*, 2021. **22**(15).
4. Hofer, L.S., et al., *Comparative Analysis of T-Cell Responses to Aquaporin-4 and Myelin Oligodendrocyte Glycoprotein in Inflammatory Demyelinating Central Nervous System Diseases*. *Front Immunol*, 2020. **11**: p. 1188.
5. Willekens, B., et al. *Longitudinal analysis of autoreactive T cells in a cohort of multiple sclerosis patients treated with natalizumab*. in *MULTIPLE SCLEROSIS JOURNAL*. 2021. SAGE PUBLICATIONS LTD 1 OLIVERS YARD, 55 CITY ROAD, LONDON EC1Y 1SP, ENGLAND.
6. Lopez, J.A., et al., *Pathogenesis of autoimmune demyelination: from multiple sclerosis to neuromyelitis optica spectrum disorders and myelin oligodendrocyte glycoprotein antibody-associated disease*. *Clin Transl Immunology*, 2021. **10**(7): p. e1316.
7. Derdelinckx, J., et al., *HLA Class II Genotype Does Not Affect the Myelin Responsiveness of Multiple Sclerosis Patients*. *Cells*, 2020. **9**(12).
8. Lee, W.-P., et al., *Immunomodulatory Effects of 1, 25-Dihydroxyvitamin D₃ on Dendritic Cells Promote Induction of T Cell Hyporesponsiveness to Myelin-Derived Antigens*. *Journal of Immunology Research*, 2016. **2016**.
9. Bronge, M., et al., *Myelin oligodendrocyte glycoprotein revisited-sensitive detection of MOG-specific T-cells in multiple sclerosis*. *J Autoimmun*, 2019. **102**: p. 38-49.
10. Höftberger, R., et al., *The pathology of central nervous system inflammatory demyelinating disease accompanying myelin oligodendrocyte glycoprotein autoantibody*. *Acta Neuropathol*, 2020. **139**(5): p. 875-892.
11. Takai, Y., et al., *Myelin oligodendrocyte glycoprotein antibody-associated disease: an immunopathological study*. *Brain*, 2020. **143**(5): p. 1431-1446.
12. Bradl, M., M. Reindl, and H. Lassmann, *Mechanisms for lesion localization in neuromyelitis optica spectrum disorders*. *Curr Opin Neurol*, 2018. **31**(3): p. 325-333.
13. Smolders, J., et al., *T-cell surveillance of the human brain in health and multiple sclerosis*. *Seminars in Immunopathology*, 2022.



Geneeskundige Stichting Koningin Elisabeth
Fondation Médicale Reine Elisabeth
Königin-Elisabeth-Stiftung für Medizin
Queen Elisabeth Medical Foundation

Progress report of the research project of the young researcher



Dr. Wouter Peelaerts
Katholieke Universiteit Leuven (KU Leuven)

Prof. Dr. Wouter Peelaerts (KU Leuven)
Department of Neurosciences
Laboratory for Neurobiology and Gene Therapy
Department of Pharmacy and pharmaceutical
O&N5b-Herestraat 49 box 1023
3000 Leuven
Belgium

Peripheral infections as a trigger of multiple system atrophy

1. Summary of project rationale and hypothesis

Multiple system atrophy (MSA) is a progressive and fatal neurodegenerative disease. The clinical presentation of MSA is heterogeneous as the disease affects a variety of central and peripheral autonomic functions. Although it is believed that MSA risk can be influenced by genetic or environmental factors no risk factors have been identified to date. In the absence of crucial insights into the molecular etiopathogenesis there are no available biomarkers for the early detection of early disease-related changes which limits efficient treatment options.

The hypothesis of this project is that MSA can be triggered by an infectious pathogen. We recently proposed that a trigger can occur before or during advanced disease stages and elicit a local or systemic host response¹. Infections are prominent in MSA also during the prodrome, and manifest months or years before MSA diagnosis²⁻⁴. Our overarching goal is study both viral and bacterial infections in MSA and identify those pathogens that might have a significant impact in the development of neuropathology.

Infections manifest frequently in MSA but can go unnoticed because of autonomic failure, lower body temperature, desensitisation of the peripheral pain response or anhidrosis which can mask sudden changes, and which would otherwise warrant for signs of infection. Peripheral symptoms can mask ongoing infection and worsen disease progression. During advanced stages, infections can lead to neuropsychiatric effects^{5,6} and sepsis⁷. Yet, and even though infections are common, it is not known if there is a causal link between infections and MSA.

This project focuses on the role of urinary tract infections in MSA. We discovered that urinary tract infections (UTIs) are strongly associated with MSA diagnosis when the infection occurs prior to disease onset. To the best of our knowledge, this is the first significant risk factor identified for MSA to date.

Our lab is currently investigating the contribution of several types of infections in MSA, including viral infections, but these studies are currently more exploratory whereas the focus of this project is on the role of UTIs in MSA. The link between UTIs and MSA is currently better established⁸. Our scientific goals build on these links with new methodological tools and animal models that recapitulate the complexity of genetic and environmental risk in MSA.

2. Scientific goals

Even though infections are thus common in MSA, it is not yet known if there is a direct or causal link between infections and MSA and/or if infections can influence disease progression. The neuroinflammatory response during UTIs has not been examined in MSA and it is also not known if infections in the lower urinary tract could influence central effects related to glial or neuronal health.

For our experimental approach, we use uropathogenic *E. coli* (UPEC) which is commonly used to experimentally model lower urinary tract infections as this pathogen leads to robust inflammatory responses in mouse.

To examine how peripheral infections influence Syn pathology and trigger central changes, we have defined the following three aims:

1. establish a direct link between peripheral infections and Syn function (**report 2023**)
2. identify neuroinflammatory triggers in response to peripheral infection (**report 2023 and this report, 2024**)
3. examine the influence of peripheral infection on MSA disease progression (**report 2023 and this report, 2024**)

The main objective of this project is to identify pathogen-related triggers of MSA and investigate how disease triggers contribute to disease progression in MSA. We will focus on the specific mechanisms underlying UTI-related disease triggers.

3. Research results

Central to MSA is Syn that deposits throughout the central nervous system in oligodendroglial cells leading to demyelination and neurodegeneration⁹. The pathognomonic feature of MSA is the presence of deposits of the protein α -synuclein (Syn) in oligodendroglial cells. Accumulation of Syn results in progressive pathology in oligodendroglia with demyelination and cellular dysfunction. We and others have shown that aggregated Syn can spread between cells and convert endogenous Syn into its pathogenic form and which is reminiscent of prions¹⁰. Glial immune activation is often found in areas with high Syn burden^{11,12}. Considerable experimental and clinical evidence suggests that interactions between Syn and the immune system occur physiologically¹³⁻¹⁵.

To further study the impact of infections in MSA pathogenesis, our lab has recently characterized a humanized Syn model to examine infectious disease triggers. To further build on this data, we are examining the effects of chronic UTIs in WT model. To this aim, we superinfected C57BL/6 mice four times with UPEC over a course of 8 months. A superinfection is performed by infecting the animals twice, first with 10^8 CFU of UPEC, followed 24 hours later with 10^7 CFU of UPEC. PBS injected mice serve as a control. After 4 weeks of every superinfection animals received antibiotics to mimic normal clinical practices and to prevent the development of chronic infections or nephritis¹⁶.

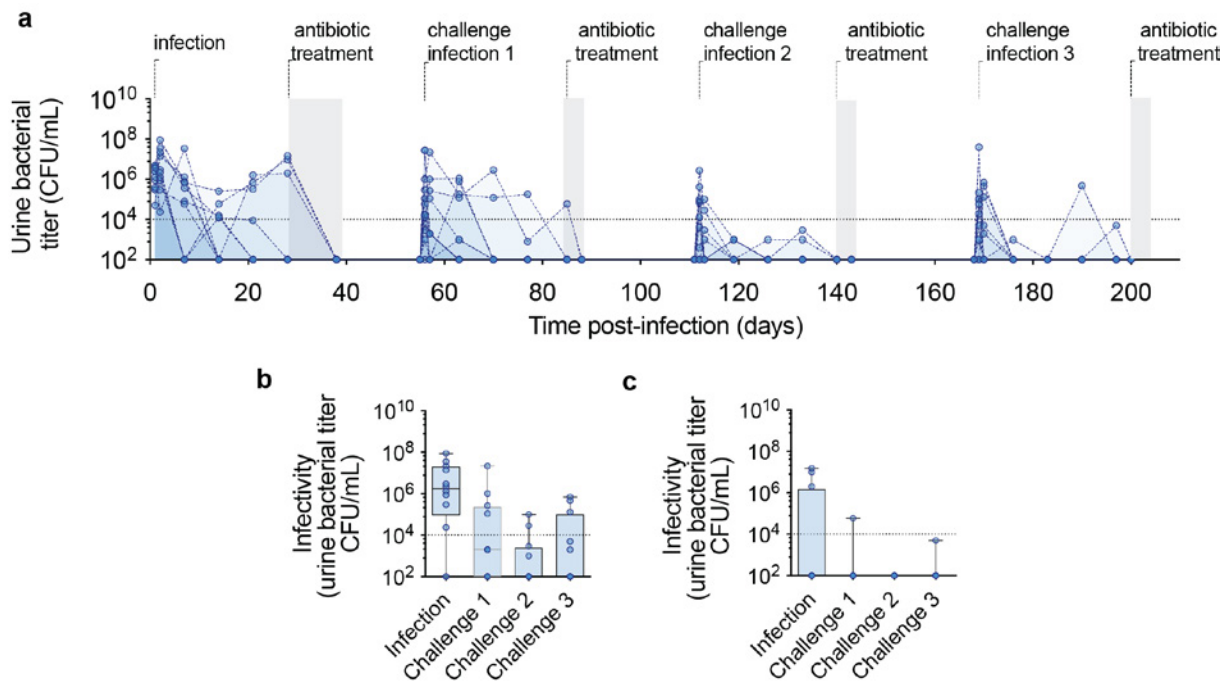


Figure 1. Repeated superinfections in WT C57BL6/N mice do not cause chronic UTIs. WT C57BL6/N mice were repeatedly superinfected with UPEC. **a)** Schematic representation for recurrent UTIs *in vivo*. For super infections, eight-weeks old female mice were infected via transurethral catheterization into the urinary bladder twice with 10^8 CFU every 24 hours. Four weeks after superinfections antibiotics were administered in the drinking water for 10 or 4 days to treat chronic UTIs. After resolution, and at 8 weeks after the initial infection, animals were challenged with a new superinfection. This challenge was repeated 3 times for a total of four superinfections over a course of 9 months until the animals were 11-months old. At 11 months, none of the animals ($n=12$) showed signs of chronic infection. **b)** At the first superinfection most animals develop acute UTIs with titers that are higher than 10^4 CFU/mL 48 hours after superinfection. At the second, third and fourth superinfection, no acute infection is observed after 48 hours. **c)** WT C57BL6/N mice do not develop chronic UTIs with at 4 weeks after superinfection or challenge superinfection ($*p < 0.05$ for Kruskal-Wallis analysis with Dunn's post hoc analysis for correction of multiple comparisons, each data point represents one individual animal).

Given increasing evidence that peripheral infections can influence central nervous system (CNS) inflammation, we next examined microglial activation in key brainstem regions involved in autonomic and immune regulation. We focused on the dorsal vagal complex, which integrates peripheral immune signals and plays a critical role in sickness behavior.

Using AI-assisted image analysis, we quantified microglial density and morphology in the area postrema (AP), the nucleus tractus solitarii (NTS), and the dorsal motor nucleus of the vagus nerve (DMX). Our findings revealed a significant increase in microglial cell numbers within the AP following rUTI, suggesting heightened immune activation in this region. Moreover, microglial morphology analysis demonstrated a shift toward a reactive phenotype in the AP, characterized by increased cell body size and altered perimeter-to-area ratios—hallmarks of neuroinflammatory activation.

Interestingly, despite the pronounced microglial response in the AP, no significant increase in microglial density or activation was observed in the NTS or DMX. This regional specificity suggests that peripheral infections may selectively influence neuroinflammatory pathways in brainstem structures that are particularly sensitive to immune challenges. The AP's heightened response aligns with previous research indicating that this brain region, due to its lack of a blood-brain barrier, serves as a critical interface for peripheral immune-to-brain communication.

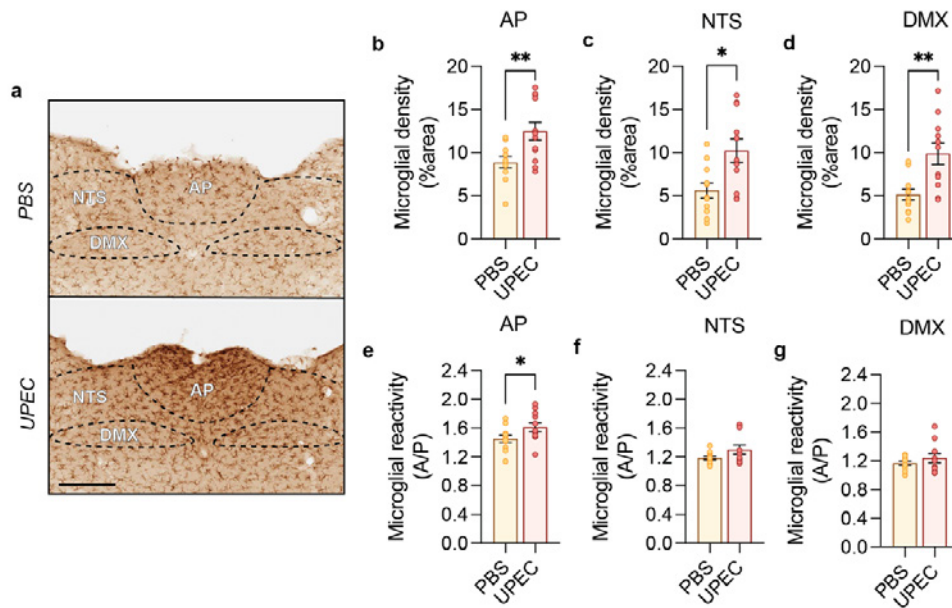


Figure 2. Microglial reactivity after rUTI in the dorsal vagal complex. The nucleus tractus solitarii (NTS) and area postrema (AP) control sickness behavior and are located dorsal from the dorsal motor nucleus of the vagal nerve (DMX). Together they integrate input from the autonomous nervous system and the humoral response. **a)** Regions for the AP, NTS and DMX are manually annotated for AI-based microglial analysis. Scale bar is 250 μ m. **b)** Quantification of the number of microglial cells in the AP, **c)** the NTS and the **d)** DMX reveals a significant increase in cell number after rUTI (* $P < 0.05$, ** $P < 0.01$ unpaired t-test, each data point represents one individual animal). **e)** Microglial cells of the AP are reactive, determined by a change in area versus perimeter (A/P) (* $P < 0.05$ unpaired t-test, each data point represents one individual animal). **f)** Microglial cells of NTS and **g)** DMX do not show reactivity after rUTI (unpaired t-test, each data point represents one individual animal).

Since the accumulation of misfolded Syn in oligodendrocytes is a defining feature of MSA, we next examined whether recurrent UTIs influence Syn pathology in the CNS. We performed immunohistochemical staining for phosphorylated Syn (Pser129-Syn), a widely recognized marker of pathogenic Syn accumulation, to determine if peripheral infection contributes to synucleinopathy. The dorsal motor nucleus of the vagus nerve (DMX) was chosen for analysis because of its role in autonomic function and its involvement in early-stage Syn pathology in PD and other synucleinopathies. The DMX is particularly vulnerable to inflammatory and neurodegenerative changes due to its connectivity with peripheral immune signals via the vagus nerve. Given prior evidence that infections can trigger inflammatory responses that propagate to the brainstem, we hypothesized that recurrent UTIs might induce an increase in Syn phosphorylation in the DMX, providing mechanistic insight into how systemic infections could contribute to synucleinopathy.

To assess potential changes in Syn pathology, we performed immunohistochemical staining for Pser129-Syn in brainstem sections from transgenic SNCA^{WT} mice following recurrent UTI exposure. The region of interest, the DMX, was manually annotated, and AI-based quantification was used to analyze the extent of Pser129-Syn accumulation. The AI-assisted approach allowed for objective, high-throughput detection and measurement of Syn inclusions, ensuring consistency in data analysis. In transgenic SNCA^{WT} mice, AI-assisted image analysis revealed no significant increase in Pser129-Syn staining in the DMX or other brain regions following rUTI. This suggests that recurrent peripheral infections alone may not be sufficient to trigger overt Syn pathology in these mice.

This result is particularly important in the context of our broader hypothesis. While previous studies have suggested that infections can modulate Syn pathology, our data indicate that the

mere presence of recurrent UTIs does not necessarily lead to pathogenic Syn accumulation. This suggests that additional factors, such as genetic susceptibility prolonged, unresolved inflammation, may be required to drive Syn pathology in the DMX.

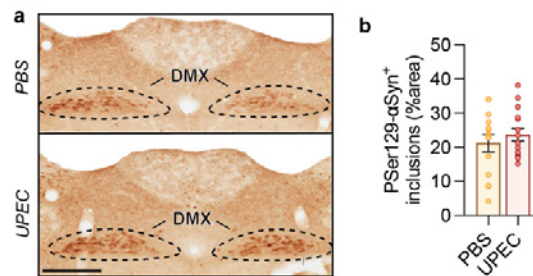


Figure 3. Pser129-Syn analysis after recurrent chronic UTI in the dorsal motor nucleus of the vagal nerve. a) The region of the dorsal motor nucleus of the vagal nerve (DMX) is manually annotated for AI-based Pser129-Syn⁺ analysis. The cell bodies of the motor nucleus of the vagal nerve are positive for Pser129-Syn⁺. Scale bar is 250 μm. b) Quantification of the area that is positively stained for Pser129-Syn in the DMX reveals no changes in Pser129-Syn signal within the DMV (unpaired t-test, each data point represents one individual animal).

To further explore the potential link between infection and synucleinopathy, we extended our analysis in WT and transgenic SNCA^{WT} mouse models. In contrast to WT animals, SNCA^{WT} mice exhibited widespread Pser129-Syn inclusions across multiple brain regions, including the cingulate cortex, striatum, amygdala, and midbrain. AI-assisted quantification of Pser129-Syn inclusions in these regions revealed distinct patterns of Syn aggregation, suggesting that genetic susceptibility plays a crucial role in determining whether infections contribute to synucleinopathy. These findings support the hypothesis that while recurrent UTIs alone do not induce Syn aggregation in WT mice, they may exacerbate Syn pathology in genetically susceptible individuals, potentially influencing MSA disease progression.

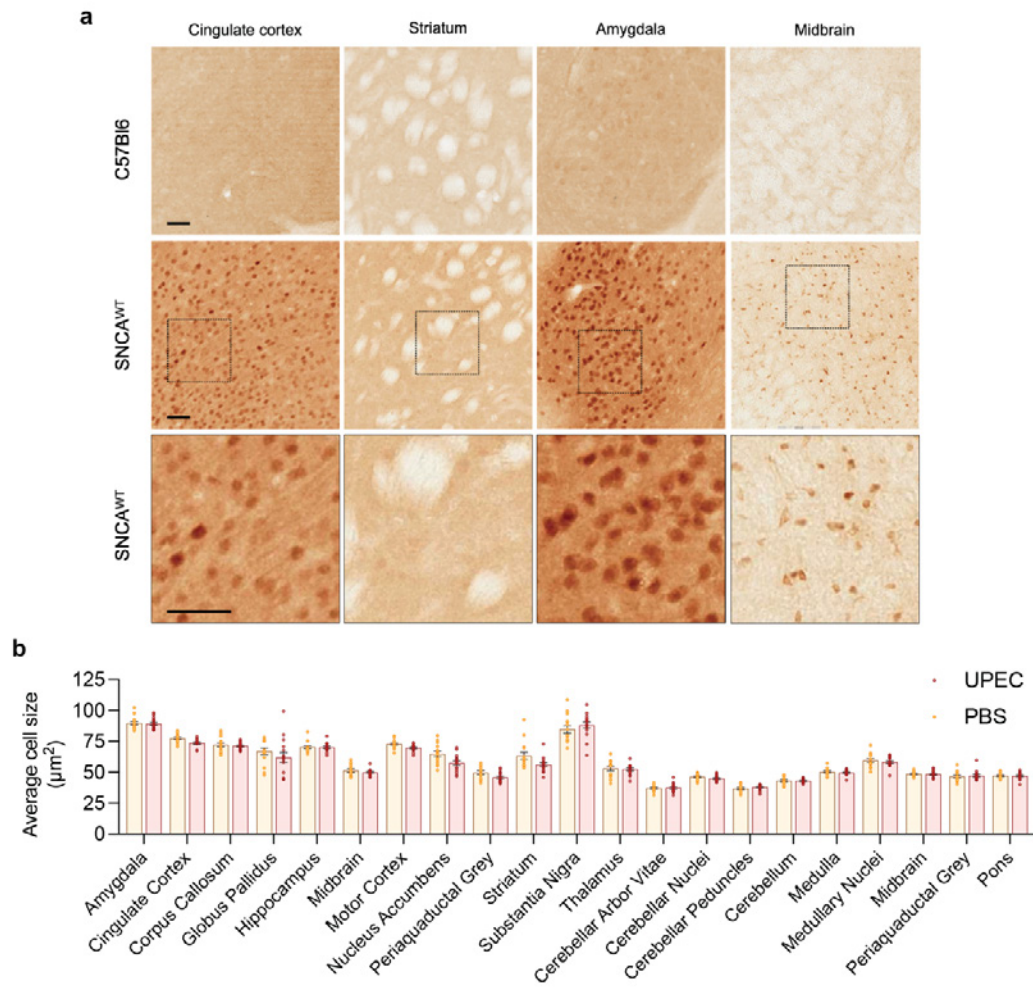


Figure 4. Analysis of Pser129-Syn inclusions in multiple brain regions of WT and SNCA^{WT} mice. An overview of different brain regions stained for Pser129-Syn. **a**) Representative images from the cingulate cortex, striatum, amygdala and midbrain for C57Bl6 mice (upper panel) and transgenic SNCA^{WT} mice (middle panel). Scale bar is 50 μm. In the lower panel more detailed 40x images are shown of Pser129-Syn inclusions for each region of SNCA^{WT} animals. In C57Bl6 mice cellular Pser129-Syn inclusions are absent. Scale bar is 50 μm. **b**) The size distribution of cellular inclusions is measured via detection of Pser129-Syn in the brain in SNCA^{WT} animals. Via object detection and segmentation of Pser129-Syn the AI model allows for precise measurement of Pser129-Syn inclusion diameter in whole brain.

Our findings highlight that transient infections, even when resolved, can provoke an inflammatory cascade that may contribute to long-term neurological consequences. Further studies will be required to assess whether prolonged immune activation from recurrent infections could accelerate Syn pathology over extended timeframes, particularly in genetically susceptible models.

4. Summary

With our epidemiological data and our experimental models⁸, this shows that a link between infections, peripheral aggregation and central pathology might exist. With this work we therefore link bacterial infections with synucleinopathy and show that a host response to environmental triggers can result in Syn pathology that bears semblance to MSA. We further identify the following points:

- Isolated peripheral infections might not be sufficient: While infections are known to contribute to neuroinflammation, our results suggest that peripheral infection alone does not directly cause Syn pathology in normal or transgenic mice. Instead, peripheral infections may act as a co-factor that accelerates pathology only in susceptible individuals.
- Although microglial activation was observed in the area postrema (AP) following rUTI, no corresponding increase in Syn phosphorylation was detected in the DMX. This suggests that while UTIs induce a neuroimmune response, inflammation alone may not be enough to trigger Syn aggregation
- Potential differences in syn-susceptible models: the absence of Syn pathology in WT mice highlights the importance of testing this model in genetically modified mice that express human Syn. In subsequent experiments, we plan to analyze the same brainstem regions in SNCA^{WT} transgenic mice combined with a seeding model, which are more susceptible to Syn aggregation.
- It is possible that UTIs trigger long-term neuroinflammatory changes that only manifest as Syn pathology later in life. Future longitudinal studies will be necessary to determine whether infections influence the rate of Syn accumulation over time rather than causing immediate pathological changes.

With the help of GSKE, we are now preparing a publication that will follow on our initial work to further describe how UTIs can trigger neuroinflammatory changes in the CNS. One study will furthermore focus on the use of AI models in animal modeling. Our goal is to disseminate these results to a wider audience including scientific conferences, patient organization meetings (Defeat MSA, MSA Coalition, de Vlaamse Parkinson Liga) and discuss the role of bacterial or viral infections in synucleinopathies.

5. References

1. Tulisak, C. T., Mercado, G., Peelaerts, W., Brundin, L. & Brundin, P. Can infections trigger alpha-synucleinopathies? in *Molecular Biology of Neurodegenerative Diseases: Visions for the Future, Part A* 299–322 (Elsevier, 2019). doi:10.1016/bs.pmbts.2019.06.002.
2. Kirchof, K., Apostolidis, A. N., Mathias, C. J. & Fowler, C. J. Erectile and urinary dysfunction may be the presenting features in patients with multiple system atrophy: a retrospective study. *Int J Impot Res* **15**, 293–298 (2003).
3. Panicker, J. N. *et al.* Early presentation of urinary retention in multiple system atrophy: can the disease begin in the sacral spinal cord? *J Neurol* **267**, 659–664 (2019).
4. Sakakibara, R. *et al.* Urinary dysfunction and orthostatic hypotension in multiple system atrophy: which is the more common and earlier manifestation? *J Neurol Neurosurg Psychiatry* **68**, 65–69 (2000).
5. Rashid, M. H. *et al.* Interleukin-6 mediates delirium-like phenotypes in a murine model of urinary tract infection. *J Neuroinflammation* **18**, 1–16 (2021).
6. Balogun, S. A. & Philbrick, J. T. Delirium, a symptom of UTI in the elderly: fact or fable? A Systematic Review. *Can Geriatr J* **17**, 22–26 (2013).
7. Papapetropoulos, S. *et al.* Causes of death in multiple system atrophy. *J Neurol Neurosurg Psychiatry* **78**, 327 (2006).
8. Wouter Peelaerts, Gabriela Mercado, Sonia George, Marie Villumsen, Alys Kasen, P. B. Urinary tract infections trigger synucleinopathy via the innate immune response. *Acta Neuropathol* (2023).
9. Grazia Spillantini, M. *et al.* Filamentous α -synuclein inclusions link multiple system atrophy with Parkinson's disease and dementia with Lewy bodies. *Neuroscience Letters* (1998) doi:10.1016/S0304-3940(98)00504-7.
10. Peelaerts, W. & Baekelandt, V. α -Synuclein strains and the variable pathologies of synucleinopathies. *J Neurochem* 256–274 (2016) doi:10.1111/(ISSN)1471-4159/homepage/special_issues.htm.
11. Hoffmann, A. *et al.* Oligodendroglial synucleinopathy-driven neuroinflammation in multiple system atrophy. *Brain Pathology* **29**, 380 (2019).
12. Ishizawa, K. *et al.* Microglial Activation Parallels System Degeneration in Multiple System Atrophy. *J Neuropathol Exp Neurol* **63**, 43–52 (2004).

13. Grozdanov, V. & Danzer, K. M. Intracellular Alpha-Synuclein and Immune Cell Function. *Frontiers in Cell and Developmental Biology* Preprint at <https://doi.org/10.3389/fcell.2020.562692> (2020).
14. Labrie, V. & Brundin, P. Alpha-Synuclein to the Rescue: Immune Cell Recruitment by Alpha-Synuclein during Gastrointestinal Infection. *J Innate Immun* **9**, 437–440 (2017).
15. Reish, H. E. A. & Standaert, D. G. Role of -synuclein in inducing innate and adaptive immunity in Parkinson disease. *J Parkinsons Dis* **5**, 1 (2015).
16. Schwartz, D. J., Conover, M. S., Hannan, T. J. & Hultgren, S. J. Uropathogenic Escherichia coli Superinfection Enhances the Severity of Mouse Bladder Infection. *PLoS Pathog* **11**, e1004599--12 (2015).



Geneeskundige Stichting Koningin Elisabeth
Fondation Médicale Reine Elisabeth
Königin-Elisabeth-Stiftung für Medizin
Queen Elisabeth Medical Foundation

Progress report of the research project of the young researcher

Dr. Sarah van Veen
Katholieke Universiteit Leuven (KU Leuven)

Dr. Sarah van Veen, PhD (KU Leuven)

FWO postdoctoral fellow

Laboratory of Cellular Transport Systems

KU Leuven, Department of Cellular and Molecular Medicine

ON Ibis Herestraat 49, box 802 – 3000 Leuven (Belgium)

T +32 (0)16 32 90 55

sarah.vanveen@kuleuven.be

The impact of ATP13A4-mediated polyamine transport in astrocytes on synaptogenesis and neurodevelopmental disorders

1. Astrocytic ATP13A4 is a polyamine transporter that controls astrocyte function

1.1. Abstract

Polyamines, such as spermidine and spermine, are essential for brain function and neurodevelopment. These soluble molecules modulate glial and neuronal ion channels, transporters and receptors, contributing to cellular communication in the brain. Within the brain, polyamines primarily accumulate in astrocytes, but the mechanisms of polyamine uptake in astrocytes, and the physiological relevance of this process in brain function, remain poorly understood. Here, we identified ATP13A4, a P5B-type transport ATPase predominantly expressed in astrocytes, as a key polyamine transporter for polyamine uptake and homeostasis in astrocytes. Using primary cultures and rodent models, we show that ATP13A4 deficiency reduces astrocyte arborization and increases excitatory synapse formation. Exogenous spermidine application recapitulated these effects, suggesting that astrocytes play a critical role in clearing extracellular polyamines. Moreover, we identified a novel homozygous p.E276K variant of ATP13A4 in a patient with intellectual disability and a heterozygous deletion spanning exons 19-25 in a patient with epilepsy. Additionally, we characterized two ATP13A4 variants previously associated with autism and language impairment. All variants exhibited loss-of-function phenotypes, pointing to a link between ATP13A4 dysfunction and neurodevelopmental disorders. In summary, astrocytes clear extracellular polyamines via ATP13A4, thereby regulating astrocyte arborization and excitatory synapse formation. This study is the first to link dysfunction in astrocytic polyamine transport to perturbations in brain development, providing novel insights into the molecular mechanisms underlying neurodevelopmental disorders.

1.2. Main

Polyamines, such as spermidine and spermine, are small and abundant organic polycations with dynamic roles in various biological processes (1), including aging (2, 3), cancer (4), and brain disorders (5, 6). Polyamines exhibit multifaceted functions – they act as antioxidants, possess anti-inflammatory properties, and are critical to fundamental cellular processes such as protein synthesis, membrane stability, signal transduction, neurotransmission, autophagy, and cell growth (reviewed in (7)).

Maintaining proper polyamine homeostasis in the brain is critical not only for proper neurodevelopment but also for preventing significant disruptions to neuronal survival and network stability (8-13). Polyamines are involved in key processes that shape neuronal connectivity and circuit formation through their modulation of ion channels, receptors, and influence on synaptic plasticity (14-17). Their balanced levels can confer neuroprotective benefits (18, 19), while disruptions in polyamine homeostasis – such as excessive accumulation or depletion – can lead to neuronal death, heightened seizure susceptibility, or other forms of neurological dysfunction (5, 6, 10, 11, 13, 20-24). Supporting this, mutations in polyamine synthesis genes are often associated with neurodevelopmental disorders (25-30), highlighting the critical need for tightly regulated polyamine levels during brain development.

Within the brain, spermidine and spermine are mainly synthesized and released by neurons, after which they primarily accumulate in astrocytes, the peri-synaptic glial cell of the central nervous system (31-35). Efficient clearance of these polyamines from the extracellular milieu is thought to be critical in preventing their excessive accumulation and potential toxicity (31, 36). In addition, research suggests that astrocytes not only buffer extracellular polyamines but can also release them to modulate neuronal activity (31, 32, 37). These observations align well with the classical roles of astrocytes, as they perform vital functions at the synapse to buffer extracellular ions and neurotransmitters to maintain synaptic homeostasis and proper circuit function (38-40).

In addition to their key roles in the adult brain, astrocytes play crucial roles in developing and remodeling synaptic circuits by secreting soluble factors to promote synaptogenesis and regulate synaptic strength; and by establishing direct contacts with pre- and post-synaptic elements through their complex arborized morphology (41-51). Through these signaling modalities, astrocytes regulate the balance of excitation and inhibition in the brain (52, 53). On the other hand, neuronal cues such as synaptic activity and adhesion molecule signaling instruct astrocytes' morphological and functional maturation, revealing a rich and bidirectional signaling between astrocytes and neurons that governs brain development (52, 54-60).

Despite the significance of polyamines in synaptic circuit function and homeostasis as well as their well-established accumulation in astrocytes, the exact mechanisms underlying the dynamic polyamine uptake in astrocytes and how this steers astrocyte-neuron communication during development remain largely elusive.

P5B-type ATPases are emerging as a novel class of polyamine transporters (5, 61-65), shedding light on the long-standing mystery of the mammalian polyamine transport system, which has remained elusive despite its critical importance to cellular homeostasis. Among these ATPases, ATP13A2 is the most extensively studied, with well-defined substrate specificity and transport mechanisms (5, 66-71). In contrast, ATP13A3 and ATP13A4 have been implicated in cellular polyamine uptake (61-65), but their precise transport mechanism and substrate specificities are yet to be fully defined, leaving significant gaps in our understanding of their functional roles.

In this study, we identified ATP13A4 as the critical polyamine uptake transporter in astrocytes. Unexpectedly, ATP13A4 function in astrocytes is required both for astrocyte morphogenesis and astrocyte-induced neuronal synaptogenesis, revealing a crucial role for polyamines in astrocyte-synapse signaling. In agreement, the global loss of ATP13A4 function leads to an imbalance between excitatory and inhibitory synaptic connectivity in the developing mouse cerebral cortex. These findings reveal a previously unknown function for polyamine homeostasis in developmental astrocyte-neuron signaling and suggest that its disruption may underlie the neurodevelopmental disorders observed in individuals carrying *ATP13A4* mutations.

2. ATP13A4 is a polyamine transporter regulating polyamine accumulation in astrocytes

P5B-type transport ATPases have recently been described as major determinants of cellular polyamine uptake. To identify the primary transporter responsible for polyamine uptake in astrocytes, we mined human and mouse astrocyte gene expression datasets to identify which P5B-type transport ATPase isoforms are enriched in astrocytes. Among these isoforms, ATP13A4 stands out due to its highly astrocyte-specific expression pattern.

Human *ATP13A4* (*hATP13A4*) mRNA is most abundantly expressed in astrocytes, with notably higher levels in mature *versus* fetal astrocytes (72, 73) (Extended Data Fig. 1a). This suggests a potential developmental regulation of ATP13A4, consistent with its elevated expression in the total brain during late fetal and early postnatal stages (Extended Data Fig. 1b) (74), a period critical for neurodevelopment. Moreover, mouse *Atp13a4* (*msAtp13a4*) mRNA is also highly enriched in astrocytes compared to other brain cell types (75) (Extended Data Fig. 1c) and is actively translated in adult murine astrocytes (76) (Extended Data Fig. 1d). Intriguingly, *msAtp13a4* is one of 825 commonly expressed genes highly enriched in astrocytes across 13 different regions of the central nervous system (CNS) (77) (Extended Data Fig. 1e), suggesting a core function for *msAtp13a4* in astrocytes.

In contrast, other P5B-type ATPases, including ATP13A2, ATP13A3, and ATP13A5, are more prominently or broadly expressed in other CNS cell types (Extended Data Fig. 1a, c). Together, ATP13A4 emerges as an astrocyte-specific isoform in the CNS, underscoring its relevance as a key candidate for mediating polyamine uptake in this cell type.

Next, we experimentally validated the astrocyte-specific *Atp13a4* expression in rodent models. Astrocytes and neurons were isolated from postnatal day 1 (P1) rat cortices (Fig. 1a) in which we confirmed a strong enrichment of rat *Atp13a4* (*rAtp13a4*) mRNA in cortical astrocytes compared to neurons (Fig. 1b). We also verified astrocytic *msAtp13a4* mRNA expression during postnatal cortical development (P7-21) in mice. We performed multiplex RNA fluorescence *in situ* hybridization (FISH) experiments for *Atp13a4* in the brain of *Aldh1L1-eGFP* transgenic mice, in which all astrocytes are labeled with eGFP (Fig. 1c). We found that *msAtp13a4* was enriched within GFP-positive astrocytes at P7, P14, and P21 across different cortical layers (L1, L2/3, L4, and L5) of the mouse V1 visual cortex (Fig. 1d). Our results indicate that rodent astrocytes express the P5B-type transport ATPase *Atp13a4* during the early postnatal period, in line with the astrocyte-specific expression of *hATP13A4* in the developing human brain.

To investigate the subcellular localization of ATP13A4, we first used a HeLa overexpression model where mCherry-labeled *msAtp13a4* predominantly localized to late endo-/lysosomal compartments (Extended Data Fig. 1f), consistent with our previous observations (78). To confirm and extend these findings in a more relevant *in vivo* context, we performed astrocyte-specific *in vivo* proximity biotinylation using a *Lamp1-TurboID* fusion protein (79) to label proteins that are associated with endo-/lysosomal compartments (Extended Data Fig. 2a-h, Fig. 1e-i). Quantitative mass spectrometry confirmed the presence of ATP13A4 in the *Lamp1* BioID fraction, with ATP13A3 also detected at lower levels (Fig. 1i). These findings suggest that ATP13A4 is the predominant P5B-type transport ATPase in astrocytes, primarily localized to endo-/lysosomal compartments.

The precise molecular function of ATP13A4 remains unclear. Although ATP13A4 was implicated in polyamine uptake in breast cancer cells (63), conclusive evidence regarding its polyamine transport function and substrate selectivity is lacking. Therefore, we conducted biochemical studies on purified *hATP13A4* to determine if ATP13A4 is a *bona fide* polyamine transporter. ATP13A4 is a member of the P-type ATPases that use ATP hydrolysis to form an auto-phosphorylated intermediate driving the selective transport of ions, polyamines, or lipids. These transporters cycle between four main conformations (E1, E1P, E2P and E2), providing alternating access to the substrate binding site from the cytosolic (in the E1 state) to extracytosolic side (in the E2P conformation) (Fig. 1j). ATP13A2 is the prototypical P5B-type ATPase, which we previously biochemically characterized as a polyamine transporter (5), a finding later validated at the structural level (66-70). ATP13A4 shares 37.13% sequence identity and 52.69% sequence similarity with ATP13A2, reflecting their structural homology (Extended Data Fig. 3a) and suggesting a conserved polyamine transport function.

Here, we followed a similar procedure as for ATP13A2 to biochemically characterize ATP13A4, and we overexpressed hATP13A4 WT or the catalytically dead p.D486N mutant (which harbors a mutation in the catalytic site required for autophosphorylation) in HEK293T cells or *Saccharomyces cerevisiae* for subsequent purification via affinity-chromatography (Extended Data Fig. 3b-g). A defining feature of P-type ATPases is that substrate binding triggers ATP hydrolysis and, hence, to assess substrate specificity of hATP13A4, we evaluated whether the main polyamine species (putrescine, spermidine and spermine) stimulate ATPase activity and at which apparent affinity. We found that the three polyamines stimulated the ATPase activity of purified hATP13A4 wild-type (WT), but not the transport-deficient mutant p.D486N (Fig. 1k), in a concentration-dependent manner, with the highest apparent affinity observed for spermidine and spermine. These results show that, like the related hATP13A2 isoform (5), spermidine and spermine represent genuine substrates of hATP13A4, in line with a conserved substrate binding site between ATP13A2 and ATP13A4 (Extended Data Fig. 3a). The broader polyamine sensitivity of ATP13A4, reflected in its putrescine-induced ATPase activity not observed for ATP13A2 (5), may be linked to the substitution of D955 in ATP13A2 with N930 in ATP13A4 (Extended Data Fig. 3a), highlighting how subtle structural differences fine-tune substrate specificity.

To determine the auto-phosphorylation activity of hATP13A4, we incubated purified hATP13A4 with radiolabeled [³²P] ATP and observed that, in the absence of polyamines, hATP13A4 spontaneously formed a phosphoenzyme, similar to ATP13A2 (80). This phosphoenzyme was sensitive to hydroxylamine, a hallmark of P-type ATPase auto-phosphorylation on a conserved aspartate residue (Extended Data Fig. 3h) and showed minimal response to ADP (Extended Data Fig. 3i-j). The latter finding suggests that phosphorylated hATP13A4 mainly exists in the E2P state, since only the E1P state can interact with ADP to regenerate ATP (Fig. 1j). We also observed a slow dephosphorylation rate when non-radiolabeled ATP was added in the absence of polyamines suggesting low phosphoenzyme turnover (Extended Data Fig. 3i-l). However, the presence of spermidine or spermine significantly accelerated this dephosphorylation (Extended Data Fig. 3k-l), consistent with the polyamine-induced ATPase activity (Fig. 1k). Corroborating this, putrescine, spermidine, and spermine reduced the steady-state levels of the hATP13A4 phosphoenzyme (Fig. 1l-m, Extended Data Fig. 3m-n). Thus, the polyamines are not required for the auto-phosphorylation of hATP13A4, which takes place in E1, but polyamines promote the dephosphorylation of E2P, the conformation with an open luminal substrate binding site. This suggests that hATP13A4 transports polyamines from the exoplasmic side of the membrane into the cytosol, which mirrors the behavior observed for hATP13A2 (5) (Fig. 1j). Taken together, our results reveal that ATP13A4 acts as a broad-specificity polyamine transporter with the highest apparent affinity to spermine and spermidine, most likely enabling polyamine transport to the cytosol.

Given its prominent expression in astrocytes, we hypothesized that ATP13A4, as a polyamine transporter directing polyamines to the cytosol, might facilitate polyamine uptake into these glial cells, potentially accounting for the so-far unidentified astrocytic polyamine uptake system (81, 82).

To test this possibility, we used two glial cell lines with modulated ATP13A4 expression to assess the uptake of fluorescently labeled BODIPY-polyamines – which are genuine transported substrates of the P5B-type ATPases (61). We first turned to stable neuroglioma H4 cell lines with lentiviral overexpression of hATP13A4 WT or p.D486N (Extended Data Fig. 4a-b) and performed flow cytometry-based BODIPY-polyamine uptake measurements (Extended Data Fig. 4c-e). Compared to H4 control cells expressing the p.D486N mutant or firefly luciferase (FLUC), hATP13A4 WT protein enhances the cellular uptake of BODIPY-labelled putrescine, spermidine,

and spermine (Extended Data Fig. 4c-e). Conversely, lentiviral microRNA-based knockdown of *msAtp13a4* in C8-D1A cells, a mouse astrocytic cell line with endogenous *msAtp13a4* expression, reduced the *msAtp13a4* mRNA levels by 80% (Extended Data Fig. 4f). This significantly decreased BODIPY-polyamine uptake compared to control cells transduced with a microRNA against the *FLUC* gene (mirFLUC), as evidenced by flow cytometry (Extended Data Fig. 4g-i) and confocal microscopy analysis (Extended Data Fig. 4j-m). In *msAtp13a4* knockdown cells, BODIPY-polyamines accumulate within puncta (Extended Data Fig. 4j, l), confirming that, like ATP13A2, ATP13A4 is required for the uptake of exogenous polyamines, which are transported from the late endo-/lysosomal lumen to cytosol (5, 71). To rule out any influence of serum polyamine oxidase activity, we repeated the uptake experiments in a serum-free medium and observed a similar phenotype (Extended Data Fig. 4n-o). In addition, mass spectrometry analysis demonstrated significantly lower endogenous spermidine levels, and a trend towards lower putrescine levels in *msAtp13a4* deficient C8-D1A cells compared to control cells (Extended Data Fig. 4p), further confirming a key role of ATP13A4 in regulating polyamine uptake and homeostasis.

Finally, we confirmed the polyamine uptake role of *Atp13a4* in primary rat astrocytes from P1 rat cortices (Fig. 1i). We silenced *rAtp13a4* expression by more than 90% using short hairpin RNA (shRNA, shAtp13a4) compared to a non-targeting scrambled shRNA (shCtrl) (Fig. 1j). Using confocal microscopy, we found that shAtp13a4 astrocytes displayed significantly reduced uptake of BODIPY-labeled spermidine (Fig. 1k-l). While the uptake of BODIPY-labeled spermine showed a trend toward lower levels in knockdown cells, this difference was not statistically significant (Fig. 1m-n). These findings suggest that *rAtp13a4* plays a key role in mediating spermidine uptake in primary astrocytes, with a potential but less pronounced contribution to spermine uptake.

Altogether, these data established ATP13A4 as a major component of the previously unexplored polyamine uptake system in astrocytes. Based on its late endo-/lysosomal localization and consistent with evidence from the related isoform ATP13A2 (5), our findings suggest that polyamine uptake in astrocytes, similar to the mechanism described in neuroblastoma cells (5), follows a two-step process: initial internalization via endocytosis, followed by transport from the endo-/lysosomal lumen into the cytosol. These results further highlight the critical role of the endo-/lysosomal system in maintaining polyamine homeostasis (83, 84).

3. ATP13A4 knockdown impairs astrocyte morphogenesis

Bidirectional signaling between astrocytes and neurons regulates the development of astrocytes and synapses (54, 85). We wondered whether this important intercellular signaling involves ATP13A4-mediated polyamine regulation in astrocytes. First, we investigated whether ATP13A4 is critical in neuronal contact-dependent astrocyte morphogenesis. Cortical grey matter astrocytes (protoplasmic astrocytes) are highly arborized cells that develop their unique morphology during the first three postnatal weeks (86-89). Astrocyte morphogenesis occurs concurrently with neuronal synapse formation (45, 56, 86, 90-92). Previous studies showed that astrocytes gain complex morphology guided by neuronal cues such as sensory experience-mediated synaptic activity and synaptic cell adhesion molecules (56-60). Importantly, proper astrocyte morphogenesis regulates astrocyte maturation and is essential for correct synaptic wiring and homeostasis within the brain (38, 93).

Since we identified ATP13A4 as the primary polyamine transporter in astrocytes, we tested how loss of this protein impacts neuronal-contact mediated astrocyte morphogenesis *in vitro*. To explore this, we used a well-established cortical astrocyte-neuron co-culture assay (56, 94, 95) (Fig. 2a), which takes advantage of the fact that astrocytes gain a complex arborization morphology

in vitro, visualized by GFP expression, only when cultured on top of neurons, mimicking what happens *in vivo*. For these assays, we independently isolated astrocytes and neurons from P1 rat cortices and specifically silenced *rAtp13a4* expression in astrocytes (Fig. 1j). After 48h of co-culture with WT neurons, the morphological complexity of GFP-labeled control (shCtrl) or *Atp13a4* silenced (sh*Atp13a4*) astrocytes was assessed by Sholl analysis (96), which measures the number of intersections at defined concentric radii, with a higher count indicating a more complex arborization pattern. When co-cultured with neurons, astrocytes transfected with shCtrl displayed the typical complex arborization morphology (Fig. 2b-c). In contrast, sh*Atp13a4* astrocytes displayed a pronounced reduction in morphological complexity (Fig. 2b-c). To validate the specificity of *Atp13a4* loss, we performed rescue experiments using an shRNA-resistant ms*Atp13a4* construct tagged with mCherry (mCherry-ms*Atp13a4*; Fig. 2d-e). Co-expression of mCherry-ms*Atp13a4* with sh*Atp13a4* resulted in a partial rescue of astrocyte morphogenesis, as demonstrated by a significant increase in overall astrocyte complexity (Fig. 2d-e). Sholl analysis showed that astrocytes co-expressing sh*Atp13a4* and mCherry-ms*Atp13a4* were not significantly different from astrocytes expressing shCtrl and mCherry-ms*Atp13a4*, but they remained statistically distinct from shCtrl astrocytes (Fig. 2e). Overexpression of mCherry-ms*Atp13a4* in shCtrl astrocytes did not further enhance complexity (Fig. 2e). These findings suggest that the morphological defects observed in sh*Atp13a4* astrocytes are largely attributable to the loss of *Atp13a4*, though the incomplete rescue points to a possible impact of the mCherry-tag on *Atp13a4* activity and/or the involvement of additional factors influencing astrocyte morphogenesis.

Next, we wondered if the *Atp13a4* function controls astrocyte morphology through a mechanism involving dynamic neuron signaling. To test this, we fixed neurons with methanol before astrocyte co-culture, which keeps the neuronal structure and adhesion signals intact while eliminating any synaptic activity of neurons. We found that loss of astrocytic *Atp13a4* still resulted in a diminished astrocyte morphology when cultured on methanol-fixed neurons (Fig. 2f-g), indicating that synaptic signaling is not required for the phenotype to manifest.

Besides *Atp13a4* loss, also a 24 h treatment with spermidine or spermine led to a dose-dependent reduction in the arborization of shCtrl astrocytes in the co-culture, with increasing concentrations progressively impairing astrocyte complexity (Extended Data Fig. 5a-d). In contrast, sh*Atp13a4*-transfected astrocytes showed no further reduction in arborization upon polyamine treatment, likely reflecting their impaired ability to take up extracellular polyamines. Interestingly, a similar reduction in complexity was observed when shCtrl astrocytes were pre-treated with polyamines for 24 h before co-culture (Extended Data Fig. 5e-h). This pre-treatment experiment confirms that the observed effects are intrinsic to astrocytes, as the polyamine exposure occurred before any interaction with neurons.

Finally, we evaluated whether *Atp13a4* function is required for cortical astrocyte morphogenesis *in vivo* and turned to postnatal astrocyte labeling by electroporation (PALE) (56, 94, 95) (Fig. 2h). For this approach, the previously described shRNAs targeting mouse/rat *Atp13a4* (sh*Atp13a4*) and a scrambled control (shCtrl; Fig. 1j) were cloned into a PiggyBac transposon system expressing mCherry-CAAX. The shRNA plasmids were then electroporated into radial glial cells in the subventricular zone at P0, leading to selective knockdown of *msAtp13a4* in a subset of cortical astrocytes. Analysis of the knockdown astrocytes revealed a striking reduction in overall territory volume compared to control astrocytes (Fig. 2i-j). Taken together, these findings show an important role for ATP13A4-mediated polyamine homeostasis in astrocyte morphogenesis during postnatal development.

4. ATP13A4 loss enhances the excitatory synaptogenic signaling by astrocytes

While neuronal cues guide astrocyte morphogenesis, astrocytes promote the assembly and maturation of excitatory and inhibitory synaptic circuits by secreting synapse-inducing factors (42-51). Polyamines have been shown to regulate protein synthesis and secretion in other cells (97-102). Thus, we wondered how impairing polyamine transport in astrocytes impacts the synaptogenic properties of these cells through secreted signals. To address this question, we used purified cortical neuron cultures that were treated with an astrocyte-conditioned media (ACM). Many previous studies have shown that ACM strongly promotes synapse formation between neurons, *in vitro* (44, 50, 51, 103-105). We treated primary WT neurons with either i) ACM derived from astrocytes transfected with control shRNA (shCtrl ACM), ii) ACM from astrocytes with *rAtp13a4* knockdown (shAtp13a4 ACM), or iii) non-conditioned medium (no ACM) (Fig. 3a). We first assessed the role of astrocytic *rAtp13a4* in neuronal dendrite morphogenesis by quantifying neuronal morphology after incubation with the different media. Consistent with previous literature (44), treatment with ACM significantly increased the length of dendritic processes compared to non-conditioned medium (Extended Data Fig. 6a-b). However, there were no significant differences of neurite elongation between neurons treated with shCtrl ACM *versus* shAtp13a4 ACM (Extended Data Fig. 6a-b) suggesting that ATP13A4 is not essential for promoting dendritic growth through astrocyte-secreted factors.

Next, we investigated the effect of ACM on synaptogenesis by labeling excitatory synapses with the presynaptic marker Bassoon and the postsynaptic marker Homer1. Neurons treated with shCtrl ACM significantly increased excitatory synaptogenesis, as expected (103, 104). Notably, neurons treated with ACM from *rAtp13a4* knockdown astrocytes exhibited a significant increase in the number of excitatory synapses in our cultures – identified by the close apposition of Bassoon and Homer1 puncta (Fig. 3a-c) – without changes in the total number of individual Bassoon or Homer1 puncta (Extended Data Fig. 6c-d). Interestingly, loss of *Atp13a4* in ACM resulted in significantly more excitatory synaptic colocalizations than shCtrl treated neurons. Given that *Atp13a4* is important for polyamine uptake by astrocytes (Fig. 1g-j), we next investigated whether astrocytic *Atp13a4* knockdown impacts extracellular polyamine levels. We performed mass spectrometry analysis of ACM and found significantly elevated endogenous spermidine levels in ACM from *rAtp13a4* knockdown astrocytes compared to control ACM (Fig. 3d), while levels of ornithine, putrescine and spermine levels remained unchanged (Extended Data Fig. 6e-g). Furthermore, treatment of purified neurons with spermidine significantly increased excitatory synapse numbers, phenocopying the effects of shAtp13a4 ACM, whereas spermine has a weaker effect (Fig. 3e-f), suggesting that extracellular spermidine at a sufficiently high concentration promotes excitatory synaptogenesis *in vitro*. The 10 nM polyamine concentration (106) was selected as the lowest concentration eliciting a significant effect on astrocyte morphology (Extended Data Fig. 5a-d), minimizing potential off-target or toxicity effects due to too high concentrations.

To further study the impact of ATP13A4 deficiency on excitatory synapse development *in vivo*, we turned to a commercial, CRISPR-Cas9-generated transgenic knockout mouse line. This model carries a deletion of exons 3-5 resulting in a premature stop codon at position 86 (p.A85*) (Fig. 3g). We confirmed genomic editing and absence of exon 3-5 in *Atp13a4* KO mice via PCR (Fig. 3h). Next, we analyzed the number of excitatory synapses – marked by the apparent colocalization of presynaptic Bassoon and postsynaptic PSD95 – in the V1 cortex of P21 *Atp13a4* KO mice. We found a significant increase in excitatory synapse numbers (~25%) in *Atp13a4* KO mice compared to WT littermates (Fig. 3i-j). To assess whether the altered synapse numbers in the V1 of *Atp13a4* KO mice affect synaptic function, we performed whole-cell patch-clamp

recordings of miniature excitatory postsynaptic currents (mEPSCs) and miniature inhibitory postsynaptic currents (mIPSCs) in layer 2/3 pyramidal neurons from acute brain slices of 8-week-old *Atp13a4* KO and WT mice (Fig. 3k-m, Extended Data Fig. 6j-l). *Atp13a4* KO neurons exhibited a significant increase (~25%) in mEPSC frequency and a leftward shift in the cumulative distribution of mEPSC inter-event intervals compared to WT neurons (Fig. 3l), while mean mEPSC amplitudes were similar (Fig. 3m). Conversely, we did not observe any change in either the amplitude or the frequency of mIPSCs (Extended Data Fig. 6k-l).

Collectively, our results show that loss of *Atp13a4* disrupts extracellular spermidine uptake in astrocytes leading to excessive excitatory synaptogenesis both *in vitro* and *in vivo*, indicating a regulatory role for astrocytic *Atp13a4* in synaptogenesis and brain wiring.

5. Human ATP13A4 loss-of-function variants are linked to neurodevelopmental disorders

Human *ATP13A4* gene mutations have been implicated in neurodevelopmental disorders, such as schizophrenia (as one of the ten genes affected by the 3q29 deletion) (107), epileptic encephalopathies (associated with duplication at 3q28-q29) (108), or specific language impairment (chromosomal inversion disrupting the *ATP13A4* gene) (109). A heterozygous *ATP13A4* p.E646D variant was identified in three individuals with childhood apraxia of speech (110). Additionally, an autism susceptibility locus was mapped near *ATP13A4* on chromosome 3q25-27, and further sequencing revealed heterozygous p.E646D and p.A356V variants in patients (109, 111). Based on data from gnomAD (the Genome Aggregation Database), the allele frequencies for the p.A356V and p.E646D variants are 0.00007992 and 0.1018, respectively. Both variants affect residues that are highly conserved across diverse species (Extended Data Fig. 7a-b). Here, we demonstrated for the first time that the purified p.E646D and p.A356V *ATP13A4* variants present loss-of-function marked by reduced phospho-enzyme levels, polyamine-induced ATPase and/or dephosphorylation activities (Fig. 4a-c; Extended Data Fig. 7c-h), which explain the significantly impaired uptake of BODIPY-labeled polyamines in H4 cells expressing these variants (Extended Data Fig. 4c-e, n).

Via *GeneMatcher* (112), we identified additional candidate pathogenic *ATP13A4* variants. First, a novel homozygous p.E276K variant in *ATP13A4* (Extended Data Fig. 7a-b), with an allele frequency of 0.000004337 (gnomAD), was identified in a patient presenting with intellectual disability, which we here functionally characterized as a complete loss-of-function variant. Indeed, we observed similar mRNA expression in HEK293T cells overexpressing the p.E276K variant as compared to WT (Fig. 4d); however, no detectable p.E276K protein was formed (Fig. 4e). Second, a 15-year-old female patient diagnosed with generalized epilepsy and a history of eyelid fluttering presented a heterozygous deletion that spans exons 19-25 of *ATP13A4* disrupting the catalytically important transmembrane and auto-phosphorylation domains (Extended Data Fig. 7b), most likely resulting in loss-of-function. No other genetic causes or candidate gene variants were identified. Of interest, a potential role of *ATP13A4* dysregulation in epilepsy pathophysiology is further reinforced by human RNA-seq data revealing that *ATP13A4* is significantly downregulated in astrocytes from patients with temporal lobe epilepsy as compared to controls (Extended Data Fig. 7i) (113). Together, our findings support a potential role for *ATP13A4* variants in a spectrum of neurodevelopmental disorders, such as seizure susceptibility, intellectual disability, specific language impairment and autism, possibly through an impact on extracellular polyamine clearance and elevated excitatory synaptogenesis.

5.1. Discussion

Polyamines are emerging as critical players in astrocyte-neuron communication, with significant implications for brain development and neurological diseases. Beyond their supportive roles in cellular processes ranging from transcription to protein synthesis and membrane stability, polyamines are also proposed to modulate synaptic plasticity and neurotransmission (114). Whereas polyamine synthesis may predominantly take place in neurons, astrocytes represent the main storage site (31). Here, we established ATP13A4 as a major polyamine transporter in astrocytes controlling cellular polyamine uptake from within the lysosomes, which most likely involves endocytosis followed by lysosomal polyamine export to the cytosol, similar to ATP13A2 in other cell types (5). ATP13A4-dependent polyamine uptake may work in conjunction with the previously characterized polyamine transporter SLC18B1 (VPAT) mediating intracellular vesicular storage and secretion of polyamines in different cell types of the CNS, including astrocytes (115, 116). Also, ATP13A2 is expressed across CNS cell types, including astrocytes, but unlike ATP13A4, ATP13A2 is linked to neuroinflammation and neurodegeneration (117, 118), suggesting that both polyamine transporters may exert distinct but complementary neuroprotective roles. Here, we demonstrated that ATP13A4 plays a dual role in regulating both intracellular and extracellular polyamine levels, which in turn determines i) astrocyte arborization, and ii) neuronal excitatory synaptogenesis.

6. ATP13A4 and spermidine regulate astrocyte arborization and morphology

Increasing concentrations of exogenous polyamines impair astrocyte arborization of WT astrocytes, which may be a result of inadequate extracellular polyamine clearance in combination with endo/lysosomal accumulation of polyamines and/or a toxic polyamine accumulation downstream of ATP13A4 activity. Since *Atp13a4* deficiency presents a similar phenotype, it is more likely that the accumulation of extracellular or endocytosed polyamines negatively regulate astrocyte arborization, suggesting that the ATP13A4 transport capacity may become inadequate at increasing extracellular polyamine concentrations. This highlights the need for a tight regulation of extracellular polyamine levels for maintaining proper astrocyte morphology.

7. Astrocytic ATP13A4 regulates neuronal excitatory synaptogenesis by controlling extracellular spermidine

The ACM from *Atp13a4* knockdown astrocytes contains elevated spermidine levels and enhances neuronal excitatory synaptogenesis without affecting neuronal morphology. The increase in synapse formation is recapitulated by exogenous spermidine supplementation to the neurons, suggesting that extracellular spermidine levels play a key role in this process. These findings establish a link between ATP13A4-mediated polyamine uptake in astrocytes and neuronal connectivity (Fig. 4f) and support the growing recognition of astrocytes as active participants in synaptogenesis and circuit formation (42, 92). By positioning polyamines as key mediators of these processes, our study highlights a previously unappreciated mechanism through which astrocytes influence neuronal network development.

Astrocytes act as gatekeepers of neuronal excitability by regulating neurotransmitter levels, maintaining extracellular ion balance, and modulating synaptic transmission (42, 45, 53, 58, 92, 119). Their dysfunction can lead to increased excitability and contribute to the development of epilepsy, highlighting their critical role in brain homeostasis (119). The clearance of extracellular

spermidine via astrocytic ATP13A4 expands our understanding of the astrocyte-neuron communication. To our knowledge, this is the first demonstration that a polyamine can act as a synaptogenic molecule, similar to other well-characterized synaptogenic factors released by astrocytes – such as thrombospondins (46, 120), hevin (121), and cholesterol (122). While traditional astrocyte-derived synaptogenic factors often act through specific neuronal receptors or scaffolding proteins (42, 85), the precise pathway and/or receptor through which spermidine enhances excitatory synapse formation remains unknown, but several possibilities exist. Polyamines may regulate synaptic ion channels such as the N-methyl-D-aspartate receptors (NMDARs), which contains extracellular polyamine binding sites (106), or inward rectifier K⁺ channels that are regulated by intracellular polyamines. However, ion channels display similar or higher sensitivity for spermine over spermidine (123-125), making them less likely candidates for mediating a mainly spermidine-dependent effect on synaptogenesis. Spermidine might also interact with astrocyte-derived factors like glypicans (126), which present a high polyamine affinity and are involved in synaptic maturation and refinement (48), but since the spermidine-effect can be reproduced in the absence of astrocytes, neuronal glypicans may instead be involved (127). Alternatively, spermidine might stimulate eIF5A hypusination, a spermidine-dependent post-translational modification (128), which may support local translation of specific mRNAs within the synaptic environment, such as scaffolding proteins and cytoskeletal regulators that are critical for synaptogenesis and synaptic plasticity (129, 130). Future studies dissecting these pathways will clarify how spermidine contributes to synapse development, potentially leading to novel therapeutic strategies for modulating synaptic connectivity in neurodevelopmental and neurodegenerative disorders.

8. ATP13A4 loss-of-function and polyamine dysregulation in neurodevelopmental disorders

Collectively, our study positions ATP13A4 as an essential regulator of extracellular spermidine levels, enabling astrocytes to maintain neuronal excitability within physiological limits. This role aligns with the temporal expression pattern of ATP13A4, which peaks during early postnatal brain development, a critical period for synaptic refinement and the establishment of functional neural networks. Conversely, disturbances in polyamine metabolism are often linked to neurodevelopmental disorders (25, 29, 30), and alterations in polyamine levels (131) as well as astrocyte dysfunction (132, 133) have been described in schizophrenia and epilepsy. Here, we identified novel loss-of-function variants in hATP13A4 associated with intellectual disability and epilepsy in two unrelated cases and demonstrated that the autism-associated hATP13A4 variants p.A356V and p.E646D disturb polyamine transport, further highlighting the role of a disturbed polyamine homeostasis in neurodevelopmental disorders. By impacting polyamine uptake and distribution, *Atp13a4* loss disturbs synaptic balance between excitatory and inhibitory synapses. In *Atp13a4* KO mice, this is associated with an increased frequency of excitatory postsynaptic currents causing synaptic hyperactivity, which may also underlie the neurodevelopmental phenotypes observed in ATP13A4 mutation carriers. Indeed, astrocytes are the primary ATP13A4-expressing cells within the brain, regulating extracellular spermidine and synaptogenesis. While non-astrocytic effects in our *Atp13a4* KO mouse cannot be excluded, this model remains valuable for studying ATP13A4's role in synapse development and its relevance to patient loss-of-function.

In conclusion, our work establishes the polyamine transporter ATP13A4 as a critical mediator of polyamine-driven astrocyte-neuron communication and neuronal excitatory synaptogenesis, and positions ATP13A4 as a novel candidate gene and/or potential therapeutic target for various neurodevelopmental disorders, including epilepsy.

9. References

1. Pegg AE. Functions of Polyamines in Mammals. *J Biol Chem.* 2016;291(29):14904-12.
2. Hofer SJ, Daskalaki I, Bergmann M, Friscic J, Zimmermann A, Mueller MI, et al. Spermidine is essential for fasting-mediated autophagy and longevity. *Nat Cell Biol.* 2024;26(9):1571-84.
3. Hofer SJ, Simon AK, Bergmann M, Eisenberg T, Kroemer G, Madeo F. Mechanisms of spermidine-induced autophagy and geroprotection. *Nat Aging.* 2022;2(12):1112-29.
4. Holbert CE, Cullen MT, Casero RA, Jr., Stewart TM. Polyamines in cancer: integrating organismal metabolism and antitumour immunity. *Nat Rev Cancer.* 2022;22(8):467-80.
5. van Veen S, Martin S, Van den Haute C, Benoy V, Lyons J, Vanhoutte R, et al. ATP13A2 deficiency disrupts lysosomal polyamine export. *Nature.* 2020;578(7795):419-24.
6. Vrijssen S, Houdou M, Cascalho A, Eggermont J, Vangheluwe P. Polyamines in Parkinson's Disease: Balancing Between Neurotoxicity and Neuroprotection. *Annu Rev Biochem.* 2023;92:435-64.
7. Madeo F, Eisenberg T, Pietrocola F, Kroemer G. Spermidine in health and disease. *Science.* 2018;359(6374).
8. Akinyele O, Munir A, Johnson MA, Perez MS, Gao Y, Foley JR, et al. Impaired polyamine metabolism causes behavioral and neuroanatomical defects in a mouse model of Snyder-Robinson syndrome. *Dis Model Mech.* 2024;17(6).
9. Zahedi K, Barone S, Soleimani M. Polyamines and Their Metabolism: From the Maintenance of Physiological Homeostasis to the Mediation of Disease. *Med Sci (Basel).* 2022;10(3).
10. Zahedi K, Brooks M, Barone S, Rahmati N, Murray Stewart T, Dunworth M, et al. Ablation of polyamine catabolic enzymes provokes Purkinje cell damage, neuroinflammation, and severe ataxia. *J Neuroinflammation.* 2020;17(1):301.
11. Cervelli M, Aversa M, Vergani L, Pedrazzi M, Amato S, Fiorucci C, et al. The Involvement of Polyamines Catabolism in the Crosstalk between Neurons and Astrocytes in Neurodegeneration. *Biomedicines.* 2022;10(7).
12. Polis B, Karasik D, Samson AO. Alzheimer's disease as a chronic maladaptive polyamine stress response. *Aging (Albany NY).* 2021;13(7):10770-95.
13. Slotkin TA, Bartolome J. Role of ornithine decarboxylase and the polyamines in nervous system development: a review. *Brain Res Bull.* 1986;17(3):307-20.
14. Rozov A, Zakharova Y, Vazetdinova A, Valiullina-Rakhmatullina F. The Role of Polyamine-Dependent Facilitation of Calcium Permeable AMPARs in Short-Term Synaptic Enhancement. *Front Cell Neurosci.* 2018;12:345.
15. Fleidervish IA, Libman L, Katz E, Gutnick MJ. Endogenous polyamines regulate cortical neuronal excitability by blocking voltage-gated Na⁺ channels. *Proc Natl Acad Sci U S A.* 2008;105(48):18994-9.
16. Burnashev N. Dynamic modulation of AMPA receptor-mediated synaptic transmission by polyamines in principal neurons. Focus on "polyamines modulate AMPA receptor-dependent synaptic response in immature layer v pyramidal neurons". *J Neurophysiol.* 2005;93(5):2371.
17. Baroli G, Sanchez JR, Agostinelli E, Mariottini P, Cervelli M. Polyamines: The possible missing link between mental disorders and epilepsy (Review). *Int J Mol Med.* 2020;45(1):3-9.
18. Arthur R, Jamwal S, Kumar P. A review on polyamines as promising next-generation neuroprotective and anti-aging therapy. *Eur J Pharmacol.* 2024;978:176804.
19. Dhara M, Matta JA, Lei M, Knowland D, Yu H, Gu S, et al. Polyamine regulation of ion channel assembly and implications for nicotinic acetylcholine receptor pharmacology. *Nat Commun.* 2020;11(1):2799.
20. Kim GH, Komotar RJ, McCullough-Hicks ME, Otten ML, Starke RM, Kellner CP, et al. The role of polyamine metabolism in neuronal injury following cerebral ischemia. *Can J Neurol Sci.* 2009;36(1):14-9.
21. Liu J, Yu Z, Maimaiti B, Meng Q, Meng H. The Potential Role of Polyamines in Epilepsy and Epilepsy-Related Pathophysiological Changes. *Biomolecules.* 2022;12(11).
22. Cervelli M, Bellavia G, D'Amelio M, Cavallucci V, Moreno S, Berger J, et al. A New Transgenic Mouse Model for Studying the Neurotoxicity of Spermine Oxidase Dosage in the Response to Excitotoxic Injury. *PLoS One.* 2013;8(6):e64810.
23. Leonetti A, Baroli G, Fratini E, Pietropaoli S, Marcoli M, Mariottini P, et al. Epileptic seizures and oxidative stress in a mouse model over-expressing spermine oxidase. *Amino Acids.* 2020;52(2):129-39.
24. Marcoli M, Cervetto C, Amato S, Fiorucci C, Maura G, Mariottini P, et al. Transgenic Mouse Overexpressing Spermine Oxidase in Cerebrocortical Neurons: Astrocyte Dysfunction and Susceptibility to Epileptic Seizures. *Biomolecules.* 2022;12(2).
25. Bachmann AS, VanSickle EA, Michael J, Vipond M, Bupp CP. Bachmann-Bupp syndrome and treatment. *Dev Med Child Neurol.* 2024;66(4):445-55.
26. Leung M, Sanchez-Castillo M, Belnap N, Naymik M, Bonfitto A, Sloan J, et al. Snyder-Robinson syndrome presenting with learning disability, epilepsy, and osteoporosis: a novel SMS gene variant. *Rare.* 2024;2.
27. Wu B, Liu S. Structural Insights into the Mechanisms Underlying Polyaminopathies. *Int J Mol Sci.* 2024;25(12).

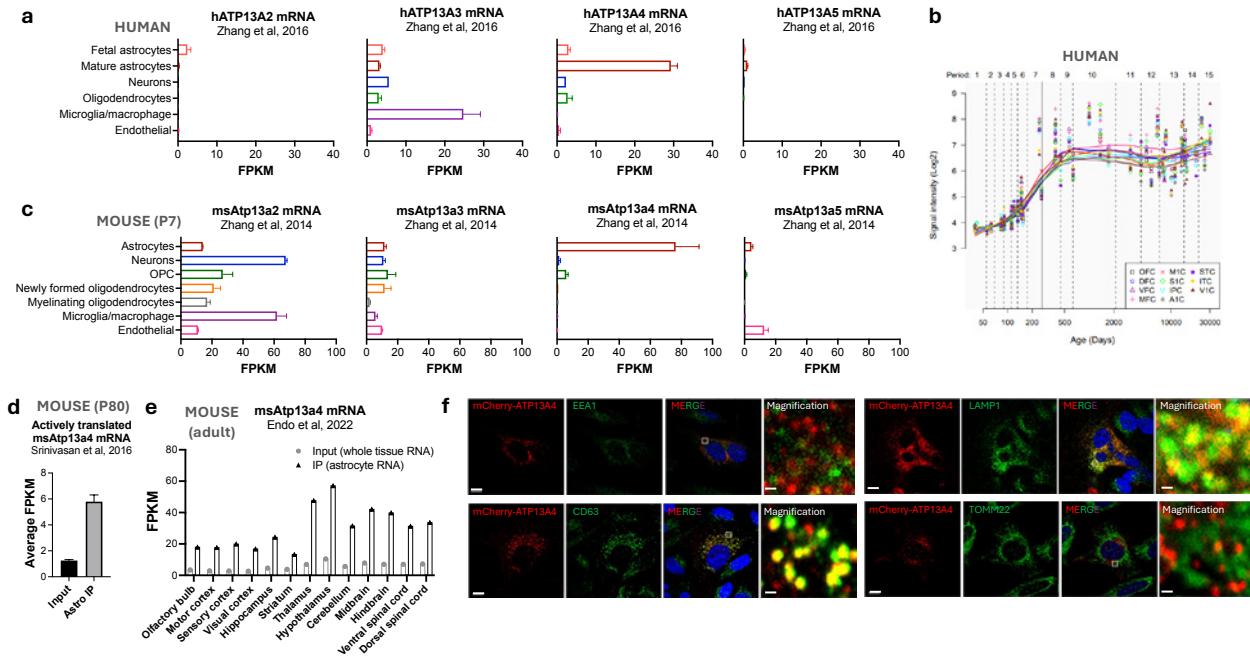
28. Alayoubi AM, Iqbal M, Aman H, Hashmi JA, Alayadhi L, Al-Regaiey K, et al. Loss-of-function variant in spermidine/spermine N1-acetyl transferase like 1 (SATL1) gene as an underlying cause of autism spectrum disorder. *Sci Rep*. 2024;14(1):5765.
29. Rodan LH, Anyane-Yeboa K, Chong K, Klein Wassink-Ruiter JS, Wilson A, Smith L, et al. Gain-of-function variants in the ODC1 gene cause a syndromic neurodevelopmental disorder associated with macrocephaly, alopecia, dysmorphic features, and neuroimaging abnormalities. *Am J Med Genet A*. 2018;176(12):2554-60.
30. Cason AL, Ikeguchi Y, Skinner C, Wood TC, Holden KR, Lubs HA, et al. X-linked spermine synthase gene (SMS) defect: the first polyamine deficiency syndrome. *Eur J Hum Genet*. 2003;11(12):937-44.
31. Skatchkov SN, Woodbury-Farina MA, Eaton M. The role of glia in stress: polyamines and brain disorders. *Psychiatr Clin North Am*. 2014;37(4):653-78.
32. Laube G, Veh RW. Astrocytes, not neurons, show most prominent staining for spermidine/spermine-like immunoreactivity in adult rat brain. *Glia*. 1997;19(2):171-9.
33. Krauss M, Langnaese K, Richter K, Brunk I, Wieske M, Ahnert-Hilger G, et al. Spermidine synthase is prominently expressed in the striatal patch compartment and in putative interneurons of the matrix compartment. *J Neurochem*. 2006;97(1):174-89.
34. Krauss M, Weiss T, Langnaese K, Richter K, Kowski A, Veh RW, et al. Cellular and subcellular rat brain spermidine synthase expression patterns suggest region-specific roles for polyamines, including cerebellar pre-synaptic function. *J Neurochem*. 2007;103(2):679-93.
35. Bernstein HG, Muller M. The cellular localization of the L-ornithine decarboxylase/polyamine system in normal and diseased central nervous systems. *Prog Neurobiol*. 1999;57(5):485-505.
36. Murray Stewart T, Dunston TT, Woster PM, Casero RA, Jr. Polyamine catabolism and oxidative damage. *J Biol Chem*. 2018;293(48):18736-45.
37. Benedikt J, Malpica-Nieves CJ, Rivera Y, Mendez-Gonzalez M, Nichols CG, Veh RW, et al. The Polyamine Spermine Potentiates the Propagation of Negatively Charged Molecules through the Astrocytic Syncytium. *Biomolecules*. 2022;12(12).
38. Vivi E, Di Benedetto B. Brain stars take the lead during critical periods of early postnatal brain development: relevance of astrocytes in health and mental disorders. *Mol Psychiatry*. 2024;29(9):2821-33.
39. Mahmoud S, Gharagozloo M, Simard C, Gris D. Astrocytes Maintain Glutamate Homeostasis in the CNS by Controlling the Balance between Glutamate Uptake and Release. *Cells*. 2019;8(2).
40. Walz W. Role of astrocytes in the clearance of excess extracellular potassium. *Neurochem Int*. 2000;36(4-5):291-300.
41. Stogsdill JA, Eroglu C. The interplay between neurons and glia in synapse development and plasticity. *Curr Opin Neurobiol*. 2017;42:1-8.
42. Baldwin KT, Eroglu C. Molecular mechanisms of astrocyte-induced synaptogenesis. *Curr Opin Neurobiol*. 2017;45:113-20.
43. Bosworth AP, Allen NJ. The diverse actions of astrocytes during synaptic development. *Curr Opin Neurobiol*. 2017;47:38-43.
44. Irala D, Wang S, Sakers K, Nagendren L, Ulloa Severino FP, Bindu DS, et al. Astrocyte-secreted neurocan controls inhibitory synapse formation and function. *Neuron*. 2024;112(10):1657-75 e10.
45. Tan CX, Burrus Lane CJ, Eroglu C. Role of astrocytes in synapse formation and maturation. *Curr Top Dev Biol*. 2021;142:371-407.
46. Christopherson KS, Ullian EM, Stokes CC, Mallowney CE, Hell JW, Agah A, et al. Thrombospondins are astrocyte-secreted proteins that promote CNS synaptogenesis. *Cell*. 2005;120(3):421-33.
47. Kucukdereli H, Allen NJ, Lee AT, Feng A, Ozlu MI, Conatser LM, et al. Control of excitatory CNS synaptogenesis by astrocyte-secreted proteins Hevin and SPARC. *Proc Natl Acad Sci U S A*. 2011;108(32):E440-9.
48. Allen NJ, Bennett ML, Foo LC, Wang GX, Chakraborty C, Smith SJ, et al. Astrocyte glypicans 4 and 6 promote formation of excitatory synapses via GluA1 AMPA receptors. *Nature*. 2012;486(7403):410-4.
49. Blanco-Suarez E, Liu TF, Kopelevich A, Allen NJ. Astrocyte-Secreted Chordin-like 1 Drives Synapse Maturation and Limits Plasticity by Increasing Synaptic GluA2 AMPA Receptors. *Neuron*. 2018;100(5):1116-32 e13.
50. Elmariah SB, Oh EJ, Hughes EG, Balice-Gordon RJ. Astrocytes regulate inhibitory synapse formation via Trk-mediated modulation of postsynaptic GABAA receptors. *J Neurosci*. 2005;25(14):3638-50.
51. Hughes EG, Elmariah SB, Balice-Gordon RJ. Astrocyte secreted proteins selectively increase hippocampal GABAergic axon length, branching, and synaptogenesis. *Mol Cell Neurosci*. 2010;43(1):136-45.
52. Eroglu C, Barres BA. Regulation of synaptic connectivity by glia. *Nature*. 2010;468(7321):223-31.
53. Chung WS, Baldwin KT, Allen NJ. Astrocyte Regulation of Synapse Formation, Maturation, and Elimination. *Cold Spring Harb Perspect Biol*. 2024;16(8).
54. Allen NJ, Eroglu C. Cell Biology of Astrocyte-Synapse Interactions. *Neuron*. 2017;96(3):697-708.
55. Saint-Martin M, Goda Y. Astrocyte-synapse interactions and cell adhesion molecules. *FEBS J*. 2023;290(14):3512-26.

56. Stogsdill JA, Ramirez J, Liu D, Kim YH, Baldwin KT, Enustun E, et al. Astrocytic neurotrophins control astrocyte morphogenesis and synaptogenesis. *Nature*. 2017;551(7679):192-7.
57. Lanjakornsiripan D, Pior BJ, Kawaguchi D, Furutachi S, Tahara T, Katsuyama Y, et al. Layer-specific morphological and molecular differences in neocortical astrocytes and their dependence on neuronal layers. *Nat Commun*. 2018;9(1):1623.
58. Chung WS, Allen NJ, Eroglu C. Astrocytes Control Synapse Formation, Function, and Elimination. *Cold Spring Harb Perspect Biol*. 2015;7(9):a020370.
59. Bernardinelli Y, Randall J, Janett E, Nikonenko I, Konig S, Jones EV, et al. Activity-dependent structural plasticity of perisynaptic astrocytic domains promotes excitatory synapse stability. *Curr Biol*. 2014;24(15):1679-88.
60. Schmidt S, Gull S, Herrmann KH, Boehme M, Irintchev A, Urbach A, et al. Experience-dependent structural plasticity in the adult brain: How the learning brain grows. *Neuroimage*. 2021;225:117502.
61. Houdou M, Jacobs N, Coene J, Azfar M, Vanhoutte R, Van den Haute C, et al. Novel Green Fluorescent Polyamines to Analyze ATP13A2 and ATP13A3 Activity in the Mammalian Polyamine Transport System. *Biomolecules*. 2023;13(2).
62. Liu B, Azfar M, Legchenko E, West JA, Martin S, Van den Haute C, et al. ATP13A3 variants promote pulmonary arterial hypertension by disrupting polyamine transport. *Cardiovasc Res*. 2024;120(7):756-68.
63. van Veen S, Kourti A, Ausloos E, Van Asselberghs J, Van den Haute C, Baekelandt V, et al. ATP13A4 Upregulation Drives the Elevated Polyamine Transport System in the Breast Cancer Cell Line MCF7. *Biomolecules*. 2023;13(6).
64. Hamouda NN, Van den Haute C, Vanhoutte R, Sannerud R, Azfar M, Mayer R, et al. ATP13A3 is a major component of the enigmatic mammalian polyamine transport system. *J Biol Chem*. 2021;296:100182.
65. Sekhar V, Andl T, Phanstiel O. ATP13A3 facilitates polyamine transport in human pancreatic cancer cells. *Sci Rep*. 2022;12(1):4045.
66. Chen X, Zhou M, Zhang S, Yin J, Zhang P, Xuan X, et al. Cryo-EM structures and transport mechanism of human P5B type ATPase ATP13A2. *Cell Discov*. 2021;7(1):106.
67. Mu J, Xue C, Fu L, Yu Z, Nie M, Wu M, et al. Conformational cycle of human polyamine transporter ATP13A2. *Nat Commun*. 2023;14(1):1978.
68. Sim SI, von Bulow S, Hummer G, Park E. Structural basis of polyamine transport by human ATP13A2 (PARK9). *Mol Cell*. 2021;81(22):4635-49 e8.
69. Tillinghast J, Drury S, Bowser D, Benn A, Lee KPK. Structural mechanisms for gating and ion selectivity of the human polyamine transporter ATP13A2. *Mol Cell*. 2021;81(22):4650-62 e4.
70. Tomita A, Daiho T, Kusakizako T, Yamashita K, Ogasawara S, Murata T, et al. Cryo-EM reveals mechanistic insights into lipid-facilitated polyamine export by human ATP13A2. *Mol Cell*. 2021;81(23):4799-809 e5.
71. Van Veen S, Martin S, Schuermans M, Vangheluwe P. Polyamine Transport Assay Using Reconstituted Yeast Membranes. *Bio Protoc*. 2021;11(2):e3888.
72. Zhang Y, Sloan SA, Clarke LE, Caneda C, Plaza CA, Blumenthal PD, et al. Purification and Characterization of Progenitor and Mature Human Astrocytes Reveals Transcriptional and Functional Differences with Mouse. *Neuron*. 2016;89(1):37-53.
73. Nowakowski TJ, Bhaduri A, Pollen AA, Alvarado B, Mostajo-Radji MA, Di Lullo E, et al. Spatiotemporal gene expression trajectories reveal developmental hierarchies of the human cortex. *Science*. 2017;358(6368):1318-23.
74. Li M, Santpere G, Imamura Kawasawa Y, Evgrafov OV, Gulden FO, Pochareddy S, et al. Integrative functional genomic analysis of human brain development and neuropsychiatric risks. *Science*. 2018;362(6420).
75. Zhang Y, Chen K, Sloan SA, Bennett ML, Scholze AR, O'Keefe S, et al. An RNA-sequencing transcriptome and splicing database of glia, neurons, and vascular cells of the cerebral cortex. *J Neurosci*. 2014;34(36):11929-47.
76. Srinivasan R, Lu TY, Chai H, Xu J, Huang BS, Golshani P, et al. New Transgenic Mouse Lines for Selectively Targeting Astrocytes and Studying Calcium Signals in Astrocyte Processes In Situ and In Vivo. *Neuron*. 2016;92(6):1181-95.
77. Endo F, Kasai A, Soto JS, Yu X, Qu Z, Hashimoto H, et al. Molecular basis of astrocyte diversity and morphology across the CNS in health and disease. *Science*. 2022;378(6619):eadc9020.
78. Sorensen DM, Holemans T, van Veen S, Martin S, Arslan T, Haagendahl IW, et al. Parkinson disease related ATP13A2 evolved early in animal evolution. *PLoS One*. 2018;13(3):e0193228.
79. Tan JX, Finkel T. A phosphoinositide signalling pathway mediates rapid lysosomal repair. *Nature*. 2022;609(7928):815-21.
80. Holemans T, Sorensen DM, van Veen S, Martin S, Hermans D, Kemmer GC, et al. A lipid switch unlocks Parkinson's disease-associated ATP13A2. *Proc Natl Acad Sci U S A*. 2015;112(29):9040-5.
81. Dot J, Lluch M, Blanco I, Rodriguez-Alvarez J. Polyamine uptake in cultured astrocytes: characterization and modulation by protein kinases. *J Neurochem*. 2000;75(5):1917-26.
82. Malpica-Nieves CJ, Rivera-Aponte DE, Tejeda-Bayron FA, Mayor AM, Phanstiel O, Veh RW, et al. The involvement of polyamine uptake and synthesis pathways in the proliferation of neonatal astrocytes. *Amino Acids*. 2020;52(8):1169-80.

83. Azfar M, van Veen S, Houdou M, Hamouda NN, Eggermont J, Vangheluwe P. P5B-ATPases in the mammalian polyamine transport system and their role in disease. *Biochim Biophys Acta Mol Cell Res.* 2022;1869(12):119354.
84. Poulin R, Casero RA, Soulet D. Recent advances in the molecular biology of metazoan polyamine transport. *Amino Acids.* 2012;42(2-3):711-23.
85. Farizatto KLG, Baldwin KT. Astrocyte-synapse interactions during brain development. *Curr Opin Neurobiol.* 2023;80:102704.
86. Baldwin KT, Murai KK, Khakh BS. Astrocyte morphology. *Trends Cell Biol.* 2024;34(7):547-65.
87. Bushong EA, Martone ME, Ellisman MH. Maturation of astrocyte morphology and the establishment of astrocyte domains during postnatal hippocampal development. *Int J Dev Neurosci.* 2004;22(2):73-86.
88. Morel L, Higashimori H, Tolman M, Yang Y. VGluT1⁺ neuronal glutamatergic signaling regulates postnatal developmental maturation of cortical protoplasmic astroglia. *J Neurosci.* 2014;34(33):10950-62.
89. Torres-Ceja B, Olsen ML. A closer look at astrocyte morphology: Development, heterogeneity, and plasticity at astrocyte leaflets. *Curr Opin Neurobiol.* 2022;74:102550.
90. Rice D, Barone S, Jr. Critical periods of vulnerability for the developing nervous system: evidence from humans and animal models. *Environ Health Perspect.* 2000;108 Suppl 3(Suppl 3):511-33.
91. Li M, Cui Z, Niu Y, Liu B, Fan W, Yu D, et al. Synaptogenesis in the developing mouse visual cortex. *Brain Res Bull.* 2010;81(1):107-13.
92. Holt MG. Astrocyte heterogeneity and interactions with local neural circuits. *Essays Biochem.* 2023;67(1):93-106.
93. Sejourne G, Eroglu C. Astrocyte-neuron crosstalk in neurodevelopmental disorders. *Curr Opin Neurobiol.* 2024;89:102925.
94. Tan CX, Bindu DS, Hardin EJ, Sakers K, Baumert R, Ramirez JJ, et al. delta-Catenin controls astrocyte morphogenesis via layer-specific astrocyte-neuron cadherin interactions. *J Cell Biol.* 2023;222(11).
95. Baldwin KT, Tan CX, Strader ST, Jiang C, Savage JT, Elorza-Vidal X, et al. HepaCAM controls astrocyte self-organization and coupling. *Neuron.* 2021;109(15):2427-42 e10.
96. Ferreira TA, Blackman AV, Oyrer J, Jayabal S, Chung AJ, Watt AJ, et al. Neuronal morphometry directly from bitmap images. *Nat Methods.* 2014;11(10):982-4.
97. Igarashi K, Kashiwagi K. The functional role of polyamines in eukaryotic cells. *Int J Biochem Cell Biol.* 2019;107:104-15.
98. Dever TE, Ivanov IP. Roles of polyamines in translation. *J Biol Chem.* 2018;293(48):18719-29.
99. Garcia-Faroldi G, Rodriguez CE, Urdiales JL, Perez-Pomares JM, Davila JC, Pejler G, et al. Polyamines are present in mast cell secretory granules and are important for granule homeostasis. *PLoS One.* 2010;5(11):e15071.
100. Kuo BS, Korner G, Dryjcki M, Bjornsson TD. Role of polyamines in the stimulation of synthesis and secretion of plasminogen activator from bovine aortic endothelial cells. *J Cell Physiol.* 1988;137(1):192-8.
101. Thams P, Capito K, Hedekov CJ. An inhibitory role for polyamines in protein kinase C activation and insulin secretion in mouse pancreatic islets. *Biochem J.* 1986;237(1):131-8.
102. Hougaard DM, Larsson LI. Localization and possible function of polyamines in protein and peptide secreting cells. *Med Biol.* 1986;64(2-3):89-94.
103. Diniz LP, Almeida JC, Tortelli V, Vargas Lopes C, Setti-Perdigao P, Stipursky J, et al. Astrocyte-induced synaptogenesis is mediated by transforming growth factor beta signaling through modulation of D-serine levels in cerebral cortex neurons. *J Biol Chem.* 2012;287(49):41432-45.
104. Smith HL, Freeman OJ, Butcher AJ, Holmqvist S, Humoud I, Schatzl T, et al. Astrocyte Unfolded Protein Response Induces a Specific Reactivity State that Causes Non-Cell-Autonomous Neuronal Degeneration. *Neuron.* 2020;105(5):855-66 e5.
105. Pfrieger FW, Barres BA. Synaptic efficacy enhanced by glial cells *in vitro*. *Science.* 1997;277(5332):1684-7.
106. Guerra GP, Rubin MA, Mello CF. Modulation of learning and memory by natural polyamines. *Pharmacol Res.* 2016;112:99-118.
107. Biamino E, Di Gregorio E, Belligni EF, Keller R, Riberi E, Gandione M, et al. A novel 3q29 deletion associated with autism, intellectual disability, psychiatric disorders, and obesity. *Am J Med Genet B Neuropsychiatr Genet.* 2016;171B(2):290-9.
108. Lesca G, Rudolf G, Labalme A, Hirsch E, Arzimanoglou A, Genton P, et al. Epileptic encephalopathies of the Landau-Kleffner and continuous spike and waves during slow-wave sleep types: genomic dissection makes the link with autism. *Epilepsia.* 2012;53(9):1526-38.
109. Kwasnicka-Crawford DA, Carson AR, Roberts W, Summers AM, Rehnstrom K, Jarvela I, et al. Characterization of a novel cation transporter ATPase gene (ATP13A4) interrupted by 3q25-q29 inversion in an individual with language delay. *Genomics.* 2005;86(2):182-94.
110. Worthey EA, Raca G, Laffin JJ, Wilk BM, Harris JM, Jakielski KJ, et al. Whole-exome sequencing supports genetic heterogeneity in childhood apraxia of speech. *J Neurodev Disord.* 2013;5(1):29.

111. Auranen M, Varilo T, Alen R, Vanhala R, Ayers K, Kempas E, et al. Evidence for allelic association on chromosome 3q25-27 in families with autism spectrum disorders originating from a subisolate of Finland. *Mol Psychiatry*. 2003;8(10):879-84.
112. Sobreira N, Schiettecatte F, Valle D, Hamosh A. GeneMatcher: a matching tool for connecting investigators with an interest in the same gene. *Hum Mutat*. 2015;36(10):928-30.
113. Pai B, Tome-Garcia J, Cheng WS, Nudelman G, Beaumont KG, Ghatan S, et al. High-resolution transcriptomics informs glial pathology in human temporal lobe epilepsy. *Acta Neuropathol Commun*. 2022;10(1):149.
114. Kovacs Z, Skatchkov SN, Veh RW, Szabo Z, Nemeth K, Szabo PT, et al. Critical Role of Astrocytic Polyamine and GABA Metabolism in Epileptogenesis. *Front Cell Neurosci*. 2021;15:787319.
115. Hiasa M, Miyaji T, Haruna Y, Takeuchi T, Harada Y, Moriyama S, et al. Identification of a mammalian vesicular polyamine transporter. *Sci Rep*. 2014;4:6836.
116. Fredriksson R, Sreedharan S, Nordenankar K, Alsio J, Lindberg FA, Hutchinson A, et al. The polyamine transporter Slc18b1(VPAT) is important for both short and long time memory and for regulation of polyamine content in the brain. *PLoS Genet*. 2019;15(12):e1008455.
117. Qiao C, Yin N, Gu HY, Zhu JL, Ding JH, Lu M, et al. Atp13a2 Deficiency Aggravates Astrocyte-Mediated Neuroinflammation via NLRP3 Inflammasome Activation. *CNS Neurosci Ther*. 2016;22(6):451-60.
118. Kett LR, Stiller B, Bernath MM, Tasset I, Blesa J, Jackson-Lewis V, et al. alpha-Synuclein-independent histopathological and motor deficits in mice lacking the endolysosomal Parkinsonism protein Atp13a2. *J Neurosci*. 2015;35(14):5724-42.
119. Verhoog QP, Holtman L, Aronica E, van Vliet EA. Astrocytes as Guardians of Neuronal Excitability: Mechanisms Underlying Epileptogenesis. *Front Neurol*. 2020;11:591690.
120. Risher WC, Kim N, Koh S, Choi JE, Mitev P, Spence EF, et al. Thrombospondin receptor alpha2delta-1 promotes synaptogenesis and spinogenesis via postsynaptic Rac1. *J Cell Biol*. 2018;217(10):3747-65.
121. Singh SK, Stogsdill JA, Pulimood NS, Dingsdale H, Kim YH, Pilaz LJ, et al. Astrocytes Assemble Thalamocortical Synapses by Bridging NRX1alpha and NL1 via Hevin. *Cell*. 2016;164(1-2):183-96.
122. Mauch DH, Nagler K, Schumacher S, Goritz C, Muller EC, Otto A, et al. CNS synaptogenesis promoted by gliaderived cholesterol. *Science*. 2001;294(5545):1354-7.
123. Biedermann B, Skatchkov SN, Brunk I, Bringmann A, Pannicke T, Bernstein HG, et al. Spermine/spermidine is expressed by retinal glial (Muller) cells and controls distinct K⁺ channels of their membrane. *Glia*. 1998;23(3):209-20.
124. Williams K. Interactions of polyamines with ion channels. *Biochem J*. 1997;325 (Pt 2)(Pt 2):289-97.
125. Chen W, Harnett MT, Smith SM. Modulation of neuronal voltage-activated calcium and sodium channels by polyamines and pH. *Channels (Austin)*. 2007;1(4):281-90.
126. Belting M, Mani K, Jonsson M, Cheng F, Sandgren S, Jonsson S, et al. Glypican-1 is a vehicle for polyamine uptake in mammalian cells: a pivotal role for nitrosothiol-derived nitric oxide. *J Biol Chem*. 2003;278(47):47181-9.
127. de Wit J, O'Sullivan ML, Savas JN, Condomitti G, Caccese MC, Vennekens KM, et al. Unbiased discovery of glypican as a receptor for LRRTM4 in regulating excitatory synapse development. *Neuron*. 2013;79(4):696-711.
128. Park MH, Wolff EC. Hypusine, a polyamine-derived amino acid critical for eukaryotic translation. *J Biol Chem*. 2018;293(48):18710-8.
129. Cavalli P, Raffauf A, Passarella S, Helmuth M, Dieterich DC, Landgraf P. Manipulation of DHPS activity affects dendritic morphology and expression of synaptic proteins in primary rat cortical neurons. *Front Cell Neurosci*. 2024;18:1465011.
130. Padgett LR, Shinkle MR, Rosario S, Stewart TM, Foley JR, Casero RA, Jr., et al. Deoxyhypusine synthase mutations alter the post-translational modification of eukaryotic initiation factor 5A resulting in impaired human and mouse neural homeostasis. *HGG Adv*. 2023;4(3):100206.
131. Fiori LM, Turecki G. Implication of the polyamine system in mental disorders. *J Psychiatry Neurosci*. 2008;33(2):102-10.
132. de Oliveira Figueiredo EC, Cali C, Petrelli F, Bezzi P. Emerging evidence for astrocyte dysfunction in schizophrenia. *Glia*. 2022;70(9):1585-604.
133. Coulter DA, Steinhauser C. Role of astrocytes in epilepsy. *Cold Spring Harb Perspect Med*. 2015;5(3):a022434.
134. Madeira F, Madhusoodanan N, Lee J, Eusebi A, Niewielska A, Tivey ARN, et al. The EMBL-EBI Job Dispatcher sequence analysis tools framework in 2024. *Nucleic Acids Res*. 2024;52(W1):W521-W5.

Extended Data Fig. 1. ATP13A4 is predominantly expressed in astrocytes.



Extended Data Fig. 1: ATP13A4 is predominantly expressed in astrocytes. **a**, Human RNA-seq data (72) showing the abundance of *hATP13A4* expression in astrocytes compared to other human CNS cell types, with other P5B-type ATPases showing no enrichment in astrocytes. **b**, *hATP13A4* expression in human cortex is upregulated during late fetal and early postnatal development. Graph was made via <http://hbatlas.org/>. OFC, orbital prefrontal cortex; DFC, dorsolateral prefrontal cortex; VFC, ventrolateral prefrontal cortex; MFC, medial prefrontal cortex; M1C, primary motor cortex; S1C, primary somatosensory cortex; IPC, posterior inferior parietal cortex; A1C, primary auditory cortex; STC, posterior superior temporal cortex; ITC, inferior temporal cortex; V1C, primary visual cortex. **c**, Mouse RNA-seq data (75) showing highest *msAtp13a4* expression in postnatal day 7 (P7) astrocytes compared to other CNS cell types. **d**, *msAtp13a4* mRNA is actively translated in P80 mouse astrocytes. Average Fragments Per Kilobase Million (FPKM) values of *msAtp13a4* mRNA within translating astrocyte-specific (Astro IP) and bulk tissue RNA (input) (76). **e**, *msAtp13a4* is enriched in astrocytes across 13 CNS regions in adult mice. FPKM values of *msAtp13a4* mRNA from (77). **f**, Immunocytochemistry of HeLa cells transiently expressing N-terminal mCherry-labeled *msAtp13a4*, co-stained with markers for specific organelles: EEA1 (early endosomes), CD63 (late endosomes), LAMP1 (lysosomes), and TOMM22 (mitochondria). Scale bar, 10 μ m. Inset shows a magnification of the indicated white rectangular region. (scale bar, 625 nm.) $n = 41-51$ cells per condition from three independent experiments.

Figure 1. ATP13A4 is an astrocytic polyamine transporter.

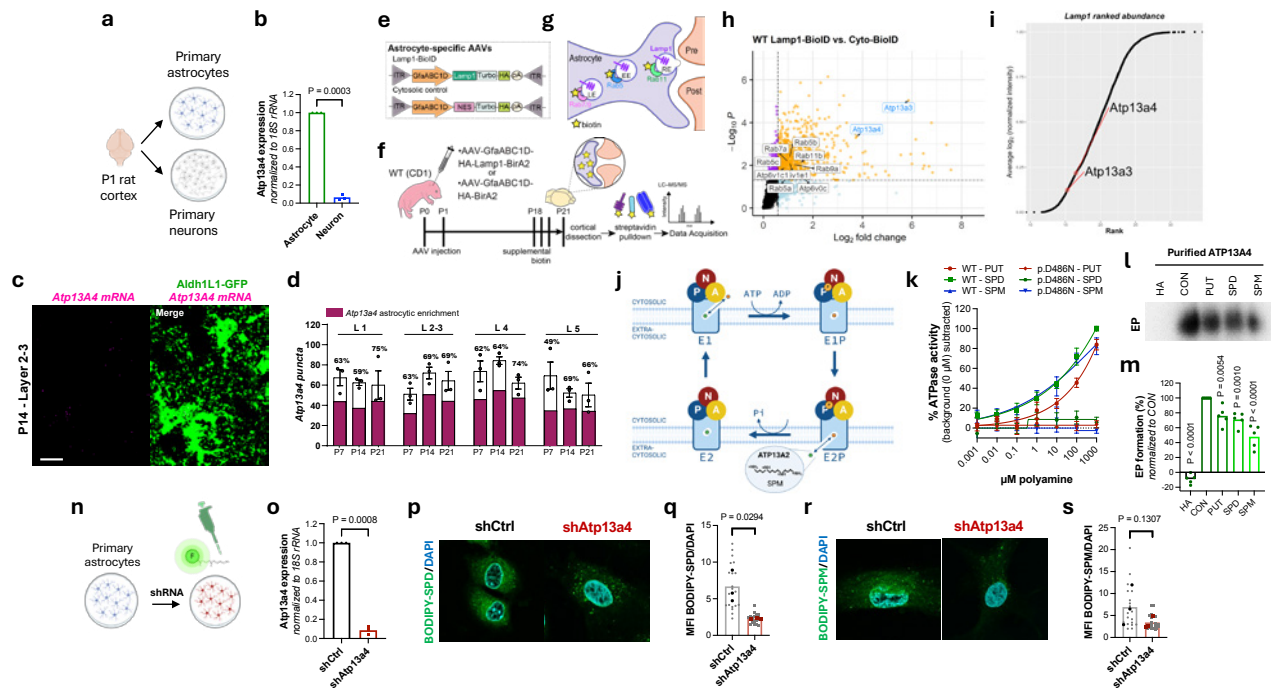
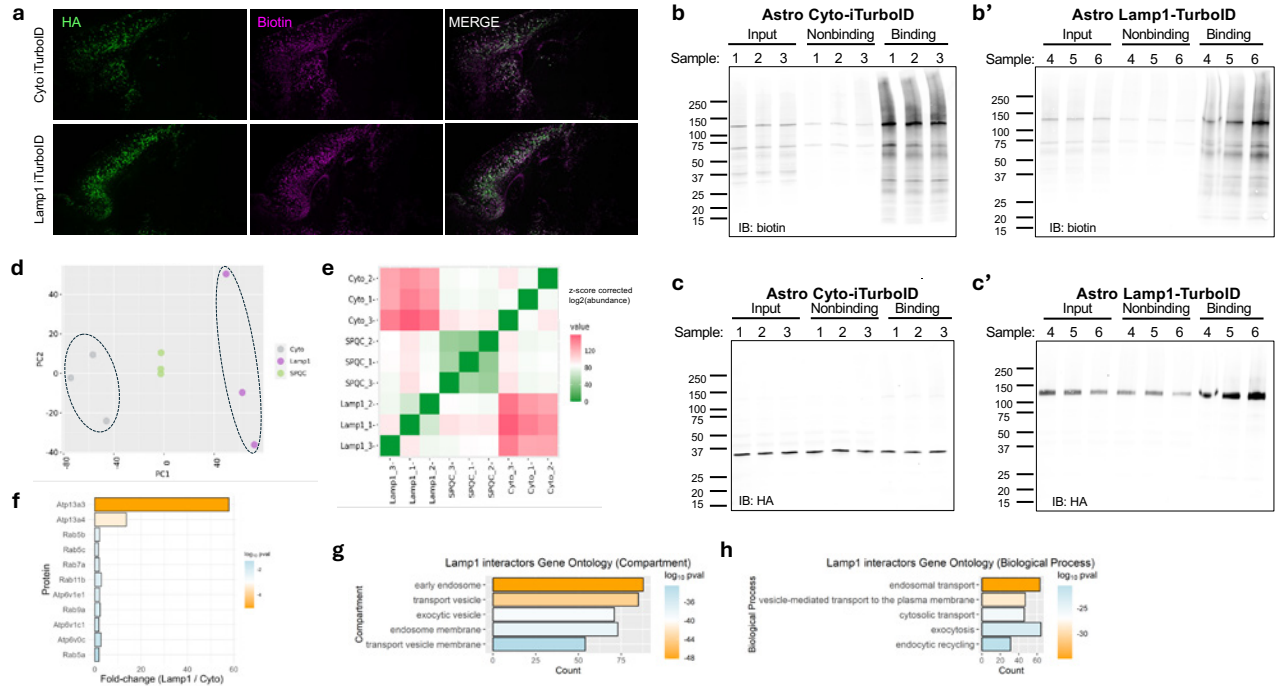


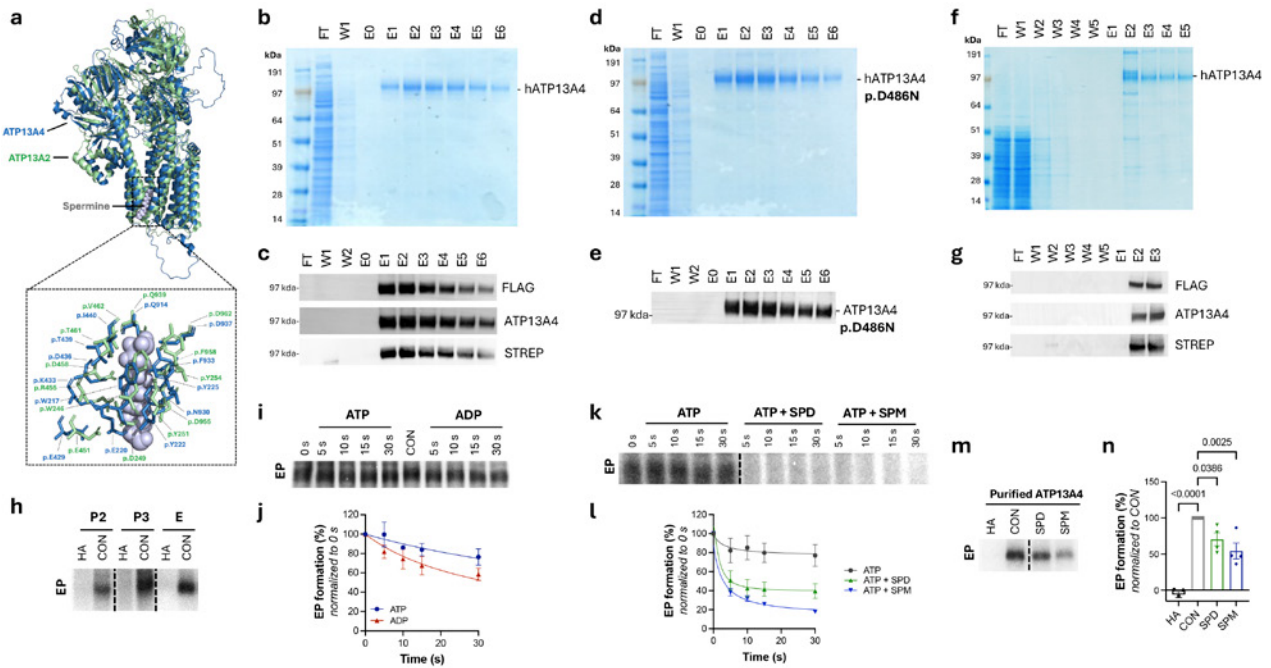
Fig. 1: ATP13A4 is an astrocytic polyamine transporter. **a**, Schematic representation of isolating primary astrocyte and primary neuron cultures from postnatal day 1 (P1) rat cortex. **b**, qPCR data showing significantly higher expression of *rAtp13a4* in rat primary cortical astrocytes compared to neurons. $n = 3$ independent cultures. Paired t test. **c**, Detection of *msAtp13a4* in cortical astrocytes by RNA FISH in Aldh1L1-EGFP mice at P14. **d**, Quantification of total and astrocyte-specific *msAtp13a4* expression across all cortical layers (L1, L2/3, L4, and L5) of the V1 cortex at P7, P14, and P21. Astrocytic *msAtp13a4* mRNA expression was quantified by normalizing the volume of *msAtp13a4* mRNA puncta with the astrocyte soma (labeled by eGFP). 3 sections per animal, 3 animals per time point. Scale bar, 10 μm . **e**, Astrocyte-specific AAVs (serotype PHP.eB) were used to express Lamp1 or nonspecific cytosolic control. NES, nuclear export sequence; ITR, inverted terminal repeats; GfaABC1D truncated GFAP promoter; HA, hemagglutinin tag; Turbo, TurboID biotin ligase; pA, polyadenylation. **f**, Outline of the experimental paradigm. $n = 3$ biological replicates per construct per genotype (1 replicate = 2 animals per pooled sample). **g**, Schematic of Lamp1 protein localization within astrocyte perisynaptic process (PAP). **h**, Volcano plot showing the differential abundance of proteins detected by Astro-Lamp1-TurboID compared to Astro-Cyto-TurboID. Dotted lines indicate threshold values $\text{FC} > 1.5$ ($\log_2\text{FC} > 0.58$), p -value < 0.05 ($\log_{10}p < -1.3$). **i**, Empirical cumulative distribution function (eCDF) listing potential endo-lysosomal polyamine transporters (red dots) among the most abundant proteins detected by Astro-Lamp1-TurboID. **j**, Schematic of the catalytic cycle of the archetypical P5B ATPase ATP13A2. **k**, Dose-response curves showing the effect of putrescine (PUT), spermidine (SPD) and spermine (SPM) on the ATPase activity of solubilized purified ATP13A4 (WT or catalytically dead p.D486N mutant). The number of independent biological experiments was as follows: $n = 3$ (D486N PUT, SPD, SPM), $n = 5$ (WT PUT), $n = 7$ (WT SPD) and $n = 4$ (WT SPM). **l-m**, ATP13A4 phosphoenzyme (EP) levels in control (CON) conditions and in the presence of PUT, SPD, SPM, or hydroxylamine (HA). **l**, Representative autoradiogram. **m**, Quantification of EP. $n = 5$ independent experiments. One-way ANOVA with Dunnett's multiple comparisons test. **n**, Schematic illustrating the BODIPY-polyamine uptake assay in primary astrocytes with ATP13A4 knockdown. **o**, shRNA targeting mouse/rat *Atp13a4* efficiently reduces *Atp13a4* expression in astrocytes compared to control in which the shRNA sequence was scrambled (shCtrl). $n = 3$ independent cultures. Paired t test. **p-s**, Confocal microscopy of BODIPY-labelled SPD (**p**) and SPM (**r**) distribution. Scale bar, μm . Mean fluorescence intensities (MFI) of BODIPY-SPD (**q**) and -SPM (**s**) shown in **p** (shCtrl, 20 cells; shAtp13a4, 18 cells) and **r** (shCtrl, 19 cells; shAtp13a4, 20 cells), respectively. $n = 3$ independent cultures. Paired t test.

Extended Data Fig. 2. TurboID construct expression and biotinylation *in vivo*.



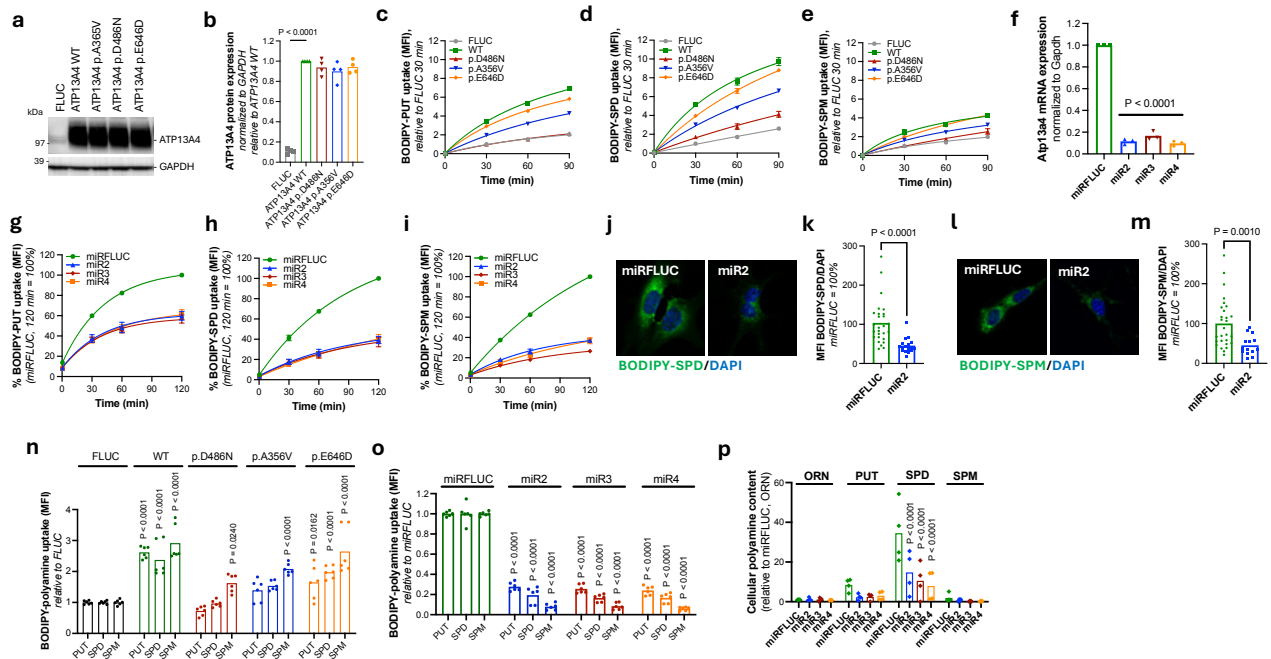
Extended Data Fig. 2: TurboID construct expression and biotinylation *in vivo*. **a**, Representative images of *in vivo* expression in the cortex of different TurboID constructs labeled with HA and the biotinylating activity labeled with streptavidin. Merged images show the colocalization of HA and biotin signals in astrocytes. Scale bar, 500 μ m. **b-c.** HA immunoblotting verifies expression of Astro-Cyto-TurboID (**b**) and Astro-Lamp1-TurboID (**b'**). Streptavidin blotting verifies biotinylation activity of Astro-Cyto-TurboID (**c**) and Astro-Lamp1-TurboID (**c'**) in cortical lysates (input) and subsequent immunoprecipitation (binding). **d**, Principal component analysis (PCA) of BioID data shows Astro-Lamp1-TurboID samples (purple) clustering separately from Astro-Cyto-TurboID samples (gray) and study pool QC (SPQC) samples (green). **e**, Heatmap displaying the correlation of protein abundance for all pairwise combinations of samples. Unsupervised hierarchical clustering shows Astro-Lamp1-TurboID samples clustering separately from Astro-Cyto-TurboID and SPQC samples. **f**, Bar graph depicting the detection ratio of Lamp1-TurboID versus Astro-Cyto-TurboID for putative polyamine transporters (Atp13a3 and Atp13a4) and selected endo-lysosomal proteins. **(g-h)** Bars show the top 10 most significant Gene Ontology (GO) terms, ordered by lowest adjusted p-value, for the proteins differentially detected by Astro-Lamp1-TurboID compared to Astro-Cyto-TurboID. **(g)** Cellular Compartment; **(h)** Biological Process.

Extended Data Fig. 3. hATP13A4 spontaneously forms a phospho-enzyme that is sensitive to polyamines.



Extended Data Fig. 3: hATP13A4 spontaneously forms a phospho-enzyme that is sensitive to polyamines. **a**, Top: overlay of hATP13A4 (blue) and hATP13A2 (green), with spermine depicted in grey. Bottom: close-up view of the spermine binding pocket. **b-g**, Coomassie staining (**b, d, f**) and Western blot analysis (**c, e, g**) showing the purification process for WT hATP13A4 (**b-c, f-g**) or the p.D486N mutant (**d-e**), starting from detergent-solubilized HEK293T cell lysates (**b-e**) or yeast membranes (**f-g**), followed by streptavidin affinity chromatography and subsequent elution with biotin. FT, flow-through; W, wash; E, elution. **h**, Representative autoradiogram showing phosphoenzyme (EP) formation of WT hATP13A4 in yeast membrane fractions (heavy membrane fraction P2 and light membrane fraction P3) and purified protein, which is sensitive to 0.3 M hydroxylamine (HA). **i-j**, Representative autoradiogram (**i**) and quantification (**j**) of pulse ($[-^{32}P]ATP$) chase (cold ATP or ADP) experiment to determine ATP and ADP sensitivity of hATP13A4 EP. $n = 3$ independent experiments. **k-l**, Representative autoradiogram (**k**) and quantification (**l**) of pulse ($[-^{32}P]ATP$) chase (cold ATP) experiment in the presence and absence of spermidine (SPD) or spermine (SPM) in yeast membranes. $n = 4$ (ATP + SPM) or 5 (ATP, ATP + SPM) independent experiments. **m-n**, Representative autoradiogram (**m**) and quantification (**n**) of purified ATP13A4 EP levels in the presence of 0.3 M HA, 1 mM SPD or SPM. $n = 4$ independent experiments. One-way ANOVA with Dunnett's post-test.

Extended Data Fig. 4. ATP13A4 increases cellular polyamine uptake.



Extended Data Fig. 4: ATP13A4 increases cellular polyamine uptake. **a**, Overexpression of firefly luciferase (FLUC), WT hATP13A4, the p.D486N mutant, or disease-associated variants p.A356V and p.E646D in H4 cells was confirmed via immunoblotting. GAPDH was used as a loading control. **b**, Densitometry of the expression of hATP13A4 presented in **a**. $n = 4$ independent cultures. One-way ANOVA with Dunnett's post-test. **c-e**, Flow cytometric analysis of cellular BODIPY-putrescine (PUT, **c**), -spermidine (SPD, **d**) or -spermine (SPM, **e**) uptake in serum-containing medium. $n = 3$ independent experiments. **f**, *msAtp13a4* mRNA expression after knockdown with lentiviral shRNA transduction (miR2-4) was assessed by qPCR. $n = 3$ independent experiments. One-way ANOVA with Dunnett's multiple comparisons test. **g-i**, Flow cytometric analysis of cellular BODIPY-putrescine (PUT, **g**), -spermidine (SPD, **h**) or -spermine (SPM, **i**) uptake in a serum-containing medium. $n = 3$ independent experiments. **j-m**, Confocal microscopy of BODIPY-SPD (**j**, **k**) and -SPM (**l**, **m**) distribution. Scale bar, 10 μ m. Mean fluorescence intensities (MFI) of BODIPY-SPD (**k**) and -SPM (**m**) shown in **j** (miRFLUC, 27 cells; miR2, 18 cells) and **l** (miRFLUC, 28 cells; miR2, 14 cells), respectively. $n = 3$ independent cultures. Mann-Whitney U test. **n-o**, Flow cytometric analysis of BODIPY-PUT, SPD or SPM uptake in H4 cells overexpressing FLUC, WT hATP13A4 or indicated variants (**n**) and in C8-D1A cells with *msAtp13a4* knockdown (**o**), performed in a serum-free medium. **p**, Metabolomics of cellular polyamines in *msAtp13a4* knockdown cells (miR2-4) compared with C8-D1A control (miRFLUC). **n-p**, $n = 3$ independent experiments. Two-way ANOVA with Sidák's multiple comparisons test.

Figure 2. ATP13A4 knockdown impairs astrocyte arborization.

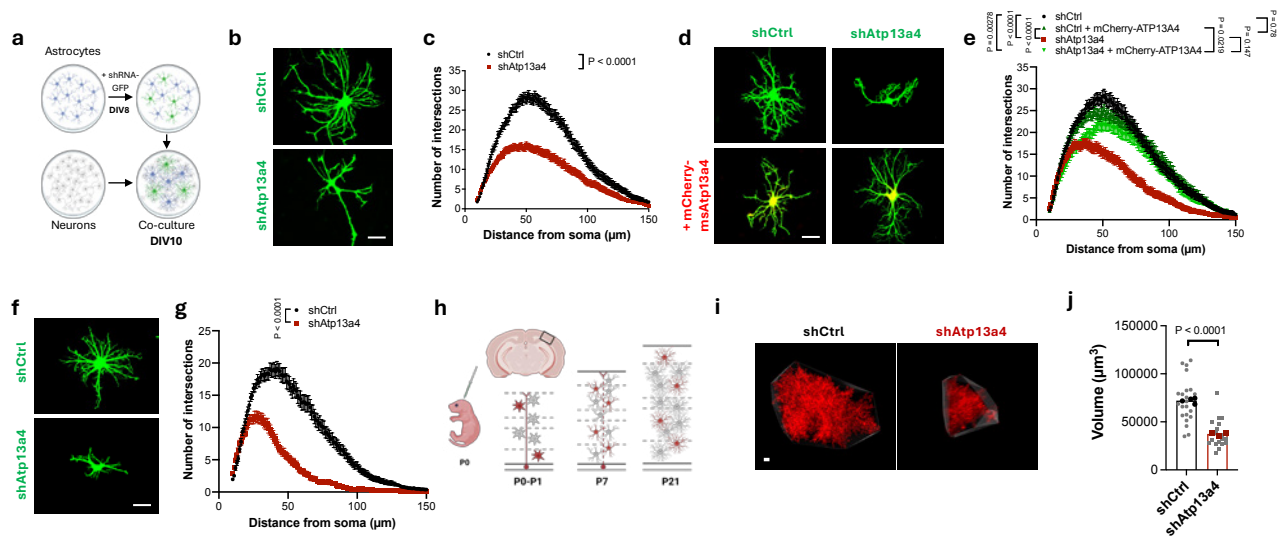
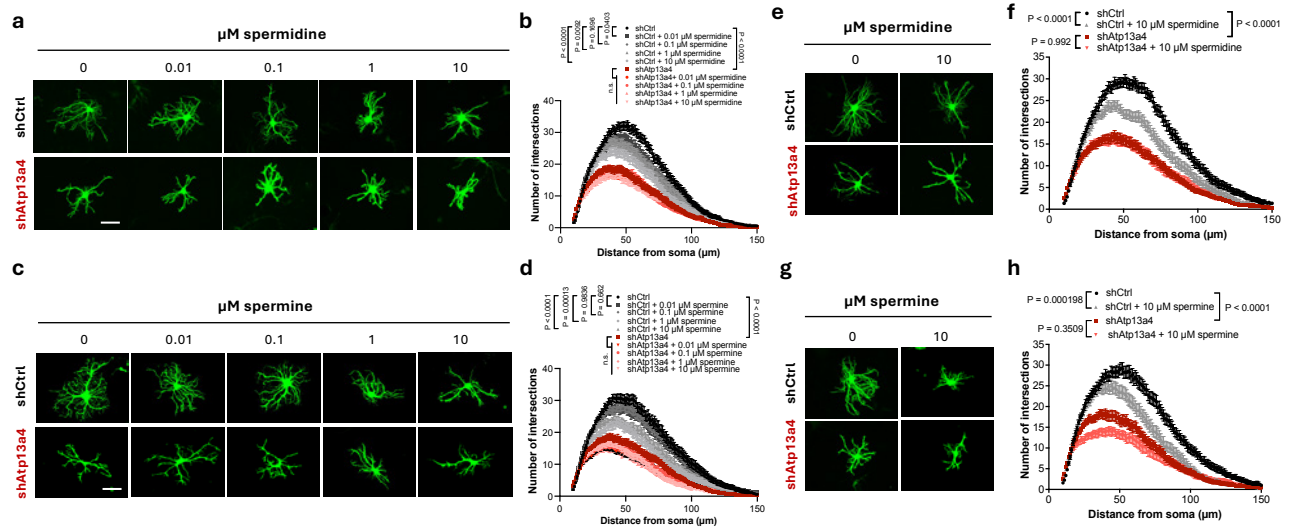


Fig. 2: ATP13A4 knockdown impairs astrocyte arborization. **a**, Schematic of astrocyte-neuron co-culture used to assess astrocyte morphology. **b**, Representative images of astrocytes (green) transfected with either shRNA targeting mouse/rat *Atp13a4* (shAtp13a4) or a scrambled control (shCtrl), co-cultured with WT neurons (not visible) for 48 h. Scale bar, 50 μ m. **c**, Quantification of astrocyte complexity via Sholl analysis for conditions in **b**. $n = 72$ astrocytes per condition from three independent experiments. **d**, Representative images of shRNA expressing astrocytes (green) in the presence or absence of an shRNA-resistant mouse *Atp13a4* (msAtp13a4) construct with an N-terminal mCherry tag (red) after 48 h co-culture with WT neurons. Scale bar, 50 μ m. **e**, Quantification of astrocyte complexity for conditions in **d**. $n = 60$ astrocytes per condition from three independent experiments. **f**, Representative images of shRNA expressing astrocytes co-cultured with methanol-fixed WT neurons for 48 h. Scale bar, 50 μ m. **g**, Quantification of astrocyte complexity for conditions in **f**. $n = 60$ astrocytes per condition from three independent experiments. **c, e, g**, Mixed effects ANOVA with Tukey's post-hoc test (**e**). **h**, Schematic of PALE. Plasmids were injected into the lateral ventricle of CD1 mice at late P0, followed by electroporation into radial glial stem cells, leading to sparse knockdown and labeling of cortical astrocytes. **i**, Representative images of *in vivo* shRNA-transfected astrocytes (labelled with mCherry) at P21. **j**, Quantification of *in vivo* astrocyte territory volumes by convex hull analysis in Imaris. Only astrocytes from V1 cortex were imaged and analyzed. The average astrocyte territory volume of individual mice is plotted in black (shCtrl) or red (shAtp13a4). $n = 18-22$ astrocytes from 3-4 mice, nested *t* test. All data are presented as mean \pm SEM, except in **j** where individual data points are shown.

Extended Data Fig. 5. Polyamines decrease astrocyte complexity in an ATP13A4-dependent manner.



Extended Data Fig. 5: Polyamines decrease astrocyte complexity in an ATP13A4-dependent manner. **a**, Representative images of astrocytes (green) transfected with shRNA targeting mouse/rat *Atp13a4* (shAtp13a4) or a scrambled control (shCtrl), co-cultured with WT neurons (not labeled) for 48 h, and treated with spermidine during the final 8 h of co-culture. Scale bar, 50 μm . **b**, Quantification of astrocyte complexity via Sholl analysis for conditions in **a**. $n = 46$ –68 astrocytes per condition from three independent experiments. **c**, Representative images of shRNA expressing astrocytes co-cultured with WT neurons for 48 h and treated with spermine during the final 8 h of co-culture. Scale bar, 50 μm . **d**, Quantification of astrocyte complexity for conditions in **c**. $n = 50$ –60 astrocytes per condition from three independent experiments. **e**, Representative images of shRNA expressing astrocytes (green), treated with spermidine for 24 h and then co-cultured with WT neurons for 48 h. Scale bar, 50 μm . **f**, Quantification of astrocyte complexity for conditions in **e**. $n = 60$ –63 astrocytes per condition from three independent experiments. **g**, Representative images of shRNA expressing astrocytes (green), treated with spermine for 24 h and then co-cultured with WT neurons for 48 h. Scale bar, 50 μm . **h**, Quantification of astrocyte complexity for conditions in **g**. $n = 60$ astrocytes per condition from three independent experiments. All data are presented as mean \pm SEM. **b**, **d**, **f**, **h**, Mixed effects ANOVA with Tukey's post-hoc test.

Figure 3. ATP13A4 controls excitatory synapse numbers and function.

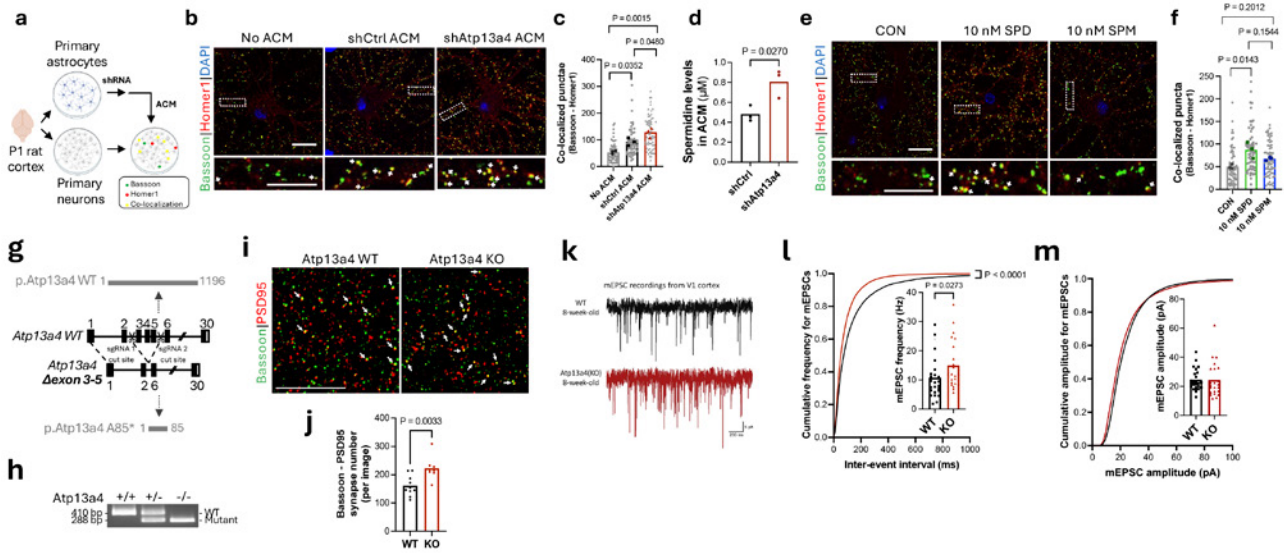
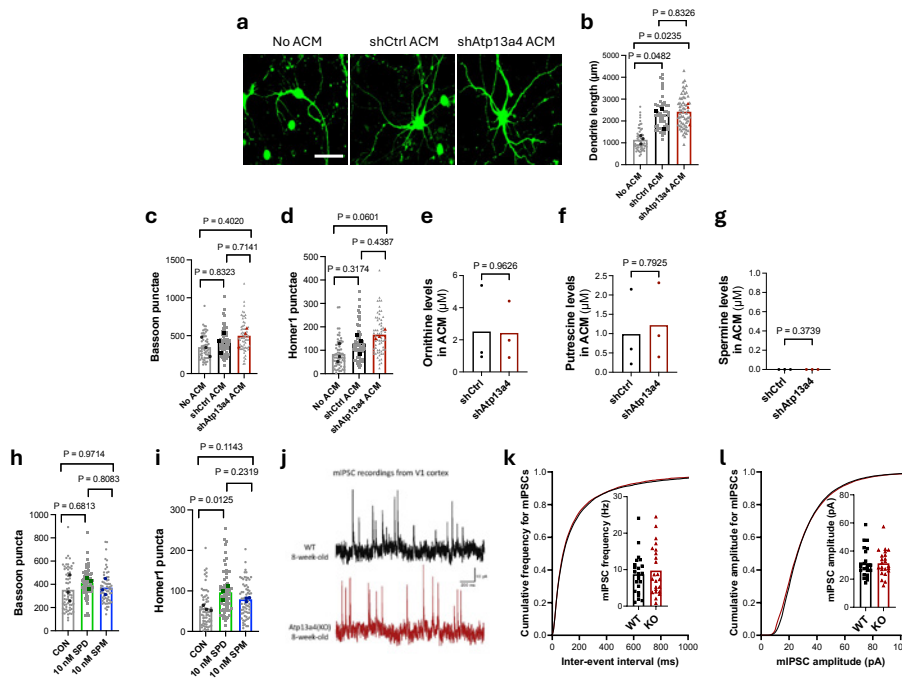


Fig. 3: ATP13A4 controls excitatory synapse numbers and function. **a**, Schematic of neuronal culture assay to evaluate the effects of astrocyte-conditioned medium (ACM) on synapse formation. **b**, Excitatory synapses marked with Bassoon and Homer1. Scale bars, 20 μ m. **c**, Quantification of excitatory synapses (Bassoon and Homer1 co-localization) in **b**. $n = 58$ -64 cells per condition from three independent experiments. Individual data points are shown, with the average of each experiment plotted in grey (no ACM), black (shCtrl ACM) or red (shAtp13a4 ACM). Nested one-way ANOVA with Tukey's post- test. **d**, Metabolomics analysis of spermidine levels in shCtrl ACM versus shAtp13a4 ACM. $n = 3$ independent experiments. Unpaired two-tailed t test. **e**, Excitatory synapses marked with Bassoon and Homer1 in neuronal cultures treated with spermidine (SPD) or spermine (SPM). Scale bars, 20 μ m. **f**, Quantification of excitatory synapses (Bassoon and Homer1 co-localization) in **e**. $n = 64$ -66 cells per condition from three independent experiments. **c**, **f**, Individual data points are shown, with the average of each experiment plotted in grey (no ACM), black (shCtrl ACM), red (shAtp13a4 ACM), green (SPD) or blue (SPM). Nested one-way ANOVA with Tukey's multiple comparisons test. **g**, Schematic of *Atp13a4* KO mice, illustrating the effects at the protein level. **h**, Genomic PCR from *Atp13a4* WT, heterozygous and KO mice. **i**, Excitatory synapses (Bassoon and Homer1 co-localization) in V1 cortex of *Atp13a4* WT and KO mice. White arrows indicate excitatory synapses. Scale bar, 10 μ m. **j**, Quantification of excitatory synapse numbers in *Atp13a4* WT and KO mice. $n = 8$ (KO), 10 (WT) mice with 2 sections/mouse and 3-4 images/section. Data points represent mouse averages. Unpaired two-tailed t test. **k**, Representative mEPSC traces from V1 cortex in acute brain slices of WT and *Atp13a4* KO mice. **l**, Quantification of frequency average (inset) and cumulative probability of mEPSC from *Atp13a4* WT and KO neurons. **m**, Quantification of amplitude average (inset) and cumulative probability of mEPSC from *Atp13a4* WT and KO neurons. **l-m**, $n = 26$ (WT), 23 (*Atp13a4* KO) neurons from 3 mice per genotype. Mann-Whitney U test (inset). Kolmogorov-Smirnov test (cumulative probability). Individual data points are shown.

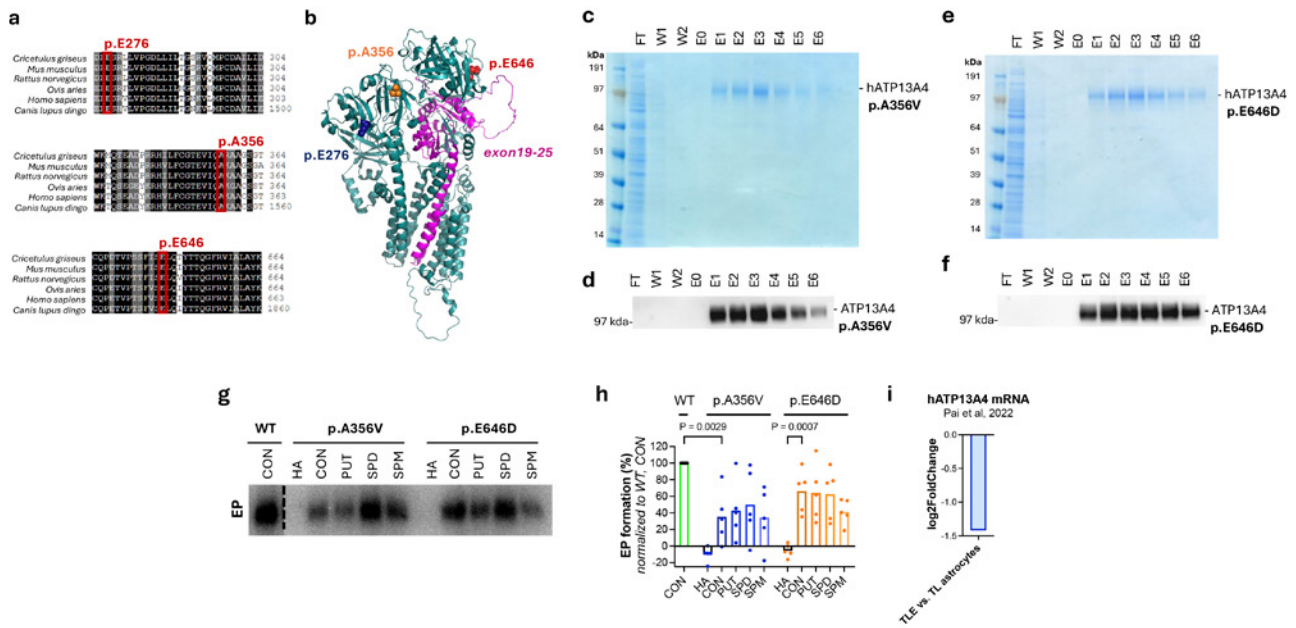
Extended Data Fig. 6. Atp13a4 knockdown in astrocytes does not impact neuronal morphology or inhibitory synapse function.



Extended Data Fig. 6: Atp13a4 knockdown in astrocytes does not impact neuronal morphology or inhibitory synapse function.

a, Representative images of neurons transfected with GFP and treated with astrocyte-conditioned medium (ACM). Scale bar: 100 μm . **b**, Quantification of dendrite tree length in **a**. $n = 52$ -60 cells per condition from three independent experiments. Nested one-way ANOVA with Tukey's post-test. **c-d**, Quantification of Bassoon (**c**) and Homer1 (**d**) puncta of neuronal cultures treated with ACM (Fig. 3b), $n = 58$ -64 cells per condition from three independent experiments. Nested one-way ANOVA with Tukey's multiple comparisons test. **e-g**, Metabolomics analysis of ornithine (**e**), putrescine (**f**) and spermine (**g**) levels in shCtrl ACM versus shAtp13a4 ACM. $n = 3$ independent experiments. Unpaired two-tailed t test. **h-i**, Quantification of Bassoon (**h**) and Homer1 (**i**) puncta of neuronal cultures treated with SPD or SPM (Fig. 3e). $n = 64$ -66 cells per condition from three independent experiments. **b-d, h-i**, Individual data points are shown, with the average of each experiment plotted in grey (no ACM), black (shCtrl ACM), red (shAtp13a4 ACM), green (SPD) or blue (SPM). Nested one-way ANOVA with Tukey's multiple comparisons test. **j**, Representative mIPSC traces from V1 cortex in acute brain slices of WT and *Atp13a4* KO mice. **k**, Quantification of frequency average (inset) and cumulative probability of mIPSC from *Atp13a4* WT and KO neurons. **l**, Quantification of amplitude average (inset) and cumulative probability of mIPSC from *Atp13a4* WT and KO neurons. **k-l**, $n = 26$ (WT), 23 (*Atp13a4* KO) neurons from 3 mice per genotype. Mann-Whitney U test (inset). Kolmogorov-Smirnov test (cumulative probability). Individual data points are shown.

Extended Data Fig. 7. Disease-associated ATP13A4 mutations.



Extended Data Fig. 7: Disease-associated ATP13A4 variants. **a**, Sequence alignment showing disease-associated residues are highly conserved. The alignment was generated using Clustal Omega (134). **b**, Predicted 3D structure of ATP13A4 (AlphaFold) with disease-associated residues indicated. **c-f**, Coomassie staining (**c, e**) and Western blot analysis (**d, f**) showing the purification process for the disease-associated ATP13A4 variants p.A356V (**c-d**) and p.E646D (**e-f**), starting from detergent-solubilized HEK293T cell lysates, followed by streptavidin affinity chromatography and subsequent elution with biotin. $n \geq 3$ independent purifications. FT, flow-through; W, wash; E, elution. **g-h**, Phosphoenzyme (EP) levels of purified, solubilized ATP13A4 (WT and disease-associated variants p.A356V and p.E646D) under control (CON) conditions and in the presence of putrescine (PUT), spermidine (SPD), spermine (SPM), or hydroxylamine (HA). **g**, Representative autoradiogram. **h**, Quantification of EP in **g**. $n = 5$ independent experiments. Two-way ANOVA with Tukey's multiple comparisons test. Individual data points are shown. **i**, Human RNA-seq data (from (113)) showing that *ATP13A4* is differentially downregulated in human epilepsy astrocytes (astrocyte temporal lobe epilepsy (TLE) versus astrocyte temporal lobe (TL) control).

Fig. 4. Disease-associated hATP13A4 mutations exhibit a loss-of-function phenotype.

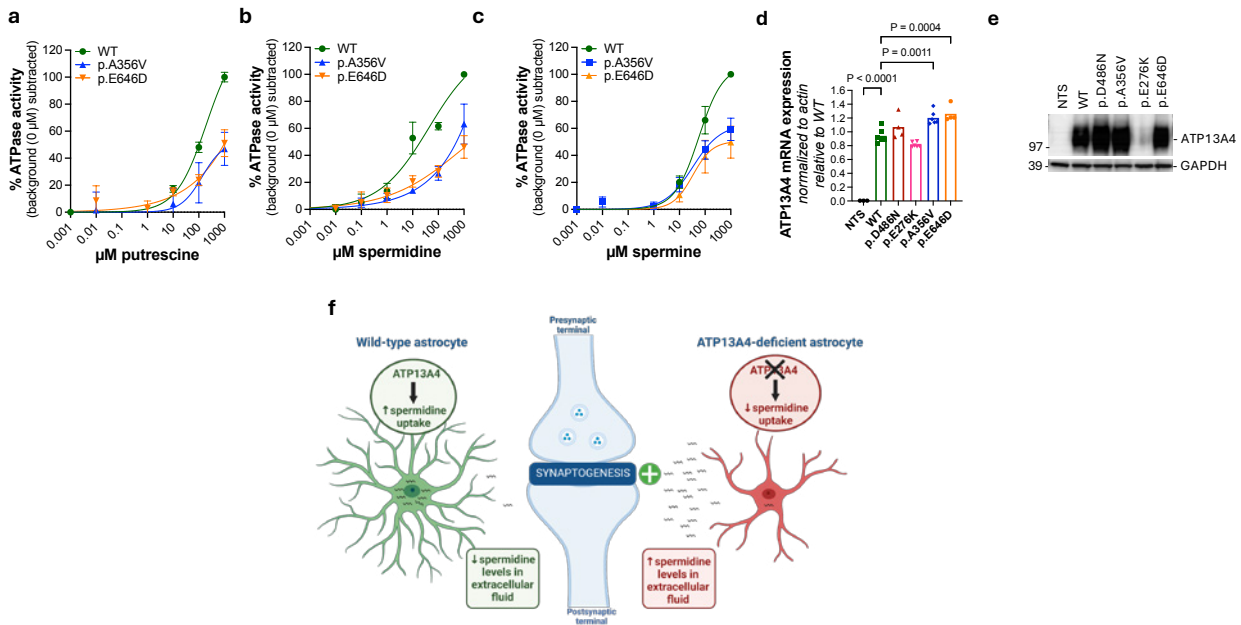


Fig. 4: Disease-associated hATP13A4 variants exhibit a loss-of-function phenotype. **a-c**, Dose-response curves showing the effect of putrescine (**a**), spermidine (**b**) and spermine (**c**) on the ATPase activity of solubilized purified ATP13A4 (WT or disease-associated p.A356V and p.E646D variants). $n = 4$ independent experiments. **d**, qPCR of HEK293T cells with stable overexpression of WT ATP13A4, the p.D486N mutant, or disease-associated variants p.A356V and p.E646D. *Atp13a4* mRNA expression was normalized to actin. $n = 3-6$ independent experiments. One-way ANOVA with Dunnett's multiple comparisons test. **e**, Overexpression of WT ATP13A4, the p.D486N mutant, or disease-associated variants p.A356V and p.E646D in HEK293T cells was confirmed via immunoblotting. GAPDH was used as a loading control. $n = 3$ independent experiments. **f**, Illustration of the role of ATP13A4 in astrocytic spermidine uptake and its impact on astrocyte arborization and synaptogenesis.



Geneeskundige Stichting Koningin Elisabeth
Fondation Médicale Reine Elisabeth
Königin-Elisabeth-Stiftung für Medizin
Queen Elisabeth Medical Foundation

Progress report of the research project of the young researcher

Prof. Giulia Liberati
Université Catholique de Louvain (UCLouvain)

Giulia Liberati (UCLouvain)

Université catholique de Louvain Institute of Neuroscience (IoNS)

Avenue Mounier 54

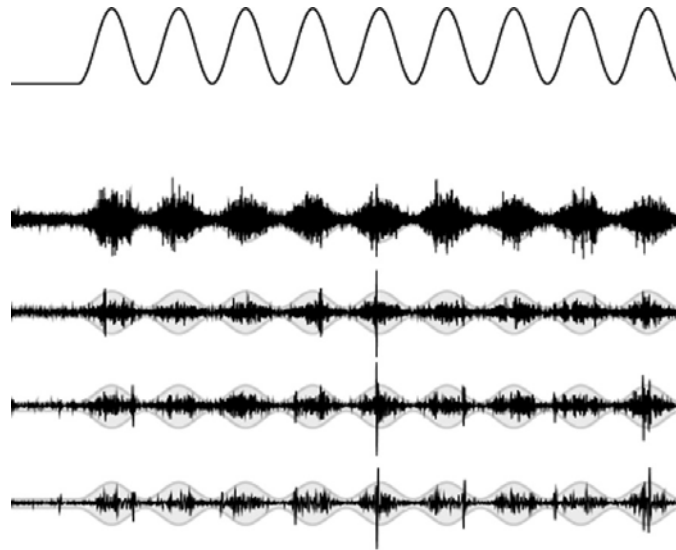
UCL 54.02 B-1200 Brussels

Belgium

T +32 (2) 7645467

giulia.liberati@uclouvain.be

Identifying biomarkers with invasive and non-invasive brain stimulation targeting ongoing neural oscillations



1. Introduction

Around 10% of adults worldwide suffer from chronic pain conditions¹. The identification of effective neural biomarkers for pain – which would allow improving the stratification of pain conditions, predicting responses to treatment, and offering personalized interventions – is of major importance². In recent years, works from our group^{3,4} and others^{5,6} have strongly suggested that pain perception may arise from the modulation of ongoing neural oscillations within different frequency bands. However, despite these encouraging findings, there is still disagreement on the degree to which these modulations of neural oscillations are actually related to pain, or whether they are merely an epiphenomenon.

My project, STIM-WAVES, remedies this gap by directly assessing the causal relationship between ongoing neural oscillations and pain perception, combining both scalp electroencephalography (**EEG**) and intracerebral electroencephalography (**iEEG**) with **invasive and non-invasive brain stimulation**, with the aim of (i) better characterizing pain-related modulations of ongoing neural oscillations, and (ii) understanding whether disrupting these modulations through brain stimulation would also affect pain perception.

Since the beginning of 2024, **7 distinct studies** – detailed below – have either been completed or are currently underway to achieve these objectives.

1.1. Cue-based modulation of pain stimulus expectation: do ongoing oscillations reflect changes in pain perception? (complete)

Team members participating in the study:

- Giulia Liberati: Principal Investigator (UCLouvain)
- Chiara Leu: PhD student (UCLouvain)
- Esther Glineur: Erasmus Master student (Université de Lyon)

Using an EEG frequency-tagging approach, sustained periodic thermonociceptive stimuli perceived as painful have been shown to modulate ongoing oscillations in the theta, alpha and beta bands, at the frequency of stimulation³⁴. Nonetheless, it remains uncertain whether these modulations are indeed linked to pain perception. To test this relationship, we modulated pain perception using a cue-based expectation modulation paradigm⁷ and investigated whether ongoing oscillations in different frequency bands mirror the changes in stimulus perception. Forty healthy participants were instructed that a visual cue could precede either a high or low-intensity stimulation. These cues were paired with three different levels of sustained periodic thermonociceptive stimuli (low, medium and high). Despite a strong effect of expectation on perceived stimulus intensity, this effect was not reflected in the modulation of the ongoing oscillations, suggesting a potential dissociation of pain perception and these oscillatory activities. Rather, it seems that the intensity of stimulation is the primary generator of the frequency tagged EEG responses.

This study, after receiving in principle acceptance as a Registered Report (<https://osf.io/qbrf2>), was recently published in a peer-reviewed journal⁸. It has also been presented at the *IASP World Congress on Pain*, Amsterdam, Netherlands, 2024.

1.2. The effect of stimulus saliency on the modulation of ongoing neural oscillations related to thermonociception (complete)

Team members participating in the study:

- Giulia Liberati: Principal Investigator (UCLouvain)
- Chiara Leu: PhD student (UCLouvain)
- Sebastien Forest: Master student and intern (UCLouvain)

To explore the relationship between pain perception, saliency, and ongoing oscillations, we employed a sustained periodic thermonociceptive stimulation paradigm with periodic oddball events and frequency-tagging analysis in a cohort of 35 healthy volunteers. Oddball stimuli were delivered at either higher or lower intensities compared to baseline stimuli, referred to as the "high oddball" and "low oddball" conditions, respectively. During the stimulation, participants provided continuous pain ratings to capture their perception in real-time. In the "high oddball" condition, continuous pain ratings closely mirrored the variations in stimulus intensity, indicating clear perception of intensity differences. In contrast, in the "low oddball" condition, participants' ratings did not distinguish between different stimulus intensities. Consistently, oddball stimuli in the "high oddball" condition modulated ongoing oscillations, whereas no such modulation was observed in the "low oddball" condition. These findings suggest that the modulation of ongoing oscillations is associated with the perception of thermonociceptive stimuli that are both salient and intense.

This study received in principle acceptance as a Registered Report (<https://osf.io/y6fb8>), and is currently under review to be published in a peer-reviewed journal (minor revisions required). It will also be presented at the *EFIC Congress*, Lyon, France, 2025.

1.3. The effect of attention on pain-related oscillations recorded from the human insula using intracerebral EEG (complete)

Team members participating in the study:

- Giulia Liberati: Principal Investigator (UCLouvain)
- Chiara Leu: PhD student (UCLouvain)
- Aïcha Boutachkourt: PhD student (UCLouvain)

If ongoing oscillations are related to the pain experience, then cognitive processes that are known to affect pain intensity (e.g. distraction) should also affect these oscillations. Using scalp EEG, Leu et al.⁹ recently investigated the effects of a distraction task on pain perception and on ongoing neural oscillations in the theta, alpha, and beta frequency bands. Whereas the intensity of pain perception was significantly reduced by the arithmetic task, no clear effect was observed on ongoing oscillations in any of the frequency bands. Hence, the fact that, unlike pain perception, these oscillations did not appear to be affected by the task suggests that they are dissociable from pain perception. However, two reasons for the lack of pain-related observable effects on neural oscillations could be (i) the lower signal-to-noise ratio of scalp EEG compared to other techniques, such as iEEG³, as well as (ii) the fact that scalp EEG might not be able to sufficiently detect activity in deeper pain-related brain regions such as the insular cortex. To this end, we conducted a study in which we used iEEG recorded using depth electrodes implanted in the insula of 8 hospitalized patients undergoing a presurgical evaluation of focal epilepsy. The patients had to perform the same task as in Leu et al.⁹, namely repeatedly subtracting 7 from a 3-digit number, while receiving a sustained periodic thermonociceptive stimulation or a frequency matched non-nociceptive vibrotactile stimulation contralaterally to the electrode implanted in the insula. A thermal cutaneous stimulator was used to deliver sustained periodic thermonociceptive stimuli (0.2 Hz). Each sustained periodic stimulation comprised 15 stimulation cycles, lasting a total of 75 s per stimulus^{3,9,10}. Inter-stimulus intervals were variable and self-paced by the experimenter to allow participants to provide intensity ratings, as well as to give responses to the arithmetic task. Sustained periodic vibrotactile stimuli were delivered via a recoil-type vibrotactile transducer driven by a standard audio, positioned between the fingertips of the index and the thumb. The vibrations consisted in a 251 Hz sine wave whose amplitude was periodically modulated at a frequency of 0.2 Hz. We chose this kind of stimulation because, despite being non-nociceptive and non-painful, it is generally perceived as highly intense, which makes it a suitable comparison to investigate whether the observed modulations might be preferential for pain perception.

The arithmetic task reduced perceived intensity for both stimulus types, but had different effects on brain activity: it decreased oscillations in the posterior insula for thermonociceptive stimuli, while increasing oscillations for vibrotactile stimuli. The posterior insula showed consistently stronger responses than the anterior insula, with thermonociceptive stimuli producing notably stronger alpha-band activity, in agreement with previous findings from the lab³. This suggests the posterior insula may have a specialized role in processing thermonociceptive signals, particularly in the alpha frequency band, though findings in other frequency bands (like theta) were less conclusive.

The manuscript of this study is currently in preparation. The study was presented at the *10th Science Factory: TMS-EEG Summer School and Workshop* — Espoo, Finland, 2024. It will also be presented at the *EFIC Congress*, Lyon, France, 2025, and the *Society for Neuroscience (SFN) Conference*, San Diego, USA, 2025.

1.4. Individualized alpha-transcranial alternating current stimulation (tACS) for modulating pain perception (complete)

Team members participating in the study:

- Giulia Liberati: Principal Investigator (UCLouvain)
- Yaser Fathi Arateh: Postdoctoral researcher (UCLouvain)
- Françoise Dissassuca: Master student and intern (UCLouvain)
- Gloria Ricci: Erasmus master student and intern (Università di Padova)

Pain encompasses sensory, affective, and cognitive dimensions, with neural oscillations increasingly recognized as key mechanisms in their integration. However, the underlying processes remain inadequately understood. Transcranial alternating current stimulation (tACS) offers a promising tool for modulating these oscillations, but its efficacy in pain modulation remains inconsistent, possibly due to a lack of individualized stimulation protocols. In this study, we investigated the effects of tACS at the individual peak alpha frequency (IAF) on both pain perception and neural oscillations. Using a within-subject, sham-controlled design, we applied tACS over the primary motor cortex (M1) contralateral to the dominant arm in 38 healthy participants. Sustained and periodic 0.2 Hz thermocceptive stimuli were applied to the dominant forearm before and after tACS. Pain perception and heat pain thresholds (HPT) were assessed before and after stimulation, while scalp electroencephalography (EEG) was recorded during the thermocceptive stimulation. To calculate IAF, we used a discriminative approach based on independent component analysis (ICA) to isolate somatosensory IAF (SM-IAF). The results revealed an overall increase in pain perception and a decrease in HPT in both sham and active conditions, with no significant interactions between conditions. However, a trend toward reduced sensitization post-tACS was observed. Exploratory analyses suggested a potential effect of tACS on HPT in women, but not in men. Furthermore, a significant correlation emerged between SM-IAF and HPT. These findings provide novel perspectives on advancing individualized neuromodulation approaches for pain.

A preprint of this study was recently published on BiorXiv¹¹. The study is also under review for publication in a peer reviewed journal. It has been presented at the *IASP World Congress on Pain*, Amsterdam, Netherlands, 2024, and at the *Transcranial Brain Stimulation Neuroscience Workshop*, Rovereto, Italy, 2024. It will also be presented at the *6th International Brain Stimulation Conferences*, Kobe, Japan, 2025, and at the *EFIC Congress*, Lyon, France, 2025.

1.5. Using periodic oscillations to analyze tACS effects on IAF (complete)

Team members participating in the study:

- Giulia Liberati: Principal Investigator (UCLouvain)
- Gloria Ricci: Erasmus master student and intern (Università di Padova)
- Yaser Fathi Arateh: Postdoctoral researcher (UCLouvain)

We aimed to assess whether tACS can modulate neural oscillations, focusing on changes in peak frequency and amplitude within the alpha band. We retrospectively analyzed EEG data from 38 healthy volunteers who followed a protocol in which tACS was delivered over M1, contralateral to a thermocceptive stimulus applied on the forearm (see Study 4 of this document). To personalize stimulation, the tACS stimulation frequency was set to the individual peak alpha frequency (IAF), with sham stimulation as a control. To allow for a more precise analysis of neural oscillations by isolating genuine oscillatory activity from background noise, we decomposed the alpha-band spectrum into aperiodic and periodic components using the FOOOF algorithm. We then fit the periodic component with a gaussian curve. Parameters of the gaussian curve - IAF, Power (PW) and Bandwidth (BW) - from the pre-stimulation condition were used to compute the Arnold tongue for each participant, namely the parameter space where synchronization between neural activity and stimulation frequency is believed to occur. A linear mixed model was used to compare the effects of "time" (pre vs post), and "condition" (active vs sham) on neural oscillations across three sessions: Eyes Open (EO), Eyes Closed (EC), and during the perception of thermocceptive stimuli (i.e. somatosensory session). While a modulation of neural oscillations was observed in all sessions under the active condition compared to sham, none of these effects reached statistical significance. However, further analysis of the BW/PW ratio using a Wilcoxon rank-sum test with Bonferroni correction revealed that the somatosensory

session had a significantly higher ratio, suggesting it provides the most effective condition for neuromodulation. This study emphasizes the importance of removing aperiodic components in analyzing neuromodulation. Importantly, it paves the way for a more personalized tACS approach, where not only the IAF is taken into account, but the stimulation frequency is tailored using each individual's Arnold tongue.

The study was recently presented at the *Transcranial Brain Stimulation Neuroscience Workshop*, Rovereto, Italy, 2024, and will guide future tACS investigations that will be conducted in 2025.

1.6. Precision targeting of temporal interference stimulation (TIS) over the insula using computational modeling and cadaver investigations (in progress)

Team members participating in the study:

- Giulia Liberati: Principal Investigator (UCLouvain)
- Yaser Fathi Arateh: Postdoctoral researcher (UCLouvain)

Noninvasive brain stimulation for the treatment of chronic pain typically targeted the primary motor cortex (M1), premotor cortex, and primary sensory cortex (S1), with a significant proportion of patients not responding to these interventions¹²⁻¹⁴. This focus is largely because these regions are easier to access due to their proximity to the brain's surface. However, deeper brain regions, particularly the insula, cannot be neglected when developing interventions¹⁵, especially considering that the dysregulation of insular oscillatory activity is often associated with chronic pain¹⁶. Crucially, because the insula is an essential hub that mediates interactions between different networks^{17,18}, it offers the potential to induce more widespread, global effects across interconnected neural systems. Unfortunately, precisely stimulating the insula without the need for invasive electrode implantation presents a significant challenge. Advances in transcranial magnetic stimulation (TMS), like cooled double-cone coils, enable deeper cortical stimulation¹⁵ but lack selectivity, possibly leading to unpredictable side effects like seizures^{19,20}. Transcranial focused ultrasound stimulation (tFUS) offers greater depth and focal resolution²¹, but requires high energy to overcome skull attenuation, risking tissue overheating and rare yet severe side effects, such as hemorrhages, cell death, cavitation damage, and blood-brain barrier disruption²². Temporal interference stimulation (TIS) could potentially enable precise targeting of deep brain structures without affecting nearby areas²³. Given its novelty and the complexity of its implementation, the application of TIS in humans has been very limited²⁴⁻²⁶, despite some preliminary research performed mostly in animals and in isolated neurons²⁷, and using computational models and simulations²⁸.

The new study, initiated at the end of 2024, aims to assess selectivity and focality of TIS in targeting different subregions of the insula while minimizing electric field (EF) exposure to adjacent or overlying cortical areas. To achieve this, we will integrate computations modeling with human cadavers, guided by simulations of EF distributions. Using high-resolution anatomical data and finite element modeling (FEM)²⁹, we will simulate EF intensity and focality across insular subregions, optimizing electrode configurations and current parameters. These models will be validated and refined by comparing simulated EFs with measurements from stereo-electroencephalography (SEEG) electrodes surgically implanted in the insula and surrounding regions of the cadavers. It is important to point out that whereas it is known that *pre-* and *post-mortem* induced EFs differ significantly in strength and frequency, *relative EF distributions* (scaled to individual minimum and maximum values) are largely comparable across conditions³⁰, meaning that the focality and spatial distribution of stimulation can be reliably assessed in human cadavers. This approach will also allow exploring the *steerability* of TIS fields, by adjusting the amplitude ratios of stimulation currents while keeping the carrier frequencies constant. Additionally, we will compare the EF

generated by insular TIS with that produced by deep brain stimulation of the insula using depth electrodes. Pilot data from 1 cadaver confirmed the feasibility of the setup and demonstrated the potential of TIS to target specific insular subregions with focal precision.

The results of our pilot study will be presented at the *6th International Brain Stimulation Conferences*, Kobe, Japan, 2025.

1.7. Exploring the link between ongoing oscillations and pain perception through high-frequency rTMS: a brain-state dependent TMS-EEG study

Team members participating in the study:

- Giulia Liberati: Principal Investigator (UCLouvain)
- Chiara Leu: PhD student (UCLouvain)
- Paolo Belardinelli: external collaborator (University of Trento)

This study initiated a collaboration between my lab and the lab of Prof. Paolo Belardinelli (University of Trento) – where Chiara Leu will spend 6 months – and will be carried out in spring 2025.

Pain is a highly flexible phenomenon, which is likely mediated by ongoing neural oscillations. To fully understand the functional relationship between ongoing oscillations and pain perception, it is imperative to investigate a causal link between these phenomena. To this end, we plan to use high-frequency brain-state dependent repetitive transcranial magnetic stimulation (rTMS) to selectively alter cortical excitability and inhibition, by stimulating either at the trough or peak of the μ -rhythm (measured online using EEG), using 200 triplets at 100 Hz at 80% of the resting motor threshold (RMT). Not unlike rTMS, pain has been shown to alter corticomotor excitability, as illustrated by a reduction in motor-evoked potentials (MEPs) following experimental pain interventions. Thus, changes in cortical excitability could potentially modulate pain perception. Using a pre-/ post-intervention paradigm, we will assess changes in the response to brief thermonociceptive stimuli (62°C, 200ms) in cortical activity measured by EEG as well as in the subjective perception of the individual. Following a high-frequency rTMS intervention targeting the trough of the μ -rhythm, we expect to induce a state of higher cortical excitability. We hypothesize that this will cause an increase in the modulation of ongoing oscillations as well as in the pain perception. Conversely, targeting the peak of the μ -rhythm would lead to an opposite effect. The obtained results will further inform us about the neurophysiology of pain and facilitate the development of novel therapeutic interventions for chronic pain patients.

The study protocol has been presented at the *Transcranial Brain Stimulation Neuroscience Workshop*, Rovereto, Italy, 2024. It will also be presented at the *6th International Brain Stimulation Conferences*, Kobe, Japan, 2025.

2. References

1. Andrews, P., Steultjens, M. & Riskowski, J. Chronic widespread pain prevalence in the general population: A systematic review. *Eur. J. Pain* **22**, 5–18 (2018).
2. Mouraux, A. & Iannetti, G. D. The search for pain biomarkers in the human brain. *Brain* **141**, 3290–3307 (2018).
3. Liberati, G. *et al.* Tonic thermonociceptive stimulation selectively modulates ongoing neural oscillations in the human posterior insula: Evidence from intracerebral EEG. *Neuroimage* **188**, 70–83 (2019).
4. Colon, E., Liberati, G. & Mouraux, A. EEG frequency tagging using ultra-slow periodic heat stimulation of the skin reveals cortical activity specifically related to C fiber thermonociceptors. *Neuroimage* **146**, 266–274 (2016).
5. Ploner, M., Sorg, C. & Gross, J. Brain rhythms of pain. *Trends Cogn Sci (Regul Ed)* **21**, 100–110 (2017).

6. Peng, W. & Tang, D. Pain related cortical oscillations: methodological advances and potential applications. *Front. Comput. Neurosci.* **10**, 9 (2016).
7. Atlas, L. Y., Bolger, N., Lindquist, M. A. & Wager, T. D. Brain mediators of predictive cue effects on perceived pain. *J. Neurosci.* **30**, 12964–12977 (2010).
8. Leu, C., Glineur, E. & Liberati, G. Cue-based modulation of pain stimulus expectation: do ongoing oscillations reflect changes in pain perception? A registered report. *Royal Society Open Science* **11**, (2024).
9. Leu, C., Courtin, A., Cussac, C. & Liberati, G. The role of ongoing oscillation in pain perception: Absence of modulation by a concomitant arithmetic task. *Cortex* **168**, 114–129 (2023).
10. Mulders, D. *et al.* Dynamics of the perception and EEG signals triggered by tonic warm and cool stimulation. *PLoS ONE* **15**, e0231698 (2020).
11. Fathi, Y., Dissassuca, F., Ricci, G. & Liberati, G. Individualized Alpha-tACS for Modulating Pain Perception and Neural Oscillations: A Sham-Controlled Study in Healthy Participants. *BioRxiv* (2025) doi:10.1101/2025.01.16.633370.
12. Garcia-Larrea, L. & Quesada, C. Cortical stimulation for chronic pain: from anecdote to evidence. *Eur. J. Phys. Rehabil. Med.* **58**, 290–305 (2022).
13. Garcia-Larrea, L. Non-invasive cortical stimulation for drug-resistant pain. *Curr. Opin. Support. Palliat. Care* (2023) doi:10.1097/SPC.0000000000000654.
14. Kong, Q., Li, T., Reddy, S., Hodges, S. & Kong, J. Brain stimulation targets for chronic pain: Insights from meta-analysis, functional connectivity and literature review. *Neurotherapeutics* e00297 (2023) doi:10.1016/j.neurot.2023.10.007.
15. Ciampi de Andrade, D. *et al.* Into the island: a new technique of non-invasive cortical stimulation of the insula. *Neurophysiol. Clin.* **42**, 363–368 (2012).
16. McBenedict, B. *et al.* The role of the insula in chronic pain and associated structural changes: an integrative review. *Cureus* (2024) doi:10.7759/cureus.58511.
17. Menon, V. & Uddin, L. Q. Saliency, switching, attention and control: a network model of insula function. *Brain Struct. Funct.* **214**, 655–667 (2010).
18. Beckmann, C. F., DeLuca, M., Devlin, J. T. & Smith, S. M. Investigations into resting-state connectivity using independent component analysis. *Philos. Trans. R. Soc. Lond. B Biol. Sci.* **360**, 1001–1013 (2005).
19. Lenoir, C. *et al.* Report of one confirmed generalized seizure and one suspected partial seizure induced by deep continuous theta burst stimulation of the right operculo-insular cortex. *Brain Stimulat.* **11**, 1187–1188 (2018).
20. Hagiwara, K., Isnard, J., Peyron, R. & Garcia-Larrea, L. Theta-burst-induced seizures reported by Lenoir *et al.*: Anterior or posterior insular seizures? *Brain Stimulat.* **12**, 200–201 (2019).
21. Badran, B. W. & Peng, X. Transcranial focused ultrasound (tFUS): a promising noninvasive deep brain stimulation approach for pain. *Neuropsychopharmacology* **49**, 351–352 (2024).
22. Pasquinelli, C., Hanson, L. G., Siebner, H. R., Lee, H. J. & Thielscher, A. Safety of transcranial focused ultrasound stimulation: A systematic review of the state of knowledge from both human and animal studies. *Brain Stimulat.* **12**, 1367–1380 (2019).
23. Grossman, N. *et al.* Noninvasive deep brain stimulation via temporally interfering electric fields. *Cell* **169**, 1029–1041.e16 (2017).
24. von Conta, J. *et al.* Benchmarking the effects of transcranial temporal interference stimulation (tTIS) in humans. *Cortex* **154**, 299–310 (2022).
25. von Conta, J. *et al.* Interindividual variability of electric fields during transcranial temporal interference stimulation (tTIS). *Sci. Rep.* **11**, 20357 (2021).
26. Violante, I. R. *et al.* Non-invasive temporal interference electrical stimulation of the human hippocampus. *Nat. Neurosci.* **26**, 1994–2004 (2023).
27. Caldas-Martinez, S. *et al.* Cell-specific effects of temporal interference stimulation on cortical function. *Commun. Biol.* **7**, 1076 (2024).
28. Rampersad, S. *et al.* Prospects for transcranial temporal interference stimulation in humans: A computational study. *Neuroimage* **202**, 116124 (2019).
29. Camera, F., Merla, C. & De Santis, V. Comparison of Transcranial Magnetic Stimulation Dosimetry between Structured and Unstructured Grids Using Different Solvers. *Bioengineering (Basel)* **11**, (2024).
30. Opitz, A., Falchier, A., Linn, G. S., Milham, M. P. & Schroeder, C. E. Limitations of ex vivo measurements for in vivo neuroscience. *Proc Natl Acad Sci USA* **114**, 5243–5246 (2017).



Geneeskundige Stichting Koningin Elisabeth
Fondation Médicale Reine Elisabeth
Königin-Elisabeth-Stiftung für Medizin
Queen Elisabeth Medical Foundation

Progress report of the research project of the young researcher

Prof. dr. Jeroen Bogie
Universiteit Hasselt (UHasselt)

Prof. dr. Jeroen Bogie (UHasselt)

Assistant Professor

T +32(0)11 26 92 61

www.uhasselt.be

Universiteit Hasselt - Campus Diepenbeek

Agoralaan Gebouw D - B-3590 Diepenbeek

Kantoor BMO-C107a

Getting a grip on slippery protein modifications in multiple sclerosis

1. State-of-the-art

A major pathological hallmark of neuroinflammatory disorders such as multiple sclerosis (MS) is the accumulation of macrophage subsets and T cells within the CNS. Driving these immune cells towards an anti-inflammatory, repair-promoting phenotype is considered a promising therapeutic strategy to halt MS disease progression and promote CNS repair. Emerging evidence indicates that fatty acids control the fate of immune cells in inflammatory disorders such as MS. We and others demonstrated that changes in the desaturation, -oxidation, and synthesis of fatty acids regulate the induction and maintenance of anti-inflammatory and reparative macrophage, microglia, and CD4⁺ T cell subsets in experimental models of MS. To date, however, the culprit fatty acids and molecular mechanisms that govern their influence on immune cell function and MS pathology remain ill-defined.

The saturated fatty acid palmitate is the most common fatty acid in the human body. It is situated at the heart of fatty acid metabolism, as it is the primary end-product of fatty acid synthesis and represents a major substrate for -oxidation and desaturation. We recently demonstrated that subtle changes in cellular palmitate levels have a major impact on the inflammatory and reparative properties of immune cells *in vitro* and in animal models of MS. Most studies on fatty acids in general, and palmitate in particular, focused on their role in energy metabolism and their effect on membrane composition. Based on our preliminary findings, we propose that S-palm, a posttranslational modification that consists of the reversible addition of palmitate to cysteine residues on proteins, is an important determinant of palmitate function in immune cells and MS pathology. In line with the importance of this modification, palmitoyl-proteome screens indicate that over 10% of the proteome is susceptible to S-palm, and accordingly, a family of 24 zinc finger DHHC-domain containing proteins (zDHHCs) have been identified as palmitoyl-transferases. Ample evidence indicates that S-palm dynamically regulates protein membrane interactions, intracellular sorting, and stability, and in doing so, tightly controls cellular function in health and disease.

Our understanding of the role of S-palm in immunity is limited. Importantly, no studies have thus far addressed how changes in the S-palm landscape and machinery impact the polarization of primary macrophage, microglia, and T cell subsets, and to what extent these alterations can be harnessed to reduce neuroinflammation and promote CNS repair. The short-term goal of this project is to address the role of S-palm in the induction of disease- and repair-associated immune cell subsets in MS. The long-term goal of this project is to identify S-palm as a novel therapeutic target to suppress neuroinflammation and promote CNS repair in MS.

2. Acquired data

The data we have acquired so far pertain to the impact of S-palmitoylation on T cell physiology and autoimmunity (1), as well as on microglia physiology and remyelination (2). In this section, we will briefly address the findings related to (1) and outline upcoming experiments. For (2), we have included a preliminary version of the manuscript, which we plan to submit by the end of Q1 2025.

2.1. Inhibition of S-palmitoylation prevents autoimmunity in MS.

Autoimmunity is widely recognized as a key driver of disease initiation and progression in MS. In this context, autoreactive T cells have been extensively studied, and promoting the formation of immunosuppressive immune cell subsets is regarded as a highly promising therapeutic strategy to halt disease progression. We identified S-palm as a pivotal driver of autoimmune-mediated brain pathology and T cell physiology in MS. In the experimental autoimmune encephalomyelitis (EAE) model¹⁰⁰, commonly utilized to study T cell-mediated autoimmunity in MS, S-palm pan-inhibition using 2-bromopalmitate completely prevented EAE disease severity. Considering the complete absence of EAE disease, we anticipated that early changes in secondary lymphoid organs underlie the benign impact of S-palm inhibition. Indeed, immunophenotyping revealed that reduced EAE disease severity was linked to diminished cognate antigen-specific T cell proliferation and an increase in regulatory and anergic T cells (Treg and Tan) in secondary lymphoid tissue. Interestingly, *in vitro* experiments revealed that S-palm does not significantly affect T cell physiology directly. Instead, it induces a tolerogenic dendritic cell (DC) phenotype, which we confirmed as being unable to activate autoreactive T cells in co-culture experiments. Furthermore, our preliminary findings suggest that the inhibition of zDHHC2 is a key driver of the effects of 2-BP on DCs. In the coming year, we aim to:

1. Obtain a holistic perspective on cellular changes in the lymph nodes of EAE mice. To achieve this, we are currently performing single-cell RNA sequencing.
2. Confirm the role of S-palmitoylation in DCs in driving the formation of autoreactive T cells in MS-related autoimmunity. This will be addressed through adoptive transfer experiments using 2-BP-treated DCs.
3. Determine the importance of zDHHC2 in regulating DC physiology both *in vitro* and *in vivo*. For this purpose, we will utilize global and DC-specific zDHHC2-deficient mice. The ethical matrices required for this work have been submitted.
4. Identify proteins that are S-palmitoylated by zDHHC2 and validate their significance in DC physiology and autoimmunity. Over the past year, we have optimized a click-chemistry approach to analyze the complete palmitoyl-proteome to support this investigation.

2.2. Inhibition of S-palmitoylation enhances remyelination by inducing reparative microglia.

Below is a preliminary version of the manuscript. For brevity, we have omitted the corresponding figures. Once the final experiments are completed, we plan to submit the manuscript, with an expected submission date of March 1, 2025.

S-palmitoylation impedes brain repair by perturbing foam cell physiology

Jeroen Guns^{1,2}, Sam Vanherle^{1,2}, Samiksha Sardana³, Brecht Moonen^{1,2}, Lien Van Otterdijk^{1,2}, Melanie Loix^{1,2}, Koen Kuipers^{1,4}, Flore Wouters^{1,2}, Tess Dierckx, Yan Lu, Leen Timmermans^{1,2}, Tim Vangansewinkel^{4,6}, Ivo Lambrechts, Esther Wolfs⁴, Bieke Broux^{1,2}, Bart Ghesquière, Florian Hermans⁴, Noam Zelcer⁷, Dante Neculai⁹, Marc Baggelaar³, Miranda Nabben^{10,11,12}, Jerome JA Hendriks^{1,2}, Joost Luiken^{10,11}, Jeroen FJ Bogie^{1,2}.

1. Hasselt University, Department of Immunology and Infection, Biomedical Research Institute, Diepenbeek, Belgium.
2. University MS Center Hasselt, 3900, Pelt, Belgium.
3. Utrecht University, Biomolecular Mass Spectrometry & Proteomics Group, Utrecht, The Netherlands.
4. UHasselt, Department of Cardio and Organ Systems, Biomedical Research Institute, Diepenbeek, Belgium.
5. Maastricht University, The Maastricht MultiModal Molecular Imaging (M4I) institute, Division of Imaging Mass Spectrometry (IMS), 6229 ER Maastricht, The Netherlands.
6. University of Leuven, VIB, Center for Brain & Disease Research, Laboratory of Neurobiology, Leuven, Belgium.

7. University of Amsterdam, Department of Medical Biochemistry, Amsterdam Cardiovascular Sciences and Gastroenterology and Metabolism, Amsterdam, The Netherlands.
8. University of Wollongong, Molecular Horizons and School of Chemistry and Molecular Bioscience, Wollongong, New South Wales 2522, Australia.
9. Zhejiang University School of Medicine, Department of Cell Biology, Hangzhou, China.
10. Maastricht University, Department of Genetics and Cell Biology, Faculty of Health, Medicine and Life Sciences, the Netherlands.
11. Maastricht University Medical Center+, Department of Clinical Genetics, the Netherlands.
12. Cardiovascular Research Institute Maastricht School for Cardiovascular Diseases, Maastricht, the Netherlands.

Corresponding author: Jeroen F.J. Bogie (Jeroen.bogie@uhasselt.be)

3. Abstract

Disturbances in the formation of disease-resolving macrophage and microglia subsets are closely implicated in failure of brain repair in neurodegenerative disorders. Despite lipids being essential in controlling the phenotypic fate of these phagocytes, the exact lipid species and the molecular mechanisms involved in driving their impact on phagocyte physiology in the brain remain poorly understood. Here, we show that S-palmitoylation, a post-translational modification involving the binding of the palmitate to proteins, is altered in actively demyelinating brain lesions. By applying pharmacological inhibitors, transgenic mice, and pre-clinical models, we find that S-palmitoylation impedes remyelination by perturbing the metabolic and inflammatory features of foamy macrophages and microglia, and identify a key role for palmitoyl acyltransferase 5 (zDHHC5) in this process. Guided by RNA sequencing, zDHHC5-mediated S-palmitoylation was found to hamper the nuclear translocation of fatty acid binding protein 5, consequently attenuating activation of PPAR α and the induction of a reparative phagocyte phenotype. Finally, we demonstrate the efficacy of lomitapide, a recently repurposed zDHHC5 inhibitor, as a promising therapeutic agent for promoting remyelination by enhancing the formation of pro-regenerative phagocytes. Collectively, our findings underscore the detrimental impact of S-palmitoylation on remyelination and highlight zDHHC5-mediated FABP5 S-palmitoylation as a novel therapeutic target for myelin regeneration.

4. Introduction

Failure of remyelination, characterized by deficient formation of myelin sheaths around demyelinated axons by newly formed oligodendrocytes, constitutes a key driver of disease progression in chronic demyelinating disorders such as multiple sclerosis (MS)¹⁻³. Recent insights underscore disruptions in the physiology of brain-resident microglia and infiltrated peripheral macrophage subsets as fundamental determinants of this failure⁴⁻⁶. Dysregulations in fatty acid (FA) metabolism, encompassing both their anabolism and catabolism, are linked to the compromised regenerative potential of these phagocytic cells within brain lesions⁷⁻⁹. Specifically, aberrations in key metabolic pathways, including FA desaturation¹⁰, elongation¹¹, and -oxidation^{12,13}, are posited to influence the dualistic roles of macrophages and microglia in the progression and resolution of MS brain lesions. This concept mirrors the critical involvement of FA metabolism in modulating the bifunctional nature of myeloid cells in peripheral disorders^{14,15}. Yet, despite serving as a central substrate and product of these metabolic cascades, the precise impact of the saturated FA palmitate on macrophage and microglia physiology within demyelinating brain lesions remains elusive and warrants further investigation at the molecular level.

Most studies on FAs in general, and palmitate in particular, have focused on their integral function in energy metabolism and membrane composition, as well as the consequences of alterations in these metabolic activities on cellular phenotypes. However, recent research spotlights S-palmitoylation, a post-translational modification involving the binding of palmitate to cysteine residues on proteins, as a crucial regulator of protein trafficking, stability, and interactions^{16,17}. Disruptions in S-palmitoylation significantly affect cellular function and metabolism across both healthy and diseased states¹⁸⁻²⁸, with ample evidence indicating a key for S-palmitoylation in controlling immune cell activity²⁹⁻³¹. Underscoring its significance and specificity, palmitoyl-proteome screens indicate that over 20% of the proteome is susceptible to S-palmitoylation, and accordingly, a family of 24 zinc finger and DHHC motif containing palmitoyl acyltransferases (zDHHCs) is identified to catalyze protein S-acetylation by palmitate¹⁶. Here, we sought to determine the impact of S-palmitoylation on MS lesion pathology and remyelination, probing whether alterations in S-palmitoylation associated with demyelination affect remyelination and the regenerative capacity of macrophages and microglia.

5. Results

5.1. Active MS lesions display an altered S-acylome

Recent studies, including our own, demonstrate marked alterations in the lipidome of human actively demyelinating MS lesions, particularly in palmitate levels^{10,32-34}. To assess changes in protein S-palmitoylation in these lesions, we applied acyl-biotin exchange (ABE), a cysteine-centric proteomic approach for assessing protein S-acetylation (workflow depicted in **supplementary Figure 1A**)³⁵. Although ABE identifies the sparse attachment of FAs other than palmitate to protein cysteine residues, S-acetylation is primarily mediated by palmitate and ABE remains the sole method to measure the S-acylome in cryopreserved tissue³⁶. Actively demyelinating MS lesions were characterized by enrichment of HLA-DR⁺ phagocytes, loss of PLP⁺ myelin sheaths, and accumulation of lipid droplet (LD)-containing ORO⁺ phagocytes (**Figure 1A** and **supplementary Figure 1B**). Prior to assessing lesional differences in protein S-acetylation, we defined the efficacy of ABE in defining the S-acylome in human post-mortem brain tissue. Our findings highlight a notable absence of proteins in active MS lesion and adjacent normal-appearing white matter (NAWM) lysates not subjected to hydroxylamine (HA; negative control), whereas lysates exposed to HA showed an enrichment of established S-palmitoylated proteins, including GNAX, GNA13, VAMP3, HRAS, SNAP25, and CAV1 (**Figure 1B**)^{16,17,37}. By consulting the SwissPalm database³⁸, we further found that the majority of differentially S-acylated proteins identified in our ABE analysis had either been recognized (63%) or validated (18%) in earlier S-acylome studies (**Table 1**). Protein hits included several S-palmitoyl transferases (zDHHC2, 5, 9, 17, and 20), pointing towards their abundance and enhanced activity in brain tissue.

Having established the robustness of our ABE analysis in post-mortem human brain tissue, we next examined differences in protein S-acetylation between MS lesions and adjacent NAWM. Our analysis revealed that 32 S-acetylated proteins distinguished active demyelinating MS lesions from adjacent NAWM, with 12 exhibiting decreased levels and 20 exhibiting increased levels in active MS lesions (**Figure 1C**). Pathway analysis using Ingenuity Pathway Analysis (IPA) showed an enrichment of these differentially S-acetylated proteins in biological processes and molecular functions associated with FA and cholesterol metabolism, cell migration, and endocytosis (**Figure 1D**). Upstream regulator analysis further revealed that differentially S-acylated proteins were linked to inflammatory signaling molecules and pathways, including LPS, IFNG, IL1, TNF, and STAT6 (**Figure 1E**). This aligns with inflammation being a driver of early MS lesion pathology and supports the molecular relationship between S-palmitoylation and immunity^{2,29,31}.

To determine whether changes in the abundance of S-palmitoylated proteins are reflected in overall protein levels, proteomic analyses was conducted on MS lesion and NAWM lysates. The majority of the proteins clustered along the $x = y$ diagonal when plotting the fold changes in abundance between MS lesions and NAWM as observed in the S-acylome compared to the proteome (**supplementary Figure 1C**), indicating an equal change in S-palmitoylated protein and total protein abundance. However, several proteins that distinguished MS lesions and NAWM in the ABE analysis, including NQO1, HSP90AB2P, EFHD2, and TTYH2, deviated from this diagonal, indicating altered S-palmitoylation stoichiometry in MS lesions compared to NAWM. The validity of our proteomic analysis was confirmed by the increased lesional abundance of proteins previously associated with MS pathology, including HLA-DRB1, HLA-DRBA, C3, and STAT3 (**supplementary Figure 1D**)³⁹⁻⁴¹. Collectively, these findings highlight that active MS lesions have an altered S-acylome, and likely S-palmitoylome, compared to adjacent NAWM.

5.2. S-palmitoylation impairs remyelination by affecting macrophage and microglia function

Aberrations in FA metabolism are tied to failure of remyelination in MS lesions^{10,11,42}. To elucidate whether S-palmitoylation impacts remyelination, the cerebellar brain slice culture model (BSC) was utilized. In this model, lysolecithin-induced demyelination is followed by spontaneous endogenous remyelination, enabling the study of remyelination at both cellular and molecular levels (workflow in **supplementary Figure 2A**)¹⁰. Our results reveal that exposure to 2-bromopalmitate (2BP), a broad-spectrum inhibitor of zDHHCs^{43,44}, substantially enhanced the colocalization of myelin (myelin basic protein; MBP) and axons (neurofilament, NF) in demyelinated BSCs (**Figure 2A-B**), indicative of increased remyelination. Three-dimensional reconstruction of these slices confirmed more efficient axonal myelination upon exposure to 2BP (**Figure 2A**)⁴⁵.

Given the abundant presence of myelin-phagocytosing foamy microglia in demyelinated BSCs and their importance in controlling efficient remyelination¹⁰, we proceeded to characterize their presence in control and 2BP exposed BSCs. Histological and immunostaining analysis revealed a decreased presence of LD-containing microglia, evidenced by a reduced ORO reactivity and a lower number of F4/80⁺ BODIPY⁺ microglia in 2BP-exposed BSCs (**Figure 2C-D** and **supplementary Figure 2B-C**). Building on our previous studies, which revealed that sustained myelin-derived lipid accumulation and the formation of LDs in foamy microglia induces a repair-inhibitory phenotype^{10,11,42}, we postulated that 2BP enhances remyelination in BSCs by modulating the physiology of foamy microglia. In support of this notion, microglia depletion using chlodronate liposomes counteracted the pro-regenerative impact of 2BP in BSCs (**Figure 2E** and **supplementary Figure 2D**). Brain slices depleted of microglia exhibited reduced remyelination efficacy compared to those sufficient in microglia (**Figure 2E**), consistent with microglia being essential for remyelination^{10,11,46}. Efficient targeting and depletion of microglia using chlodronate liposomes was confirmed using immunostainings (**supplementary Figure 2E**). Collectively, these findings show that pharmacological inhibition of S-palmitoylation enhances remyelination in brain slices in a microglia-dependent manner.

To evaluate the significance of these findings *in vivo*, the cuprizone-induced de- and remyelination model was applied. Cuprizone feeding leads to reproducible toxic demyelination in distinct brain regions, the corpus callosum (CC) in particular, while discontinuing its use prompts endogenous remyelination (workflow depicted in **supplementary Figure 2F**; efficient demyelination/remyelination is depicted in **supplementary Figure 2G-I**). Intraperitoneal administration of 2BP, starting after cessation of cuprizone feeding (5w), significantly increased MBP abundance in the CC during remyelination (5w+1) (**Figure 2F-G**). Mirroring these findings, mice treated with 2BP exhibited an increase in myelinated axons and a reduced g-ratio in the CC, indicative of

thicker myelin sheaths, a proxy of effective remyelination (**Figure 2H-J**). In particular, small diameter axons showed thicker myelin sheaths in 2BP treated cuprizone mice as compared with control mice (**supplementary Figure 2J**). Similar to BSCs, improved remyelination in 2BP-treated cuprizone mice was paralleled by a reduced ORO abundance in the CC (**Figure 2K-L**). These observations indicate that pharmacological blockade of S-palmitoylation augments remyelination in the cuprizone model, potentially through a mechanism reliant on changing foamy microglia physiology.

Studies indicate that 2BP impacts cellular metabolism in ways unrelated to S-palmitoylation⁴⁷. Hence, to confirm the importance of S-palmitoylation on remyelination and foam cell abundance, we next defined the impact of inhibition of acylprotein thioesterases 1 and 2 (APT1 and APT2) – the primary enzymes involved in depalmitoylation^{16,17} – on remyelination. Exposure to the APT1 inhibitor (ML348), but not the APT2 inhibitor (ML349), reduced the colocalization of MBP and NF in BSCs (**supplementary Figure 3A-B**), which was paralleled by an increased ORO load (**supplementary Figure 3C-D**). Similarly, intraperitoneal administration of ML348, starting after cessation of cuprizone feeding, reduced MBP abundance and increased ORO reactivity in the CC (**supplementary Figure 3E-H**). These findings corroborate the repair-inhibitory impact of S-palmitoylation in the CNS and argue for APT1 being essential in controlling S-palmitoylation dynamics during remyelination.

5.3. S-palmitoylation promotes LD formation and enhances myelin uptake by macrophages and microglia

We and others recently found that the accumulation of LDs induces a highly inflammatory, repair-inhibitory foamy macrophage and microglia phenotype^{10,11,42}. To study the impact of S-palmitoylation on LD accumulation in more detail, *in vitro*-generated mouse foamy bone marrow-derived macrophages (BMDMs) were used. Analogous to the BSC and cuprizone models, 2BP exposure reduced ORO and BODIPY load in foamy BMDMs *in vitro* (**Figure 3A-C**). Conversely, inhibition of APT1, but not APT2, led to an increased ORO and BODIPY load in these cells (**supplementary Figure 4A-C**). A similar increase in ORO load was observed when using the dual APT1/APT2 inhibitor palmostatin B (**supplementary Figure 4A-C**)⁴⁸. Cell viability was not affected in macrophage cultures exposed to the divergent S-palmitoylation modulators (**supplementary Figure 4D**). Noteworthy, alongside BMDMs, 2BP also reduced ORO and BODIPY load in mouse microglia and human monocyte-derived macrophages (MDMs) exposed to isolated mouse and human myelin, respectively (**Figure 3D-E** and **supplementary Figure 4E**). These experiments demonstrate that S-palmitoylation enhances the intracellular LD burden in foamy macrophages and microglia.

Cellular lipid accumulation in foam cells is regulated through a complex interplay of myelin-derived lipid uptake, intracellular processing, and efflux⁹. Here, we explored the impact of S-palmitoylation on these different metabolic processes. By using Dil- and pHrodo-labeled myelin, we found that 2BP exposure resulted in a marked reduction in the internalization and lysosomal accumulation of myelin by BMDMs (**Figure 3F-G** and **supplementary Figure 4F**). Interestingly, 2BP did not impact the uptake of latex beads (**supplementary Figure 4G**), excluding an impact of 2BP on non-specific phagocytosis. Similar to BMDMs, 2BP reduced pHrodo-labeled myelin uptake by mouse microglia and human MDMs (**Figure 3J**). Despite affecting ORO load in a manner opposite to 2BP, blocking depalmitoylation with palmostatin B, ML348, and ML349 did not enhance myelin uptake by BMDMs (**supplementary Figure 4H**). The latter finding could potentially indicate the multifaceted impact of S-palmitoylation on the metabolic phenotype of foam cells or point towards an already diminished activity of APTs in foam cells *in vitro*. In our hands, 2BP did not affect cholesterol efflux via ATP binding cassette transporter A1 and G1 (ABCA1 and

ABCG1) (**supplementary Figure 4I**), nor did it impact the processing of intracellular ORO⁺ LDs after BMDMs were pre-treated with myelin (**supplementary Figure 4J**). The latter finding suggests that changes in LD degradation via lipolysis and lipophagy - processes we previously demonstrated to be essential for controlling LD load in foam cells^{42,49} - are not influenced by S-palmitoylation. Overall, these findings demonstrate that S-palmitoylation drives the internalization of myelin by foamy macrophages and microglia, without affecting the intracellular processing or efflux of myelin-derived lipids.

5.4. S-palmitoylation induces an inflammatory foamy macrophage and microglia phenotype

To further study the impact of S-palmitoylation on the phenotype of foam cells, bulk RNAseq was performed on control and foamy BMDMs exposed to 2BP. Prior to sequencing, cultures were exposed to LPS/IFN to mimic the inflammatory activation seen in active MS lesions¹⁰. Differential gene expression analysis revealed that 3938 genes distinguished control and 2BP-exposed BMDMs, with 1724 upregulated and 2214 downregulated in 2BP-exposed BMDMs (**Figure 3H** and **supplementary Table 2**). Foamy BMDMs treated with 2BP displayed a remarkably similar transcriptional profile, with 4,137 differentially expressed genes (DEGs), of which 2,221 were upregulated, 1,916 were downregulated, and 1,978 (~50%) overlapped between control and 2BP-treated foamy BMDMs (**Figure 3H** and **supplementary Table 2**). Mirroring the overlap in DEGs, upstream regulator analysis using IPA demonstrated that DEGs in 2BP-exposed control and foamy BMDMs were associated with a reduced activation of IFN and TLR signaling pathways (e.g., IRF3, IRF7, IRF9, IFNAR, STAT1, IFNA, IFNG, and LPS), increased anti-oxidative stress response (e.g., NFE2L2 and quercetin), and peroxisome proliferator-activated receptor (PPAR) ligation (e.g., rosiglitazone, pioglitazone, genistein, and troglitazone) (**Figure 3I**). Consistent with these findings, the transcriptional profile of 2BP-treated control and foamy BMDMs showcased heightened engagement in biological pathways associated with ROS detoxification and nuclear receptor activation, and a reduced activity of biological pathways linked to inflammation, endocytosis, and MS pathology (**Figure 3J**). Taken together, the RNAseq analysis indicates that pharmacological inhibition of S-palmitoylation leads to a less-inflammatory macrophage phenotype, characterized by enhanced activation of nuclear receptors such as PPARs. This phenotype resembles a macrophage profile that we previously demonstrated to alleviate neuroinflammation and promote remyelination^{10,11}.

To confirm alterations in inflammatory and antioxidant pathways observed in the RNA-seq analyses, we assessed the expression and abundance of cytokines, along with the formation of reactive nitrogen and oxygen species (RNS and ROS) in macrophages and microglia exposed to 2BP. We find that 2BP reduced the expression and abundance of IL1B, IL6, and CCL5 in myelin-treated mouse BMDMs (**Figure 3K-L**). Similarly, 2BP reduced the intracellular abundance and release of ROS and NO, respectively, in foamy murine BMDMs and microglia (**Figure 3M-N**). While APT1 inhibition using ML348 increased ROS and NO formation by foamy BMDMs, it reduced *Il1b*, *Il6*, and *Ccl5* expression, albeit to a lesser extent than 2BP (**supplementary Figure 5A-C**). Alike mouse macrophages, 2BP decreased *Il1b*, *Il6*, and *Ccl5* expression and ROS/RNS formation by foamy microglia (**supplementary Figure 5D-F**). Human foamy MDMs exposed to 2BP showed a decreased expression of *IL6* and *CCL5*, but not *IL1B*, and also generated less ROS (**supplementary Figure 5G-H**). No NO was detected in culture supernatants of foamy MDM cultures (data not shown), which could point towards murine and human macrophages differing in their responses to inflammatory stimuli⁵⁰. Thus, S-palmitoylation promotes the formation of an inflammatory (foamy) macrophage and microglia phenotype.

5.5. S-palmitoylation suppresses PPAR γ signaling and FABP5 nuclear translocation

Alongside affecting the endocytic and inflammatory features of (foamy) macrophages and microglia, RNAseq analysis identified increased PPAR activation in macrophages upon 2BP exposure. With PPARs being drivers of cellular metabolism and inflammation⁵¹, we reasoned that their enhanced activation may underpin the metabolic and inflammatory phenotype of macrophages and microglia upon exposure to 2BP. First, by using luciferase reporter assays, we confirm that 2BP increases the ligation of PPAR, PPAR γ , and PPAR upon myelin exposure, with PPAR γ showing the most pronounced increase (**Figure 5A**). No ligation of PPAR isoforms was observed in control cultures exposed to 2BP, excluding a direct impact of 2BP on PPAR γ ligation⁵². Consistent with enhanced PPAR ligation, 2BP increased the expression of responsive genes such *Cpt1a*, *Cd36*, and *Scd1* in foamy BMDMs (**Figure 5B**). Next, we explored whether antagonism of PPAR isoforms counteracted the less-inflammatory phenotype of macrophages exposed to 2BP. Our data indicate that antagonism of PPAR γ , but not PPAR and PPAR, nullified the reduced expression of *Il1b*, *Il6*, and *Ccl5* (**Figure 5C** and **supplementary Figure 7A**), as well as the formation of ROS and NO (**Figure 5D-E**), by foamy BMDMs exposed to 2BP. In conjunction with mitigating the effects of 2BP on the inflammatory and oxidative stress response of macrophages and microglia, PPAR γ antagonism counteracted the reduced LD load and myelin internalization observed following 2BP exposure (**Figure 5F-H**). While the latter finding does not match the reported positive correlation between PPAR γ activation and receptor-mediated endocytosis of FAs and apoptotic cells⁵³, few studies indicate that PPAR γ may not affect, or could even suppress, the uptake of (lipid-containing) macromolecules^{54,55}. In this respect, PPAR γ agonism attenuated the uptake of myelin by macrophages (**supplementary Figure 7B**). Overall, this data emphasizes that enhanced PPAR γ activation underlies the effects of 2BP on the metabolic and inflammatory phenotype of foamy macrophages.

FA binding protein 5 (FABP5) is tuned to selectively stimulate PPAR γ transactivation through its capability to localize to the nucleus and distribute FAs to PPAR γ ^{56,57}. As 2BP enhanced PPAR γ activation (**Figure 5A-F**) and MS lesions showing showed increased FABP5 acylation (**Figure 1C**), we next sought to determine to what extent FABP5 S-palmitoylation controls its nuclear translocation and underpins PPAR γ ligation in foam cells. By using an untargeted click-chemistry approach, we first confirmed FABP5 S-palmitoylation in macrophages and the inhibitory impact of 2BP on this process (**Figure 5G**; a complete list of differentially S-palmitoylated proteins can be found in **supplementary table 3**). Next, site-directed mutagenesis experiments were performed to identify cysteine residues, predicted by SwissPalm³⁸, involved in driving FABP5 S-palmitoylation. Our findings indicate that Cys127, and not Cys43, Cys120, or Cys67, is essential for FABP5 S-palmitoylation (**Figure 5H**). To study the impact of S-palmitoylation on the nuclear trafficking of FABP5, FABP5^{C127S} mutants and 2BP were used. Immunostainings demonstrated that reduced FABP5 S-palmitoylation markedly increased its nuclear localization (**Figure 5I-J**). Accordingly, similar to 2BP, palmitoylation-deficient FABP5^{C127S} mutants showed increased PPAR γ ligation. To further proof the importance of nuclear trafficking of FABP5 in driving PPAR γ ligation in foam cells, FABP5 mutants lacking the nuclear localization signal (FABP5^{nlsm}) were used⁵⁸. Abrogation of FABP5 nuclear translocation was found to confirm cytosolic retention and reduce PPAR γ ligation in foam cells. All in all, these findings confirm FABP5 S-palmitoylation and highlight a key role of S-palmitoylation in suppressing nuclear import of FABP5, thereby controlling PPAR γ ligation.

Few studies demonstrated that FABP5 facilitates the uptake of exogenous FAs^{59,60}. Having established increased FABP5 nuclear localization upon 2BP exposure, we asked whether the resulting decrease in cytosolic FABP5 underpins the reduced capacity of these cells to internalize myelin. Supporting this notion, phagocytosis assays revealed that both FABP5^{C127S} mutants exhibited a reduced ability to internalize myelin. Accordingly, FABP5^{C127S} mutants demonstrated

a lower ORO load. These findings strongly suggest that 2BP reduces myelin internalization by decreasing the cytosolic abundance of FABP5.

5.6. zDHHC5 induces an inflammatory macrophages and microglia phenotype

S-palmitoylation is catalyzed by the action of 24 zDHHCs that attach FAs to cysteine residues on proteins^{16,17}. Here, we set out to identify zDHHCs whose inhibition underlies the impact of 2BP on the phagocyte physiology and remyelination. To this end, we measured the expression of zDHHCs in actively demyelinating MS lesions, the corpus callosum of cuprizone-fed mice, and inflammatory control and myelin-treated macrophage subsets *in vitro*. An increase in the expression of both *zDHHC5* and *zDHHC18* was observed across all four models, suggesting that their inhibition could be a principal target of 2BP. To confirm elevated expression of *zDHHC5* and *zDHHC18* in microglia in MS lesions, we re-analyzed published single nuclei RNAseq (snRNAseq) data of distinct MS lesion types⁶¹. Microglia were identified using the marker *P2RY12*, extracted using Seurat, and clustered at a resolution of 0.3 with a threshold of <15% mitochondrial RNA using the clustering markers described by Schirmer et al.⁶¹. While enhanced microglial *zDHHC5* expression was observed in MS lesions compared to control tissue, *zDHHC5* did not map to specific microglia subclusters. Through analysis of DEGs between *zDHHC5*⁺ compared to *zDHHC5*⁻ microglia, IPA did, however, identify that DEGs distinguishing these microglia subsets were associated inflammation, endocytosis, and lipid metabolism, based on increased expression of *IL1B*, *IL6*, and *CCL5*. Elevated *zDHHC5* abundance in HLA-DR⁺ macrophages and microglia in actively demyelinating MS lesions was confirmed using immunostainings. In contrast to *zDHHC5*, snRNAseq analysis showed that *zDHHC18* was barely expressed in brain microglia, both in MS lesions and control tissue, and instead was enriched in astrocytes.

Upon verifying enhanced *zDHHC5* abundance in lesional and inflammatory macrophage and microglia subsets, we next asked whether deficiency of *zDHHC5* induces an inflammatory and metabolic phagocyte phenotype akin to cells exposed to 2BP. To this end, BMDMs were isolated from *zDHHC5*^{fl/+}*Lysm*^{cre+/-} mice²⁰. Alike 2BP-exposed BMDMs, *zDHHC5*^{-/-} foamy BMDMs showed decreased intracellular ORO and BODIPY load, endocytosis of pHrodo-labeled myelin, release of ROS and NO, and *IL1b* expression. In accordance with the importance of PPAR α in driving the phenotype of *zDHHC5*^{-/-} BMDMs, PPAR α antagonism nullified the impact of *zDHHC5* deficiency on the metabolic and inflammatory phenotype of macrophages. An unsupervised click-chemistry proteomic approach to study the S-palmitoylome further showed absence of FABP5 S-palmitoylation in *zDHHC5*^{-/-} BMDMs. All in all, these findings convincingly show that absence of *zDHHC5* induces a favorable metabolic and inflammatory foamy phagocyte phenotype.

5.7. zDHHC5 knockout boosts remyelination in a phagocyte-specific manner

With *zDHHC5* deficiency mimicking the impact of 2BP on (foamy) phagocyte physiology, we next determined if deficiency of *zDHHC5* in macrophages and microglia enhances remyelination. Our findings indicate that *zDHHC5*^{fl/+}*LysM*^{-/-} mice showed an increased MBP abundance and a reduced g-ratio in the CC during remyelination (5w+1) as compared to wild-type mice. Of note, macrophage and microglia-specific depletion of *zDhhc5* did not impact cuprizone-mediated demyelination in the CC (5w), indicating that its absence in phagocytes does not protect against demyelination. Similar to 2BP exposed cuprizone mice, enhanced remyelination was associated with a reduced ORO load in the CC. Thus, these findings provide evidence that *zDHHC5* impedes the formation of reparative (foamy) phagocyte subsets during active demyelination.

5.8. Lomitapide induces a benign phagocyte phenotype and enhances remyelination

Lomitapide is an FDA-approved microsomal triglyceride transfer protein (MTTP) inhibitor utilized to reduce (very) low-density lipoprotein (vLDL) cholesterol levels⁶². However, a recent study has introduced a compelling repositioning of lomitapide, identifying it as an inhibitor of zDHHC5⁶³. In this context, we explored the impact of lomitapide on the phenotype of foamy BMDMs and remyelination. Lomitapide paralleled the effects observed with pharmacological inhibition of S-palmitoylation and genetic deficiency of *zDhhc5*. It not only reduced myelin phagocytosis and intracellular lipid accumulation, but also induced a less-inflammatory BMDM phenotype. Mechanistically, lomitapide exposure decreased S-palmitoylation of FABP5, leading to increased nuclear localization of FABP5 and enhanced PPAR γ ligation. To assess its potential to enhance remyelination, we next used the BSC and cuprizone models. Lomitapide enhanced axonal myelination and reduced the ORO abundance in the BSC model, a pro-regenerative effect that was lost upon elimination of microglia using chlodronate liposomes. Accordingly, in the cuprizone model, intraperitoneal administration of lomitapide enhanced remyelination, evidenced by an increased MBP abundance and decreased g-ratio, and reduced ORO load in the CC. As expected, lomitapide administration reduced serum vLDL cholesterol levels (Figure), confirming its efficacy in inhibiting hepatic MTTP but complicating the isolation of its direct regenerative effects on remyelination through S-palmitoylation. All and all, these experiments position lomitapide as a promising therapeutic tool to enhance remyelination.

6. Discussion

In this study, we demonstrate that active human MS lesions exhibit significant alterations in their S-palmitoylation and that pharmacological inhibition of S-palmitoylation enhances remyelination. Foamy macrophages and microglia were found to serve as a critical cellular conduit for this enhanced remyelination. Specifically, we show that abrogation of zDHHC5-mediated S-palmitoylation enhances nuclear translocation of FABP5, leading to heightened activation of PPAR γ and the formation of disease-resolving foam cells. Finally, our findings highlight that the vLDL-lowering drug lomitapide promotes remyelination, at least partially, through the suppression of the zDHHC5-FABP5-PPAR γ signaling axis in macrophages and microglia. All in all, we show for the first time that S-palmitoylation by zDHHC5 impairs remyelination by inducing the formation of repair-inhibitory foam cells, having significant mechanistic and therapeutic implications for MS and other demyelinating disorders.

Within the CNS, palmitate plays a multifaceted role, supporting both energy homeostasis and membrane structure⁶⁴. Alongside these canonical functions, S-palmitoylation has emerged as a key mechanism of palmitate action in the CNS, particularly in fine-tuning neuronal morphology and physiology, synaptic plasticity, and oligodendrogenesis^{65,66}. Accordingly, alterations in S-palmitoylation dynamics contribute to neuropathological, locomotor, and cognitive deficits observed in conditions like Alzheimer's disease (AD), Parkinson's disease, psychiatric disorders, and intellectual disabilities⁶⁷⁻⁷⁸. Here, loss-of-function mutations in acyltransferases, particularly zDHHC8, 9, 13, 15, and 17, underlie brain pathology, leading to locomotor and cognitive impairments, whereas inhibition of depalmitoylation reverses these deficits. While these studies argue for attenuated S-palmitoylation driving various brain pathologies, our findings indicate that active S-palmitoylation can have detrimental effects in the CNS as well. We show that 2BP (pan-zDHHC inhibition), lomitapide (zDHHC5 inhibition), and phagocyte-specific deficiency of *Zdhhc5* enhance remyelination following toxin-induced demyelination by promoting the formation of pro-regenerative foam cells. Supporting these findings, inhibition of APT1-mediated depalmitoylation perturbs myelin regeneration and the pro-regenerative features of foam cells.

This discrepancy may reflect disease- and cell-type-specific expression patterns of zDHHCs, the varying involvement of zDHHCs in brain disorders, or alternatively, point towards the high abundance of lipid-overloaded foam cells in MS lesions compared to other CNS disorders⁹. Though, lipid-loaded microglia accumulate in the AD brain, where they contribute to Tau phosphorylation and neurotoxicity⁷⁹. It is further worth noting that we did not observe significant abnormalities in neuronal and axonal morphology; however, we did not conduct an in-depth assessment of dendritic and axonal structures or evaluate potential behavioral and locomotor deficits. Thus, while we provide strong evidence that palmitate impacts MS lesion progression via S-palmitoylation, specifically identifying increased zDHHC5-mediated S-palmitoylation in foam cells as a key factor in remyelination failure, further research is necessary to investigate deficits in neuronal physiology and cognition in our models.

Recent studies demonstrate that foamy macrophages and microglia exhibit dual phenotypes in demyelinating lesions⁹. Early foam cells display a less inflammatory, pro-regenerative phenotype marked by the formation of protective lipid species and intermediates, such as oxysterols, desmosterol, and FAs, which activate PPAR/ and LXRs⁸⁰⁻⁸⁴. Conversely, disruptions in FA desaturation and elongation, lipophagy, and lysosomal processing, and the resulting accumulation of LDs and inflammatory lipid species, are associated with late-stage, lipid-overloaded, disease-promoting foam cells^{4,10,11,42,49,85}. With zDHHC5-mediated S-palmitoylation impacting functional parameters characteristic of both early- and late-stage foam cells, including PPAR/ activation, myelin internalization, LD accumulation, and the release of ROS, RNS, and inflammatory mediators, our findings indicate that S-palmitoylation serves as a critical molecular regulator of early- and late-stage foam cell physiology. Of note, the importance of zDHHC5 in driving the harmful phenotype switch of foam cells in our study aligns with other studies showing that zDHHC5 activity correlates with inflammatory myeloid cell formation²⁰, NLRP3 inflammasome activation and pyroptosis^{86,87}, and heightened lipid endocytosis^{19,25}. Similarly, the interplay between zDHHC5-mediated FABP5 S-palmitoylation and PPAR/ activation fits with reports showing that FABP5 is a FA chaperone that promotes nuclear PPAR activation^{57,88}. However, given that FABP5 is susceptible to S-glutathionylation, a process that relies on Cys127 and also controls FABP5 nuclear translocation and PPAR/ activation, it would be valuable to investigate the interaction and necessity of both S-glutathionylation and S-palmitoylation in nuclear trafficking of FABP5 in future studies⁸⁹. Collectively, we present a deeper layer of molecular complexity regarding foam cell physiology in the CNS, and identify several therapeutically targetable regulators that mitigate the harmful impact of S-palmitoylation on foamy phagocyte physiology and remyelination, including zDHHC5, PPAR/, and FABP5.

With macrophages and microglia being the most abundant cell types in early demyelinating brain lesions, ample evidence links changes in their functional phenotypes to the fate of these lesions. In this context, several functional properties of foamy phagocytes are associated with efficient remyelination, including the release of neurotrophic and anti-inflammatory mediators^{90,91}, the clearance of inhibitory myelin debris⁹²⁻⁹⁴, and the intercellular recycling of lipids, including cholesterol, via lipoproteins to oligodendrocytes^{4,10,11,42,85,95}. Our findings highlight that changes in (foamy) macrophages and microglia underpin enhanced remyelination upon exposure to 2BP and lomitapide, as well as following genetic deficiency of *Zdhhc5*. However, this pro-myelinating effect did not seem to rely on increased ABCA1- and ABCG1-mediated horizontal transfer of lipids from phagocytes to oligodendrocytes, nor did it depend on increased clearance of myelin debris. In fact, *Zdhhc5* deficiency and exposure to 2BP and lomitapide attenuated endocytosis of myelin debris by macrophages and microglia *in vitro*. Given the pronounced anti-inflammatory effects and antioxidant response, it is tempting to speculate that reduced zDHHC5-mediated S-palmitoylation enhances oligodendrogenesis and remyelination by alleviating the differentiation

block induced by overt inflammation and oxidative stress⁹⁶⁻⁹⁸. Yet, more research is needed to identify changes in the microenvironment involved, and assess to what extent and how these outweigh the accumulation of myelin debris, or, alternatively, drive compensatory clearance of myelin debris by other cell types such as astrocytes⁹⁹⁻¹⁰¹. Likewise, given that S-palmitoylation controls various aspects of extracellular vesicle (EV) production and release¹⁰², it would be of interest to assess the impact of EVs released by macrophages and microglia in the regenerative impact of 2BP, lomitapide and *Zdhhc5* deficiency. In this regard, we recently demonstrated that macrophages enhance remyelination by recycling cholesterol via EVs to oligodendrocytes⁴⁶. Thus, while our findings indicate that S-palmitoylation impairs remyelination by modulating foam cell biology, further research is necessary to elucidate the molecular mechanisms and cellular interactions involved.

Several other unresolved questions persist concerning our findings. We cannot entirely rule out that S-palmitoylation of targets beyond FABP5, such as CD36, beclin-1, or NOD1^{19,20,25,103}, impact foam cell function and remyelination in our experiments^{42,104,105}. Additionally, we did not clarify the mechanisms behind reduced myelin uptake downstream of PPAR γ , which based on our RNAseq analysis could involve reduced caveolar endocytosis. Finally, with palmitate levels being increased in MS brain¹⁰⁶, it would be of interest to study a substrate-dependent harmful impact of S-palmitoylation on phagocyte physiology and remyelination. Despite these remaining gaps, our findings underscore the zDHHC5-FABP5-PPAR γ axis in foam cells as a promising therapeutic target for remyelination.

7. Material and methods

7.1. Antibodies and chemical reagents

The following antibodies were used for immunofluorescent/immunohistochemical stains: antiMBP (1:250 (*in vivo* and *ex vivo*), cat. no. MAB386, Millipore), antiNF (1:1000, cat. no. ab8135, SigmaAldrich), anti-PLIN2 (1:30, cat. no. ab108323, Abcam), anti-CD68 (1:100, cat. no. 14-0688-82, Invitrogen), anti-zDHHC5 (1:100, cat. no. 21324-1-AP, ProteinTech), anti-F4/80 (1:100, cat. no. MCA487G, Bio-Rad), anti-FABP5 (1:1000, cat. no. 12348-1-AP, ProteinTech). The according secondary Alexa Fluor antibodies were Alexa Fluor488 (1:500, Invitrogen) and Alexa Fluor555 (1:500, Invitrogen). BODIPY® 493/503 (2 μ M, Thermo Fisher Scientific, D3922) was used to stain the lipid droplets. 2BP (20 μ M, cat. no. 238422, Sigma-Aldrich) was used to inhibit general S-palmitoylation. Palmostatin B (50 μ M, cat. no. 5.08738, Sigma-Aldrich), ML348 (20 μ M, cat. no. SML1901, Sigma-Aldrich) and ML349 (20 μ M, cat. no. SML1918, Sigma Aldrich) were used to inhibit depalmitoylation via APT1/2, APT1, and APT2, respectively. Lomitapide (1 μ M, cat. no. 182431-12-5, Simson Pharma Limited) was used to inhibit zDHHC5. FABP5 inhibitor. Wy14643 (25 μ M, xxx), GW501516 (1 μ M, xxx), and rosiglitazone (1 μ M, xxx) were used as agonist of peroxisome proliferator-activated receptor (PPAR), PPAR γ , and PPAR α , respectively. Inhibitors PPAR.

7.2. Animals

Wild-type C57BL/6J mice were purchased from Envigo and were housed in a 12 h light/dark cycle with ad libitum access to water and a standard chow diet or specific formulations as indicated. All procedures were conducted in accordance with the institutional guidelines and approved by the Ethical Committee for Animal Experiments of Hasselt University (protocol numbers 202402K, 202404). For zDHHC5 knockout mice, mice were maintained in a barrier facility in a 12 h light/dark cycle with ad libitum access to water and a standard chow diet or specific formulations as indicated. All animal experiments were performed under the guidelines of the institutional Animal Care and Use Committee at Zhejiang University (ZJU20170473). zDHHC5 knockout mice were

generated by CRISPR/Cas9 technology. Briefly, the targeting vector containing the 5'-arm-LoxP-zDHHC5 intron 3-LoxP-3'-arm cassette was constructed and the linearized construct plus pX330-sgRNA was electroporated into embryonic stem (ES) cells. Correctly targeted ES cell clones were microinjected into C57BL/6J blastocysts to generate chimeric mice. The resulting progenies were backcrossed to C57BL/6J mice to generate zDHHC5^{fl^{ox}/+} mice, which were intercrossed to generate zDHHC5^{fl^{ox}/fl^{ox}} (zDHHC5^{fl^{ox}/fl^{ox}}) mice. To delete zDHHC5 in LysM-Cre, zDHHC5^{fl^{ox}/fl^{ox}} mice were crossed to LysM-Cre mice (Model Animal Research Center of Nanjing University, Nanjing, China), which express Cre recombinase under the control of the LysM promoter. For PCR genotyping, genomic DNA was isolated from mouse tails and amplified by standard PCR. For the conditional knockout mice, forward primer *zdhhc5*-seq 5 (TTAAGTTGCTTCAGAGATAGGAGTGTAAC) and reverse primer *zdhhc5*-seq-R (TTGACACCAGCACAAATCTAAAGAG- were used to detect both 306 bp and 356 bp PCR products for zDHHC5^{+/+} and zDHHC5 floxed alleles, respectively. LysM-cre transgene was amplified by the forward primer Cre-seq-F (GCCTGCATTACCGGTCGATGCA) and reverse primer Cre-seq-R (ATCGCCATCTTCCAGCAGGCGC) to obtain a specific 997 bp product.

7.3. Macrophage and microglia differentiation and treatments

Bone marrow-derived macrophages (BMDMs) were obtained as described previously³³. Briefly, femoral and tibial bone marrow was isolated from 11-week-old female wild-type, *zdhhc5*^{-/-} C57BL/6J mice and cultured in 14.5 cm petri dishes (Greiner, cat. No. 639,161) at a concentration of 10 × 10⁶ cells/Petri dish in RPMI1640 medium (Lonza) supplemented with 10% fetal calf serum (FCS; Biowest), 50 U/mL penicillin (Invitrogen), 50 U/mL streptomycin (Invitrogen), and 15% L929-conditioned medium (LCM; in house production as described by³⁴) for 7 days. Next, cells were cultured at a density of 0.5 × 10⁶ cells/mL in RPMI1640 supplemented with 10% FCS, 50 U/mL penicillin, 50 U/mL streptomycin, and 5% LCM. Microglia were obtained from the cortices of postnatal day 1–3 wild-type C57BL/6J mice and cultured in poly-L-lysine (PLL, 50 µg/mL, Sigma-Aldrich)-coated T75 flasks (Greiner) in high-glucose Dulbecco's Modified Eagle Medium (DMEM) medium (Gibco), supplemented with 10% FCS, 50 U/mL penicillin and 50 U/mL streptomycin. 3 days after isolation, cultures were supplemented with 33% LCM. After 14 days, microglia were collected by means of the orbital shake-off method (230 rpm, 3h), after which the cells were cultured at a density of 0.5 × 10⁶ cells/mL in high-glucose DMEM supplemented with 10% FCS, 50 U/mL penicillin, 50 U/mL streptomycin, and 15% LCM. BMDMs and microglia were treated daily with 2BP, depalmitoylation inhibitors, lomitapide and/or 100 µg/mL myelin for 24h or 72h. For phenotyping, BMDMs and microglia were stimulated with LPS and IFN- (100 ng/mL and 20 ng/mL, respectively) for 6h to assess gene expression.

7.4. Myelin isolation and phagocytosis

Myelin was purified from postmortem mouse and human brain tissue by means of density gradient centrifugation, as described previously³³. Myelin protein concentration was determined by using the BCA protein assay kit (Thermo Fisher Scientific), per the manufacturer's guidelines. By using the Chromogenic Limulus Amebocyte Lysate assay kit (Genscript), endotoxin content of isolated myelin was determined to be negligible. To evaluate the ability and extent of myelin phagocytosis, myelin was fluorescently labeled with 1,1-dioctadecyl-3,3,3,3-tetramethylindocarbocyanine perchlorate (Dil; cat. no. 468495, Sigma-Aldrich) or pH rodo, succinimidyl ester (cat. no. P36600, Invitrogen). Cells were exposed to 100 µg/ml Dil- or pH rodo-labeled myelin for 1.5 h and analyzed for fluorescence intensity by using the FACS Fortessa (BD Biosciences) or the CLARIOstar PLUS microplate reader (BMG Labtech). To define the uptake of latex beads, cells were exposed to fluorescent red latex beads for 1.5 h (1:100, cat. no. L3030, Sigma-Aldrich) and analyzed for fluorescence intensity by using the FACS Fortessa.

7.5. Flow cytometry

BMDMs and microglia were stained for intracellular lipid load by 15 min incubation with BODIPY (493/503) at 37°C. The FACS Fortessa was used to quantify cellular fluorescence. Data is represented as relative lipid droplet load compared to vehicle.

7.6. Cuprizone-induced acute demyelination *in vivo* model

To induce acute demyelination, 9weekold male wildtype C57BL/6J mice were fed a diet containing 0.3% (w/w) cuprizone (bis[cyclohexanone]oxaldihydrazone, SigmaAldrich) mixed in powdered standard chow ad libitum for 5 weeks. After these 5 weeks, cuprizone diet was withdrawn to allow spontaneous remyelination for 1 week. During this week, mice were subsequently subjected to a daily intraperitoneal (IP) injection of either vehicle, 2BP (20 mg/kg), ML348 (25 mg/kg), or lomitapide (10 mg/kg) for 7 days. 5 or 6 weeks after the start of cuprizone diet, mice were sacrificed and tissue was collected for histological and biochemical analysis.

7.7. Cerebellar brain slice cultures

Cerebellar brain slices were obtained from wildtype C57BL/6J mouse pups at postnatal day 10 (P10), as described previously^{35,36}. Brain slices were cultured in MEM medium (Thermo Fisher Scientific) supplemented with 25% horse serum (Thermo Fisher Scientific), 25% Hank's balanced salt solution (SigmaAldrich), 50 U/mL penicillin, 50 U/mL streptomycin, 1% Glutamax (Thermo Fisher Scientific), 12.5 mM HEPES (Thermo Fisher Scientific) and 1.45 g/L glucose (SigmaAldrich). For phagocyte depletion, slices were treated with clodronate or empty liposomes (0.5 mg/mL, LIPOSOMA) immediately after isolation for 24 h. For BMDM repletion experiments, slices were first treated with clodronate liposomes immediately after isolation for 24 h. Next, slices were repleted with 4×10^3 WT, zDHHC5 overexpression and zDHHC5 knockdown BMDMs. The BMDMs were added directly to the slice in a 1.5 μ L drop, without touching the slice. Next, slices were left to recover for 2 days. To induce demyelination, brain slices were treated with 0.5 mg/mL lysolecithin (SigmaAldrich) at 3 days post isolation for 16 h. Next, brain slices were allowed to recover in culture medium for 1 day and subsequently treated daily with vehicle, 2BP (20 μ M), lomitapide (1 μ M), Palmostatin B (100 μ M), ML348 (40 μ M), ML349 (40 μ M) for 1 week, followed by histological and biochemical analysis.

7.8. Transmission electron microscopy

Mouse brain samples were fixed with 2% glutaraldehyde. Next, postfixation was done with 2% osmiumtetroxide in 0.05 M sodium cacodylate buffer for 1 h at 4°C. Dehydration of the samples was performed by ascending concentrations of acetone. Next, the dehydrated samples were impregnated overnight in a 1:1 mixture of acetone and araldite epoxy resin. Next, the samples were embedded in araldite epoxy resin at 60°C and were cut in slices of 70 nm, perpendicular to the corpus callosum, with a Leica EM UC6 microtome. The slices were transferred to copper grids (Veco B.V) that were coated with 0.7% formvar. Analysis was performed with a Jeol JEM1400 Flash at 80 kV equipped with an Emsis 20 NP XAROSA camera system; around 5–12 images were taken for each mouse brain section. ImageJ was used to calculate the gratio (ratio of the inner axonal diameter to the total outer diameter). All analyses were conducted by observers blinded to the experimental arm of the study.

7.9. Immunofluorescence

Cells were cultured on glass cover slides and fixed in 4% paraformaldehyde (PFA) for 20 min at room temperature. Cerebellar brain slices were fixed in 4% PFA for 15 min at room temperature. Brain tissue of cuprizone mice was isolated, snapfrozen, and sectioned with a Leica CM1900UV cryostat (Leica Microsystems) to obtain 10 μ m slices. Snap-frozen brain material containing active MS lesions was obtained from the Netherlands Brain Bank (NBB, Amsterdam,

Netherlands) and sectioned with a Leica CM1900UV cryostat (Leica Microsystems) to obtain 10 µm slices. Cryosections were fixed in icecold acetone for 10 min at -20°C. Immunostaining and analysis of cryosections were performed as described previously³³. Nuclei were stained using 4,6-diamidino-2-phenylindole (DAPI; cat. no. Invitrogen). ImageJ was used to align the corpus callosum (coronal section between bregma 0 and -0.5 mm), followed by determination of the MBP, or a F4/80 and PLIN2 positive signal in this area. Analysis of cells and cerebellar brain slices was performed using the LeicaDM2000 LED fluorescence microscope and the LSM 880 confocal microscope (Zeiss), respectively. ImageJ was used to determine the XXX positive area per cell and the percentage myelinated axons (MBP⁺ NF⁺ axons/NF⁺ axons) which is presented in a relative normalized manner. Threedimensional analysis of cerebellar brain slices was performed using the zstack feature, and images were 3D rendered using the 3D rendering software Vaa3D³⁷. Representative images shown in figures are digitally enhanced to increase the readability. All analyses were conducted by observers blinded to the experimental arm of the study.

7.10. Cell viability

To assess cellular viability, cells were incubated with 7-aminoactinomycin D (7-AAD; cat. no. oA1310, Thermo Fisher Scientific). The FACS Fortessa was used to quantify cellular fluorescence. Mean fluorescence intensity (MFI) was corrected for background MFI.

7.11. Oil red O staining

PFA fixed cells and cerebellar brain slices, and unfixed *in vivo* cryosections, were stained with 0.3% Oil Red O (ORO, cat. no. O0625, Sigma-Aldrich) for 10 min. Counterstaining of cell nuclei was done using haematoxylin (cat. no. H9627, Sigma-Aldrich) incubation for 1 min. Analysis was carried out using a Leica DM 2000 LED microscope and ImageJ software. For ORO quantification in cells, ORO was extracted by incubating the cells with isopropanol for 10 min, while shaking. Absorbance was measured using the CLARIOstar PLUS microplate reader at 510 nm.

7.12. Cholesterol measurement

Total and free cholesterol was measured in cell lysates and supernatant using the Amplex™ Red Cholesterol Assay Kit (Thermo Fisher Scientific), according to the manufacturer's instructions. Cholesteryl ester concentration was calculated by subtracting free cholesterol concentration from total cholesterol concentration. To measure cholesterol efflux, cells were exposed to 10% FCS, apoA-I (50 µg/ml) or high-density lipoprotein (HDL, 50 µg/ml) in phenol- and serum-free RPMI1640 medium for 4 h prior to measuring intracellular and extracellular total cholesterol. Cholesterol efflux was determined by dividing fluorescence in the supernatants by the total fluorescence in supernatants and cells. Fluorescence was measured at an excitation wavelength of 540 nm and an emission wavelength of 590 nm using the CLARIOstar PLUS optima microplate reader.

7.13. RNA extraction and real-time quantitative PCR

Total RNA from cells and tissue was isolated using Qiazol (Qiagen, Venlo, The Netherlands) and the RNeasy mini kit (Qiagen), according to the manufacturer's guidelines. Complementary DNA (cDNA) was synthesized using qScript™ cDNA SuperMix (Quanta Biosciences, VWR, Leuven, Belgium) according to the manufacturer's instructions. Real-time quantitative PCR was conducted on a Step One Plus detection system (Applied biosystems, California, USA). Cycle conditions were 95 °C for 20 s, followed by 40 cycles of 95 °C for 3 s, and 60 °C for 30 s. The PCR reaction mixture contained SYBR green master mix (Thermo Fisher Scientific), 0.3 µM forward and reverse primer (IDT technologies, Leuven, Belgium), RNase free water and 12.5 ng cDNA template. Data were analyzed using the comparative Ct method and normalized to the most

stable reference genes.

7.14. Measurement of nitric oxide

BMDMs were pretreated with 2BP (20 μ M) and lomitapide (1 μ M) for 24 h. Afterwards, cells were stimulated with LPS (24 h, 100 ng/ml). Nitric oxide (NO) was indirectly monitored using the Griess reagent nitrite measurement kit (Abcam). Briefly, nitrite reacts with sulphanilamide and N-(1-naphthyl)ethylenediamine dihydrochloride to produce a pink azo dye. Absorbance of this azo derivative was then measured at 540 nm using the CLARIOstar PLUS microplate reader.

7.15. Total reactive oxygen species production

BMDMs were pretreated with 2BP (20 μ M) or lomitapide (1 μ M) for 24 h. Afterwards, cells were stimulated with PMA (15 min, 100 ng/ml) and reactive oxygen species (ROS) production was measured using the fluorescent probe 2,7-dichlorodihydrofluorescein diacetate at 10 μ M in PBS for 30 min. Fluorescence was measured using the fluorescence CLARIOstar PLUS microplate reader at 495 nm excitation and 529 nm emission.

7.16. Western blot

Cells were lysed in icecold Radiolimmunoprecipitation Assay (RIPA) buffer (150 mM NaCl, 50 mM Tris, 1% SDS, 1% Triton X100, and 0.5% sodium deoxycholate) supplemented with protease phosphatase inhibitor cocktail (Roche). Pierce BCA Protein Assay kit (Thermo Fisher Scientific) was used to determine protein concentration, according to the manufacturer's guidelines. Samples were separated by electrophoresis on a 10% SDSPAGE gel and were transferred onto a PVDF membrane. Blots were blocked using 5% dried skimmed milk powder (Marvel) in 1x PBS0.1% Tween20 (PBST), incubated overnight with the relevant primary antibody, followed by incubation with the appropriate HRPconjugated secondary antibody. Chemiluminescent signals were detected with the Amersham Imager 680 (GE Healthcare Life Sciences), using the enhanced chemiluminescence (ECL) Plus detection kit (Thermo Fisher Scientific).

7.17. Luciferase-based nuclear receptor reporter assay

To determine the activation of PPAR, PPAR α , and PPAR γ , ligand-binding luciferasebased reporter assays were performed using the ONEGloTM Luciferase Assay System kit (Promega). COS7 cells were transfected with bacterial plasmid constructs expressing luciferase under the control of the ligandbinding domain for PPAR, PPAR α , and PPAR γ , which were kindly provided by Prof. dr. Bart Staels (National Institute of Health and Medical Research, University of Lille, Lille, France). Cells were grown to 60% confluency in 60 mm petri dishes and subsequently transfected with 1.8 μ g plasmid DNA, including 0.2 μ g pGAL4hLXR or pGAL4hLXR, 1 μ g pG5TKGL3 and 0.6 μ g pCMV galactosidase. JetPEI (Polysciences) was used as transfection reagent. After overnight incubation, transfected cells were seeded at a density of 10,000 cells/well in a 96well plate in DMEM medium enriched with 50 U/mL penicillin and 50 U/mL streptomycin, and treated with XXX (hoe invullen voor pos controles en welke stimulaties) for 18 h. Following treatment, cells were lysed in lysis buffer (25 mM GlycylGlycine, 15 mM MgSO₄, 4 mM EGTA, and 1x Triton, all from SigmaAldrich). To correct for transfection efficacy, galactosidase activity was measured using cell lysate (10%) in gal buffer, consisting of 20% 2Nitrophenyl Dgalactopyranoside (ONGP; SigmaAldrich) and 80% BufferZ (0.1 M Na₂HPO₄, 10 mM KCl, 1 mM MgSO₄, and 3.4 μ L/mL 2mercaptoethanol; all from SigmaAldrich). Luminescence and absorbance (410 nm) were measured using the CLARIOstar PLUS microplate reader.

7.18. Statistical analysis

Data were statistically analysed using GraphPad Prism v10 and are reported as mean \pm SEM. The D'Agostino and Pearson omnibus normality test was used to test for normal distribution. When datasets were normally distributed, an ANOVA (Tukey's post hoc analysis) or twotailed

unpaired Student's *t* test (with Welch's correction if necessary) was used to determine statistical significance between groups. If datasets did not pass normality, the KruskalWallis or Mann Whitney analysis was applied. *p* values < 0.05 were considered to indicate a significant difference (*, *p* < 0.05; **, *p* < 0.01; ***, *p* < 0.001; ****, *p* < 0.0001).

8. References

1. Franklin, R. J. M. & Simons, M. CNS remyelination and inflammation: From basic mechanisms to therapeutic opportunities. *Neuron* **110**, 3549-3565 (2022). <https://doi.org/10.1016/j.neuron.2022.09.023>
2. Klotz, L., Antel, J. & Kuhlmann, T. Inflammation in multiple sclerosis: consequences for remyelination and disease progression. *Nat Rev Neurol* **19**, 305-320 (2023). <https://doi.org/10.1038/s41582-023-00801-6>
3. Gruchot, J. *et al.* The Molecular Basis for Remyelination Failure in Multiple Sclerosis. *Cells* **8** (2019). <https://doi.org/10.3390/cells8080825>
4. Cantuti-Castelvetri, L. *et al.* Defective cholesterol clearance limits remyelination in the aged central nervous system. *Science* **359**, 684-688 (2018). <https://doi.org/10.1126/science.aan4183>
5. McNamara, N. B. *et al.* Microglia regulate central nervous system myelin growth and integrity. *Nature* **613**, 120-129 (2023). <https://doi.org/10.1038/s41586-022-05534-y>
6. Kent, S. A. & Miron, V. E. Microglia regulation of central nervous system myelin health and regeneration. *Nat Rev Immunol* **24**, 49-63 (2024). <https://doi.org/10.1038/s41577-023-00907-4>
7. Bittner, S., Pape, K., Klotz, L. & Zipp, F. Implications of immunometabolism for smouldering MS pathology and therapy. *Nat Rev Neurol* **19**, 477-488 (2023). <https://doi.org/10.1038/s41582-023-00839-6>
8. Bogie, J. F. J., Haidar, M., Kooij, G. & Hendriks, J. J. A. Fatty acid metabolism in the progression and resolution of CNS disorders. *Adv Drug Deliv Rev* **159**, 198-213 (2020). <https://doi.org/10.1016/j.addr.2020.01.004>
9. Grajchen, E., Hendriks, J. J. A. & Bogie, J. F. J. The physiology of foamy phagocytes in multiple sclerosis. *Acta Neuropathol Commun* **6**, 124 (2018). <https://doi.org/10.1186/s40478-018-0628-8>
10. Bogie, J. F. J. *et al.* Stearoyl-CoA desaturase-1 impairs the reparative properties of macrophages and microglia in the brain. *J Exp Med* **217** (2020). <https://doi.org/10.1084/jem.20191660>
11. Garcia Corrales, A. V. *et al.* Fatty acid elongation by ELOVL6 hampers remyelination by promoting inflammatory foam cell formation during demyelination. *Proc Natl Acad Sci U S A* **120**, e2301030120 (2023). <https://doi.org/10.1073/pnas.2301030120>
12. van der Poel, M. *et al.* Transcriptional profiling of human microglia reveals grey-white matter heterogeneity and multiple sclerosis-associated changes. *Nat Commun* **10**, 1139 (2019). <https://doi.org/10.1038/s41467-019-08976-7>
13. Kornberg, M. D. *et al.* Dimethyl fumarate targets GAPDH and aerobic glycolysis to modulate immunity. *Science* **360**, 449-453 (2018). <https://doi.org/10.1126/science.aan4665>
14. O'Neill, L. A., Kishton, R. J. & Rathmell, J. A guide to immunometabolism for immunologists. *Nat Rev Immunol* **16**, 553-565 (2016). <https://doi.org/10.1038/nri.2016.70>
15. Wculek, S. K., Dunphy, G., Heras-Murillo, I., Mastrangelo, A. & Sancho, D. Metabolism of tissue macrophages in homeostasis and pathology. *Cell Mol Immunol* **19**, 384-408 (2022). <https://doi.org/10.1038/s41423-021-00791-9>
16. F, S. M. *et al.* Mechanisms and functions of protein S-acylation. *Nat Rev Mol Cell Biol* (2024). <https://doi.org/10.1038/s41580-024-00700-8>
17. Linder, M. E. & Deschenes, R. J. Palmitoylation: policing protein stability and traffic. *Nat Rev Mol Cell Biol* **8**, 74-84 (2007). <https://doi.org/10.1038/nrm2084>
18. Dong, G. *et al.* Palmitoylation couples insulin hypersecretion with beta cell failure in diabetes. *Cell Metab* **35**, 332-344 e337 (2023). <https://doi.org/10.1016/j.cmet.2022.12.012>
19. Hao, J. W. *et al.* CD36 facilitates fatty acid uptake by dynamic palmitoylation-regulated endocytosis. *Nat Commun* **11**, 4765 (2020). <https://doi.org/10.1038/s41467-020-18565-8>
20. Lu, Y. *et al.* Palmitoylation of NOD1 and NOD2 is required for bacterial sensing. *Science* **366**, 460-467 (2019). <https://doi.org/10.1126/science.aau6391>
21. Ko, P. J. & Dixon, S. J. Protein palmitoylation and cancer. *EMBO Rep* **19** (2018). <https://doi.org/10.15252/embr.201846666>
22. Cho, E. & Park, M. Palmitoylation in Alzheimer's disease and other neurodegenerative diseases. *Pharmacol Res* **111**, 133-151 (2016). <https://doi.org/10.1016/j.phrs.2016.06.008>
23. Milnerwood, A. J. *et al.* Memory and synaptic deficits in Hip14/DHHC17 knockout mice. *Proceedings of the National Academy of Sciences of the United States of America* **110**, 20296-20301 (2013). <https://doi.org/10.1073/pnas.1222384110>

24. Bekhouche, B. *et al.* A toxic palmitoylation of Cdc42 enhances NF-kappaB signaling and drives a severe autoinflammatory syndrome. *J Allergy Clin Immunol* **146**, 1201-1204 e1208 (2020). <https://doi.org/10.1016/j.jaci.2020.03.020>
25. Wang, J. *et al.* DHHC4 and DHHC5 Facilitate Fatty Acid Uptake by Palmitoylating and Targeting CD36 to the Plasma Membrane. *Cell Rep* **26**, 209-221 e205 (2019). <https://doi.org/10.1016/j.celrep.2018.12.022>
26. Kim, Y. C. *et al.* Toll-like receptor mediated inflammation requires FASN-dependent MYD88 palmitoylation. *Nat Chem Biol* **15**, 907-916 (2019). <https://doi.org/10.1038/s41589-019-0344-0>
27. Zhou, B., Hao, Q., Liang, Y. & Kong, E. Protein palmitoylation in cancer: molecular functions and therapeutic potential. *Mol Oncol* **17**, 3-26 (2023). <https://doi.org/10.1002/1878-0261.13308>
28. (!!! INVALID CITATION !!!).
29. Guns, J., Vanherle, S., Hendriks, J. J. A. & Bogie, J. F. J. Protein Lipidation by Palmitate Controls Macrophage Function. *Cells* **11** (2022). <https://doi.org/10.3390/cells11030565>
30. Zhang, Y., Qin, Z., Sun, W., Chu, F. & Zhou, F. Function of Protein S-Palmitoylation in Immunity and Immune-Related Diseases. *Front Immunol* **12**, 661202 (2021). <https://doi.org/10.3389/fimmu.2021.661202>
31. Das, T., Yount, J. S. & Hang, H. C. Protein S-palmitoylation in immunity. *Open Biol* **11**, 200411 (2021). <https://doi.org/10.1098/rsob.200411>
32. Penkert, H. *et al.* Proteomic and lipidomic profiling of demyelinating lesions identifies fatty acids as modulators in lesion recovery. *Cell Rep* **37**, 109898 (2021). <https://doi.org/10.1016/j.celrep.2021.109898>
33. Bergholt, M. S. *et al.* Correlated Heterospectral Lipidomics for Biomolecular Profiling of Remyelination in Multiple Sclerosis. *ACS Cent Sci* **4**, 39-51 (2018). <https://doi.org/10.1021/acscentsci.7b00367>
34. Ho, P. P. *et al.* Identification of naturally occurring fatty acids of the myelin sheath that resolve neuroinflammation. *Sci Transl Med* **4**, 137ra173 (2012). <https://doi.org/10.1126/scitranslmed.3003831>
35. Sardana, S., Nederstigt, A. E. & Baggelaar, M. P. S-Palmitoylation during Retinoic Acid-Induced Neuronal Differentiation of SH-SY5Y Neuroblastoma Cells. *J Proteome Res* **22**, 2421-2435 (2023). <https://doi.org/10.1021/acs.jproteome.3c00151>
36. Wang, Y. & Yang, W. Proteome-Scale Analysis of Protein S-Acylation Comes of Age. *J Proteome Res* **20**, 14-26 (2021). <https://doi.org/10.1021/acs.jproteome.0c00409>
37. Ocasio, C. A. *et al.* A palmitoyl transferase chemical-genetic system to map ZDHHC-specific S-acylation. *Nat Biotechnol* **42**, 1548-1558 (2024). <https://doi.org/10.1038/s41587-023-02030-0>
38. Blanc, M., David, F. P. A. & van der Goot, F. G. SwissPalm 2: Protein S-Palmitoylation Database. *Methods Mol Biol* **2009**, 203-214 (2019). https://doi.org/10.1007/978-1-4939-9532-5_16
39. Attfeld, K. E., Jensen, L. T., Kaufmann, M., Friese, M. A. & Fugger, L. The immunology of multiple sclerosis. *Nat Rev Immunol* **22**, 734-750 (2022). <https://doi.org/10.1038/s41577-022-00718-z>
40. Lu, H. C. *et al.* STAT3 signaling in myeloid cells promotes pathogenic myelin-specific T cell differentiation and autoimmune demyelination. *Proc Natl Acad Sci USA* **117**, 5430-5441 (2020). <https://doi.org/10.1073/pnas.1913997117>
41. Dalakas, M. C., Alexopoulos, H. & Spaeth, P. J. Complement in neurological disorders and emerging complement-targeted therapeutics. *Nat Rev Neurol* **16**, 601-617 (2020). <https://doi.org/10.1038/s41582-020-0400-0>
42. Haidar, M. *et al.* Targeting lipophagy in macrophages improves repair in multiple sclerosis. *Autophagy* **18**, 2697-2710 (2022). <https://doi.org/10.1080/15548627.2022.2047343>
43. Webb, Y., Hermida-Matsumoto, L. & Resh, M. D. Inhibition of protein palmitoylation, raft localization, and T cell signaling by 2-bromopalmitate and polyunsaturated fatty acids. *J Biol Chem* **275**, 261-270 (2000). <https://doi.org/10.1074/jbc.275.1.261>
44. Pedro, M. P. *et al.* 2-Bromopalmitate reduces protein deacylation by inhibition of acyl-protein thioesterase enzymatic activities. *PLoS One* **8**, e75232 (2013). <https://doi.org/10.1371/journal.pone.0075232>
45. Peng, H., Bria, A., Zhou, Z., Iannello, G. & Long, F. Extensible visualization and analysis for multidimensional images using Vaa3D. *Nat Protoc* **9**, 193-208 (2014). <https://doi.org/10.1038/nprot.2014.011>
46. Vanherle, S. *et al.* Extracellular vesicle-associated cholesterol supports the regenerative functions of macrophages in the brain. *J Extracell Vesicles* **12**, e12394 (2023). <https://doi.org/10.1002/jev2.12394>
47. Davda, D. *et al.* Profiling targets of the irreversible palmitoylation inhibitor 2-bromopalmitate. *ACS Chem Biol* **8**, 1912-1917 (2013). <https://doi.org/10.1021/cb400380s>
48. Cai, J., Cui, J. & Wang, L. S-palmitoylation regulates innate immune signaling pathways: molecular mechanisms and targeted therapies. *Eur J Immunol* **53**, e2350476 (2023). <https://doi.org/10.1002/eji.202350476>
49. Loix, M. *et al.* Perilipin-2 limits remyelination by preventing lipid droplet degradation. *Cell Mol Life Sci* **79**, 515 (2022). <https://doi.org/10.1007/s00018-022-04547-0>
50. Vijayan, V. *et al.* Human and murine macrophages exhibit differential metabolic responses to lipopolysaccharide - A divergent role for glycolysis. *Redox Biol* **22**, 101147 (2019). <https://doi.org/10.1016/j.redox.2019.101147>
51. Vazquez-Carrera, M. & Wahli, W. PPARs as Key Mediators in the Regulation of Metabolism and Inflammation. *Int J Mol Sci* **23** (2022). <https://doi.org/10.3390/ijms23095025>

52. Berger, J. & Moller, D. E. The mechanisms of action of PPARs. *Annu Rev Med* **53**, 409-435 (2002). <https://doi.org/10.1146/annurev.med.53.082901.104018>
53. Mukundan, L. *et al.* PPAR-delta senses and orchestrates clearance of apoptotic cells to promote tolerance. *Nat Med* **15**, 1266-1272 (2009). <https://doi.org/10.1038/nm.2048>
54. Adhikary, T. *et al.* The transcriptional PPARbeta/delta network in human macrophages defines a unique agonist-induced activation state. *Nucleic Acids Res* **43**, 5033-5051 (2015). <https://doi.org/10.1093/nar/gkv331>
55. Li, A. C. *et al.* Differential inhibition of macrophage foam-cell formation and atherosclerosis in mice by PPARalpha, beta/delta, and gamma. *J Clin Invest* **114**, 1564-1576 (2004). <https://doi.org/10.1172/JCI18730>
56. Yu, S., Levi, L., Casadesus, G., Kunos, G. & Noy, N. Fatty acid-binding protein 5 (FABP5) regulates cognitive function both by decreasing anandamide levels and by activating the nuclear receptor peroxisome proliferator-activated receptor beta/delta (PPARbeta/delta) in the brain. *J Biol Chem* **289**, 12748-12758 (2014). <https://doi.org/10.1074/jbc.M114.559062>
57. Levi, L., Wang, Z., Doud, M. K., Hazen, S. L. & Noy, N. Saturated fatty acids regulate retinoic acid signalling and suppress tumorigenesis by targeting fatty acid-binding protein 5. *Nat Commun* **6**, 8794 (2015). <https://doi.org/10.1038/ncomms9794>
58. Armstrong, E. H., Goswami, D., Griffin, P. R., Noy, N. & Ortlund, E. A. Structural basis for ligand regulation of the fatty acid-binding protein 5, peroxisome proliferator-activated receptor beta/delta (FABP5-PPARbeta/delta) signaling pathway. *J Biol Chem* **289**, 14941-14954 (2014). <https://doi.org/10.1074/jbc.M113.514646>
59. Jin, R. *et al.* Dietary Fats High in Linoleic Acids Impair Antitumor T-cell Responses by Inducing E-FABP-Mediated Mitochondrial Dysfunction. *Cancer Res* **81**, 5296-5310 (2021). <https://doi.org/10.1158/0008-5472.CAN-21-0757>
60. Pan, Y. *et al.* Survival of tissue-resident memory T cells requires exogenous lipid uptake and metabolism. *Nature* **543**, 252-256 (2017). <https://doi.org/10.1038/nature21379>
61. Schirmer, L. *et al.* Neuronal vulnerability and multilineage diversity in multiple sclerosis. *Nature* **573**, 75-82 (2019). <https://doi.org/10.1038/s41586-019-1404-z>
62. Alonso, R., Cuevas, A. & Mata, P. Lomitapide: a review of its clinical use, efficacy, and tolerability. *Core Evid* **14**, 19-30 (2019). <https://doi.org/10.2147/CE.S174169>
63. Wang, Y. *et al.* Repositioning Lomitapide to block ZDHHC5-dependant palmitoylation on SSTR5 leads to anti-proliferation effect in preclinical pancreatic cancer models. *Cell Death Discov* **9**, 60 (2023). <https://doi.org/10.1038/s41420-023-01359-4>
64. Smith, M. E. & Bazinet, R. P. Unraveling brain palmitic acid: Origin, levels and metabolic fate. *Prog Lipid Res* **96**, 101300 (2024). <https://doi.org/10.1016/j.plipres.2024.101300>
65. Liao, D. *et al.* The role of s-palmitoylation in neurological diseases: implication for zDHC family. *Front Pharmacol* **14**, 1342830 (2023). <https://doi.org/10.3389/fphar.2023.1342830>
66. Ma, Y. *et al.* DHC5 facilitates oligodendrocyte development by palmitoylating and activating STAT3. *Glia* **70**, 379-392 (2022). <https://doi.org/10.1002/glia.24113>
67. Andrew, R. J. *et al.* Lack of BACE1 S-palmitoylation reduces amyloid burden and mitigates memory deficits in transgenic mouse models of Alzheimer's disease. *Proc Natl Acad Sci U S A* **114**, E9665-E9674 (2017). <https://doi.org/10.1073/pnas.1708568114>
68. Bhattacharyya, R., Barren, C. & Kovacs, D. M. Palmitoylation of amyloid precursor protein regulates amyloidogenic processing in lipid rafts. *J Neurosci* **33**, 11169-11183 (2013). <https://doi.org/10.1523/JNEUROSCI.4704-12.2013>
69. Li, W. *et al.* Aberrant palmitoylation caused by a ZDHHC21 mutation contributes to pathophysiology of Alzheimer's disease. *BMC Med* **21**, 223 (2023). <https://doi.org/10.1186/s12916-023-02930-7>
70. Lemarie, F. L. *et al.* Rescue of aberrant huntingtin palmitoylation ameliorates mutant huntingtin-induced toxicity. *Neurobiol Dis* **158**, 105479 (2021). <https://doi.org/10.1016/j.nbd.2021.105479>
71. Singaraja, R. R. *et al.* Altered palmitoylation and neuropathological deficits in mice lacking HIP14. *Hum Mol Genet* **20**, 3899-3909 (2011). <https://doi.org/10.1093/hmg/ddr308>
72. Sutton, L. M. *et al.* Hip14l-deficient mice develop neuropathological and behavioural features of Huntington disease. *Hum Mol Genet* **22**, 452-465 (2013). <https://doi.org/10.1093/hmg/dds441>
73. Virlogeux, A. *et al.* Increasing brain palmitoylation rescues behavior and neuropathology in Huntington disease mice. *Sci Adv* **7** (2021). <https://doi.org/10.1126/sciadv.abb0799>
74. Mukai, J. *et al.* Palmitoylation-dependent neurodevelopmental deficits in a mouse model of 22q11 microdeletion. *Nat Neurosci* **11**, 1302-1310 (2008). <https://doi.org/10.1038/nn.2204>
75. Mukai, J. *et al.* Molecular substrates of altered axonal growth and brain connectivity in a mouse model of schizophrenia. *Neuron* **86**, 680-695 (2015). <https://doi.org/10.1016/j.neuron.2015.04.003>
76. Raymond, F. L. *et al.* Mutations in ZDHHC9, which encodes a palmitoyltransferase of NRAS and HRAS, cause X-linked mental retardation associated with a Marfanoid habitus. *Am J Hum Genet* **80**, 982-987 (2007). <https://doi.org/10.1086/513609>

77. Kouskou, M. *et al.* Disruption of the *Zdhhc9* intellectual disability gene leads to behavioural abnormalities in a mouse model. *Exp Neurol* **308**, 35-46 (2018). <https://doi.org/10.1016/j.expneurol.2018.06.014>
78. Mejias, R. *et al.* Increased novelty-induced locomotion, sensitivity to amphetamine, and extracellular dopamine in striatum of *Zdhhc15*-deficient mice. *Transl Psychiatry* **11**, 65 (2021). <https://doi.org/10.1038/s41398-020-01194-6>
79. Haney, M. S. *et al.* APOE4/4 is linked to damaging lipid droplets in Alzheimer's disease microglia. *Nature* **628**, 154-161 (2024). <https://doi.org/10.1038/s41586-024-07185-7>
80. Berghoff, S. A. *et al.* Microglia facilitate repair of demyelinated lesions via post-squalene sterol synthesis. *Nat Neurosci* **24**, 47-60 (2021). <https://doi.org/10.1038/s41593-020-00757-6>
81. Maillieux, J. *et al.* Active liver X receptor signaling in phagocytes in multiple sclerosis lesions. *Mult Scler* **24**, 279-289 (2018). <https://doi.org/10.1177/1352458517696595>
82. Bogie, J. F. *et al.* Myelin-derived lipids modulate macrophage activity by liver X receptor activation. *PLoS One* **7**, e44998 (2012). <https://doi.org/10.1371/journal.pone.0044998>
83. Wouters, E. *et al.* Altered PPARgamma Expression Promotes Myelin-Induced Foam Cell Formation in Macrophages in Multiple Sclerosis. *Int J Mol Sci* **21** (2020). <https://doi.org/10.3390/ijms21239329>
84. Bogie, J. F. *et al.* Myelin alters the inflammatory phenotype of macrophages by activating PPARs. *Acta Neuropathol Commun* **1**, 43 (2013). <https://doi.org/10.1186/2051-5960-1-43>
85. Vanherle, S. *et al.* The ApoA-I mimetic peptide 5A enhances remyelination by promoting clearance and degradation of myelin debris. *Cell Rep* **41**, 111591 (2022). <https://doi.org/10.1016/j.celrep.2022.111591>
86. Zheng, S. *et al.* ZDHHC5-mediated NLRP3 palmitoylation promotes NLRP3-NEK7 interaction and inflammasome activation. *Mol Cell* **83**, 4570-4585 e4577 (2023). <https://doi.org/10.1016/j.molcel.2023.11.015>
87. Du, G. *et al.* ROS-dependent S-palmitoylation activates cleaved and intact gasdermin D. *Nature* **630**, 437-446 (2024). <https://doi.org/10.1038/s41586-024-07373-5>
88. Schug, T. T., Berry, D. C., Shaw, N. S., Travis, S. N. & Noy, N. Opposing effects of retinoic acid on cell growth result from alternate activation of two different nuclear receptors. *Cell* **129**, 723-733 (2007). <https://doi.org/10.1016/j.cell.2007.02.050>
89. Guo, Y. *et al.* Oxidative stress-induced FABP5 S-glutathionylation protects against acute lung injury by suppressing inflammation in macrophages. *Nat Commun* **12**, 7094 (2021). <https://doi.org/10.1038/s41467-021-27428-9>
90. Miron, V. E. *et al.* M2 microglia and macrophages drive oligodendrocyte differentiation during CNS remyelination. *Nat Neurosci* **16**, 1211-1218 (2013). <https://doi.org/10.1038/nn.3469>
91. Kotter, M. R., Zhao, C., van Rooijen, N. & Franklin, R. J. Macrophage-depletion induced impairment of experimental CNS remyelination is associated with a reduced oligodendrocyte progenitor cell response and altered growth factor expression. *Neurobiol Dis* **18**, 166-175 (2005). <https://doi.org/10.1016/j.nbd.2004.09.019>
92. Ruckh, J. M. *et al.* Rejuvenation of regeneration in the aging central nervous system. *Cell Stem Cell* **10**, 96-103 (2012). <https://doi.org/10.1016/j.stem.2011.11.019>
93. Kotter, M. R., Li, W. W., Zhao, C. & Franklin, R. J. Myelin impairs CNS remyelination by inhibiting oligodendrocyte precursor cell differentiation. *J Neurosci* **26**, 328-332 (2006). <https://doi.org/10.1523/JNEUROSCI.2615-05.2006>
94. Lampron, A. *et al.* Inefficient clearance of myelin debris by microglia impairs remyelinating processes. *J Exp Med* **212**, 481-495 (2015). <https://doi.org/10.1084/jem.20141656>
95. Berghoff, S. A., Spieth, L. & Saher, G. Local cholesterol metabolism orchestrates remyelination. *Trends Neurosci* **45**, 272-283 (2022). <https://doi.org/10.1016/j.tins.2022.01.001>
96. Liddelov, S. A. *et al.* Neurotoxic reactive astrocytes are induced by activated microglia. *Nature* **541**, 481-487 (2017). <https://doi.org/10.1038/nature21029>
97. Makinodan, M. *et al.* Social isolation impairs remyelination in mice through modulation of IL-6. *FASEB J* **30**, 4267-4274 (2016). <https://doi.org/10.1096/fj.201600537R>
98. Spaas, J. *et al.* Oxidative stress and impaired oligodendrocyte precursor cell differentiation in neurological disorders. *Cell Mol Life Sci* **78**, 4615-4637 (2021). <https://doi.org/10.1007/s00018-021-03802-0>
99. Wan, T. *et al.* Astrocytic phagocytosis contributes to demyelination after focal cortical ischemia in mice. *Nat Commun* **13**, 1134 (2022). <https://doi.org/10.1038/s41467-022-28777-9>
100. Ponath, G. *et al.* Myelin phagocytosis by astrocytes after myelin damage promotes lesion pathology. *Brain* **140**, 399-413 (2017). <https://doi.org/10.1093/brain/aww298>
101. Baaklini, C. S. *et al.* Microglia promote remyelination independent of their role in clearing myelin debris. *Cell Rep* **42**, 113574 (2023). <https://doi.org/10.1016/j.celrep.2023.113574>
102. Yang, X. *et al.* Protein palmitoylation regulates extracellular vesicle production and function in sepsis. *J Extracell Biol* **1** (2022). <https://doi.org/10.1002/jex2.50>
103. Guo, R. *et al.* Reduction of DHHC5-mediated beclin 1 S-palmitoylation underlies autophagy decline in aging. *Nat Struct Mol Biol* **31**, 232-245 (2024). <https://doi.org/10.1038/s41594-023-01163-9>
104. Grajchen, E. *et al.* CD36-mediated uptake of myelin debris by macrophages and microglia reduces neuroinflammation. *J Neuroinflammation* **17**, 224 (2020). <https://doi.org/10.1186/s12974-020-01899-x>

105. Shaw, P. J. *et al.* Signaling via the RIP2 adaptor protein in central nervous system-infiltrating dendritic cells promotes inflammation and autoimmunity. *Immunity* **34**, 75-84 (2011). <https://doi.org/10.1016/j.immuni.2010.12.015>
106. Hayes, C. E. & Ntambi, J. M. Multiple Sclerosis: Lipids, Lymphocytes, and Vitamin D. *Immunometabolism* **2** (2020). <https://doi.org/10.20900/immunometab20200019>



Geneeskundige Stichting Koningin Elisabeth
Fondation Médicale Reine Elisabeth
Königin-Elisabeth-Stiftung für Medizin
Queen Elisabeth Medical Foundation

Progress report
of the research group of

Prof. dr. Bieke Broux
Universiteit Hasselt (UHasselt)

Bieke Broux, PhD (she, her) (UHasselt)

Assistant Professor Immunology

Chronic inflammation and Blood brain barrier disruption in Neurodegeneration (CBN)

Neuroimmune Connections & Repair (NIC&R) lab
Hasselt University – Biomedical Research Institute
Agoralaan, building C – B-3590 Diepenbeek
T +32 11 26 92 54
T +32 468 14 30 54

High salt diet causes blood-brain barrier disturbances in multiple sclerosis: involvement of the renin-angiotensin-aldosterone system

1. Research summary

Multiple sclerosis (MS) is a chronic neurodegenerative disease that affects millions globally, leading to significant physical and cognitive deterioration due to demyelination and neurodegeneration. Central to the disease's pathogenesis is the disruption of the blood-brain barrier (BBB), which allows immune cells to migrate into the brain, exacerbating neuronal damage. The BBB, a critical defense mechanism in maintaining the neuronal microenvironment, is formed by specialized endothelial cells (ECs) that, in collaboration with astrocyte, regulate the passage of molecules and cells between the blood and the brain. Despite extensive research into the genetic and environmental factors influencing MS, its exact etiology remains unclear, hindering the development of effective treatments.

Dietary factors, particularly high-salt diets (HSD), have been implicated as significant contributors to MS progression. High-salt intake has been shown to exacerbate experimental autoimmune encephalomyelitis (EAE), a preclinical model for MS, and alter the integrity of the BBB. However, the impact of HSD on the human BBB, especially in the context of neuroinflammation and the interactions between endothelial cells and astrocytes, remains largely unexplored. Moreover, emerging studies have suggested that salt sensitivity and the renin-angiotensin-aldosterone system (RAAS) may play a crucial role in MS, with RAAS activation linked to increased BBB permeability. Despite these findings, the precise effects of high salt concentrations on the RAAS in the human neurovascular unit (NVU) and its role in MS-related BBB disruption have not been thoroughly investigated.

The goal of this study is to elucidate the effects of high salt concentrations on BBB activation and integrity in human endothelial cells and astrocytes, both in isolation and under inflammatory conditions. By generating detailed protein expression profiles and RAAS fingerprint datasets, this project aims to uncover salt-induced, RAAS-mediated alterations in BBB integrity. Additionally, the research will explore the interactions between BBB endothelial cells and astrocytes under high-salt conditions and their impact on BBB function in MS. Ultimately, this project seeks to establish the link between salt sensitivity, RAAS dysregulation, and BBB impairment in MS, providing new insights into the role of dietary factors in disease progression and offering potential therapeutic targets for intervention.

2. Results

2.1. Evaluation of Cell Viability in Astrocytes (ASTs) and Endothelial Cells (ECs) Under Varying NaCl Concentrations

As key cellular components of the blood-brain barrier (BBB), endothelial cells (ECs) HCMEC/D3 human cerebral microvascular endothelial cell line and primary astrocytes (ASTs) were selected for cellular experiments. To better determine the appropriate cellular stimulation concentration that corresponds to a high-salt diet, we reevaluated the experimental NaCl stimulation concentrations. The cytotoxic effects of these concentrations on ECs and ASTs were meticulously examined

using the LDH assay (Figure 1 and Figure 2). The results demonstrated that in both cell type, a 40 mM NaCl concentration was manageable and corresponded well to high-salt conditions (with or without inflammatory) observed in vivo, making it suitable for subsequent experiments. Additionally, a 10 mM NaCl concentration was used as a control in certain experiments to provide comparative insights.

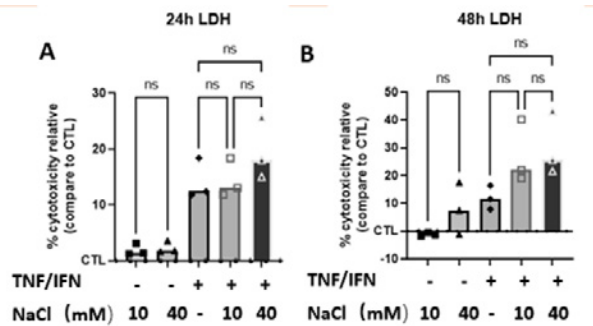


Figure 1. A/B: LDH kit analysis of cytotoxicity in hCMEC/D3 cells (n=3) after treated 24 and 48h with 10mM or 40mM NaCl in the presence/absence of 10 ng/ ml TNF-/IFN-. Results were analyzed by one-way analysis of variance (ANOVA) with Friedman test, and correction for multiple comparisons performed with Dunn's test.

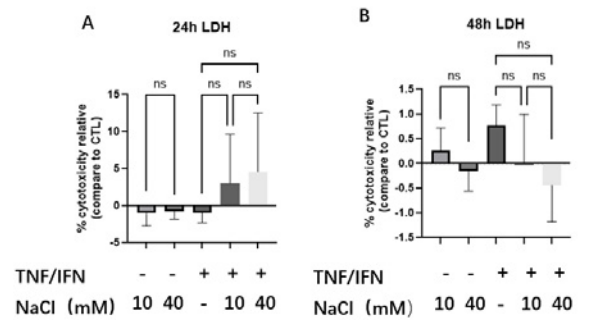


Figure 2. A/B: LDH kit analysis of cytotoxicity in astrocytes (n=3) after treated 24 and 48h with 10mM or 40mM NaCl in the presence/absence of 10 ng/ ml TNF-/IFN-. Results were analyzed by one-way analysis of variance (ANOVA) with Friedman test, and correction for multiple comparisons performed with Dunn's test.

2.2. Tight Junction Gene and Protein Expression in ECs

To investigate the effects of high sodium concentration on the tight junctions of EC cells, we examined the gene and protein expression levels of Claudin-5. The results indicated that there was no significant difference in the mRNA and protein expression of Claudin-5 between the non-inflammatory and inflammatory control groups and the high-salt groups. (Figure 3)

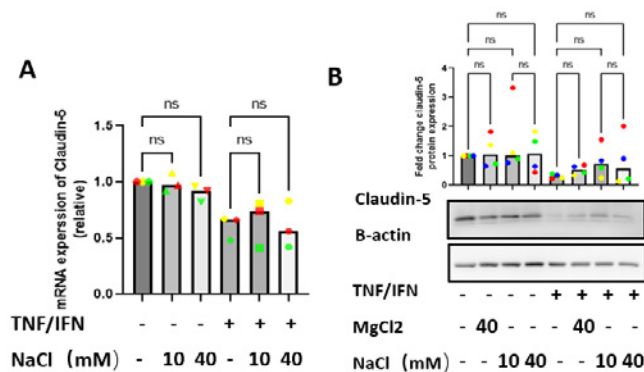


Figure 3. A. qPCR analysis of Claudin-5 mRNA in hCMEC/D3 cells (n=3) treated 24h. B. Western blot analysis of Claudin-5 in hCMEC/D3 cells (n=3) treated 48h. Here, MgCl2 be taken as Anion control. Results were analyzed by one-way analysis of variance (ANOVA) with Friedman test, and correction for multiple comparisons performed with Dunn's test.

2.3. Adhesion Molecule Expression in ECs

Adhesion molecules such as ICAM-1, VCAM-1, and VE-Cadherin are critical for the maintenance of endothelial cell function and integrity. Therefore, we also investigated the expression of these adhesion molecules in ECs at the transcriptional level. The results showed no significant difference in the expression of ICAM-1, VCAM-1, and VE-Cadherin between the non-inflammatory/inflammatory control groups and the high-salt groups. (Figure 4)

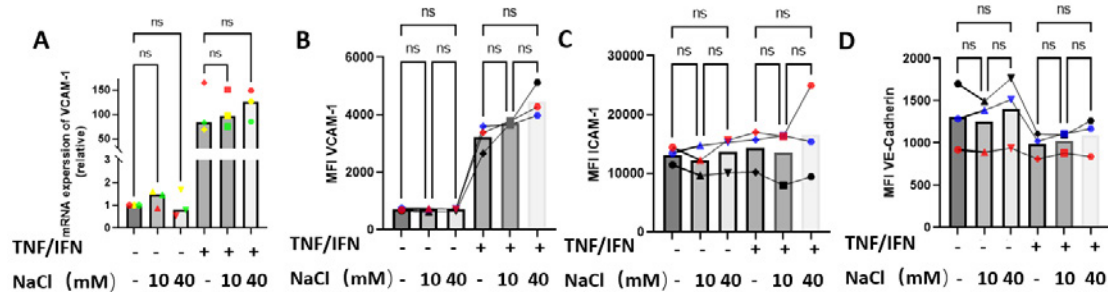


Figure 4. A: qPCR analysis of VCAM-1 mRNA in hCMEC/D3 cells ($n=3$), treated 24h. B/C/D: Flow cytometry analysis of VCAM-1, ICAM-1 and VE-Cadherin in hCMEC/D3 cells ($n=3$) treated 48h. Results were analyzed by one-way analysis of variance (ANOVA) with Friedman test, and correction for multiple comparisons performed with Dunn's test.

2.4. Differential Gene Expression Analysis in ECs and ASTs under high-salt conditions

For the ECs, a total of 45 differentially expressed genes (DEGs) were identified in the comparison between the CTL and 40 mM NaCl groups. Of these, 34 genes were relatively upregulated in the NaCl group, while 11 were upregulated in the CTL group ($p < 0.05$). Genes with \log_2 fold change > 1 were selected to create the volcano plot shown in the Figure 5A. In the comparison between inflammation without or with high salt concentration, a total of 57 differentially expressed genes (DEGs) were identified. Of these, 41 genes were relatively upregulated in the inflammation with NaCl group, while 16 were upregulated in the inflammation group ($p < 0.05$). Genes with \log_2 fold change > 1 were selected to create the volcano plot shown in the Figure 5B.

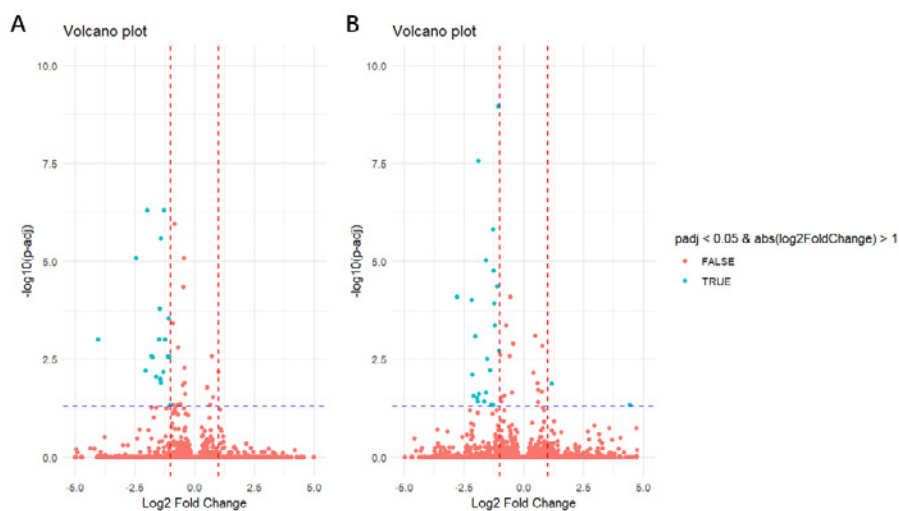


Figure 5. Overview of the gene expression profile in ECs under high-salt conditions. (A) Volcano plot of differential gene expression patterns from the control group ($n=4$) versus the NaCl(40mM) treated group ($n=4$). The blue plots indicate the significantly dysregulated genes. (\log_2 fold change > 1 and adjust p value < 0.05). (B) Volcano plot of differential gene expression patterns from the inflammation group (treated with 10 ng/ ml TNF-/IFN-) ($n=4$) versus the group treated with both NaCl (40mM) and inflammation treated($n=4$). The blue plots indicate the significantly dysregulated genes. (\log_2 fold change > 1 and adjust p value < 0.05).

For the ASTs, 8 differentially expressed genes (DEGs) were identified in the comparison between the CTL and 40 mM NaCl groups. Genes with log₂ fold change > 1 were selected to create the volcano plot shown in the Figure 6A. A total of 14 differentially expressed genes (DEGs) were identified in the comparison between inflammation group versus the inflammation with high salt concentration group, Genes with log₂ fold change > 1 were selected to create the volcano plot shown in the Figure 6B.

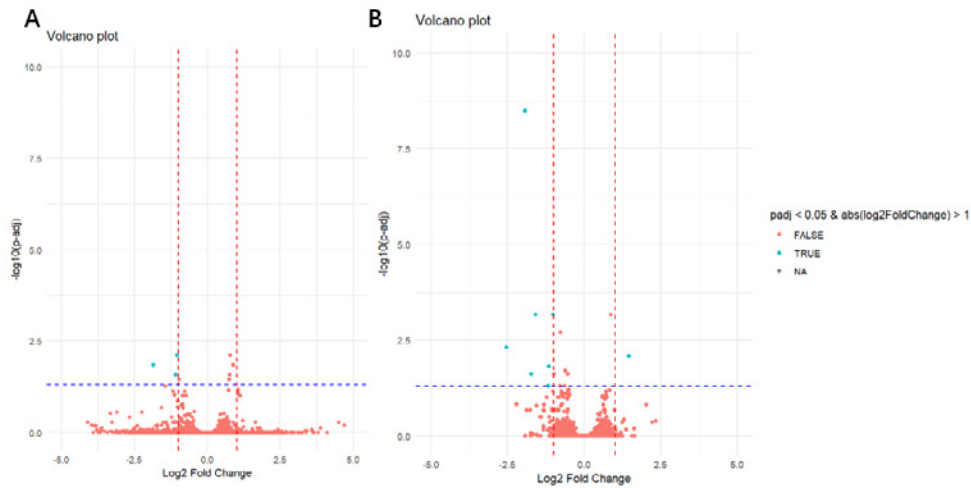


Figure 6. Overview of the gene expression profile in ASTs under high-salt conditions. (A) Volcano plot of differential gene expression patterns from the control group ($n=4$) versus the NaCl(40mM) treated group ($n=4$). The blue plots indicate the significantly dysregulated genes. (\log_2 fold change > 1 and adjust p value < 0.05). (B) Volcano plot of differential gene expression patterns from the inflammation group (treated with 10 ng/ ml TNF-/IFN-) ($n=4$) versus the group treated with both NaCl (40mM) and inflammation treated($n=4$). The blue plots indicate the significantly dysregulated genes. (\log_2 fold change > 1 and adjust p value < 0.05).

GO and KEGG Pathway enrichment analysis in ASTs Figure 7

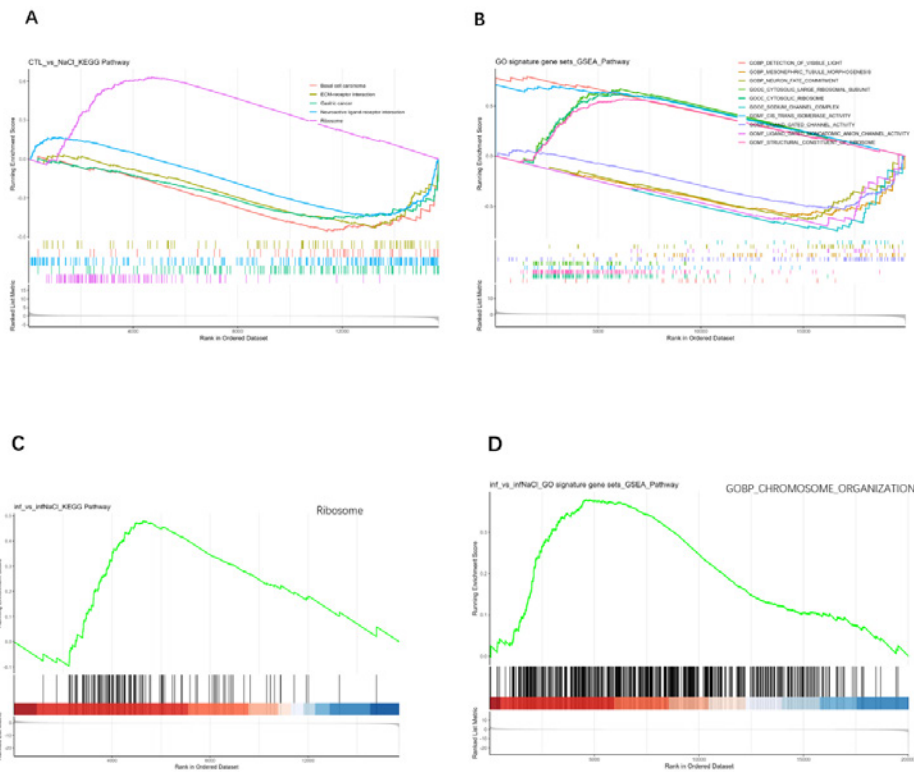


Figure 7. ...

Through STRING database, protein-protein interaction analysis was performed based on differentially expressed genes (adjust $p < 0.05$). The results are shown in Figure 8. Interestingly, we found that under the CTL_versus_NaCl DEGs, ARG2 in EC cells interacts with ODC1 in AST cells, and under the inflammation versus inflammation with NaCl condition, PGM2L1 in EC cells interacts with IMPA2 in AST cells.

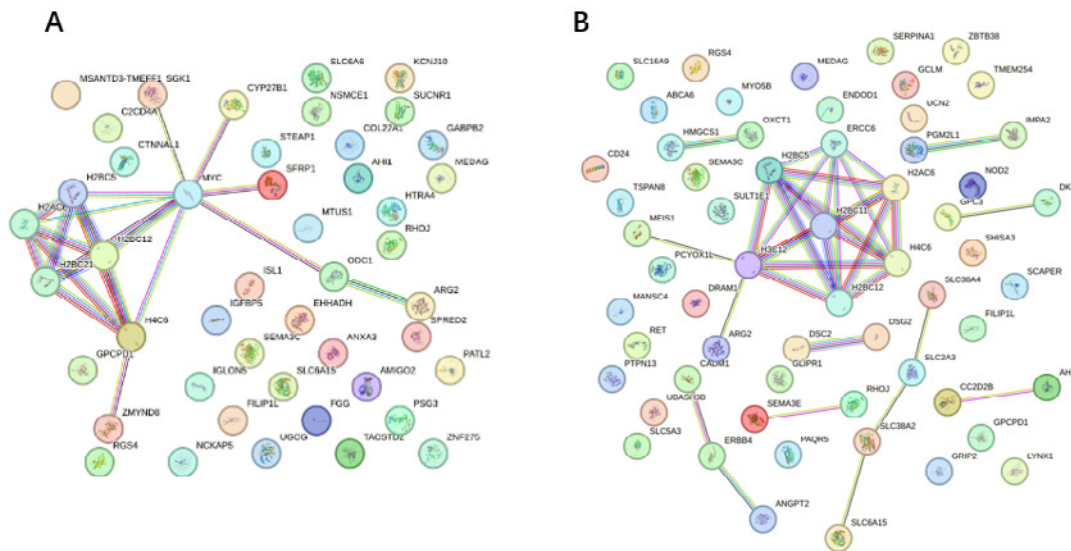


Figure 8. Protein–protein interaction network analysis under the same treatment conditions, a joint analysis of differentially expressed genes (DEGs) from ECs and ASTs. (A) DEGs between the CTL and 40 mM NaCl groups, while (B) DEGs between inflammation (treated with 10 ng/ ml TNF-/IFN-) versus inflammation with 40 mM NaCl groups. The analysis was conducted on the STRING database official website (https://string-db.org/cgi/about?footer_active_subpage=references), each gene is represented as a node, and the minimum required interaction score is set to medium confidence (score = 0.400).

3. Future plans

Building on the progress achieved last year, our focus this year will be to further explore the high-salt-related differentially expressed genes (DEGs) and the enriched pathways or protein-protein interaction analysis identified in both ECs and astrocytes (ASTs). These findings will undergo additional validation through comprehensive mechanistic studies to uncover the underlying processes involved in the blood-brain barrier (BBB) under high-salt conditions. Alongside these *in vitro* investigations, we will conduct *in vivo* animal experiments to validate the physiological relevance of our findings. Furthermore, we will incorporate the use of iPSC-derived BBB-endothelial cells in our experiments, as part of the new BBB model. This will not only enhance the translational value of the study but also allow for the application of more sophisticated models that better mimic the human BBB. Through these efforts, we aim to deepen our understanding of the molecular mechanisms linking high salt intake to BBB and its implications in neuroinflammatory diseases like multiple sclerosis.



Geneeskundige Stichting Koningin Elisabeth
Fondation Médicale Reine Elisabeth
Königin-Elisabeth-Stiftung für Medizin
Queen Elisabeth Medical Foundation

Progress report
of the research group of

Dr. Sophie Laguesse
Université de Liège (ULiège)

Dr. Sophie Laguesse (ULiège)

Liège University

F.R.S-FNRS Research Associate

Giga-Stem Cells, Giga-Neurosciences

Laboratory of molecular regulation of Neurogenesis – Addiction development

Quartier Hôpital

15, Avenue Hippocrate

B-4000 Liège

Belgium

T +32 4 366.59.51

slaguesse@uliege.be

ORCID 0000-0002-9217-0087

Unveiling the alcohol-dependent alterations in mRNA local translation and its consequences on adolescent prefrontal cortex maturation and function

1. Goals of the research

Alcohol use disorder (AUD) is characterized by an impaired ability to control alcohol use and ranks among the most prevalent mental disorders globally. The neural mechanisms of AUD have remained uncertain, and multiple genetic, psychological and environmental factors are thought to be involved. For decades, AUD has been considered as a pathological condition that develops in adults, but growing evidence suggests that its roots may emerge during adolescence. Indeed, studies have shown that adolescent alcohol exposure (AAE) may interfere with the maturation of some frontal brain regions, including the prefrontal cortex (PFC) and lead to heightened vulnerability to develop AUD and comorbid psychopathology later in life. However, **the precise mechanisms by which alcohol perturbs the maturation of the PFC are not fully understood.** Addiction has been conceptualized as a maladaptive form of memory involving persistent drug-associated memories. In this view, alcohol is thought to usurp the molecular mechanisms underlying memory, including synaptic plasticity which depends on the local translation of mRNAs at synaptic sites. Here, **we hypothesize that AAE interferes with local translation of mRNAs, thereby impairing prefrontal cortex maturation.** The main goals of this research are (i) To unveil whether AAE leads to PFC malfunction in mice, (ii) To decipher whether AAE modulates the activity of specific local translation regulators in the PFC, (iii) To identify the pool of mRNAs whose local translation is modulated by AAE in specific neuronal populations and (iv) unveil their involvement in AAE-induced PFC defects, and finally (v) To decipher whether AAE differentially impacts male and female PFC.

1.1. **Task 1: Characterizing PFC malfunction induced by adolescent alcohol binge-drinking**

By using a modified version of the Drinking in the Dark paradigm, we previously reported that voluntary alcohol binge-drinking in adolescent mice significantly increases anxiety-like, depressive-like behaviors and alcohol consumption, while impairing recognition memory and behavioral flexibility in adulthood, suggesting that AAE compromises long-term PFC function (Van Hees, Didone *et al.* 2022).

1.2. **Uncovering the structural and transmission defects induced by AAE in the PFC**

1.2.1 Transmission defects

We performed whole cell patch-clamp recordings in layer V glutamatergic neurons of the prelimbic subregion of the PFC in adolescent (P43) and adult (P80) male mice.

In late adolescent mice, we showed a significant increase in the frequency of spontaneous excitatory post-synaptic currents in AAE animals as compared to control littermates, without significant change in their amplitude (**Figure 1**).

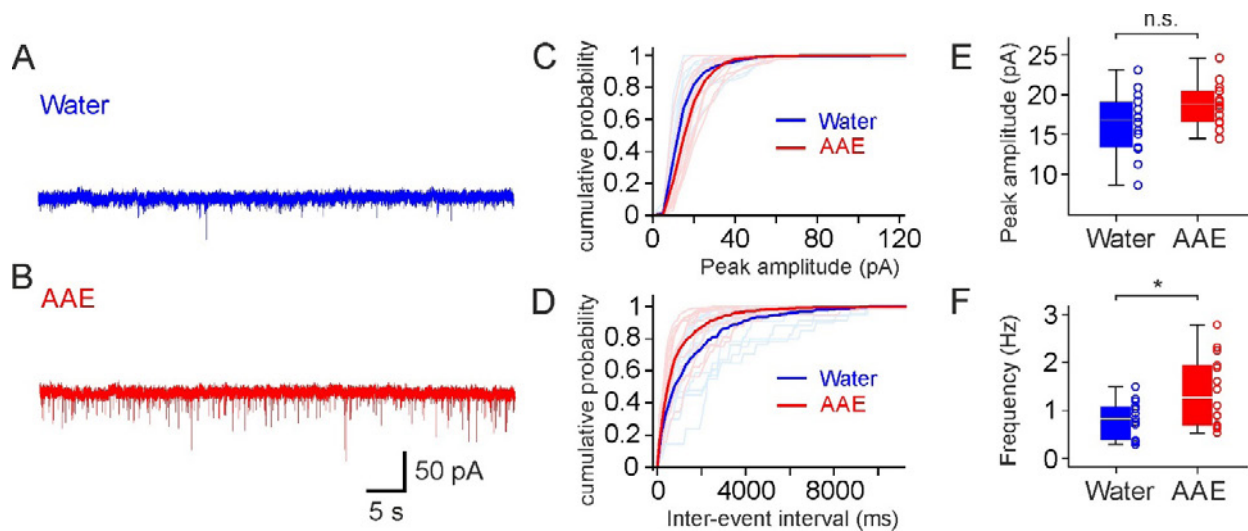


Figure 1. Alcohol consumption increases sEPSC frequency in layer 5 pyramidal neurons of the prelimbic cortex at P43. (A, B) Current traces showing spontaneous EPSCs at -60 mV in slices from water-consuming mice (top, blue traces) and from alcohol-consuming mice (bottom, red traces). External solution contained 50 μ M picrotoxin to block inhibitory synaptic currents. (C, D) Cumulative distributions of spontaneous EPSC amplitude (C) and inter-event intervals (D). Thick lines are average cumulative distributions from pyramidal neurons in water- (blue) and alcohol-consuming (red) mice, respectively. Thin lines are from individual cells. Data are from 14 and 14 individual neurons, respectively. (E, F) Histograms of EPSC peak amplitude (E) and frequency (F) for water-consuming mice and alcohol-consuming mice. Data are from 14 pyramidal neurons (water) and 14 pyramidal neurons (AAE). * $p < 0.05$.

We investigated the possibility of pre-synaptic defects induced by AAE, such as increased NT vesicles release or increased number of afferent synapses. Paired-pulse ratio analysis in layer V projection neurons of the prelimbic cortex of males P43 did not show any difference in the probability of neurotransmitter vesicles release between water and AAE animals (Figure 2).

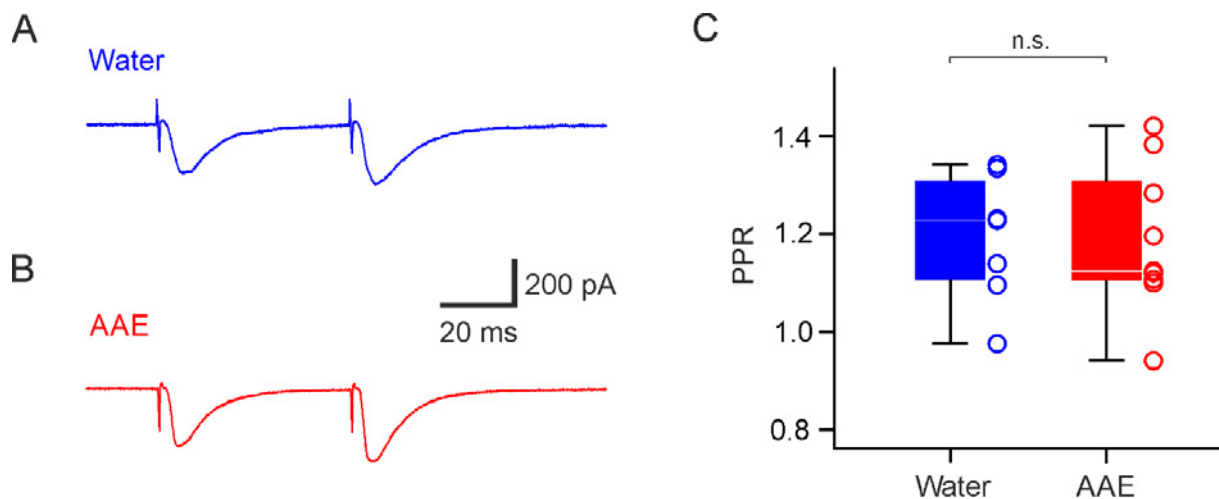


Figure 2. Alcohol consumption does not modify paired-pulse ratio in layer 5 pyramidal neurons of the prelimbic cortex at P43. (A, B) Current traces in response to a paired-pulse protocol (50 Hz) from water-consuming mice (top, blue traces) and from alcohol-consuming mice (bottom, red traces). (C) Histograms of PPR from 8 water neurons and 9 AAE neurons.

We then examined potential postsynaptic effects, including increased spine density, modifications in the NMDA/AMPA ratio, or changes in the subunit composition of AMPARs and NMDARs. Such alterations could contribute to an increase in functional synapse numbers or impact synaptic plasticity. Spine density was not increased at P43 but rather decreased (see structural analysis below). NMDA/AMPA ratio was significantly increased in AAE condition, mainly due to increased NMDAR current amplitude (Figure 3).

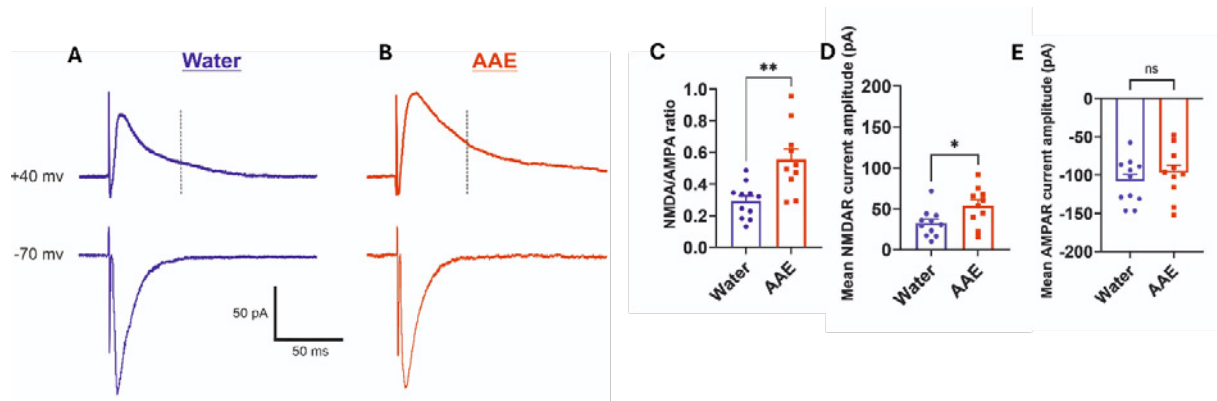


Figure 3. Adolescent alcohol exposure impacts NMDAR currents in layer 5 pyramidal neurons of the prelimbic cortex at P43. (A,B) Averaged traces of evoked excitatory post-synaptic currents +40 mV (upper traces) and -70 mV (lower traces) from water-consuming mice (blue traces) and from alcohol-consuming mice (red traces). (C) Bar graph representing the NMDA/AMPA ratio. (D) bar graph showing the mean NMDAR current amplitude calculated at 40 ms after the onset of the event at +40 mV (dashed line A and B). (E) Bar graph representing the mean AMPAR current amplitude calculated at -70 mV. * $p < 0.05$. ** $p < 0.01$.

We further dig into potential modification of NMDAR subunits upon AAE. Preliminary data suggest that AAE may affect the subunit composition of NMDAR at P43 (Figure 4)

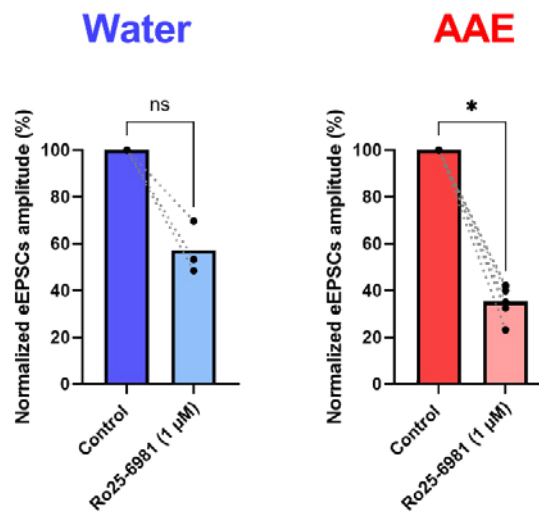


Figure 4. Adolescent alcohol exposure impact the subunits composition of NMDAR in layer 5 pyramidal neurons of the prelimbic cortex at p43. (A,B) Bar graph showing the effect of 1 μM of Ro25-6981 (specific antagonist of GluN2B) on normalized NMDAR current in from water-consuming mice (blue graphs) and from alcohol-consuming mice (red graphs) (preliminary data).

In adulthood, no difference was observed in the frequency or amplitude of sEPSCs between AAE and water animals (Figure 5).

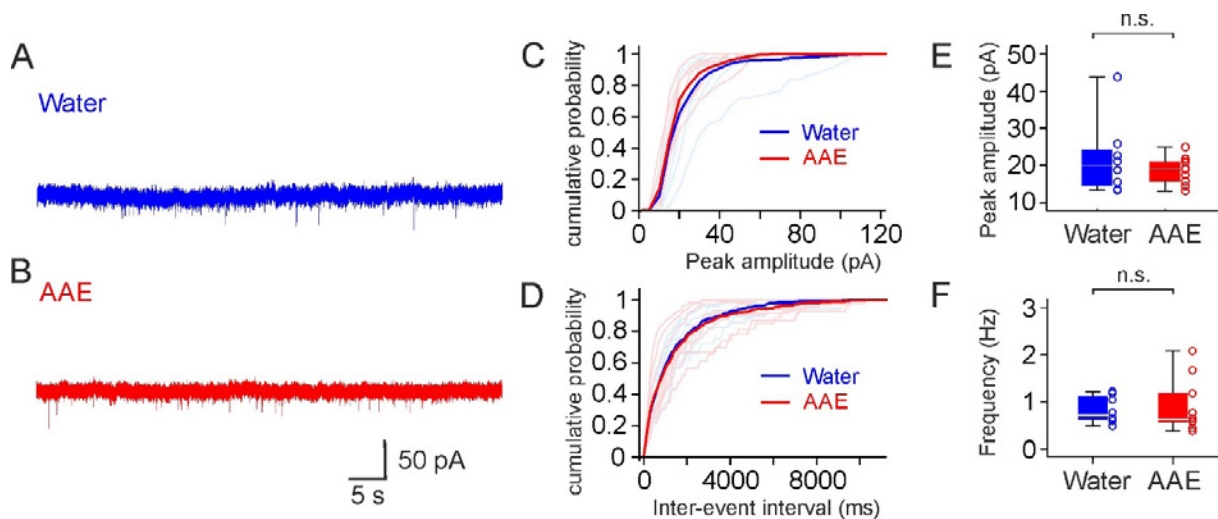


Figure 5. Alcohol consumption does not modify sEPSC frequency in layer 5 pyramidal neurons of the prelimbic cortex at P80. (A, B) Current traces showing spontaneous EPSCs at -60 mV in slices from water-consuming mice (top, blue traces) and from alcohol-consuming mice (bottom, red traces). External solution contained 50 μ M picrotoxin to block inhibitory synaptic currents. (C, D) Cumulative distributions of spontaneous EPSC amplitude (C) and inter-event intervals (D). Thick lines are average cumulative distributions from pyramidal neurons in water- (blue) and alcohol-consuming (red) mice, respectively. Thin lines are from individual cells. Data are from 8 and 10 individual neurons, respectively. (E, F) Histograms of EPSC peak amplitude (E) and frequency (F) for water-consuming mice and alcohol-consuming mice. Bars represent mean \pm SEM; open circles indicate data from individual recordings. Data are from 8 pyramidal neurons (water) and 10 pyramidal neurons (AAE).

However, analysis of the NMDA/AMPA ratio at P80 showed significant increase in mice exposed to alcohol during adolescence, caused by increased in NMDAR currents (**Figure 6**).

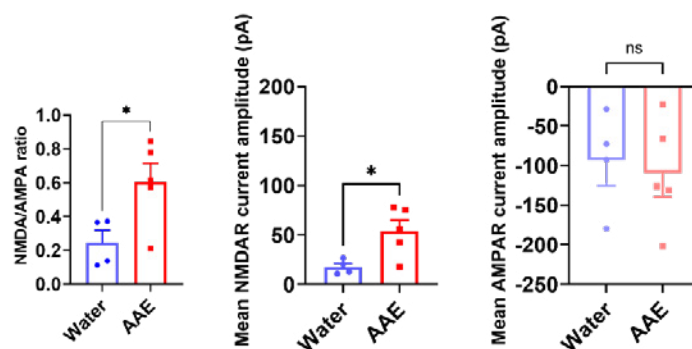


Figure 6. Adolescent alcohol exposure impacts NMDAR current in layer 5 pyramidal neurons of the prelimbic cortex at P80 (A) Bar graph representing the NMDA/AMPA ratio. (B) bar graph showing the mean NMDAR current amplitude calculated at 40 ms after the onset of the event at +40 mV. (C) Bar graph representing the mean AMPAR current amplitude calculated at -70 mV. (preliminary data)

Moreover, spontaneous and evoked inhibitory post-synaptic currents (sIPSCs and mIPSCs) are currently recorded to assess potential AAE-induced changes in inhibitory responses. Finally, layer II-III projection neurons will also be analyzed.

1.2.2 Structural defects

Neurons were filled with biocytin for *post hoc* immunohistochemistry, 3D reconstruction and morphological analysis. We did not observe any defect in dendritic arborization of layer V glutamatergic neurons of the prelimbic PFC, neither at P43 or P80 (**Figure 7**).

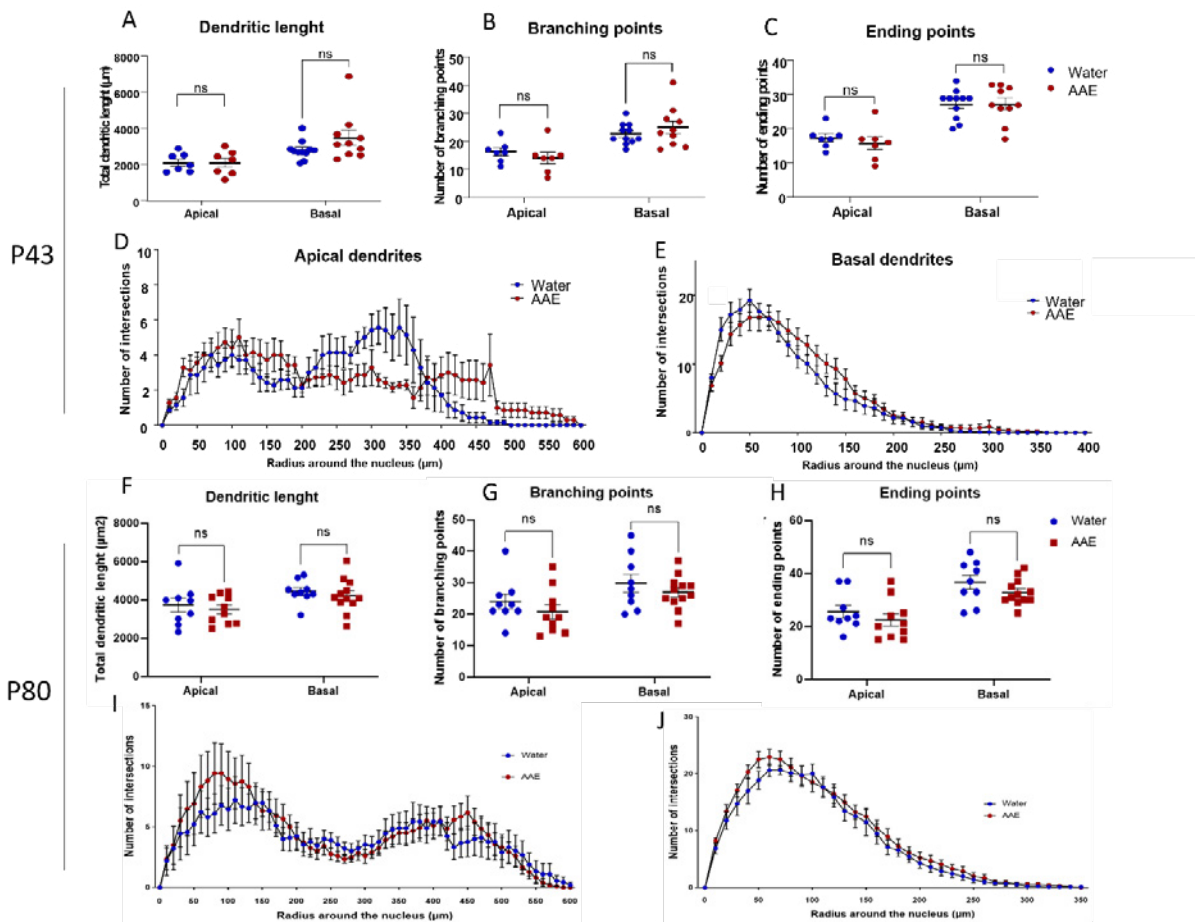


Figure 7. No change in apical and basal dendrites morphometric measurements after AAE in prelimbic layer V projection neurons at P43 or P80. (A) Total length of apical (left) and basal (right) dendritic arborizations. Unpaired t test showed no effect of alcohol on apical dendritic length ($p=0.9854$) nor on basal dendritic length ($p=0.1361$). (B-C) Number of branching and ending points per apical and basal dendritic arborization per neuron. Unpaired t test showed no effect of alcohol on the number of apical ($p=0.4114$) and basal ($p=0.8279$) branching points nor on the number of apical ($p=0.50$) and ($p=0.9731$) basal ending points. (D-E) Sholl analysis of apical (D) and basal (E) dendrites. Two-way ANOVA showed no effect of AAE (*apical*: $p=0.715$, $F_{(1,12)}=0.1403$; *basal*: $p=0.5116$, $F_{(1,19)}=0.4474$). Data are presented as mean \pm SEM; for apical dendrites: $n=7$ water, $n=7$ AAE; for basal dendrites: $n=11$ water, $n=10$ AAE. (F) Total length of apical (left) and basal (right) dendritic arborizations, expressed in μm . Unpaired t test did not show any significant difference in apical ($p=0.5773$) and basal dendritic length ($p=0.5274$). (G-H) Number of branching and ending points per apical (left) and basal (right) dendritic arborization per neuron. Unpaired t test showed a similar number of apical ($p=0.3406$) and basal ($p=0.3518$) branching points and a constant number of apical ($p=0.3627$) and ($p=0.1907$) basal ending points between water and AAE mice. (I-J) Sholl analysis of apical (I) and basal (J) dendrites. Two-way ANOVA showed no effect of AAE (*apical*: $p=0.5814$, $F_{(1,19)}=0.3146$; *basal*: $p=0.341$, $F_{(1,19)}=0.9539$). Data are presented as mean \pm SEM; for apical dendrites: $n=9$ water, $n=10$ AAE; for basal dendrites: $n=9$ water, $n=12$ AAE

However, we identified changes in dendritic spine morphology in late adolescence following AAE, including decreased spine density, increased mean spine head size and volume. We also observed increased proportion of mushroom-type spines at the expense of thin spines, which is mostly due to a significant reduction in the density of thin spine subtypes (Figure 8).

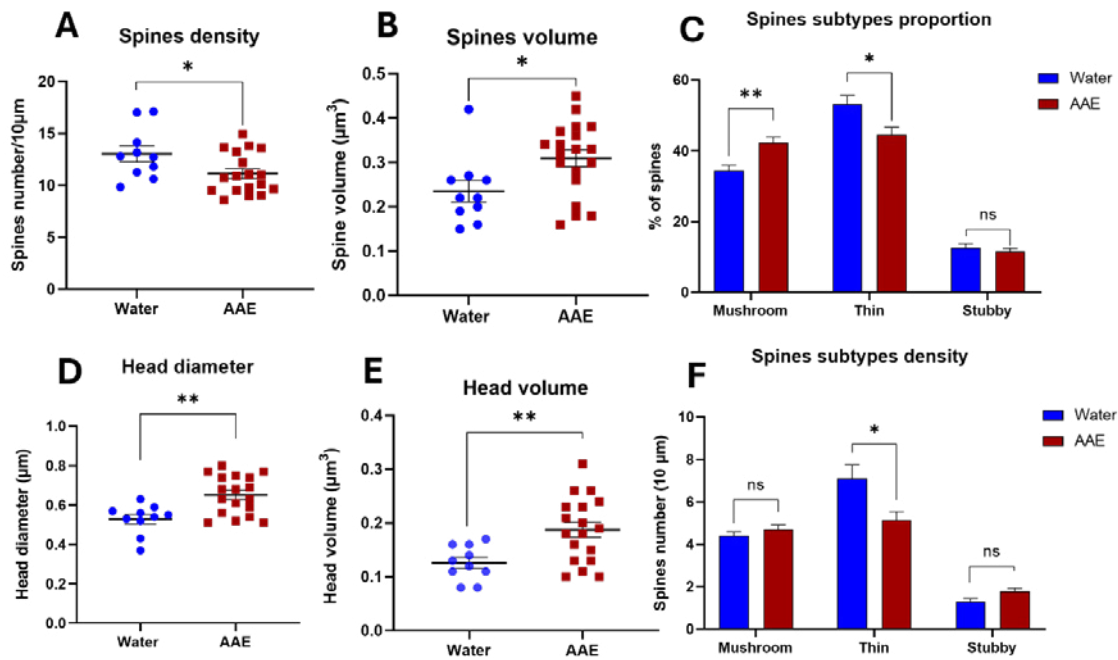


Figure 8. AAE modifies dendritic spine morphology in PFC layer V projection neurons at P43. (A) Spine density defined as the number of spines per 10µm of dendrite. Unpaired t test revealed a significant difference in spines density between alcohol and control groups ($p=0.03$). (B) Spine volume. Unpaired t test revealed a significant difference in spines density between alcohol and control groups ($p=0.02$). (C) Percentage of mushroom, thin and stubby-type spines. Percentage is measured as the number of each type of spines on the total number of spines per dendrite*100. Two-ways ANOVA showed a significant effect of AAE on the percentage of mushroom-type spines ($p=0.0427$), and thin- ($p=0.035$) but not stubby-type ($p=0.3597$) percentage. (D,E) Average head max diameter and head volume of water and AAE mice. Unpaired t test showed a significant increased head max diameter (D) ($p=0.045$) and head volume (E) ($p=0.02$). (F) Spine subtypes density. Two-ways ANOVA showed a significant effect of AAE on thin spines density ($p=0.035$) but not stubby-type or mushroom-type. Data are presented as mean \pm SEM; $n=14$ water, $n=16$ AAE; $p<0.05$.

In adulthood, dendritic spine density and morphology were not affected by AAE (Figure 9).

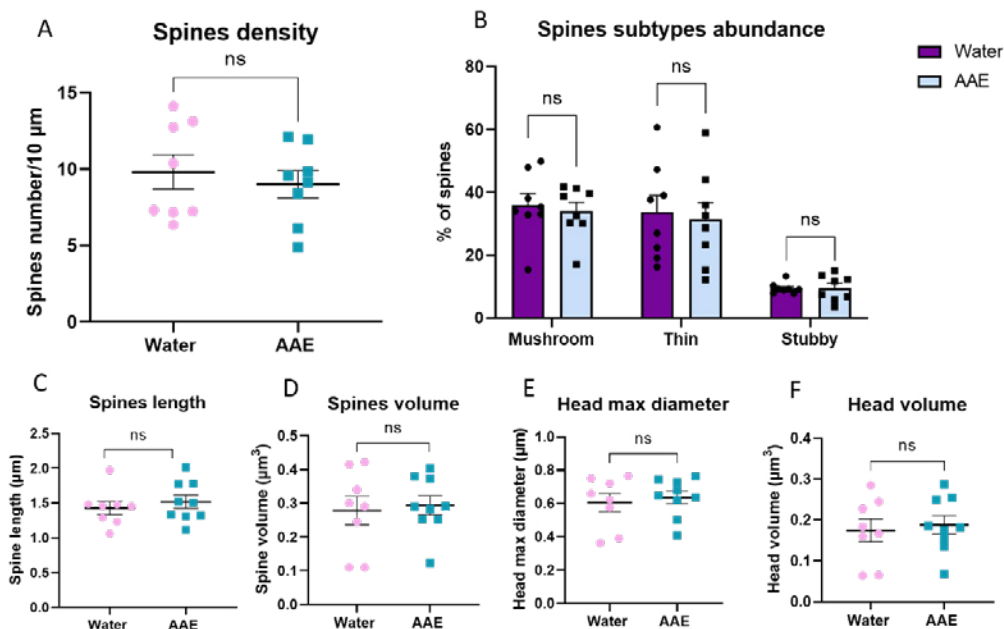


Figure 9. No defect in dendritic spine number or morphology in PFC layer V projection neurons at P80 (A) Spines density defined as the number of spines per 10µm of dendrite. Unpaired t test showed no significant difference between alcohol and control groups ($p=0.5838$). (B) Percentage of mushroom, thin and stubby-type spines. Percentage is measured as the number of each type of spines on the total number of spines per dendrite*100. Unpaired t test showed no main effect of AAE on the percentage of mushroom- ($p=0.6882$), thin- ($p=0.77$) and stubby-type ($p=0.999$) spines. (C-F) Average spine length, volume, head max diameter and head volume of water and AAE mice. Unpaired t test showed that AAE did not significantly modify spine length ($p=0.5098$), spine volume ($p=0.7667$), head max diameter ($p=0.6508$) and head volume ($p=0.711$). Data are presented as mean \pm SEM; $n=8$ water neurons, $n=9$ AAE neurons.

Our results suggest that AAE leads to impaired behaviors in adulthood together with transmission defects in layer V neurons of the vmPFC (NMDAR currents), which are not associated with structural defects. On the other hand, although AAE has no short-term effect on behaviors, it modulates transmission of layer V PFC neurons (sEPSCs and NMDAR currents) as well as dendritic spines density and morphology. As the transition from adolescence to adulthood is characterized by spine elimination and morphological changes in layer V projection neurons, we hypothesize that alcohol interferes with this maturation process, to in fine induces impaired behaviors. In order to analyze the developmental trajectory of layer V projection neurons rather than two arbitrary time-points, we are currently investigating synaptic density at different time-points following AAE in adolescence as a measure of synaptic pruning (**Figure 10 – preliminary results**).

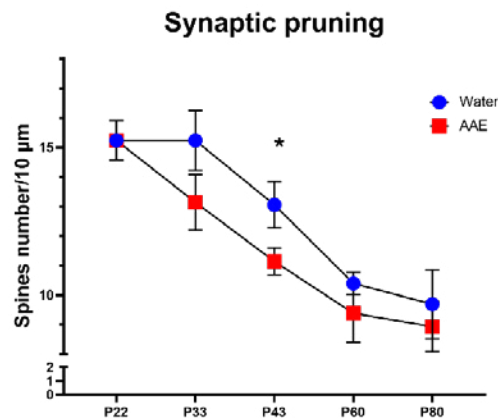


Figure 10. Developmental trajectory of dendritic spines density on layer V projection neurons of the prelimbic cortex from early adolescence to adulthood.

To further characterize the consequences of AAE on synaptic pruning during adolescence in projection neurons of the PFC, we are currently analyzing the excitatory/inhibitory balance in the three subregions of the PFC (**Figure 11 – preliminary results**). Excitatory synapses are defined by the co-localization of PSD95 and VGlut1, whereas inhibitory synapses are shown by the co-labeling of Gephyrin and VGat. Images are reconstructed and analyzed by Imaris software.

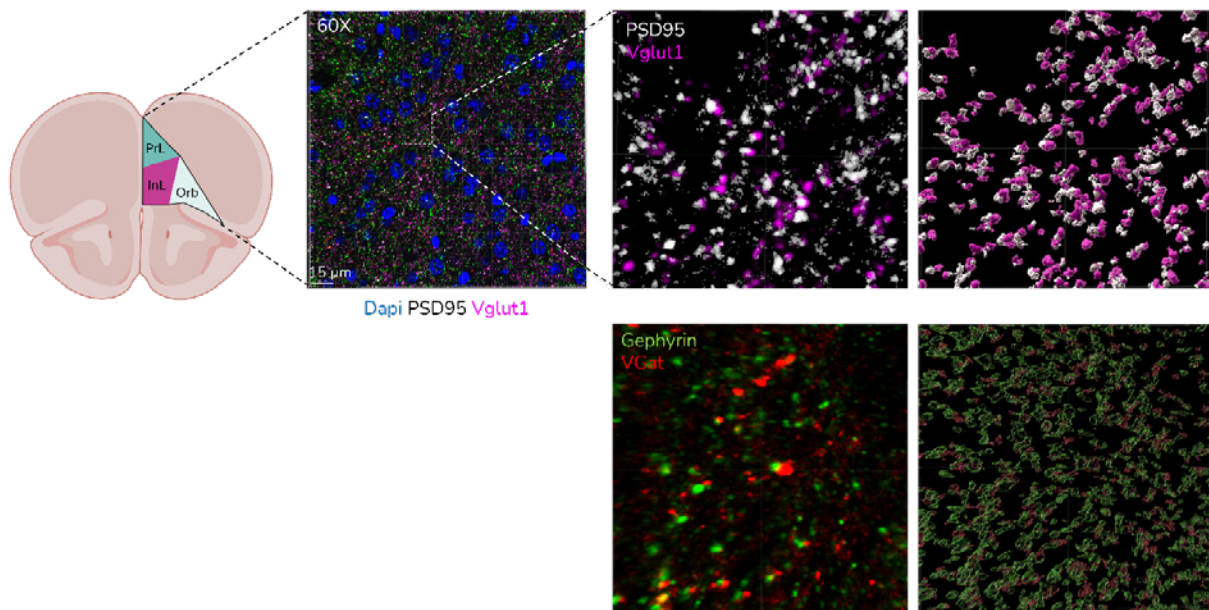


Figure 11. Excitatory and inhibitory synapses analysis in PFC.

1.2.3. Circuitry analysis

The PFC is known to be an integration center, receiving inputs from several brain regions, including the Nucleus accumbens, the dorso-medial striatum (DMS), the basolateral amygdala (BLA) and the dorsal raphe nucleus (DRN). It also sends outputs to several brain regions including the DMS, BLA, and DRN. Altered maturation of the PFC during adolescence could induce alterations in top-down circuitry in the adult brain, contributing to the behavioral defects observed following AAE. We are currently collaborating with the IMMI-CMMI at ULB (Gilles Doumont) to analyze synaptic activity via glucose intake by micro-PET-CT after injection of ¹⁸F-Fluorodesoxyglucose (Figure 12 – preliminary results). Synaptic activity was analyzed at basal level and following alcohol priming – low dose alcohol injection. Analysis is currently ongoing. The same mice were then analyzed for a global c-fos staining (basal conditions vs alcohol priming).

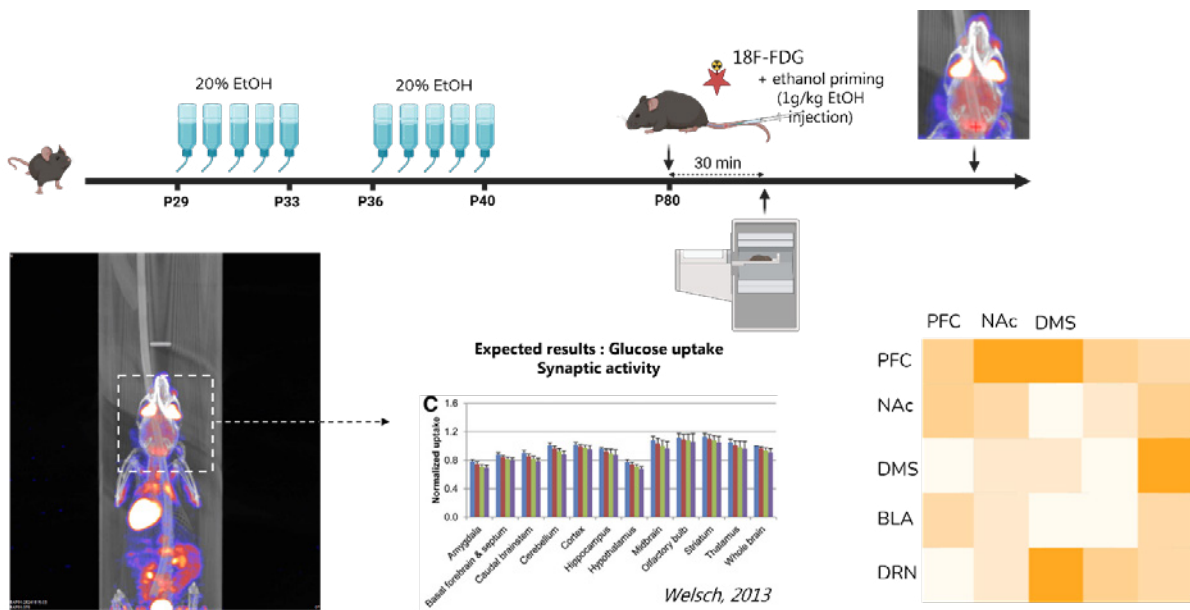


Figure 12. Scheme of the micro-PET CT experiment.

2. Task 2: Deciphering whether AAE modulates local translation in the adolescent PFC

2.1. Analysis of mTORC1 activity in the PFC following AAE

By western blot analysis on total PFC extracts, we have reported that AAE increases the phosphorylation levels of S6 Kinase and S6 in the PFC of males and females at P40, suggesting AAE-induced activation of mTORC1 activity following acute alcohol consumption (Figure 13).

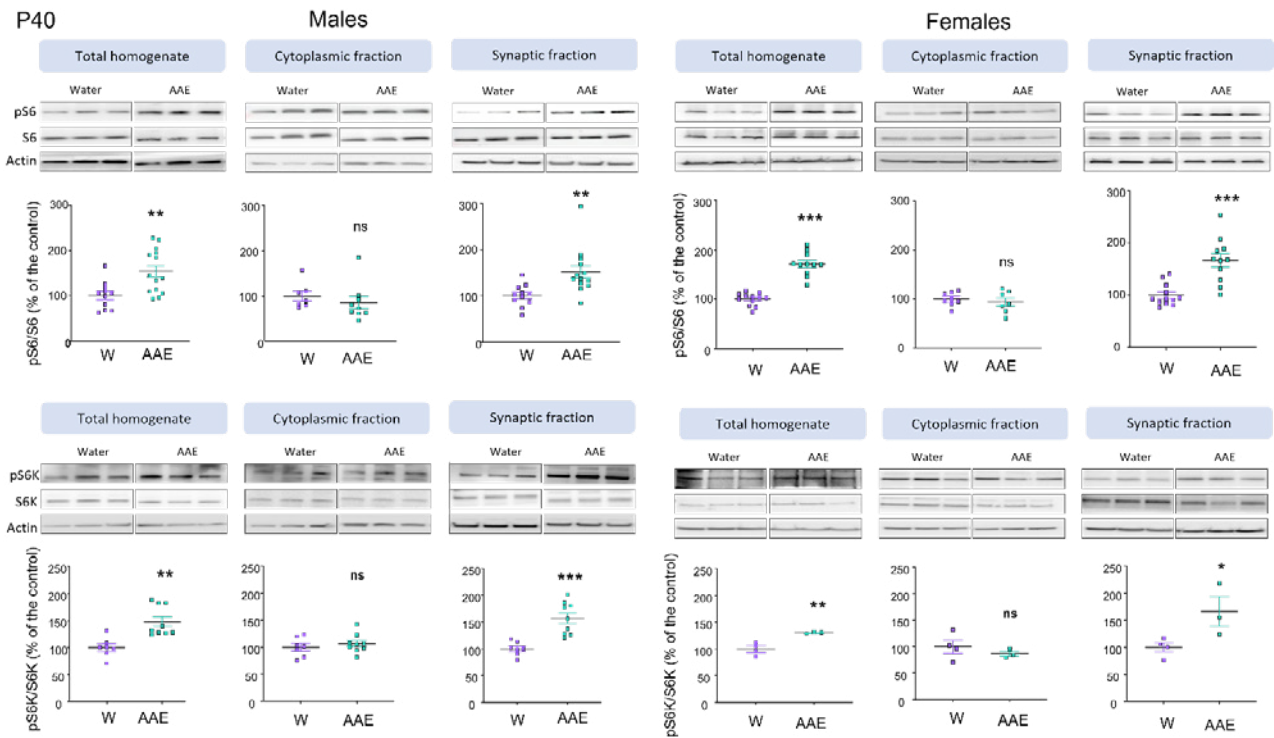


Figure 13. AAE activates mTORC1 in the adolescent PFC. Western blot analysis of phosphorylation levels of ribosomal protein S6 and S6 kinase in the PFC of males and females adolescent mice. Immediately after the last drinking session, PFC samples were dissected and analyzed by western blot. Significant increased phosphorylation of S6 and S6K were observed in the total homogenate and synaptic fraction of PFC extracts, both in males and females. * $p < 0.05$; ** $p < 0.01$; *** $p < 0.001$.

Moreover, by performing cytoplasmic and synaptic purification, we demonstrated that this increased mTORC1 activity is specifically found in the synaptic fraction, suggesting that alcohol exposure might specifically modulate the activity of mTORC1 in local translation rather than in global translation in the adolescent PFC (**Figure 13**).

Importantly, phosphorylation levels of S6 were not increased in the motor cortex or nucleus accumbens of alcohol-exposed adolescent mice (data not shown), suggesting that the alcohol-induced modulation of local translation might be specific to discrete brain regions including the PFC.

We also assessed S6 phosphorylation levels 72 hours after the last drinking session. As shown in **Figure 14**, S6 phosphorylation levels were significantly increased in the PFC of both males and females at P43, suggesting long-lasting activation of mTORC1 following AAE. Finally, when assessed at P80, no change in S6 phosphorylation levels were detected between water and AAE male mice (**Figure 15**). Additional western blot to assess p-S6K and p-4E-BP are currently performed in cytoplasmic and synaptic fractions of the PFC in both sexes at P43.

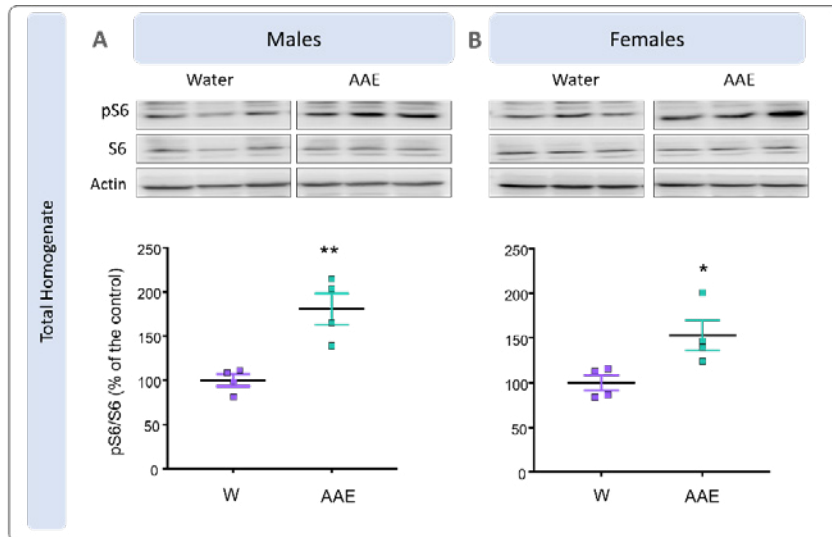


Figure 14. AAE-induced activation of mTORC1 is long-lasting. Western blot analysis of phosphorylation levels of ribosomal protein S6 in the PFC of males and females adolescent mice. Seventy-two hours after the last drinking session, PFC samples were dissected and analyzed by western blot. Significant increased phosphorylation of S6 were observed in the total homogenate of PFC extracts, both in males and females. * $p < 0.05$; ** $p < 0.01$.

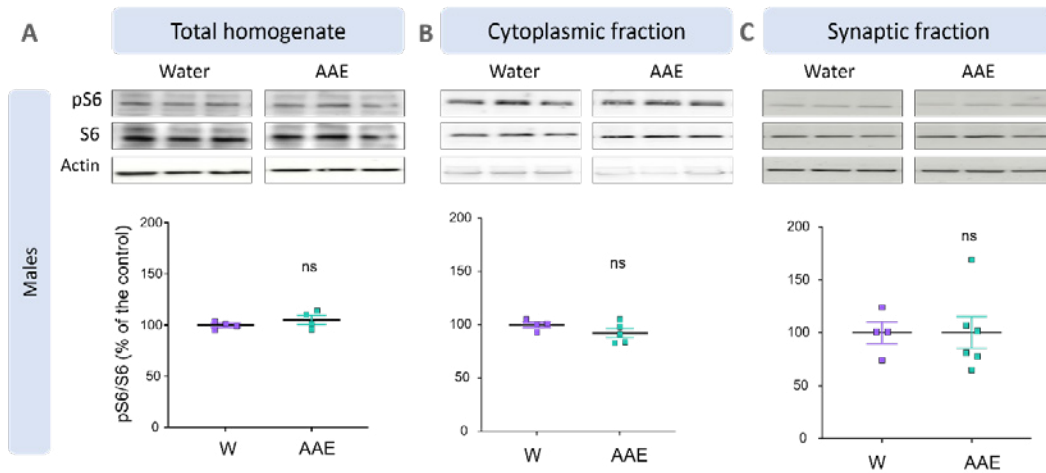


Figure 15. AAE-induced mTORC1 activation in the PFC is no longer present in adulthood. Western blot analysis of phosphorylation levels of ribosomal protein S6 in the PFC of males adult mice. Forty days after the last drinking session, PFC samples were dissected and analyzed by western blot. No significant change in S6 phosphorylation were observed in the total homogenate or synaptic/cytoplasmic fractions of PFC extracts.

We also assessed mTORC1 activation following AAE by immunofluorescence. As shown in **Figure 16**, we observed a significant increased phosphorylation of S6 in AAE animals at P40, both in males and females, which may specifically localize in the Ctip2+ layer V projection neurons.

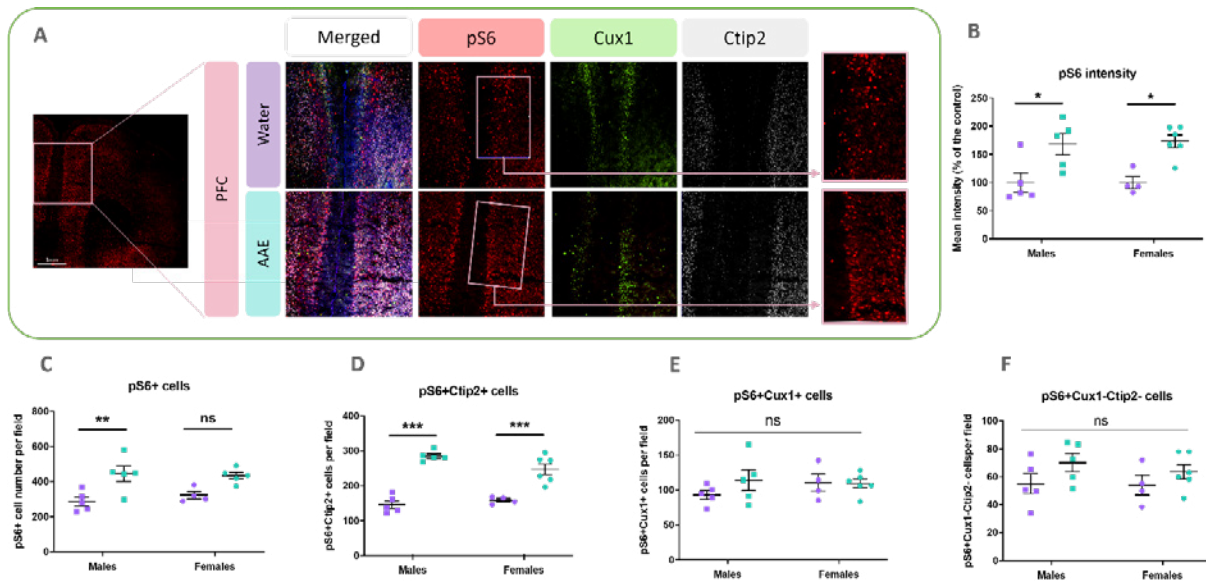


Figure 16. AAE increases S6 phosphorylation levels in PFC layer V neurons. Immunolabeling of the phosphorylated form of the ribosomal protein S6 in the PFC of males and females P40 adolescent mice. Immediately after the last drinking session, brains were dissected, fixed and used for Immunofluorescence. **(A)** pS6 in red, Cux1 in green, Ctip2 in gray. **(B)** Significant increased S6 phosphorylation intensity were observed in AAE animals compared to water controls extracts in both sexes. **(C)** Significant increased number of pS6-positive cells in AAE animals as compared to water controls. **(D-F)** The increased phosphorylation levels of S6 are localized mostly in layer V Ctip2-positive cells. * $p < 0.05$; ** $p < 0.01$; *** $p < 0.001$.

Additional experiments were conducted with additional neuronal identity markers (SatB2, Tbr1,...), and at later time-points (P43, P80), in both sexes. In order to analyze all the required neuronal identity markers and different brain regions, we set up the IF to perform automatically the analysis with the slide scanner Axioscan 7. **Figure 17** shows an example of coronal brain slice labelled with phospho-S6, Cux1, Satb2, Ctip2 and DAPI. All images have been taken and are currently analyzed by automated program using Imaris Software. Furthermore, we will use the Super-resolution Zeiss LSM880 AiryScan Elyra S1 confocal, to more specifically study pS6 intra-cellular localization.

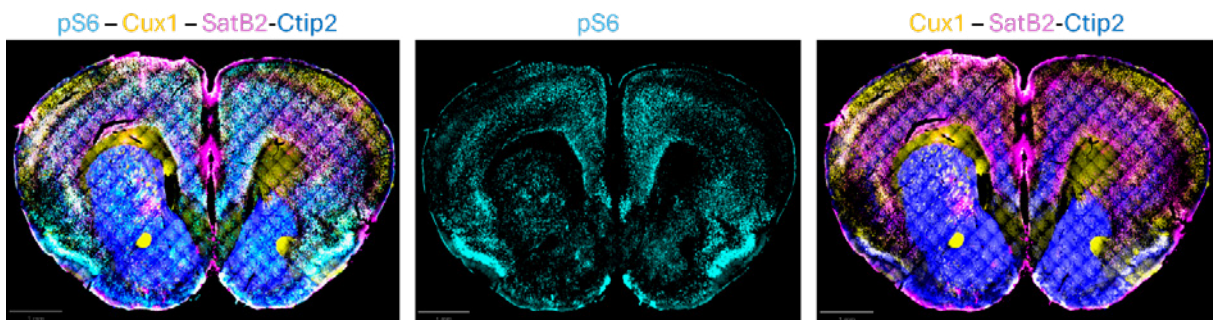


Figure 17. representative picture of P40 coronal brain slice stained with phospho-S6 and neuronal identity markers.

Finally, eIF2 and eEF2 activity are currently assessed in the PFC of males and females by western blot and immunolabeling (data not shown).

2.2. Task 2.2 Deciphering whether mTORC1, eIF2 and/or eEF2 mediate the structural and transmission defects induced by AAE in the PFC, as well as behavioral defects

We first conducted a pilot experiment where we inhibited mTORC1 activity by using systemic rapamycin injections, at the end of session 5 and session 10 of the AAE paradigm (**Figure 18**). Such timing of injections was used to avoid decreased alcohol consumption following rapamycin injections (Beckley, Laguesse *et al.* 2016). As shown in **Figure 18**, rapamycin treatment during adolescence significantly reduced alcohol consumption in adulthood in AAE animals. These findings

suggest that counteracting alcohol-dependent activation of mTORC1 during AAE may partially rescue the increased alcohol intake observed in adulthood following AAE.

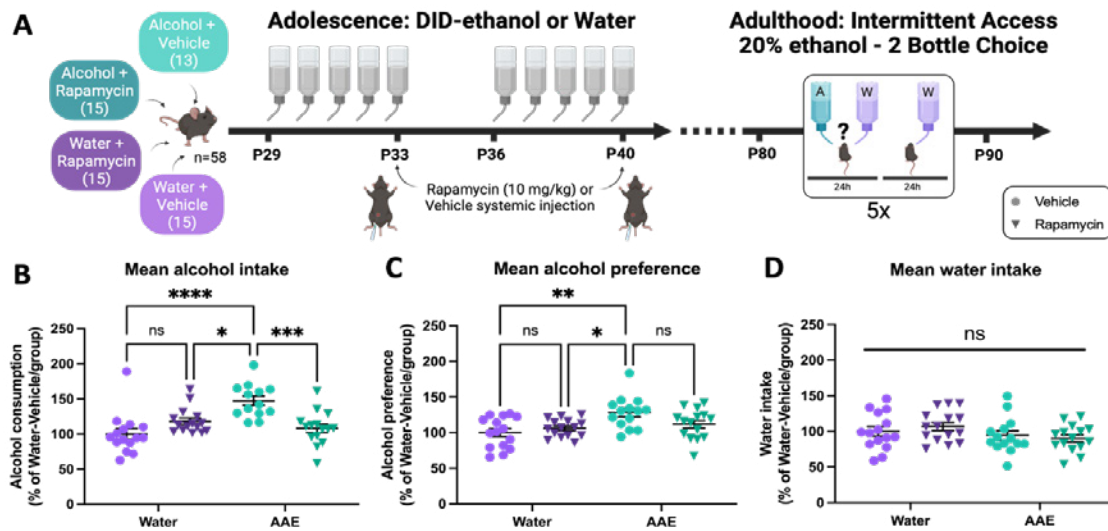


Figure 18. mTORC1 systemic inhibition during adolescent alcohol exposure reduces alcohol consumption and preference in adulthood. 4 groups of mice underwent the DID paradigm between P29 and P40. Rapamycin and Vehicle injections are shown in the scheme. After 40 days of abstinence, adult female mice underwent the Intermittent access to alcohol 20%-two-bottle choice (IA-20%-BC) paradigm for five sessions. **(B)** Mean alcohol consumption. Two-way ANOVA revealed a main effect of AAE ($p < 0.0001$) and an interaction ($p < 0.01$) but no significant main effect of rapamycin ($p = 0.10$). Post hoc Tukey test showed a significant difference between AAE/Vehicle and Water/Vehicle ($p < 0.0001$) as well as between AAE/Vehicle and AAE/Rapamycin ($p < 0.001$). **(C)** Alcohol preference. Two-way ANOVA showed a main effect of AAE ($p < 0.01$) and an interaction ($p < 0.05$) but no significant main effect of rapamycin. **(D)** Water consumption. Two-way ANOVA showed no significant main effect of AAE or rapamycin and no interaction. * $p < 0.05$; ** $p < 0.01$; *** $p < 0.001$; **** $p < 0.0001$.

As we previously reported that AAE leads to increased anxiety levels in adulthood, we tested anxiety levels in adult animals exposed to alcohol or water during adolescence, and which have received rapamycin or vehicle injections on days 5 and 10 (**Figure 19**). Our results confirm that AAE induces anxiety-like disorder in adult animals and suggest that rapamycin treatment during adolescence inhibits this increased anxiety levels.

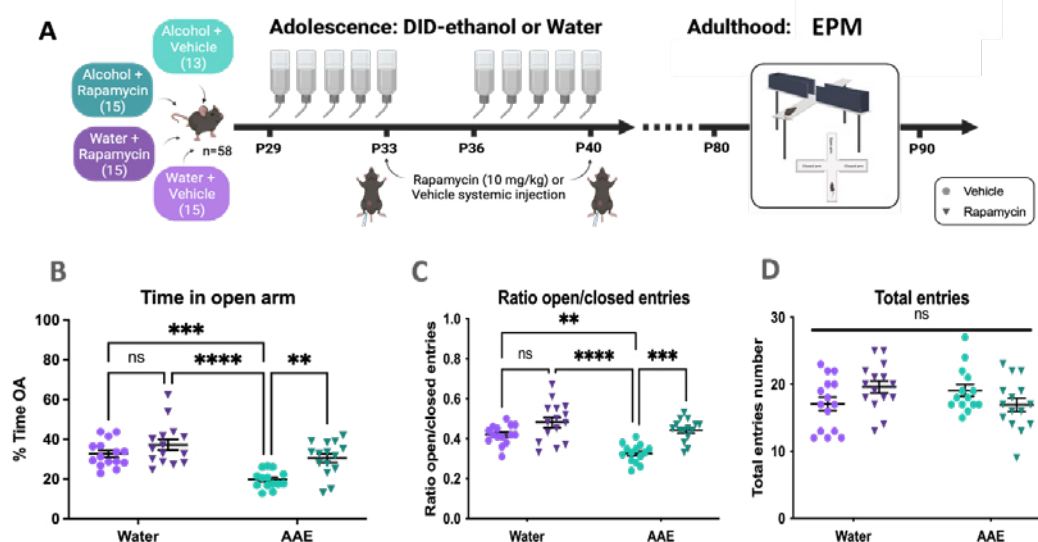


Figure 19. mTORC1 systemic inhibition during adolescent alcohol exposure reduces anxiety-like disorder in adulthood. 4 groups of mice underwent the DID paradigm between P29 and P40. Rapamycin and Vehicle injections are shown in the scheme. After 40 days of abstinence, adult female mice underwent the EPM test. **(B)** Time in open arms. Two-way ANOVA revealed a main effect of AAE ($p < 0.0001$), of rapamycin ($p < 0.001$) but no interaction. Post hoc Tukey test showed a significant difference between AAE/Vehicle and Water/Vehicle ($p < 0.001$) as well as between AAE/Vehicle and AAE/Rapamycin ($p < 0.01$). **(C)** Ratio Open/closed arm entries. Two-way ANOVA showed a main effect of AAE ($p < 0.001$) and rapamycin ($p < 0.001$) an interaction ($p < 0.05$). **(D)** Total entries. Two-way ANOVA showed no significant main effect of AAE or rapamycin and no interaction. * $p < 0.05$; ** $p < 0.01$; *** $p < 0.001$; **** $p < 0.0001$.

Those findings are very interesting as they suggest that mTORC1 signaling may be involved in the development of behavioral disorders following AAE. However, for the next steps, we will use intra-PFC AAV-delivery of shRNA against Raptor, which will allow for brain region specificity. Specific DNA constructs have been produced, and we set up stereotaxic coordinates for targeting the PFC at several time-points between P21 and P40 (**Figure 20**). Following intra-PFC infusion of shRNA against Raptor, we will test anxiety levels (EPM), alcohol consumption (IA20%-2BC), and flexibility (Barnes maze) in adulthood.

Sexe – Age	PFC coordinates	
Male P21	From Lambda (Bregma invisible)	AP: +3.2
		ML: +0.2
		DV: -2.1
Male P26	From Lambda (Bregma invisible)	AP: +4
		ML: +0.4
		DV: -2.3
Male P33	From Bregma	AP: +3.2
		ML: +0.2
		DV: -1.2
Male P40	From Bregma	AP: +3.0 ML: +0.2 DV: -1.7



Figure 20. Set up of stereotaxic coordinated for PFC targeting between P21 and P40.

2.3. **Task 3: Global approach: identify the mRNAs whose local translation is modulated by AAE in specific neuronal populations.**

Following validation of the Ribotag technology specificity (**Figure 21**), we performed the Ribotag-RNAseq profiling at P43 and P80 on male mice (Rpl22^{tm11Psam} mice crossed with VGlut1-cre mice, in order to purify the ribosome-associated mRNA from PFC projection neurons only).

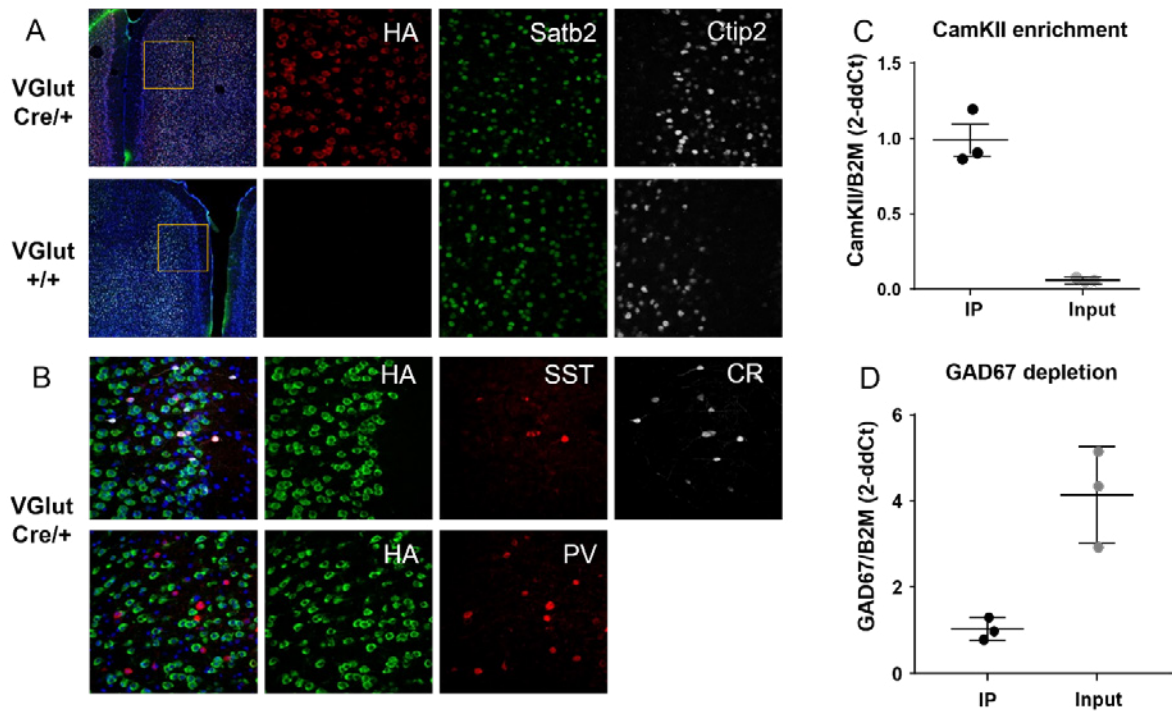


Figure 21. Validation of the specificity of the Ribotag mouse. (A) HA (red) co-localizes with glutamatergic markers Satb2 (green) and Ctip2 (grey) in prefrontal cortex of VGLutcre/+ mice, but is not expressed in absence of the Cre driver. (B) HA (green) does not co-localize with interneuron markers somatostatin (SST, red), calretinin (CR, grey), or parvalbumin (PV, red) in the PFC of VGLutcre/+ mice. (C, D) qRT-PCR after Ribotag immunoprecipitation shows that CamKII expression is enriched in the immunoprecipitate fraction from PFC of VGLutCre/+ mice as compared to the input (total mRNA) (C), whereas GAD67 expression is depleted (D).

The PCA plots of RNA-seq experiment nicely separates the data obtained in the neuronal translatoome (IP) and the PFC transcriptome (input) but it did not show major difference between water and AAE conditions (Figure 22).

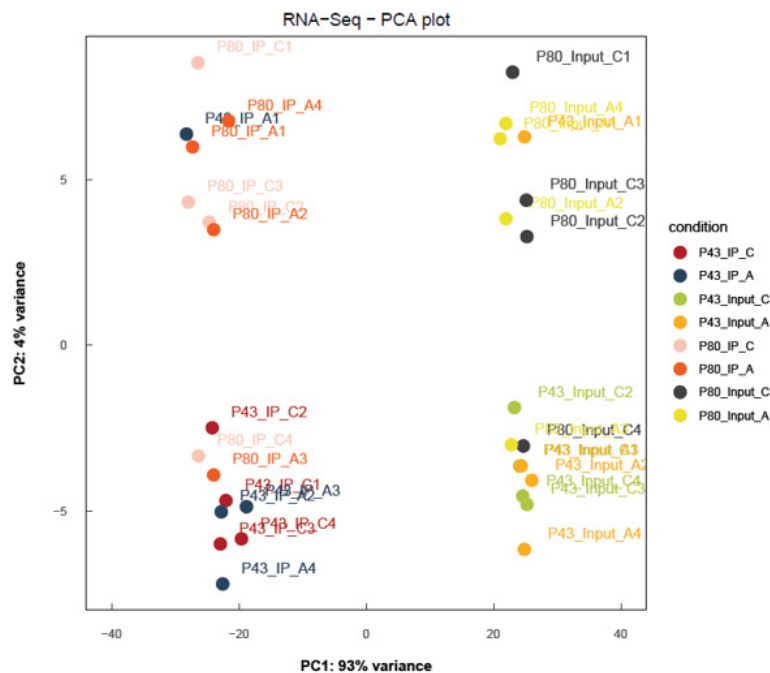


Figure 22. PCA plots of Ribotag-RNA seq experiment on P43 and P80 IP and input samples.

At P43, several ribosome-bound mRNA candidates were differentially expressed within the projection neuron population such as the lysine demethylase 6B (Kdm6b), the tribbles pseudokinase 1 (Trib1) and the nuclear receptor Nr4A1, which were increasingly expressed in the AAE projection neurons (**Figure 23**). Especially, Kdm6B and Nr4A1 are very interesting as they have been linked with synaptic plasticity, synaptic pruning and alcohol dependence.

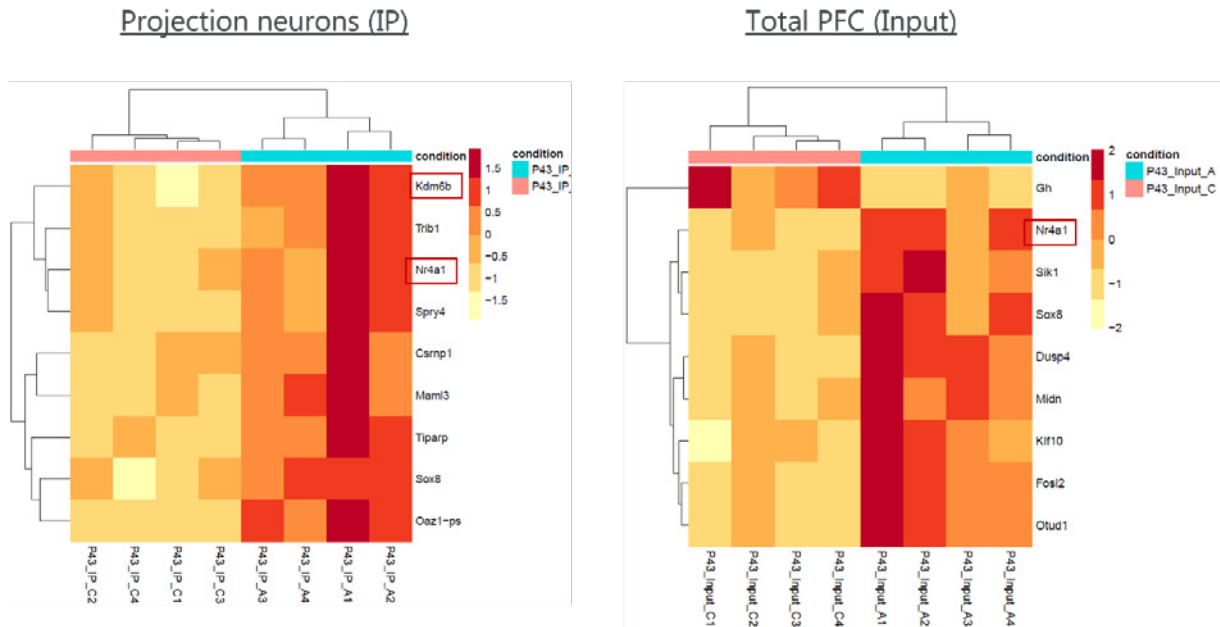


Figure 23. Differential expression of candidate genes at P43 in projection neurons (IP) or total PFC (input).

In addition, the Acetyl-Coenzyme A acetyltransferase (ACAT3) and the Neuropeptide FF (NPFF) showed reduced expression in AAE animals as compared to water controls. We validated some of the profiling results by ribosome-bound mRNA purification from PFC projection neurons and qRT-PCR analysis. Our results suggest AAE-dependent reduced expression of ACAT3 and NPFF in the PFC of P43 animals (but not the motor cortex (data not shown)) (**Figure 24**).

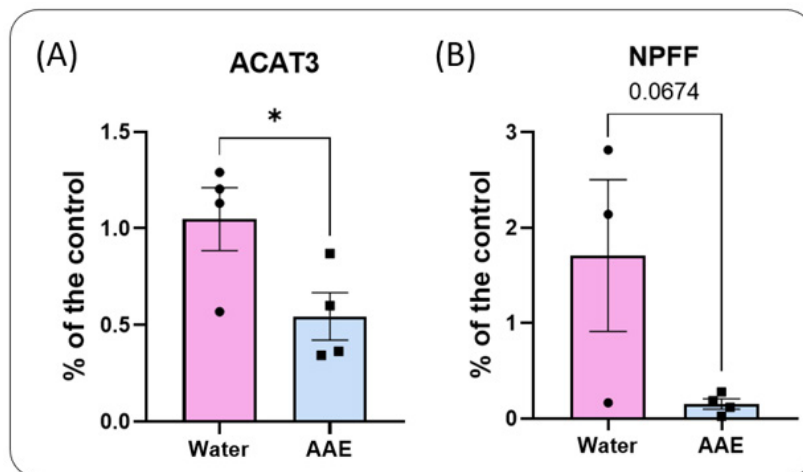


Figure 24. qRT-PCR analysis of ACAT3 and NPFF mRNAs in the IP and fraction after Ribotag IP in PFC samples at P43. (A) Unpaired t test showed ACAT3 mRNAs expression is decreased in alcohol-exposed mice as compared to water-exposed animals in IP fraction ($p=0.0488$). (B) NPFF mRNAs expression shows a tendency but is not significantly decreased in alcohol-exposed mice as compared to water-exposed mice in the IP fraction ($p=0.0674$). Data are presented as the average ratio of ACAT3 and NPFF to the mean of B2M and HPRT1 \pm SEM and expressed as the percentage of water control; * $p<0.05$.

At P80, RNA-seq analysis has revealed 144 differentially expressed genes (DEG) in the IP fraction by at least 1.2 or 0.8-fold and 236 DEG in the input fraction (**Figure 25**).

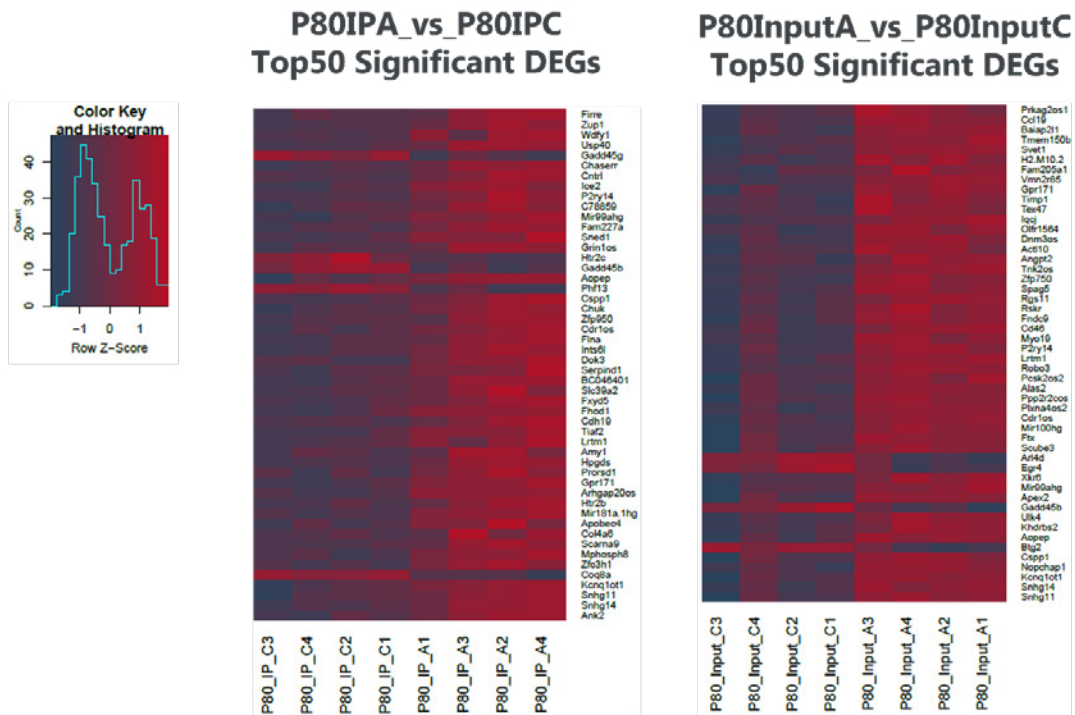


Figure 25. Differentially expressed genes in the IP (left) and input (right) fractions at P80.

We first chose to follow upon the actin-binding protein Filamin A (FLNA), the Glutamate kainate receptor subunit GRIK1 and the microtubule scaffolding protein IQ motif containing GTPase activating protein 1 (IQGAP1). qRT-PCR analysis showed significantly increased levels of the ribosome-bound FLNA and GRIK1 mRNAs content in IP fraction from PFC extracts of AAE animals as compared to water controls (**Figure 26**). In motor cortex (the control region), we did not report any significant difference in the level of FLNA and GRIK1 transcripts being translated in IP fraction (data not shown). In addition, we did not find any significant variation of ribosome-bound IQGAP1 transcripts expression between alcohol- and water-exposed mice in IP fraction in the prefrontal cortex (**Figure 26**). Hence, we did not confirm RNA-seq data for this transcript.

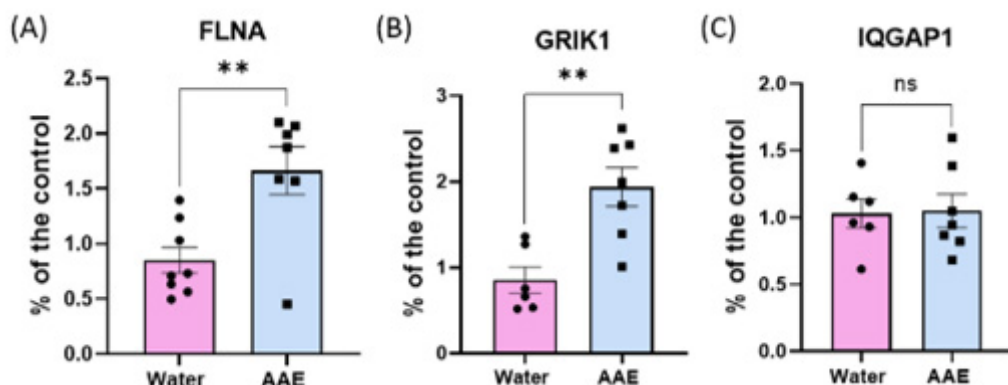


Figure 23. qRT-PCR analysis of FLNA, GRIK1 and IQGAP1 candidates at P80. Unpaired t test showed that (A) FLNA mRNAs expression is increased in the PFC IP fraction of alcohol-exposed mice as compared to water-exposed mice ($p=0.0046$). (B) GRIK1 mRNAs expression is also increased in the PFC IP fraction of alcohol-exposed mice as compared to water-exposed mice ($p=0.0026$). (C) No difference in the level of IQGAP1 mRNAs in the PFC IP fraction between the AAE and water groups was reported ($p=0.9133$). ** $p<0.01$.

As for P43, additional potential targets are currently being validated. Next step will be further analysis of AAE-induced dysregulation of mRNA expression in projection neurons, by immunofluorescence and western blot following FACS sorting of PFC projection neurons. Finally, the involvement of candidates mRNAs in AAE-induced PFC defects will be studied by using the multidisciplinary method described in Task 4 of the proposal.



Geneeskundige Stichting Koningin Elisabeth
Fondation Médicale Reine Elisabeth
Königin-Elisabeth-Stiftung für Medizin
Queen Elisabeth Medical Foundation

**Geneeskundige Stichting Koningin Elisabeth – G.S.K.E.
Fondation Médicale Reine Elisabeth – F.M.R.E.
Queen Elisabeth Medical Foundation – Q.E.M.F.**

Mailing address:

The scientific director:

Prof. dr. Jean-Marie Maloteaux
3, avenue J.J. Crocq laan
1020 Bruxelles – Brussel
Belgium
Tel.: +32 2 478 35 56
E-mail: jean-marie.maloteaux@uclouvain.be

Secretary:

Mr. Erik Dhondt
3, avenue J.J. Crocq laan
1020 Bruxelles – Brussel
Belgium
Tel.: +32 2 478 35 56
E-mail: fmre.gske@skynet.be
erik.dhondt@skynet.be
e.l.dhondt@skynet.be

www.fmre-gske.be
www.fmre-gske.eu
www.fmre-gske.com